Search for Magnetic Monopoles and Stable High-Electric-Charge Objects in 13 TeV Proton-Proton Collisions with the ATLAS and MoEDAL Detectors

LIONTI, Anthony Eric

Abstract

Malgré un succès indiscutable du modèle standard de la physique des particules, de nombreux aspects fondamentaux connus de la nature ne peuvent être expliqués par celui-ci. Une recherche de longue date de nouvelle physique est celle du monopole magnétique, jamais observé alors que théoriquement justifié et hypothétique symétrique de la charge électrique. Les particules magnétiquement chargées, telles que le monopole magnétique ou les dyons, interagiraient fortement avec la matière et seraient des particules hautement ionisantes, en anglais Highly Ionising Particles (HIP). Cette thèse se concentre sur la recherche des HIPs et en particulier du monopole magnétique avec deux détecteurs distincts, le détecteur ATLAS et le piège à monopole du détecteur MoEDAL, de l'anglais Monopole and Exotics Detector At the LHC (MoEDAL). Les deux analyses portent sur les collisions proton-proton du grand collisionneur de hadrons, Large Hadrons Collider (LHC) en anglais, avec une énergie au centre de masse de 13 TeV.

LIONTI, Anthony Eric. *Search for Magnetic Monopoles and Stable High-Electric-Charge Objects in 13 TeV Proton-Proton Collisions with the ATLAS and MoEDAL Detectors*. Thèse de doctorat : Univ. Genève, 2020, no. Sc. 5505

DOI : 10.13097/archive-ouverte/unige:144337
URN : urn:nbn:ch:unige-1443379

UNIVERSITÉ DE GENÈVE
Département de physique nucléaire et corpusculaire

FACULTÉ DES SCIENCES
Professeur Philippe Mermod
Professeur Tobias Golling

Search for Magnetic Monopoles and Stable High-Electric-Charge Objects in 13 TeV Proton-Proton Collisions with the ATLAS and MoEDAL Detectors

THÈSE

présentée à la Faculté des sciences de l'Université de Genève
pour obtenir le grade de Docteur ès sciences, mention physique

par

Anthony Lionti

de Aix-en-Provence (France)

Thèse N° 5505

GENÈVE
Atelier d'impression ReproMail
2020

UNIVERSITÉ
DE GENÈVE
FACULTÉ DES SCIENCES

DOCTORAT ÈS SCIENCES, MENTION PHYSIQUE

Thèse de Monsieur Anthony Eric LIONTI

intitulée :

«Search for Magnetic Monopoles and Stable High-Electric-Charge Objects in 13 TeV Proton-Proton Collisions with the ATLAS and MoEDAL Detectors»

La Faculté des sciences, sur le préavis de Monsieur T. GOLLING, professeur associé et directeur de thèse (Département de physique nucléaire et corpusculaire), Monsieur P. MERMOD, professeur assistant et codirecteur de thèse (Département de physique nucléaire et corpusculaire), Madame A. SFYRLA, professeure assistante (Département de physique nucléaire et corpusculaire), Monsieur D. MILSTEAD, professeur (Department of Physics, Stockholm University, Stockholm, Sweden), autorise l'impression de la présente thèse, sans exprimer d'opinion sur les propositions qui y sont énoncées.

Genève, le 18 octobre 2020

Thèse - 5505 -

Le Doyen

N.B. - La thèse doit porter la déclaration précédente et remplir les conditions énumérées dans les "Informations relatives aux thèses de doctorat à l'Université de Genève".

Résumé

La physique des particules est la branche de la physique qui postule que la matière et les radiations sont faites de particules élémentaires et étudie ces particules et leurs intéractions. Elle est modélisée par le modèle standard, Standard Model (SM) en anglais, de la physique des particules dont la formulation actuelle a été finalisée dans les années 1970. Les propriétés prédites par le SM ont été mesurées avec grande précision par de nombreuses expériences en physique des hautes énergies et la confirmation de l'existence des particules inclues dans le SM a contribué au succès de celui-ci. Pour pouvoir atteindre de très hauts niveaux d'énergies et observer des preuves des prédictions du SM, des expériences internationales à grandes échelles ont été conçues. Le grand collisionneur de hadrons, Large Hadrons Collider (LHC) en anglais, est le plus grand et le plus énergétique collisionneur au monde, avec une énergie au centre de masse maximale théorique de 14 TeV et une circonférence de 27 kilomètres. Il est à l'origine de la découverte du boson de Higgs en 2012, la dernière particule manquante prédite par le SM, détectée indépendamment par le détecteur CMS, de l'anglais Compact Muon Solenoid (CMS), et le détecteur ATLAS, de l'anglais A Toroidal LHC ApparatuS (ATLAS). Malgré un succès indiscutable du SM, de nombreux aspects fondamentaux connus de la nature ne peuvent être expliqués par celui-ci. La matière noire par exemple ne peut pas être accomodée au SM, de même celui-ci ne peut pas expliquer l'asymmétrie matière anti-matière, ou bien l'oscillation des neutrinos et donc l'existence de leurs masses. Naturellement des modèles essayant de résoudre les limitations du SM ont été développés et forment la physique au-delà du modèle standard, en anglais Beyond Standard Model (BSM). Les expérimentateurs en physique des particules recherchent de la nouvelle physique et la validation d'un modèle BSM. Une recherche de longue date de nouvelle physique est celle du monopole magnétique, jamais observé alors que théoriquement justifié et hypothétique symmétrique de la charge électrique. Les particules magnétiquement chargées, telles que le monopole magnétique ou les dyons, interagiraient fortement avec la matière et seraient des particules hautement ionisantes, en anglais Highly Ionising Particles (HIP). Cette thèse se concentre sur la recherche des HIPs et en particulier du monopole magnétique avec deux détecteurs distincts, le détecteur ATLAS et le piège à monopole du détecteur MoEDAL, de l'anglais Monopole and Exotics Detector At the LHC (MoEDAL). Les deux analyses portent sur les collisions proton-proton du LHC avec une énergie au centre de masse de 13 TeV. Ces analyses sont la suite naturelle des recherches précédentes réalisées à plus faibles énergies, conséquences de l'incertitude théorique sur la masse du monopole magnétique.

Abstract

Particle physics is the branch of physics that postulates that matter and radiation are made of elementary particles and studies those particles and their interactions. It is modelled by the Standard Model (SM) of particle physics whose current formulation was finalised in the 1970s. Properties predicted by the Standard Model have been measured with high accuracy in numerous high energy physics experiments and the confirmation of the existence of the particles included into the model contributed to its success. In order to reach very high energy levels and observe evidences of the model predictions, large scale international experiments were designed. The Large Hadron Collider (LHC) is the world's largest and highest energy particle collider with a design energy at centre of mass of 14 TeV and a 27 kilometres circumference. It is responsible for the discovery of the Higgs boson in 2012, last missing particle predicted by the Standard model, detected by both the Compact Muon Solenoid (CMS) detector and the A Toroidal LHC ApparatuS (ATLAS) detector. Despite the indisputable success of the Standard Model of particle physics, many fundamental known aspects of nature cannot be explained by it. The dark matter for example cannot be accommodated into the Standard Model, similarly it cannot explain the matter-antimatter asymmetry, or the neutrino oscillations and hence their existence as massive particles. Naturally models attempting to formalise possible solutions to the standard model limitations were developed and are known as physics Beyond the Standard Model (BSM). Experimentalists in particle physics are searching for new physics and confirmation of a BSM model. One of the long-time search for new physics is the search for a magnetic monopole, never observed in nature while theoretically justified and hypothetical symmetric equivalent of the electric charge. Magnetically charged particles, such as the magnetic monopoles or the dyons, would interact strongly with matter and are known as Highly Ionising Particles (HIP). This thesis focus on the search of HIPs and in particular the magnetic monopole with two distinct detectors, the ATLAS detector and the Monopole and Exotics Detector At the LHC (MoEDAL) magnetic monopole trapping array. Both analyses were done with LHC proton-proton collisions with an energy at centre of mass of 13 TeV. Those analyses are the natural continuations of previous searches done at lower energies resulting of the unknown theoretical mass of the magnetic monopole.

Acknowledgements

My PhD time will for sure remain in my memory forever. Not because, as one could expect, of the hard work required to success this challenge, but rather because of all the amazing people from all over the world I had the chance to meet. It goes without saying that not all of those people will appear in the following paragraphs and I apologise for it. But I can only emphasise that I am very thankful to all the people I met during this adventure.

First of all, I would like to thank my thesis supervisor Philippe Mermod for giving me the chance to work on such an interesting topic, in possibly the best environment for HEP. Philippe gave me precious advices and guidance all along the path of my PhD and I am very grateful for all the memorable exchanges we could have.

I would like to offer my special thanks to the York University HIP analysis team Wendy Taylor, Ana Maria Rodriguez Vera and Wen-Yi Song. It was a pleasure working with you on the search for monopoles and I am glad to see that the analysis is continuing.

Special thanks also to Akshay Katre and Gabriel Palacino, whose experience on the previous analysis was very helpful.

I want to thank my office mates, Arnaud Dubreuil and Avishek Chatterjee. Avi stayed with Arnaud and I for only a year, but I can tell that we both missed its strong personality for the remaining of the PhD. I have so many memories in the CERN office with Arnaud. I would simply like to say: thank you Arnaud.

On a more general level, I would like to thank all the DPNC members. The professors, in particular Anna Sfyrla and Tobias Golling who accepted to review my thesis and gave me precious advices. The postdocs who all are incredible people, ready to answer any questions I could have had. In particular Lucian Ancu which I had the pleasure to meet again in Zurich, Steven Schramm and Teng Jian Khoo. The administration, in particular Catherine Blanchard and Nathalie Chaduiron. The students: I had so much fun with all of you.

This PhD was a unique opportunity to meet amazing students, not only from the UniGe, but from all around the world, at CERN, in summer schools or during conferences. I cannot wait to get a chance to meet you again.

I would like to express my gratitude to the TRT team with who I spent a year during my qualification task and learned so much. I have had the support and encouragement of Alexey Boldyrev and Frederick Luehring. I would like also to thank Artem Maevskiy who in addition to his support on the TRT work, exchanged with the HIP analysis on the multi-charged particles analysis. I want to thank Dimitrii Krasnopevtsev and Joany Manjarres for their support. My deepest appreciation goes to Narei Lorenzo. Without her guidance and persistent help my qualification task would not have been possible.

I want to thank the e-gamma trigger team, in particular Ryan Mackenzie White and Gabriella Pasztor, who gave me precious support during the HIP trigger development. I am also thankful to be given the chance to be at the trigger desk in the ATLAS control room.

I would like to show my greatest appreciation to the MoEDAL team. It was a unique chance to be part of the MoEDAL collaboration and I am very grateful for that. While the magnetic monopole search in a collaboration as big as ATLAS was atypical and exotic, it was comforting to be part of a collaboration where every member was enthusiastic about the magnetic monopole.

Special thanks to Richard Soluk and Ameir Shaa Bin Akber Ali with who we scanned multiple times the MoEDAL trapping detector in the Zurich SQUID magnetometer. I would also like to thank Ann Hirt and Hanspeter Hächler from the LNM laboratory for their warm welcome and support.

I would like to offer my special thanks to Christoph Renner who gave me the opportunity to assist him in the classes of "Mécanique I" and then allowed me to join the Physiscope. I owe my deepest gratitude to Olivier Gaumer and to the entire team of the Physiscope. The physiscope was an incredible experience and leaves me so many wonderful memories. Special thanks also to the "Physique Générale B" team.

Finally I would like to thank my family and friends, for their support and motivation, but also for giving me a chance from time to time to exit the physicists world and enjoy other aspects of life. A tremendous thank you to all my friends, from Marseille, from Geneva, from Phelma, from everywhere. We had countless moments of fun and you definitely contributed to my PhD success too.

My family's encouragements were invaluable. I owe a very important debt to my parents and my brother who believed in me my whole life.

The last and most important goes to my wife, Huan, who never gave up and encouraged me without ceasing during the writing of this thesis at the cost of long nights and weekends locked down at home.

Dedication

À mamie, ma plus fervente supportrice.

À Huan, ma femme, ma plus belle découverte de cette aventure.

致我心爱的小史迪奇，没有她，我将永远不会写这篇论文。

‘I always thought they were balls of gas burning billions of miles away.’
Pumbaa

Contents

List of Tables

List of Figures

Chapter 1

Introduction

After a succinct overview of the Standard Model (SM) of particle physics, this section introduces the main theories of magnetic monopoles and a summary of the different detection techniques and searches.

1.1 The Standard Model of particle physics

The SM aims at describing matter at a fundamental level. It describes elementary particles and their interactions, the electromagnetic, weak and strong interactions.

Represented by the group $SU(3)_C \times SU(2)_L \times U(1)_Y$, the SM is a gauge invariant theory under transformations of this group. $SU(3)_C$ represent the colour charged particles strong intereaction, and $SU(2)_L \times U(1)_Y$ the electroweak interaction. First theorised by Glashow [1], Weinberg [2] and Salam [3] the electroweak theory was a major contribution to the standard model theory and led to the discovery of the electroweak force bosons, the Z and $W^{\pm}$ bosons, in 1983.

The SM introduces a particles zoo composed of Bosons, following the Bose-Einstein's statistics, and Fermions, following the Fermi-Dirac's statistics. Bosons included into the SM are either scalar or vector forces carriers and thus have integer spin equal to 0, that is the case of the

Higgs boson discovered in 2012 at CERN, or 1, for all vectors such as the photon γ, the gluon g and the Z and W bosons. Fermions have half-integer spins and represent the matter separated into two catagories: the leptons and the quarks. The leptons are particles electrically charged at the exception of the neutrino being as his name stands for a neutral particle. The leptons are separated into families or generation. Only three generation of leptons have been observed in nature, the electron e, the muon μ and the tau τ. The quarks are colour charged particles and are the elementary composants of the hadrons in turn regrouped into: the mesons, composed of an even number of quarks and gluons, the baryons, composed of an odd number of quarks and gluons, that is triquarks and recently discovered pentaquarks [4], composed of five quarks and gluons.

Fig. 1.1 gives an overview of the SM elementary particles including their, electric charge, spin and approximated mass. Each of those particles have an associated antiparticle. Those antimatter particles are differing from their matter counterparts in the charge, electric or colour charge, and chirality being the opposites. Neutral particles such as the photon, the gluons, Z and H bosons are their own antiparticles. Neutrinos on the other hand depending on the theories are allowed to have distinct anti-particles having an opposite chirality.

1.2 Magnetic monopoles

Electromagnetic interactions have been observed in nature for elementary particles with an electric charge only. Those interactions are carried by the photons and are classically described by Maxwell's equations.

1.2.1 Magnetic monopoles and electromagnetisms

Maxwell's equations are classically written as:

$$\begin{aligned} &\vec{\nabla} \cdot \vec{E} = \tfrac{\rho_e}{\epsilon_0}, \quad \vec{\nabla} \times \vec{E} = -\tfrac{\partial \vec{B}}{\partial t} \\ &\vec{\nabla} \cdot \vec{B} = 0, \quad \vec{\nabla} \times \vec{B} = \mu_0 \epsilon_0 \frac{\partial \vec{E}}{\partial t} + \mu_0 \vec{j}_e \end{aligned} \tag{1.1}$$

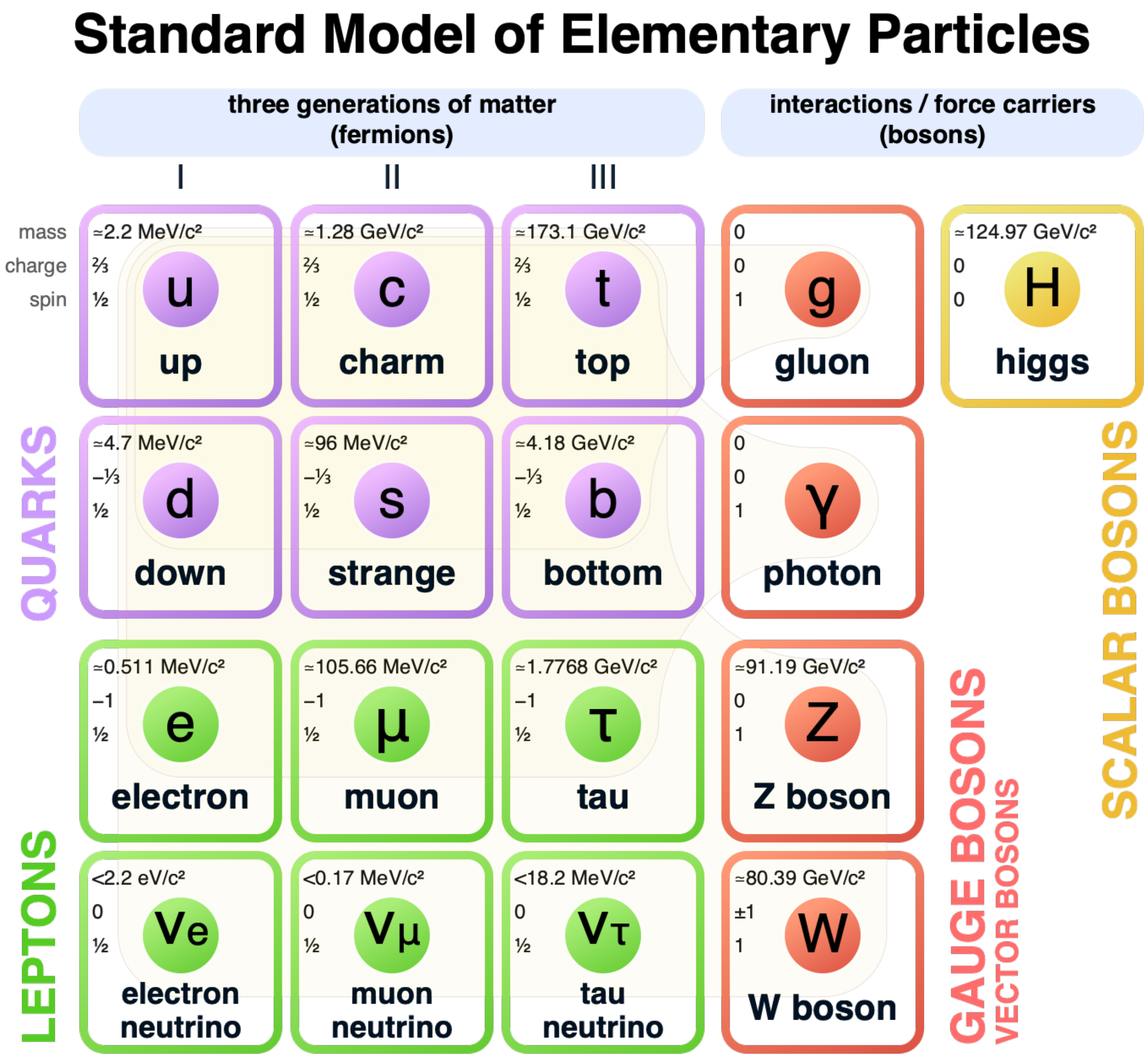

Figure 1.1: The standard model of particle content

where $\vec{E}$ and $\vec{B}$ are the electric and magnetic fields, respectively, $\vec{j}_e$ the electric charge density, and ρ_e the electric current density.

The equation 1.1 is asymmetric with respect to the electric and magnetic fields. That is to reflect the assumption that there is no magnetic field source in nature. Relaxing this hypothesis and hypothesising the existence in nature, yet unobserved, of a magnetically charged elementary particle, the magnetic monopole, one could formulate a more general version of Maxwell's equations:

$$\begin{aligned} \vec{\nabla}\cdot\vec{E} &= \tfrac{\rho_e}{\epsilon_0}, & \vec{\nabla}\times\vec{E} &= -\tfrac{\partial\vec{B}}{\partial t} - \mu_0\vec{\jmath}_m \\ \vec{\nabla}\cdot\vec{B} &= \mu_0\rho_m, & \vec{\nabla}\times\vec{B} &= \mu_0\epsilon_0\tfrac{\partial\vec{E}}{\partial t} + \mu_{00}\vec{\jmath}_e \end{aligned} \tag{1.2}$$

with ρ_m and $\vec{\jmath}_m$ the magnetic charge and current densities, respectively.

Seen as a source of magnetic charge, Monopoles are point-like particles with magnetic charge density $\rho_m = g\delta(\vec{x})$. The symmetry is now restored and equations 1.2 are invariant under the following transformation:

$$\begin{pmatrix} \vec{E} \\ c\vec{B} \end{pmatrix} = \begin{pmatrix} \cos\xi & \sin\xi \\ -\sin\xi & \cos\xi \end{pmatrix} \begin{pmatrix} \vec{E}' \\ c\vec{B}' \end{pmatrix}, \quad \begin{pmatrix} c\rho_e \\ \rho_m \end{pmatrix} = \begin{pmatrix} \cos\xi & \sin\xi \\ -\sin\xi & \cos\xi \end{pmatrix} \begin{pmatrix} c'_e \\ \rho'_m \end{pmatrix} \tag{1.3}$$

where ξ is the transformation parameter and c is the speed of light.

In particular for $\xi = \pi/2$, $\vec{E}$ can transform in $\vec{B}$ and reciprocally.

1.2.2 Dirac Monopoles

Introduced as an hypothetical particle by Pierre Curie in 1894 [5], the magnetic monopole was incorporated into electromagnetism and quantum physics by Dirac in the first half of the twentieth century [6, 7].

The Dirac string

To accommodate the magnetic field $\vec{B}$ of a magnetic monopole:

$$\vec{B}(\vec{r}) = \frac{\mu_0 g}{4\pi r^2}\hat{r} \tag{1.4}$$

Dirac introduced an infinitely thin and long solenoid, extending from the source to infinity. Such a magnetic dipole has thus one pole at the source and one pole at infinity. The associated magnetic vector potential is:

$$\vec{A}(\vec{r}) = \frac{\mu_0 g(1-\cos\theta)}{4\pi r\sin\theta}\hat{\phi} \tag{1.5}$$

Although this potential has a singularity for $\theta = \pi$ the derived observable $\vec{B} = \vec{\nabla} \times \vec{A}$ is in the form of Eq. 1.4

One can note that Dirac monopoles can be bosons or fermions and that no assumption on the mass of the monopole was made.

Charge quantization condition

While the potential vector of magnetic and electric fields are not observables, associated quantum effects can occurs. The most famous example of such effect is the Aharonov-Bohm effect [8]. The Dirac string potential vector is thus not trivial anymore at the quantum level.

Considering a point particle with electric charge q going around the Dirac string describing an infinitesimally small loop, the wave function's phase given by:

$$\Delta\phi = \frac{q}{\hbar} \int \vec{A} \cdot d\vec{l} = \lim_{\theta \to \pi} \frac{q}{\hbar} \frac{\mu_0 g(1 - \cos\theta)}{4\pi r \sin\theta} \int_0^{2\pi} r \sin\theta d\phi = \frac{\mu_0 q g}{\hbar} \tag{1.6}$$

is affected by the Dirac string. In order to cancel this effect and to obtain a true monopole-like string the phase change as to be a multiple of 2π. This condition leads to a quantized electric charge and is known as the Dirac quantization condition:

$$qg = \frac{nh}{\mu_0} \tag{1.7}$$

where n is a non-negative integer.

The lowest electric charge observed in nature is the charge of the electron e. Replacing q by e in equation 1.7 leads to:

$$g = \frac{n}{2\alpha}(ce) \quad \xrightarrow{n=1} \quad g_{\mathrm{D}} = \frac{(ce)}{2\alpha} \tag{1.8}$$

with $\alpha = \frac{\mu_0 e^2 c}{4\pi\hbar}$. For n=1 the magnetic charge is thus the lowest and known as the Dirac charge.

From Eq. 1.8 one can derives that g_{D} is approximately equivalent to 68.5 times the elementary electric charge, e. The magnetic monopole is thus considered as a Highly Ionising Particle

(HIP).

Dirac's quantization condition can also be derived from the angular momentum of a system formed by a magnetic monopole and an electrically charged particle. This work is of great importance in the quantum mechanics theory of the magnetic monopole and Dirac opened the way to many theories of the magnetic monopole.

1.2.3 Magnetic monopoles in more recent theories

Schwinger

Revising Dirac's theory of monopoles and studying its relativistic invariance, Julian Schwinger came up with a vector potential solution for a magnetic monopole field [9] given by:

$$\vec{A}(\vec{r}) = -\frac{\mu_0 g}{4\pi r} \cot\theta \hat{\phi} \tag{1.9}$$

The Dirac quantization condition is now restricted to even n values:

$$qg = \frac{2nh}{\mu_0} \tag{1.10}$$

The minimal charge of a magnetic monopole according to Schwinger theory is thus two times the Dirac charge.

The difference arrises from the fact that Schwinger string is infinite while the Dirac string is semi-infinite.

Schwinger also introduced hypothetical particles carrying both an electric and a magnetic charge. Those particles are known as dyons.

Cho-Maison

Y. M. Cho and D. Maison presented an electro-weak monopole [10] in the Weinberg-Salam model. Such monopoles or dyons follow Schwinger's charge quantization condition and thus monopoles would have a minimum magnetic charge of $2g_{\mathrm{D}}$. In the initial publication, Cho-Maison monopoles do not have a defined mass, as it is the case for Dirac monopole. However recent developments [11] restrain the mass of electroweak monopoles between 4 and 10 TeV. In turn the Cho, Kim and Yoon model has been generalised to take into account the LHC measurement of the Higgs boson decay rate. It has been found that the monopole mass could be below 5.5 TeV, so that it could be pair-produced at the LHC.

T'hooft-Polyakov

Magnetic monopoles are predicted by Grand Unified Theories (GUT) as shown by 't Hooft [12] and Polyakov [13]. GUT models allow monopoles as topological defects. The direction of the scalar field can be coupled to the spatial direction. The vacuum symmetry breakdown thus admit such a solution known as the hedgehog configuration:

$$\phi^a = v\frac{r^a}{r}, \quad a = 1, 2, 3 \tag{1.11}$$

As a local minimum of the scalar potential, this is a topologically stable solution [12]. Equation 1.11 leads to a solution of the non-Abelian electromagnetic gauge potential, which represents the Coulomb-like non-Abelian field of a point particle from which the Dirac string vector potential can be extracted [14].

1.2.4 Interaction of monopoles with matter

Magnetically charged particles have similar interaction with matter than electrically charged ones. In the presence of an electromagnetic field they experience the Lorentz force.

$$\vec{F} = q(\vec{E} + \vec{v} \times \vec{B}) + g\left(\vec{B} - \vec{v} \times \frac{\vec{E}}{c^2}\right) \tag{1.12}$$

with q and g the electric and magnetic charges. The electric charge equivalent of the Dirac charge $g_\mathrm{D} \approx 68.5(\mathrm{ce})$ implies that the interaction of a monopole with an electric field is much stronger than the one an electron would experience in the same field.

Energy loss via ionisation

The Bethe-Bloch formula describe the energy losses by ionization of an electrically charged particle:

$$-\frac{dE}{dx} = \frac{4\pi e^4 z^2 N_e}{m_e c^2 \beta^2}\left[\ln\left(\frac{2m_e c^2 \beta^2 \gamma^2}{I}\right) - \beta^2 - \frac{\delta}{2}\right] \tag{1.13}$$

where z is the atomic number of the particle corresponding to the charge in units of e and β its velocity in natural units, $m_e c^2$ the electron rest mass, N_e and I are the electron density and mean ionization energy of the material, and δ is a density effect correction that becomes relevant for ultrarelativistic particles. A magnetic monopole travelling through matter will generate a magnetic field interacting will the orbiting electrons and deposit large amount of energy. It is thus considered as a highly ionizing particle.

The interaction of magnetically charged particles with the electric charges in the matter appears from Eq. 1.13 to be proportional to $g\vec{v}\times\vec{E}$. In order to derive the Bethe-Bloch formula for magnetically charged particles a first simple solution thus consist in substituting the electric charge ze in the Eq. 1.13 by βg. The β contribution makes two distinct regimes of energy losses of magnetic monopoles: a low-momentum transfer and a high-momentum one. The low-momentum transfer or distant-interaction regime can be modelled using the dipole approximation. The high-momentum transfer or close-interaction regime has been modelled by Kazama, Yang and

Goldhaber (KYG) by solving the Dirac's equation of an electron in the magnetic field of a monopole [15].

In order to accommodate the Bethe-Bloch formula to both close- and distant-interaction regimes for monopoles with $\beta > 0.2$ and $\gamma \lesssim 100$, Ahlen came up with the stopping-power formula [16]:

$$-\frac{dE}{dx} = \frac{4\pi e^2 g^2}{m_e c^2} N_e \left[\ln\left(\frac{2m_e c^2\beta^2\gamma^2}{I}\right) + \frac{k(g)}{2} - \frac{1}{2} - \frac{\delta}{2} - B(g)\right] \tag{1.14}$$

where $g = ng_{\mathrm{D}}$, $k(g)$ is the KYG correction given by

$$k(g) = \begin{cases} 0.406 & |n| \leq 1 \\ 0.346 & |n| \geq 1.5 \end{cases} \tag{1.15}$$

which arises from the relativistic cross section calculated in Ref. [15], and B(g) is the Bloch correction given by

$$B(g) = \begin{cases} 0.248 & |n| \leq 1 \\ 0.672 & |n| \geq 1.5 \end{cases} \tag{1.16}$$

which accounts for higher order effects for low-energy collisions in which the monopole velocity approaches the orbital velocity of the electron. For $\gamma \gtrsim 100$, spin effects and contributions from the internal structure of nuclei become important and the formula is not valid anymore. For $\beta < 0.01$, the energy losses of monopoles are approximated by [17]

$$-\frac{dE}{dx} = \left(45 \quad \mathrm{GeVcm}^{-1}\right) n^2\beta \tag{1.17}$$

with $n = g/g_{\mathrm{D}}$ This formula does not consider interactions with the electron spin. For $0.01 < \beta < 0.1$ the stopping power is modelled by interpolating between the predictions of Eq. 1.14 and Eq. 1.17.

Energies involved in magnetic monopoles spin-flip transitions are non-negligeable only at very low β where the Lorentz force experienced by the electron is weak and the ionization is null [16]. From (Eqs. 1.13 and 1.14), one can derive that the ionization power of a monopole of charge

$|g| = 1.0g_{\mathrm{D}}$ is four orders of magnitude higher than the one of an electrically charged particle with $|z| = 1$.

The Bragg peak is not applicable to magnetic monopoles, indeed the monopoles energy loss dependancy in velocity is opposite from electrically charged particles one and the energy loss decrease with decreasing velocities. This effect can be see in Figure 1.2 showing the energy losses by ionization by an electrically charged particle of charge $|z| = 68.5$ (left) and a magnetic monopole of charge $|g| = 1.0g_{\mathrm{D}}$ (right) as a function of the particle velocity, β, for different materials.

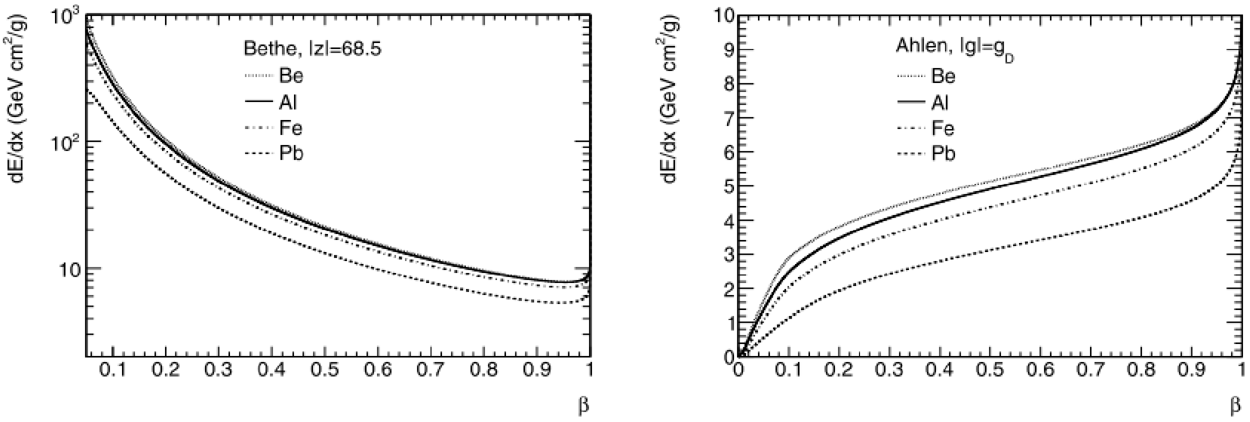

Figure 1.2: Energy loss per unit length, dE/dx, by an electrically charged particle with $|z| = 68.5$ (left) and a magnetic monopole of charge $|g| = 1.0g_{\mathrm{D}}$ (right) as a function of the particle velocity, β, for different materials [18].

Energy loss via bremsstrahlung

The energy loss via bremsstrahlung radiation is also to take into consideration for magnetic monopoles [19]:

$$-\frac{dE_{\mathrm{rad}}}{dx} = \begin{cases} \frac{16NZ^2e^2}{\hbar}\frac{g^4}{\hbar c}\frac{g^4}{mc^2}, \beta \ll 1, \\ \frac{16}{3}\frac{NZ^2e^2}{\hbar c}\frac{g^4}{mc^2}\gamma \ln\left(\frac{233m}{Z^{1/3}m_e}\right), \gamma \gg 1 \end{cases} \tag{1.18}$$

where m is the monopole mass, N and Z are the atomic density and number of the material such that $N_e = ZN$. The ratio of energy losses by bremsstrahlung to energy losses by ionization

(Eq. 1.14) can be written as

$$-\frac{dE_{\text{rad}}}{dE_{\text{ion}}} = \begin{cases} \frac{4}{3\pi}\frac{Zg^2}{\hbar c}\frac{m_e}{m}\frac{1}{\lambda}, \beta \ll 1, \\ \frac{4}{3\pi}\frac{Zg^2}{\hbar c}\frac{m_e}{m}\frac{1}{\lambda}\gamma \ln\left(\frac{233m}{Z^{1/3}m_e}\right), \gamma \gg 1 \end{cases} \tag{1.19}$$

where λ represents the factor multiplying the leading term of Eq. 1.14.

As pointed out in Figure 1.3 the energy losses of a monopoles produced at a collider would be dominated by the ionization of the detector. This high ionization power plays a key role in the signature of monopoles in the detector.

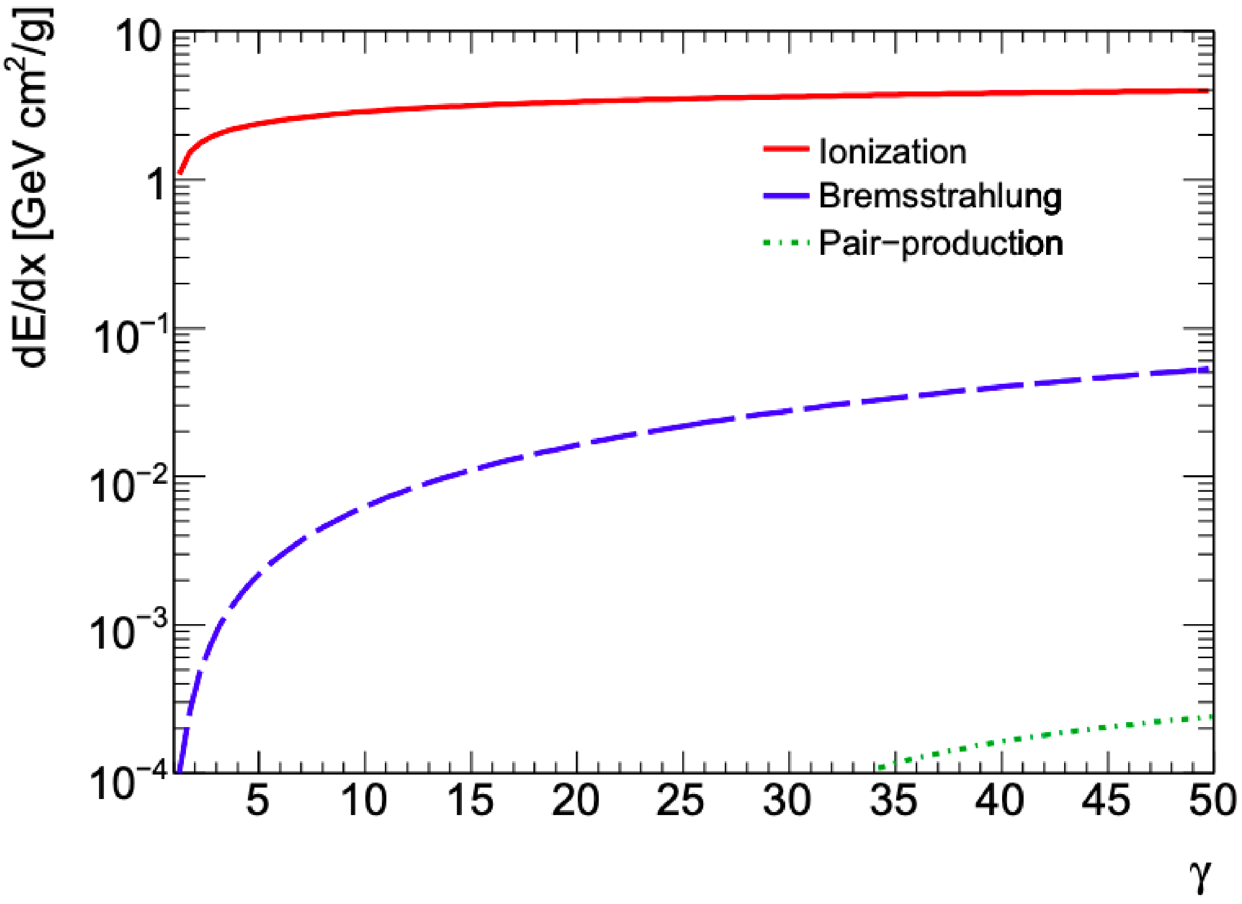

Figure 1.3: Energy loss per unit distance, dE/dx, for a magnetic monopole of charge $|g| = 1.0g_{\text{D}}$ and mass 1000GeV in argon as a function of gamma, shown in a range relevant for pair-produced massive particles at the LHC. Three energy loss mechanisms are shown: ionization (solid-red line), bremsstrahlung (dashed-blue line) and pair production (dotted-green line) [20].

1.3 Searches for monopoles

1.3.1 Searches for cosmic monopoles

Grand Unified Theory (GUT) models predict the creation during the Big Bang of monopoles in an abundance similar to the one of baryons and monopoles would actually be the dominant matter in the universe. This leads to the monopole problem as the observed density or flux of cosmic monopoles is not in line with the expectation. The monopole problem is solved by the cosmological inflation theory that states that in the early phase of the universe, the latter exponentially expended diluting the monopoles density to a very low flux compatible with the observations. Numerous searches for cosmic monopoles, remnant from the Big Bang, were designed and the search for a cosmic monopole is still an active field [21].

GUT monopoles could not be produced by colliders due to their high predicted mass of the order of $10^{16}\ GeV$. Accelerated either by the gravitational attraction for heavy GUT monopoles or by the galaxies' magnetic fields for lighter monopoles, GUT monopoles would have a velocity of about $\beta = 10^{-3}$. The very low speed of cosmic monopoles would lead following equation 1.14 to an interaction with matter too weak to allow monopoles to stop into the Earth or to be detected via high ionization detection method. Under the exception of the induction technique which is only relying on the monopole magnetic charge, most searches are thus sensitive to lower mass monopoles.

The monopoles accelerated by the galaxies magnetic fields drain the energy from those fields. Parker derived an upper limit for the flux of monopoles in the universe in order for the galaxy magnetic field to exist [22]. Based on the parameters described in [23] the condition on the monopoles flux is:

$$F < \begin{cases} 10^{-15}\mathrm{cm}^{-2}\mathrm{sr}^{-1}\mathrm{sec}^{-1}, & M \lesssim 10^{17}\mathrm{GeV}\ , \\ 10^{-15}\left(\frac{M}{10^{17}\mathrm{GeV}}\right)\mathrm{cm}^{-2}\mathrm{sr}^{-1}\mathrm{sec}^{-1}, & M \gtrsim 10^{17}\mathrm{GeV}\ . \end{cases} \tag{1.20}$$

The Parker bound was reached by a small amount of cosmic monopole search experiments.

The MACRO experiment [24]

In order to cover a broad range of velocities with $4 \times 10^{-5} < \beta < 1$, the MACRO experiment was designed with multiple sub-detectors combining different detection methods: low speed monopoles with $\beta \sim 10^{-4}$ are covered by liquid scintillator detectors, streamer tubes detectors are covering the highly ionising signature of the monopoles with $\beta > 10^{-3}$ and the tracking of the monopoles is ensured by Nuclear Track Detectors (NTD). The MACRO experiment set an upper limit on the flux of monopoles with the Dirac charge of $1.4 \times 10^{-16}\text{cm}^{-2}\text{s}^{-1}\text{sr}^{-1}$ which is below the Parker bound.

The RICE experiment [25]

Initially designed for the detection of high energy neutrinos, the south pole located RICE experiment was sensitive to cosmic monopole detection in the range $\gamma \geq 10^7$. Cosmic monopoles with such a velocity would have a mass $m \lesssim 10^8\text{GeV}$. The RICE experiment was a Cherenkov detector using an array of radio antennas to detect the particles going through the south pole ice. The RICE experiment set an upper limit on the flux of monopoles with the Dirac charge of $10^{-18}\text{cm}^{-2}\text{s}^{-1}\text{sr}^{-1}$ for monopoles with $\gamma \geq 10^8$. In this range of velocity, the MACRO limit has thus been exceeded.

The ANITA-II experiment [26]

Also seeking for cosmic monopoles interacting with Antarctic ice, the ANITA-II balloon-borne radio interferometer accumulated 31 days of flight data with no evidence of monopole. The experiment set an upper limit on the flux of monopoles with the Dirac charge of $10^{-19}\text{cm}^{-2}\text{s}^{-1}\text{sr}^{-1}$ for monopoles with $\gamma \geq 10^{10}$.

The ANTARES experiment [27]

Located in the Mediterranean sea, close from the south of France cost, the ANTARES experiment consisted in a 3D array of photomultipliers, 2500m underwater. The experiment could detect the Cherenkov radiation produced by delta-electrons generated along the monopoles path. The ANTARES experiment set an upper limit to the monopoles with the Dirac charge of $1.3 \times 10^{-17}\text{cm}^{-2}\text{s}^{-1}\text{sr}^{-1}$ in the range $\beta > 0.625$.

The IceCube experiment [28]

Located in the Antarctic the IceCube experiment, thanks to photomultipliers, detects the Cherenkov radiation of cosmic particles going through the ice. The IceCube detector is sensitive to monopoles below the Cherenkov thresholds thanks to the highly energetic delta-rays that a monopole would produce when interacting with the ice. The sensitivity of the IceCube detector to the monopoles is in the range $\beta \geq 0.51$. No monopole event was observed and an upper limit to the flux of cosmic monopoles was set to $1.55 \times 10^{-18}\text{cm}^{-2}\text{s}^{-1}\text{sr}^{-1}$.

Super-Kamiokande [29]

Continuing the search for nucleon decays started by the KamiokaNDE experiment, the Super-Kamiokande experiment searches for cosmic monopoles is indirect and based on the Callan-Rubakov solar protons decays catalysed by cosmic monopoles. The proton decays would produce a neutrino excess with an anergy of 29.79 MeV that would be detected by the Super-Kamiokande detector. No events were observed and an upper limit to the flux of magnetic monopoles was set to $6.3 \times 10^{-24} \left(\beta_{\mathrm{M}}/10^{-3}\right)^2 \text{cm}^{-2}\text{s}^{-1}\text{sr}^{-1}$ where β_{M} is the monopole velocity in units of the speed of light and σ_0 is the catalysis cross section at $\beta_{\mathrm{M}} = 1$.

1.3.2 Searches for monopoles bound in matter

Considering the fact that magnetic monopoles could be bound to bulk ferromagnetic material, searches for cosmic monopoles trapped in matter were done using SQUID magnetometers to detect the magnetic field of such trapped magnetic monopoles in various materials, such as meteorites, moon rocks and sea water [30, 31]. No event was observed and an upper limit to the ratio of monopoles per nucleon was set to $\sim 10^{-29}$ [31].

1.3.3 Searches for production of monopoles at colliders

Limited by the energy at the center of mass, searches of magnetic monopoles at colliders are focusing on low masses far from the GUT monopoles. The mass ranges probed by searches increased with accelerator energy improvements.

Searches at LEP

The L3 experiment [32] Magnetic monopoles are expected to couple to Z bosons in BSM models and $Z \rightarrow \gamma\gamma\gamma$ process would be observed with an excess compared to the standard model predictions. The observations were consistent with the background-only hypothesis and a limit on the branching ratio was set to BR$(Z \rightarrow \gamma\gamma\gamma) < 0.8 \times 10^{-5}$. A magnetic monopole lower limit was set to $m < 520\ GeV$.

The MODAL experiment [33] The MODAL experiment was the first reporting results for a search for highly ionizing particles and monopoles at the $e^{+}e^{-}$ LEP collider at CERN at $\sqrt{s} = 91.1$GeV. Based on dielectric track detectors, the search was sensitive to magnetic monopoles with 0.1gD < g < 3.6gD and mass up to 45 GeV. With no observed event, an upper limit on the cross section of monopoles production assuming the Drell-Yan mechanism [34], was set to 70 pb.

The L6-MODAL experiment [35] Similar to the MODAl experiment using NTD around the OPAL detector, the L6-MODAL experiment was sensitive to magnetic monopoles with charge 0.9gD < g < 3.6gD and mass up to 45 GeV. A cross section limits of 0.3 pb was set.

The OPAL experiment [36] The OPAL experiment was the only experiment searching for magnetic monpoles at LEP2 at $\sqrt{s} = 206.3GeV$. The search was based on the highly ionizing signature of magnetic monopoles and the bending of the tracks in a plane perpendicular to electrically charged particules bending planes. Upper limit on the production cross section was set to 0.05 pb for 1.0 gD monopoles with mass $45 < m < 102$ GeV.

Searches at Tevatron

The D0 experiment [37] Using $70pb^{-1}$ of data collected by the D0 experiment at $\sqrt{s} =$ 1.8TeV at the Tevatron, the D0 collaboration searched for high energy pair of photons, assuming Dirac monopoles could rescatter pairs of photons into this final state via a box diagram. No excess above the background was observed and lower limit to the mass of monopoles was set to 610, 870 or 1580 GeV for respectively spin 0, 1/2 or 1 monopoles.

The E882 experiment [38] The E882 experiment at Tevatron used the induction technique on D0 and CDF (Collider Detector at Fermilab) material exposed to $175pb^{-1}$ of collisions at $\sqrt{s} =$ 1.8TeV. No event was observed and upper limits on cross-sections for 1, 2 3 and 6 gD monopoles were set to respectively 0.6, 0.2, 0.07 and 0.2 pb.

The CDF experiment [39] The CDF experiment searched for pair produced monopoles using 35.7 pb^{-1} of $p\bar{p}$ collisions at $\sqrt{s} = 1.96$ TeV. No event was observed and an upper limit to the cross section was set to 0.2 pb for monopoles with a mass $200\ GeV < m < 700\ GeV$. Resulting in a lower mass limit of 360 GeV assuming a Drell-Yan production.

Searches at HERA

The H1 experiment [40] A search of trapped monopoles, bound into the H1 beam-pipe material, was conducted using the induction method. No event was observed and an upper limit to the production cross-section was set for monopoles with magnetic charge up to 6gD and mass $m < 140\ GeV$.

Searches at LHC

The ATLAS experiment [41, 42] The ATLAS experiment conducted two searches of the magnetic monopole at respectively $\sqrt{s} = 7$ TeV and $\sqrt{s} = 8$ TeV. The searches rely on the highly ionising signature of the magnetic monopoles. No event was observed and upper limit to the production cross-section was set for monopoles with magnetic charge up to 2 gD and mass $200\ GeV < m < 2500\ GeV$.

The work presented in this thesis is the continuation of the ATLAS searches at an energy at the centre of mass of $\sqrt{s} = 13$TeV.

The MoEDAL experiment [43] The MoEDAL experiment at LHC is a dedicated experiment for the search of the magnetic monopole. It is the continuation of the MODAL experiment at LEP and uses a combination of detection techniques such as NTD and induction technique on material exposed to proton-proton collisions at the LHCb interaction point. The monopole-trapping test array was exposed to 0.75fb^{-1} of 8 TeV collisions in 2012. The trapping detector allowed to probe for monopoles with a mass up to 3500 GeV and charge 1gD < g < 4gD. The full scale detector is more than 4 times larger and cover a much broader solid angle.

The results of the MoEDAL full scale trapping detector are presented in this thesis.

Chapter 2

The Large Hadron Collider, ATLAS and MoEDAL

2.1 The Large Hadron Collider

The Large Hadron Collider (LHC) is the biggest circular proton-proton (pp) collider in the world with a circumference of 27 km. With a design centre-of-mass energy of 14 TeV, it is also the world most powerful particle accelerator. Approved in 1994, its construction started in 1998 and lasted for 10 years. The LHC is located at CERN in Geneva, Switzerland, in the previous Large Electron Positron collider tunnel. Besides protons, lead ions can be used in collisions. This thesis will focus on collisions between protons.

The protons are pre-accelerated in a chain of different accelerators before being injected into the LHC and brought into collision. Fig. 2.1 shows the complete accelerator complex at CERN. By stripping their electrons in an electric field, the protons are extracted from a simple bottle of hydrogen gas and accelerated to an energy of 50 MeV in the LINAC2 linear accelerator.

In the Proton Synchrotron Booster, they are then brought to an energy of 1.4 GeV before being transferred to the Proton Synchrotron (PS), which accelerates the protons to an energy of 25 GeV. The protons reach an energy of 450 GeV in the Super Proton Synchrotron (SPS) and are

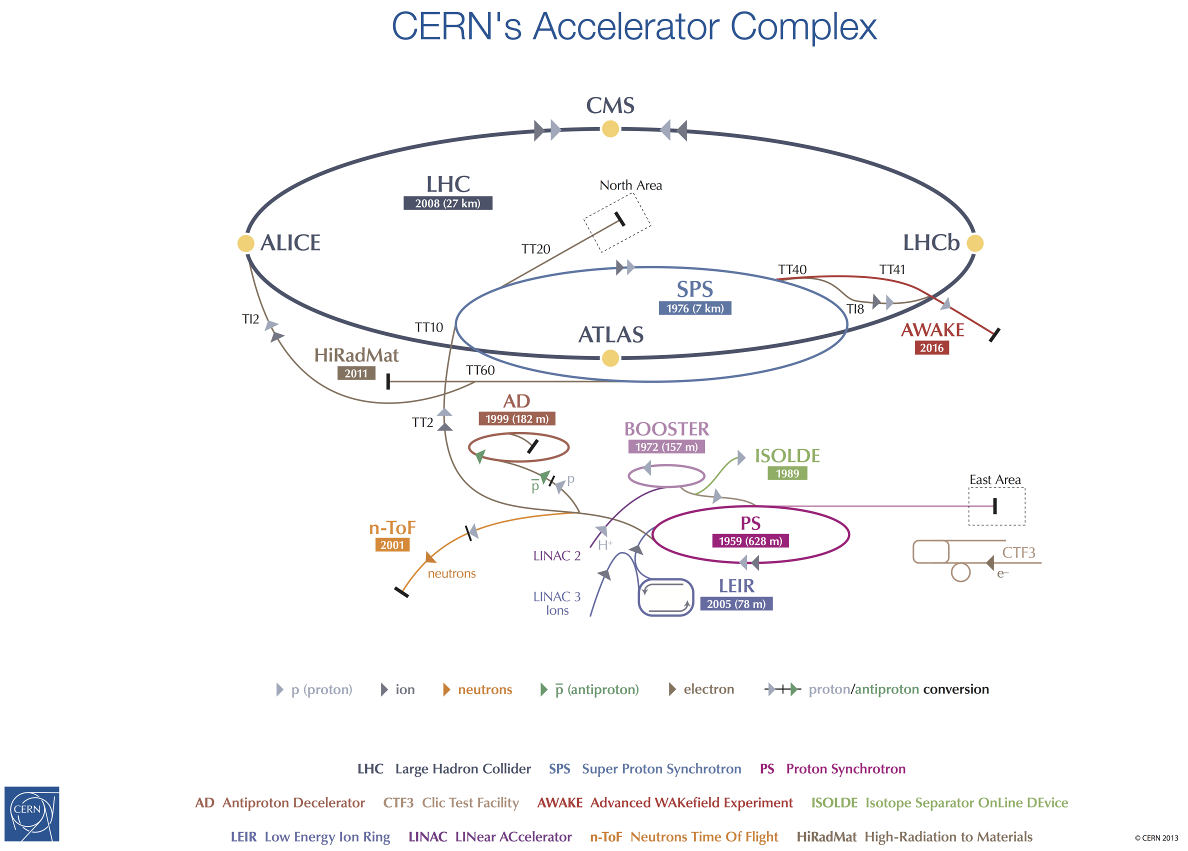

Figure 2.1: Graphical illustration of the accelerator complex at CERN with its flagship, the Large Hadron Collider and the different pre-accelerators used for the proton and heavy ion injection

then injected into the two beam pipes of the LHC.

The beam, consisting of several hundreds of bunches, is accelerated by the radio frequency cavities to its final energy of 3.5 TeV (2010-2011), 4.0 TeV (2012) or 6.5 TeV (2015) with the design value being 7 TeV. Superconducting dipole and quadripole magnets with a maximum magnetic field strength of 8.33 T assure that the protons are kept on their circular path and focused.

At four different interaction points, where the main LHC experiments ALICE, ATLAS, CMS and LHCb are located, the circulating hadrons are brought into collision. Superconducting quadrupole magnets, cooled with liquid helium at a temperature of 1.9 K, are used to focus the beams before the points of interaction. The two general-purpose detectors ATLAS [44] and CMS (Compact Muon Solenoid) [45] explore a wide range of physics topics, including SM accuracy measurements and physics searches beyond the SM. The experiment ALICE (A Large Ion Collider Experiment) [46] was designed to investigate the quark-gluon plasma created in heavy ion collisions (proton-lead or lead-lead). LHCb focus on b-physics studies, related for example to the asymmetry of matter and antimatter.

For a given SM process, the estimated number of events per second N is directly proportional to its cross-section σ:

$$\frac{\mathrm{d}N}{\mathrm{d}t} = \sigma \cdot L \tag{2.1}$$

where L is the instant luminosity determined by the parameters of the beam.

The discovery of the SM Higgs boson was a key objective of the LHC. The estimated number of events per second N with a higgs boson is relatively small and directly proportional to its cross-section.

By increasing the luminosity depending on the number of bunches n_b, the number of protons per bunch N_1, N_2, the revolution frequency f and the overlapping area of the colliding bunches A, the production rate of interesting events can then be increased:

$$L = \frac{n_b N_1 N_2 f}{A} = \frac{n_b N_1 N_2 f}{4\pi \sigma_x \sigma_y} \tag{2.2}$$

The second part in Eq. 2.2 holds only for Gaussian-shaped beams with equal vertical and horizontal beam sizes, x and y, for the two colliding bunches. To increase the luminosity, the number of bunches and the maximum number of protons per bunch have been increased whereas the bunch spacing and the bunch size have been reduced sequentially since the beginning of data-taking in 2010. The design peak luminosity, of $1 \times 10^{34}\mathrm{cm}^{-2}\mathrm{s}^{-1}$, has been surpassed for the first time in June 2016. The peak luminosity is obtained at the beginning of the fill since the instantaneous luminosity decreases during the run due to the beam losses caused by the collisions. The accumulation of more protons in the bunches to increase the instantaneous luminosity results in the occurrence of multiple pp interactions in the same bunch crossing and is referred to as in-time pile-up. These additional interactions are uncorrelated with the hard-scatter interaction and are considered as background. The in-time pile-up is characterised by the number of reconstructed vertices N_{vtx} as measured in the tracking detectors. Out-of-time pile-up describes the impact of the signal of adjacent bunch crossings on the signal of the current bunch crossing. It occurs mostly due to the short bunch spacing compared to the readout time of the detector systems such as the ATLAS liquid-argon calorimeter (LAr), described in Section 2.7. The average number of interactions per bunch crossing $< \mu >$ is used to parameterise the amount of out-of-time pile-up and is calculated from the luminosity.

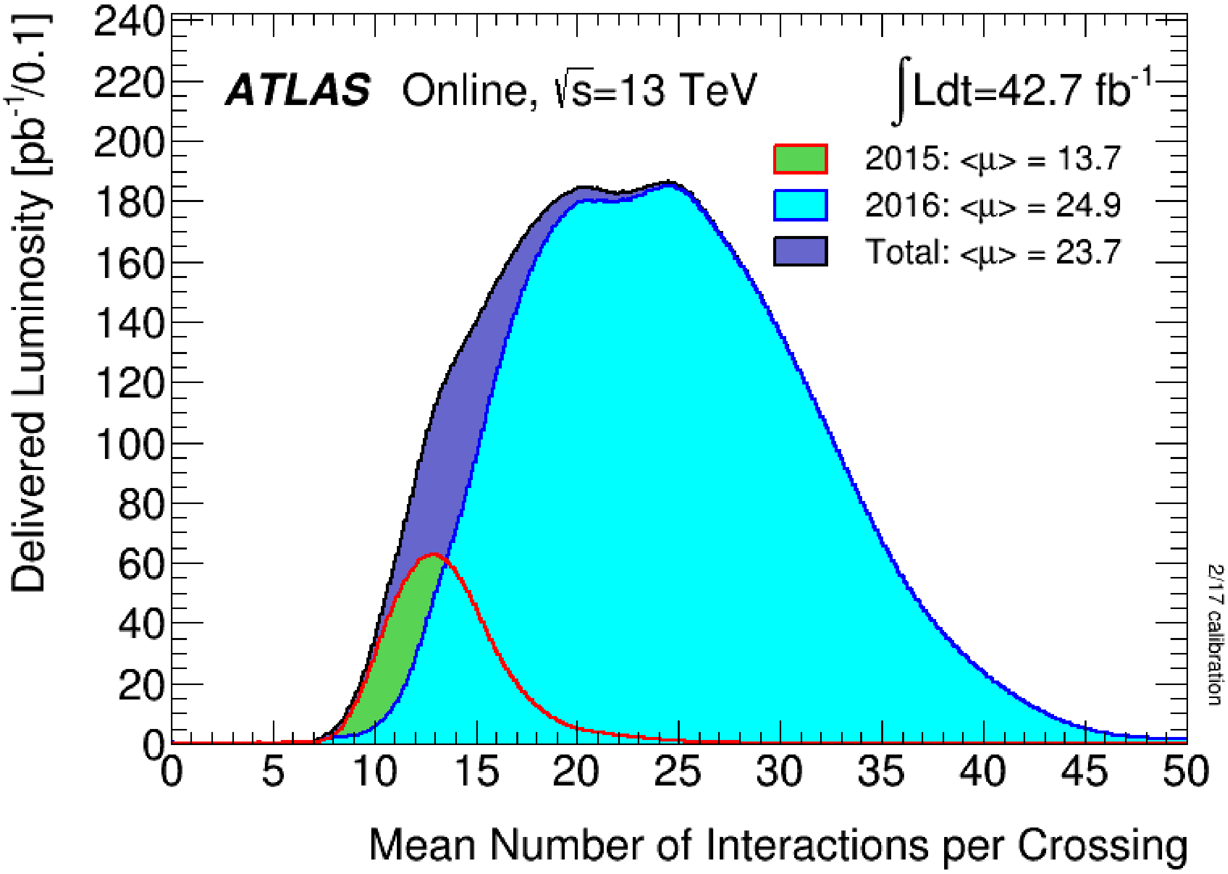

Figure 2.2: Number of interactions per crossing

The distribution of $< \mu >$ for 2015 and 2016 data-taking is shown in Fig. 2.2. Both in-time and out-of-time pile-up will be referred to as pile-up in the remainder of this thesis. The suppression of pile-up plays an important role in the reconstruction of final states including hadrons. The integrated luminosity is the amount of data collected over a certain period of time, $L = \int Ldt$. For the data-taking in 2015 and 2016, the integrated luminosity as accumulated over time is shown in Fig. 2.3. In 2015, the LHC delivered 4.2 fb^{-1} of 13 TeV proton-proton collisions and 38.5 fb^{-1} in 2016.

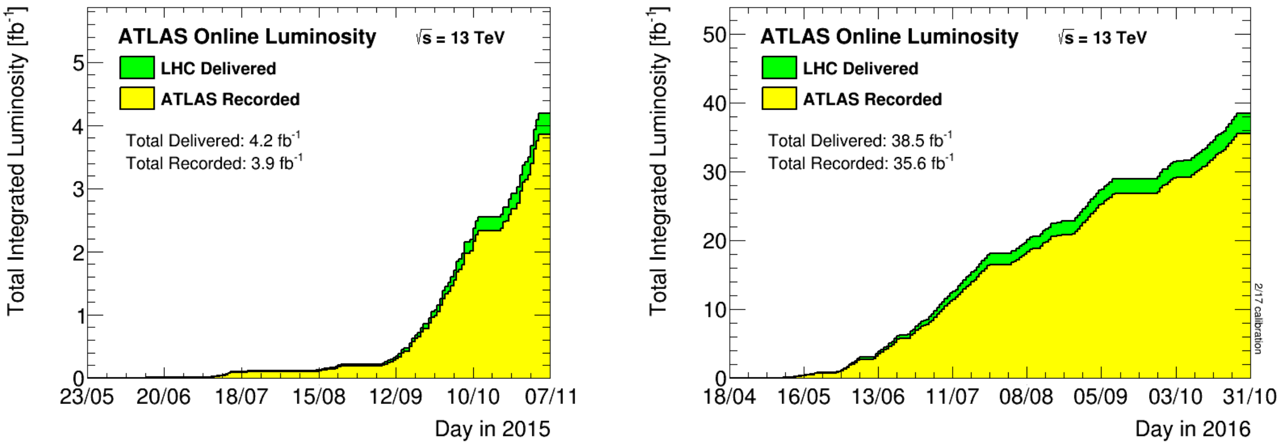

Figure 2.3: Total integrated luminosity in 2015 (left) and 2016 (right).

In the remainder of the thesis, the data-taking period before the long shutdown in 2013 will be referred to as Run-1, whereas the data-taking after the upgrade, in 2015 and 2016, will be denoted as Run-2.

2.2 The ATLAS experiment

The ATLAS detector is one of the multi-purpose detectors at the LHC and enables precision measurements of SM parameters and searches for new physics beyond the SM.

With a cylindrical shape the ATLAS detector covers most of the solid angle, as shown in figure 2.4. ATLAS is composed of many sub-detectors forming the successive layers of its onion geometry. Surrounding the beam pipe at the centre of the detector, the first layers of the ATLAS detector consist in tracking detectors referred to as the inner detector. A 2 T solenoidal magnetic field passes through the whole inner detector. Following the inner detector come the electromagnetic and hadronic calorimeters, and in turn the muon spectrometer immersed in a toroidal magnetic field.

Three distinct regions are composing the ATLAS detector: the barrel, closer to the interaction point with sub-detectors parallel to the beam-pipe, the end-caps, with the sub-detectors perpendicular to the beam-pipe, and the forward region, where the sub-detectors are close to the beam pipe.

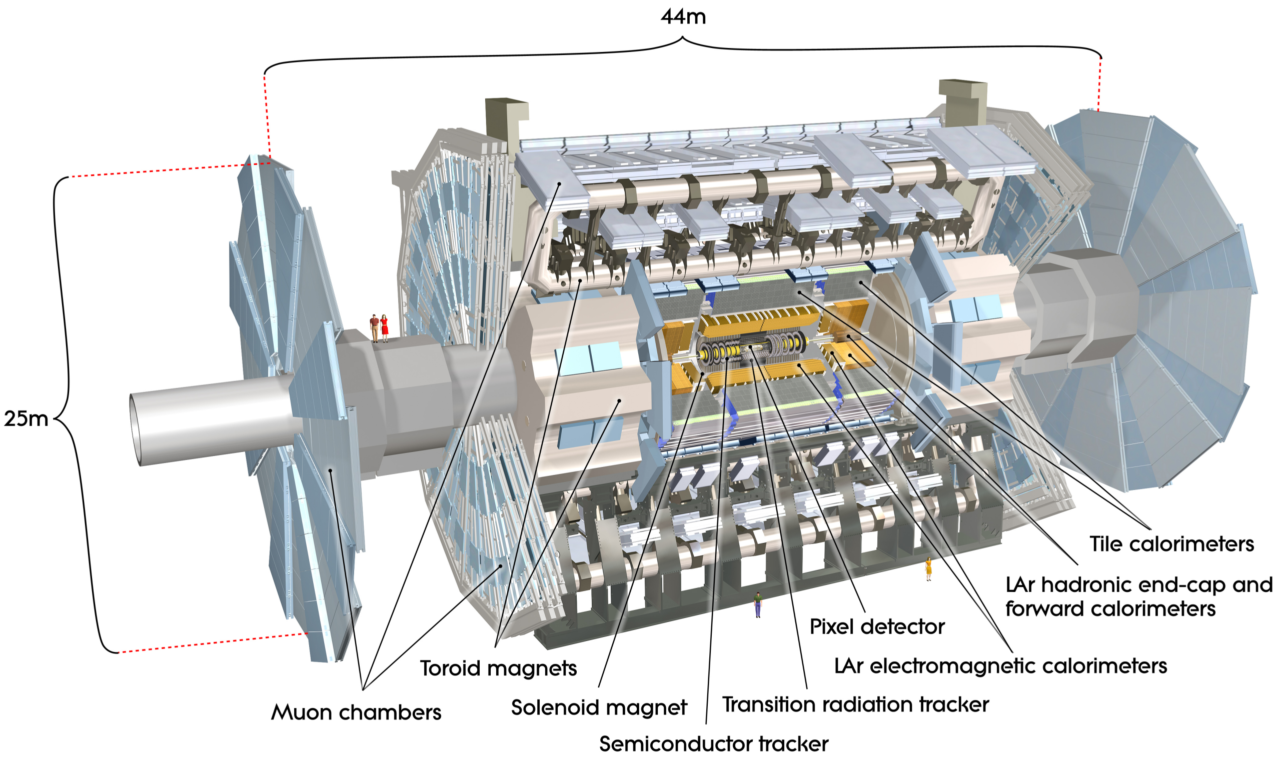

Figure 2.4: The ATLAS detector and its sub-detectors

2.2.1 Coordinate System

The ATLAS coordinate system has its origin at the centre of the detector, at the interaction point. It is a right-handed coordinate system with its x-axis pointing at the centre of the LHC ring, the y-axis pointing upwards and the z-axis along the beam-pipe in the anti-clockwise direction. The symmetry of the detector makes the use of cylindrical coordinates natural. In cylindrical coordinates, we define r as the distance from the z-axis, the azimuthal angle ϕ as the angle with the x-axis in the xy plane and the polar angle θ as the angle with the z-axis in the yz plane. In the literature, the polar angle is generally represented by the pseudo-rapidity $\eta = -\ln\left(\tan\left(\frac{\theta}{2}\right)\right)$. The pseudo-rapidity of massless particles is equal to their rapidity $y = \frac{1}{2}\ln\left(\frac{E+p_z}{E-p_z}\right)$, where E is the particle energy and p_z is the particle momentum in the +z direction. The angular separation between two particles or points of the detector is now defined as $\Delta\mathrm{R} = \sqrt{(\Delta\eta)^2 + (\Delta\phi)^2}$.

2.2.2 The ATLAS Inner Detector

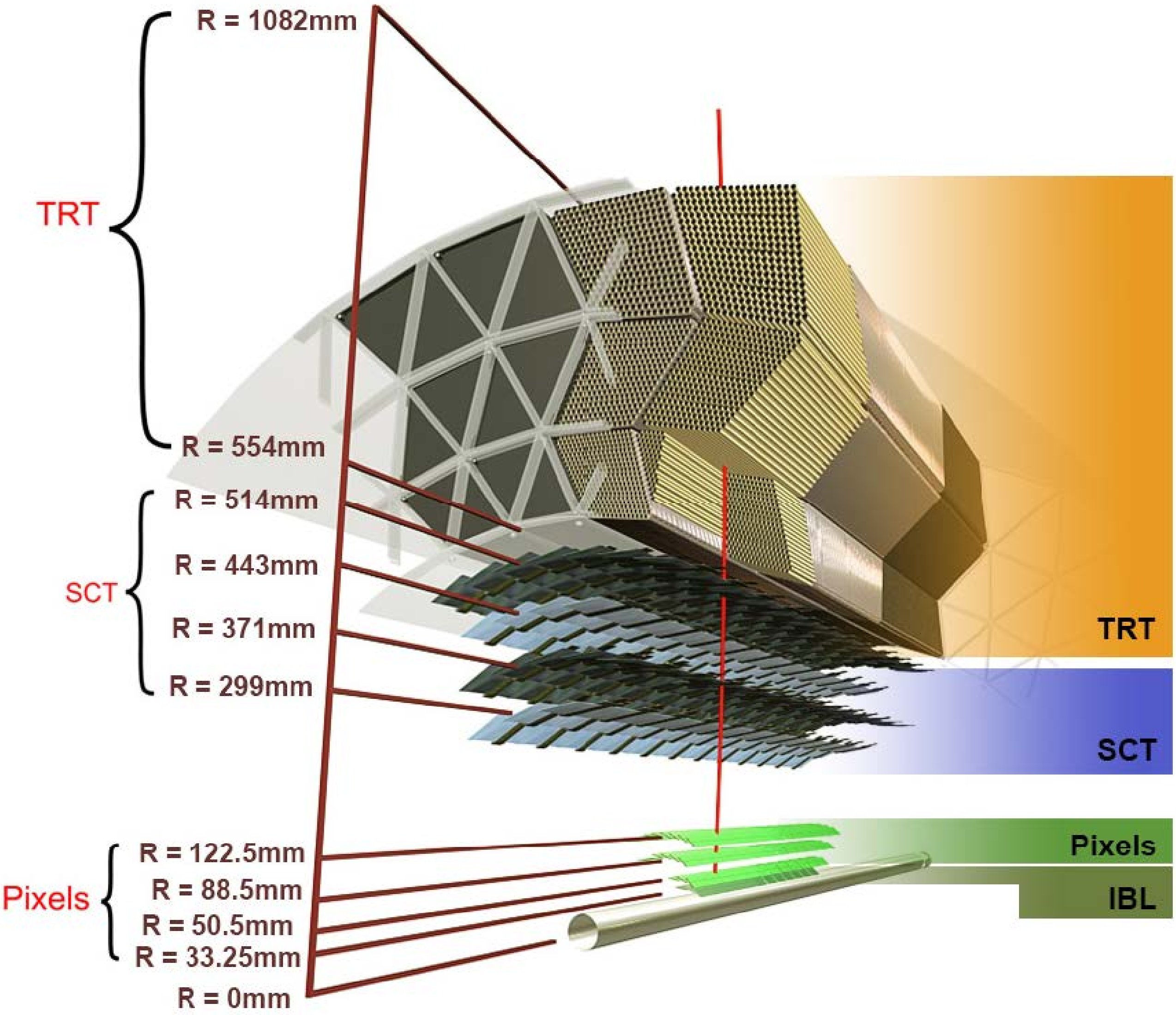

Figure 2.5: The sub-detectors of the inner detector in the barrel region: the Insertable B-layer (IBL), the pixel detector, the Semiconductor Tracker (SCT), and the Transition Radiation Tracker (TRT).

The Inner Detector (ID) allows to reconstruct the path of charged particles within the range $|\eta| < 2.5$. It is composed of two silicon detectors, the pixel and micro-strips detector, and the Transition Radiation Tracker (TRT) made of straw tubes filled with Xenon or Argon gas mixture as shown in figure 2.5.

All the sub-detectors of the ID detect charged particles and record hits at a given position of the detector. Using a minimum of three hits, the tracks of the particles can be reconstructed and in turn from the tracks the primary and secondary vertices. The ID being immersed in a magnetic field, charged particles are bent in the xy plane with a curvature proportional to $\frac{p_T}{q}$, with p_T the transverse momentum and q the charge of the particle. The particles charge sign, as well as its momentum can thus be derived from the track curvature assuming an elementary charge. Common reconstruction algorithms are assuming particles charges to be $\pm e$ and thus multi-charged particles momentum would be underestimated.

The Pixel detector is the innermost sub-detector of the ATLAS experiment. It consists in 4 layers of pixels in the barrel and three disks of pixels in each of the end-caps. The overall number of pixels is above 80 millions. The first Pixel layer, the Insertable B-Layer (IBL) [47], only at a radius $r = 33.25\ mm$ from the beam-pipe, was added to the detector during the Long Shutdown 1 (LS1) of the LHC for the Run 2 analysis. With a design spatial resolution of $\sim 8\ \mu$m in $r - \phi$ and $\sim 40\ \mu$m in z [48], as well as its proximity to the beam-line, the IBL improves the tracking and vertexing of the Pixel detector.

The Semiconductor Tracker (SCT) starts after the last layer of the Pixel detector at a radius of $r = 299\ mm$. The SCT micro-strip modules are spread in pairs over 4 layers in the barrel and 9 disks for each end-caps sides. The modules have a stereo rotation angle of $\pm 20\ mrad$, allowing to reconstruct an additional dimension, z(r) in the the barrel(end-caps).

Starting at a radius of 554 mm, the Transition Radiation Tracker (TRT) is the outer-most sub-detector of the ID, extending to a radius of 1082 mm and covering $|\eta| < 2$. The TRT was designed with more than 350 000 straws filled with Argon and Xenon gas mixture. The straws are disposed parallel to the beam-pipe in the barrel allowing to reconstruct the r and ϕ coordinates of the hits, and radially in the end-caps, allowing to derive the ϕ and z coordinates of the hits. In addition, the TRT is also used for particle identification. The detector is tuned to allow two levels of hits, low and high threshold hits. While typically electrons would generate high threshold hits, muons or pions would have a lower probability to generate high threshold hits. The fraction of high threshold hits is then used to identify particles.

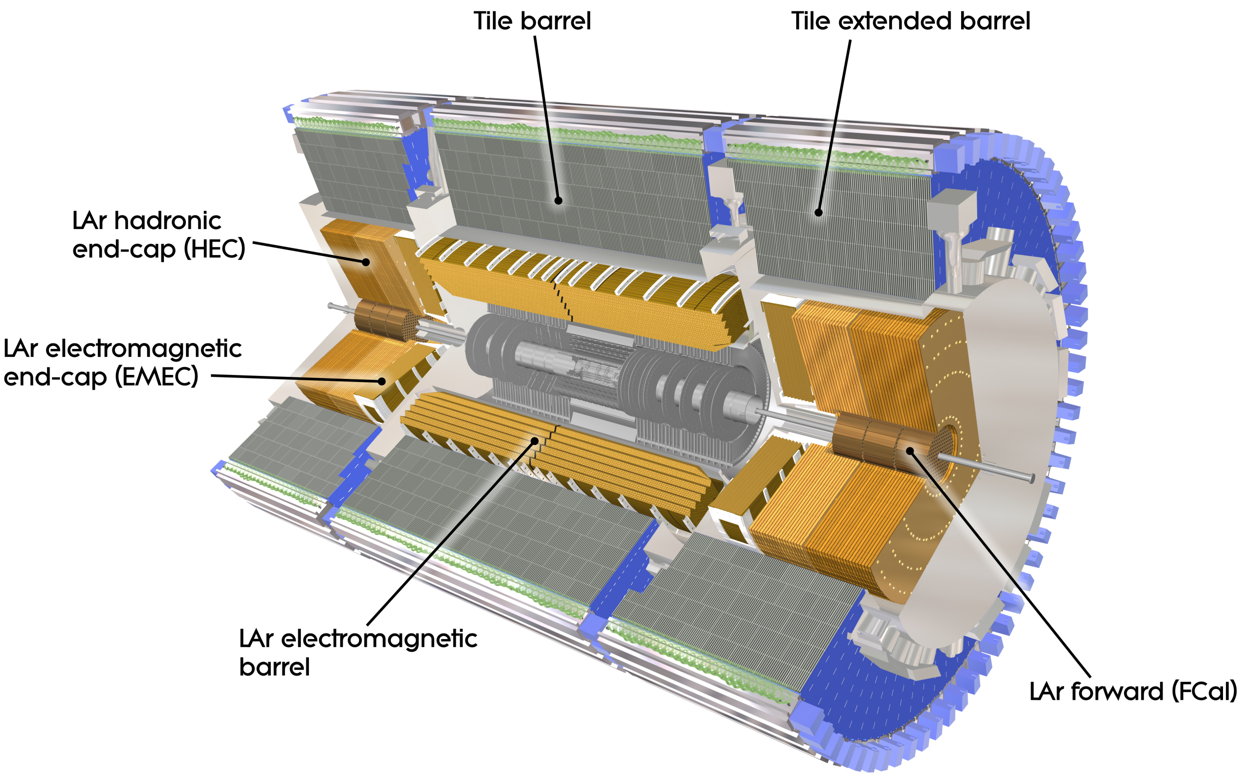

Figure 2.6: The layout and sub-detectors of the calorimeter systems.

2.2.3 The Calorimeter System

The calorimeter systems start after the ID. The calorimeters' goal is to measure the particles' energies. Calorimeters are composed of dense material through which particles are generating showers, cascades of interactions. The initial particles energies can be reconstructed from energies of all the showers' particles. The ATLAS calorimeters [49, 50] are sampling calorimeters, ie designed with alternating layers of active materials, such as scintillators, and absorber materials.

The radiation length X_0 is defined as the average length over which an electron energy is reduced to $\frac{1}{e} \sim 37\%$ of its energy via bremsstrahlung . A photon travels on average $\frac{9}{7}X_0$. On average a hadron travels one λ_{int}, the nuclear interaction length, before interacting with the nuclei. As shown in figure 2.6 the calorimeters are thick detectors. The EM calorimeter is thicker than 20 X_0 and the hadronic calorimeter's thickness is about 10 λ_{int}.

The Electromagnetic Calorimeter

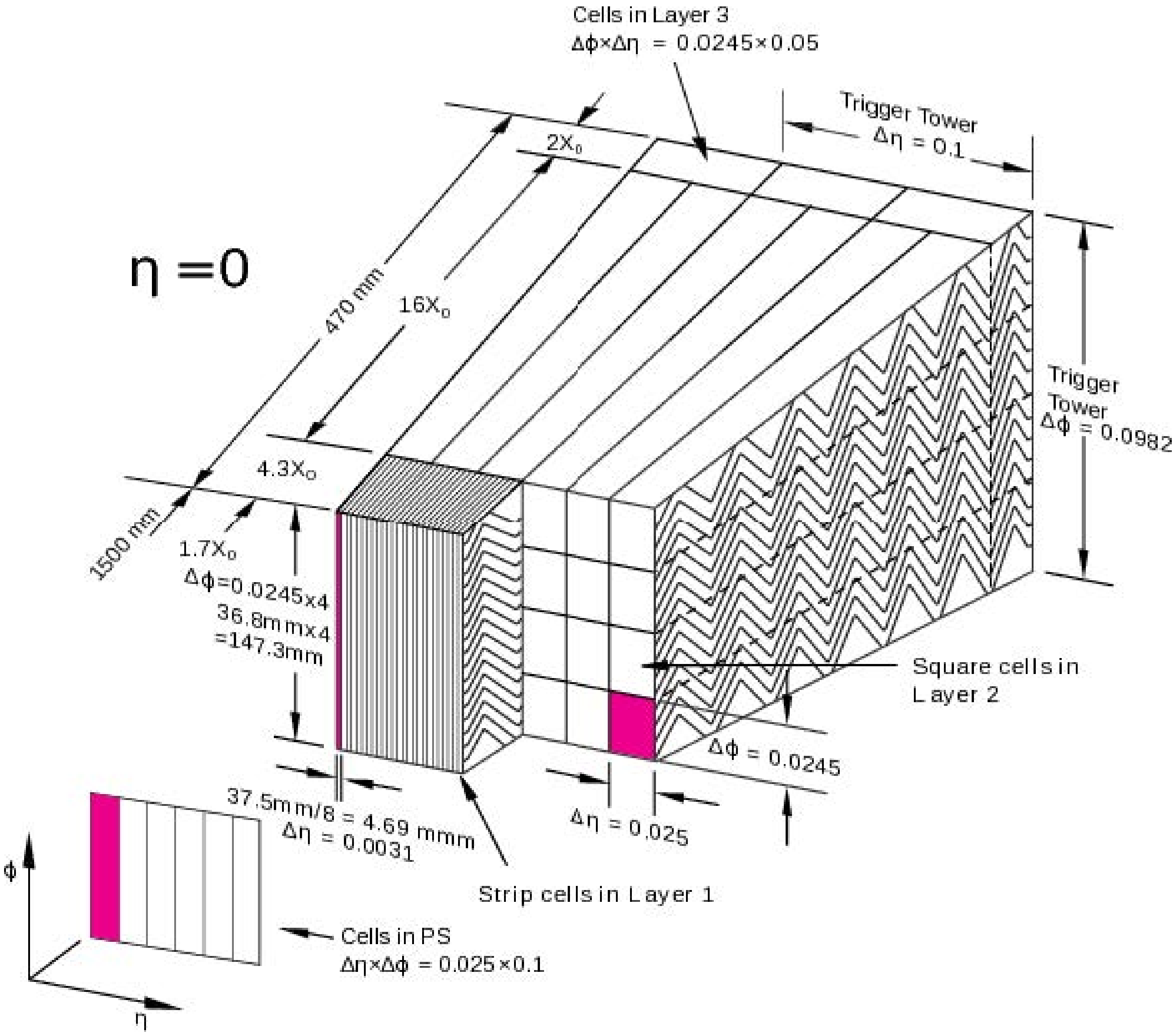

Figure 2.7: The electromagnetic barrel calorimeter and the pre-sampler (PS).

The electromagnetic calorimeter (EM calorimeter) is as stated above a sampling calorimeter. The lead layers, absorbers, and the liquid argon layers, active materials, are in accordion patterns allowing a good solid angle coverage as shown in figure 2.7. The EM calorimeter is covering a range of $|\eta| < 3.2$. The barrel extends up to $|\eta| < 1.475$ and the end-caps cover the region $1.375 < |\eta| < 3.2$. The transition region for $1.37 < |\eta| < 1.52$, also known as the crack region, has a lower energy resolution due to the presence of cables and services.

A charged particle passing through a liquid argon layer will ionise it. The generated electrons will drift to electrodes and produce a current proportional to the charge of the initial particle [51].

As shown in figure 2.6, the barrel region of the EM calorimeter is divided into 3 layers, the front, middle and back layers also numbered respectively layers 1, 2 and 3. The layer 1 being the closest from the beam-pipe and the layer 3 the furthest. The layers are segmented into cells of different granularities. The layer 1 granularity is the finest and is used to accurately locate the showers, while the other layers are coarser. The layer 1 fine granularity only extends up to $|\eta| < 2.37$. In addition, a liquid argon layer 0 covers the region $|\eta| < 1.8$. This layer is known as the pre-sampler (PS) and is used to measure the particles' energy-loss before entering the calorimeter.

Some analysis, relying for example on photons, usually exclude the crack region and the region $|\eta| > 2.37$ as the spatial and energy resolutions are not sufficient.

The Hadronic Calorimeter

Starting after the EM calorimeter is the hadronic calorimeter. The hadronic calorimeter consists in 3 different parts as shown in figure 2.6: the tile calorimeter covering $|\eta| < 1$ in the barrel region and $0.8 < |\eta| < 1.7$ in the end-caps, the Hadronic End-Cap calorimeter (HEC) covering $1.5 < |\eta| < 3.2$ and the Forward Calorimeter (FCal) covering $3.1 < |\eta| < 4.9$. As for the EM calorimeter, the transitions regions are poorly instrumented and have lower performances.

The tile calorimeter The tile calorimeter alternates layers of plastic scintillators, the active material, with thicker layers of steel, the absorber. In both the barrel and end-caps regions the tile calorimeter is split in 3 layers of different granularities. The first layer has cells of size $0.1 \times 0.1 (\Delta\eta \times \Delta\phi)$, while the second and third layers have cells of size $0.2 \times 0.1 (\Delta\eta \times \Delta\phi)$. The hadronic calorimeters granularity is coarser than the EM colorimeter, as hadronic showers are typically larger than EM showers. A particle passing through the scintillator will deposit energy, exciting the scintillator atoms which will then emit photons during their de-excitement [52]. The photons will then be collected by photo-multiplier tubes (PMT), generating a signal proportional to the energy deposited by the particle [53].

The HEC At high-eta in the very forward direction, the particles' rate is particularly high. The high occupancy of the detectors in this region enforce both the HEC and FCal design to be radiation hard, dense and have faster read-out systems. The HEC design is simple, using flat layers of copper disks in alternance with layers of liquid argon.

The FCal The FCal first layer is typically used for energy measurements of electromagnetic interactions, using copper as absorber and liquid argon as active material. The second and third layer of the FCal, for hadroninc interactions, are also unsing liquid argon as active material, but use a denser absorber, the tungsten. The FCal has a complex geometry using absorber tubes and rods leaving a gap filled with liquid argon between the rods and the tubes. This geometry allows to have a liquid argon layer of 250 μm compared to the more conventional 2 mm. Smaller gaps allow to avoid the ion buildup problem [54] and are required at high pile-up. In addition they lead to a much faster signal.

2.2.4 Muon Spectrometer

Muons deposit only a small amount of energy in the calorimeters and thus pass through the detector and reach the last sub-detector of ATLAS, the Muon Spectrometer as shown in figure 2.9. The Muon Spectrometer is measuring muons momentum derived from the track curvature. The curvature is ensured thanks to the powerful magnetic field generated by the toroidal magnets system and the tracking via Monitored Drift Tubes (MDT). The MDTs are disposed into three layers in the barrel and four layers in the end-caps. The end-caps first layer MDT coverage is only until $\eta < 2$. In the region $2 < |\eta| < 2.7$ the MDTs are replace by Cathode Strip Chambers (CSC) which bring a finer granularity required in the forward region due to the higher rate of particles. The Muon Spectrometer trigger sub-detector, the Resistive-Plate Chambers (RPC) [55] and the Thin-Gap Chambers (TGC) [56, 57], are coarser and faster detectors. The RPC covers $|\eta| < 1.05$ and the TGC the region $1.05 < |\eta| < 2.4$.

2.2.5 The Trigger System

The LHC bunch crossing period was lowered during the Run 2 from 50 ns to 25 ns, doubling the collisions rate to 40 MHz. It is not possible with such a very high frequency to record all events. A filter is thus required assessing the relevance of events before storing the data. This filter is ensured by the ATLAS trigger system, updated for Run 2 [58]. The trigger system was designed in two levels of filters, the Level 1 (L1), fast hardware-based system with decision time $\sim 2.5\ \mu$s, and the High Level Trigger (HLT), software-based system with decision time ~ 200 ms. The L1 trigger is using coarse granularity information from the calorimeters and from the muons chambers. It reduces the events rate to ~ 100 kHz. The HLT can use additional sub-detectors, such as trackers, and allows to reduce the events rate to ~ 1 kHz. The HLT algorithms are seeded by L1 triggers, so that events passing both levels would be recorded and the data used in analysis. Some triggers would still have a too high rate and would take a too big part of the available bandwidth. In order to prevent such situations, a prescale can be applied to reduce the rate by randomly discarding a fixed ratio of events. The use of prescales for signal triggers, implies the potential loss of signal events and should be avoided as much as possible. It can also happen that a trigger stream exceeds punctually the allowed bandwidth if the decision algorithm is taking too long to compute. In such cases a debug-stream was designed allowing to recover those events. A particular attention to the debug-stream events is generally given in the analysis as they are likely to differ from the rest of the events. The magnetic monopole search analysis presented in this work is using a dedicated HLT trigger, discussed into more detail in the section 4.2.1.

2.3 The MoEDAL experiment

The MoEDAL experiment is searching for highly ionising avatars of new physics covering more than 30 fundamentally important beyond-the-standard-model scenarios involving electrically and magnetically charged particles [59]. It started data-taking in 2015 at interaction point 8 of the Large Hadron Collider (LHC), thus sharing the cavern with the LHCb [60] experiment

(Figure 2.10). It is located around the vertex locator of the LCHb experiment, being as close as possible from the interaction point.

2.3.1 The MoEDAL subdetectors

MoEDAL is split in subdetectors, most of which are passive detectors : the trapping detectors array and the Nuclear Track Detectors (NTD) (Figure 2.11). The NTDs, acting like a giant camera, are first processed through chemical etching and then analysed offline by ultra-fast scanning microscopes to find etch pits and are sensitive to new physics. Thinner NTDs called "high-charge catchers" are inserted in the LHCb acceptance. In addition to passive sub-detectors, a state-of-the-art real-time TimePix pixel detector array is used to monitor MoEDAL's radiation environment.

2.3.2 The magnetic monopole trapping array

As mentioned in section 2.3.1 the second part of the passive sub-detectors of MoEDAL is the trapping detectors array consisting in aluminium bars, so-called the Magnetic Monopole Trappers (MMT). Assuming the binding of magnetically charged particles such as magnetic monopoles or dyons with the aluminium nuclei, the new particles produced at the LHC would stop in the MMTs and be trapped in the aluminium bars. The MMTs are located all around the interaction point forming a trapping array. The results discussed in this work are containing data coming from the scanning of the forward trapping detectors only as seen on figure 2.12.

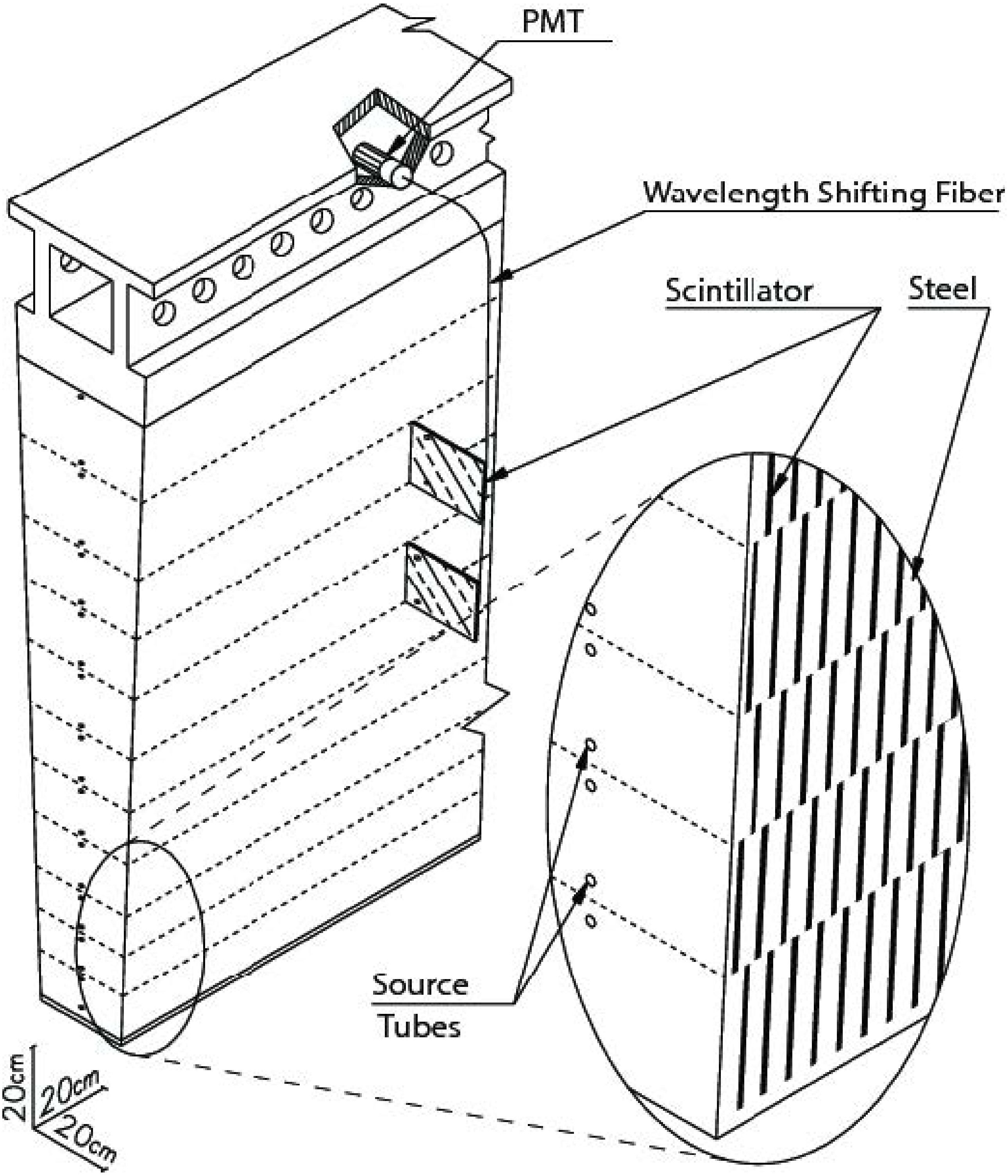

Figure 2.8: The tile barrel calorimeter.

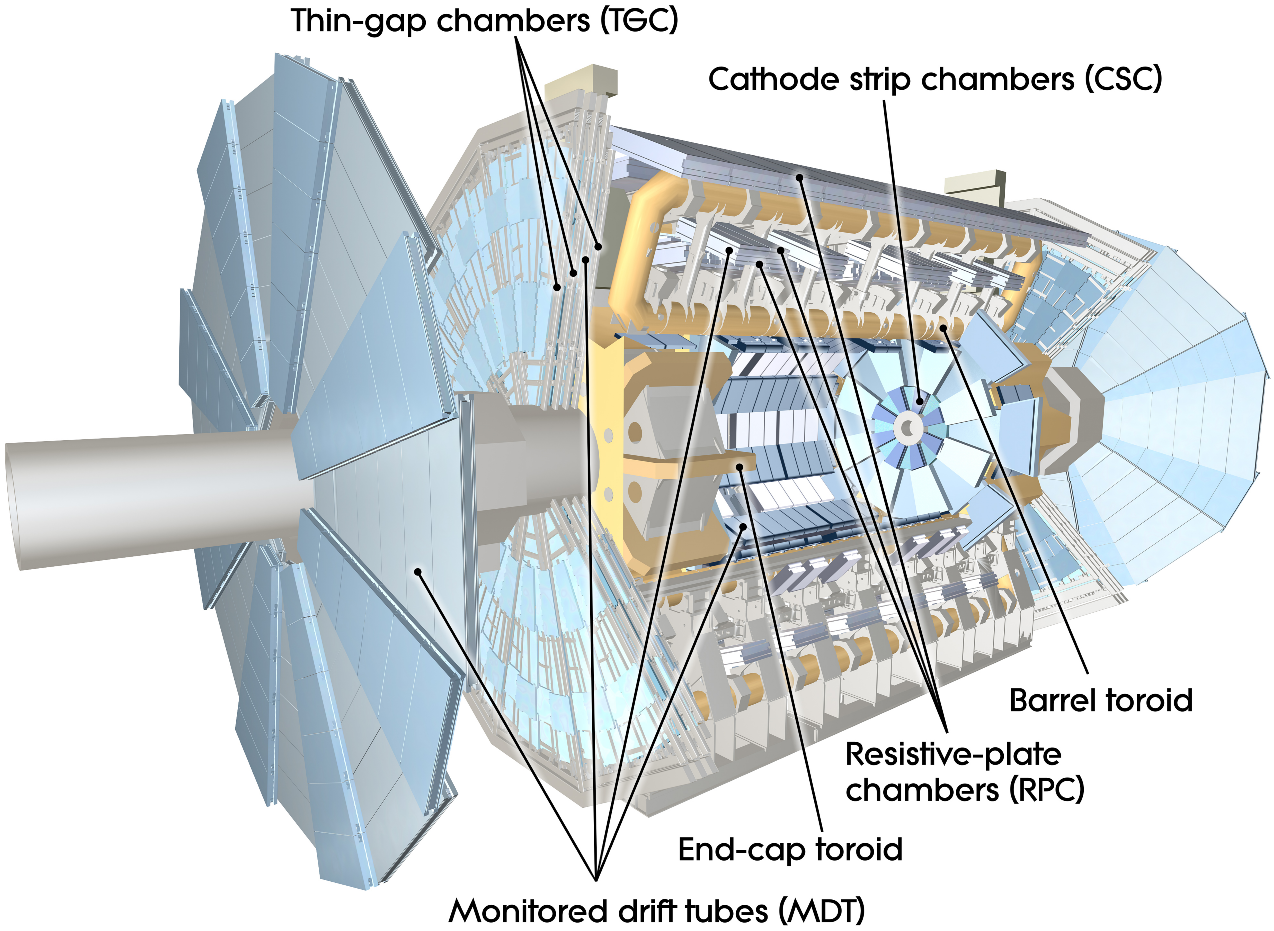

Figure 2.9: The sub-detectors of the muon spectrometer and the toroidal magnet system.

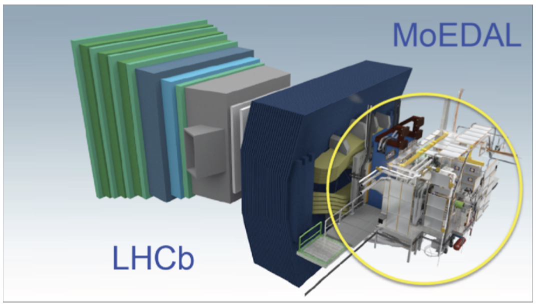

Figure 2.10: The MoEDAL apparatus at the LHC point 8 cavern

Figure 2.11: Nuclear Track Detectors and MMT

Figure 2.12: The MoEDAL forward trapping detector

Chapter 3

Double counting of δ-electrons in the Transition Radiation Tracker simulation package

As discussed into more detail in the next chapter, the Transition Radiation Tracker (TRT) sub-detector is at the centre of the ATLAS magnetic monopole search analysis, used both at trigger and analysis level, based on a discriminating variable derived as the fraction of high-thresholds hits in the regions aligned with the calorimeter Regions of Interest (RoI). The following work was presented as an ATLAS author qualification task.

3.1 Introduction

The TRT is the outermost sub-detector of the Inner Detector of the ATLAS experiment. The TRT is a straw based detector allowing two different features, indeed in addition to a tracking capability, the TRT is used as a particle identification tool.

The separation power is tuned thanks to the High Threshold (HT) discriminator, corresponding in the Monte-Carlo (MC) to the minimum energy deposit of a hit to be flagged as a HT hit.

Once this HT fixed on the hardware part, the TRT digitisation package needs to be tuned in order to match MC probability of high threshold (pHT) with the TRT collisions data. Due to a not well known Transition Radiation (TR) intensity and spectrum and in order to apply a correction, a TR efficiency parameter was added to the TRT digitisation package. This parameter allows to correct the TR photons production rate and absorption rate. The TR absorption cross-section being gas dependent a specific TR efficiency is thus required for each gas. A tuning of the TRT digitisation parameters for xenon was performed and validated during run I, but the suppression of the double-counting of δ-electrons during the TRT MC production is affecting the pHT and a full re-tuning of the TRT digitisation parameters must be achieved. While the pile-up during run 1 was quite low, the effects of the double counting of δ-electrons together with the run 2 high pile-up are expected to be worse, deepening the discrepancy between MC and data pHT.

After a short introduction of the δ-electrons double-counting issue, this note describes the tuning in two steps of the ATLAS MC model parameters. The first step (section 3.3) of the tuning is using 2010 proton-proton data[61] while the fine tuning (section 3.4) is using data from proton-lead run from the beginning of 2013 with a TRT gas geometry including both argon and xenon straws, closer to run 2 data.

3.2 Double counting of δ-electrons

A study made during the implementation of Argon gas mixture into the TRT simulation and digitisation revealed some unexpected discrepancies between Athena and Garfield[62]. Further investigations revealed that too many electrons were present in the TRT electrons spectrum after digitisation. This issue was from then on referred as double counting of δ-electrons. The double counting is explained by the fact that the TRT software is using at the digitisation step the PhotoAbsorption Ionisation model (PAI model). The GEANT4 calculation of the ionisation energy loss of a relativistic charged particle in gases is assumed to be inaccurate and is recomputed by the PAI model at the digitisation level. The PAI model was designed to account for the whole ionisation process, including the δ-rays production. The energy loss due to the δ-rays being propagated from GEANT4 into the digitisation in addition to the PAI model, there is a double counting of this energy. The solution envisaged and implemented was to cut at the simulation level the δ-ray production. To realise such a cut, the range cut of the electrons in the TRT straws was increased from 0.05 mm corresponding to about 1 keV of energy loss to 3 cm corresponding to about 75 keV energy loss in xenon. This new range cut allows to suppress most of the δ-electrons within a given straw as shown in figure 3.1.

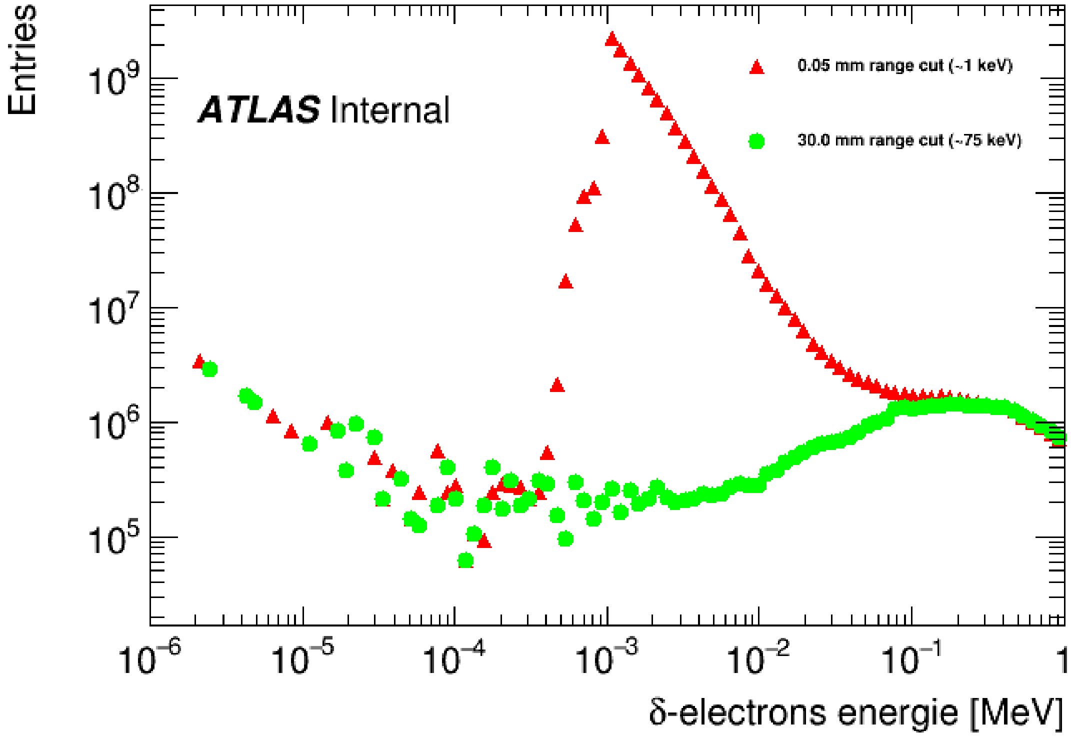

Figure 3.1: Electrons spectrum in the TRT after digitization

3.3 Preliminary tuning of the transition radiation efficiencies and rough high threshold tuning

The double counting of the δ-electrons being suppressed, the amount of energy deposit in the TRT is lowered, lowering the pHT. The TRT digitisation package was tuned to data with the double counting effect. It was thus mandatory to re-tune the TR efficiencies and the HT energy cut values to data in the TRT digitisation after the suppression of double counted δ-rays.

The TR efficiencies are first tuned using July 2010 data corresponding to an integrated luminosity of 20 nb $^{-1}$ with different HT settings. The selected data samples are electrons and pions as described in ATLAS note [61]. Those data are the only available for different hardware tuning of the HT. Single particle muons and electrons MC samples for different HT values and different TR efficiencies were generated. Muons and pions are known to have the same behaviour in the TRT, making consistent the comparison between data and MC. The TR efficiencies were tuned by comparing MC and data in electrons pHT versus muons pHT plots in the different detector regions[63], ie barrel (Figure 3.2), end-caps type A wheels (ECA) (Figure 3.3) and end-caps type B wheels (ECB) (Figure 3.4).

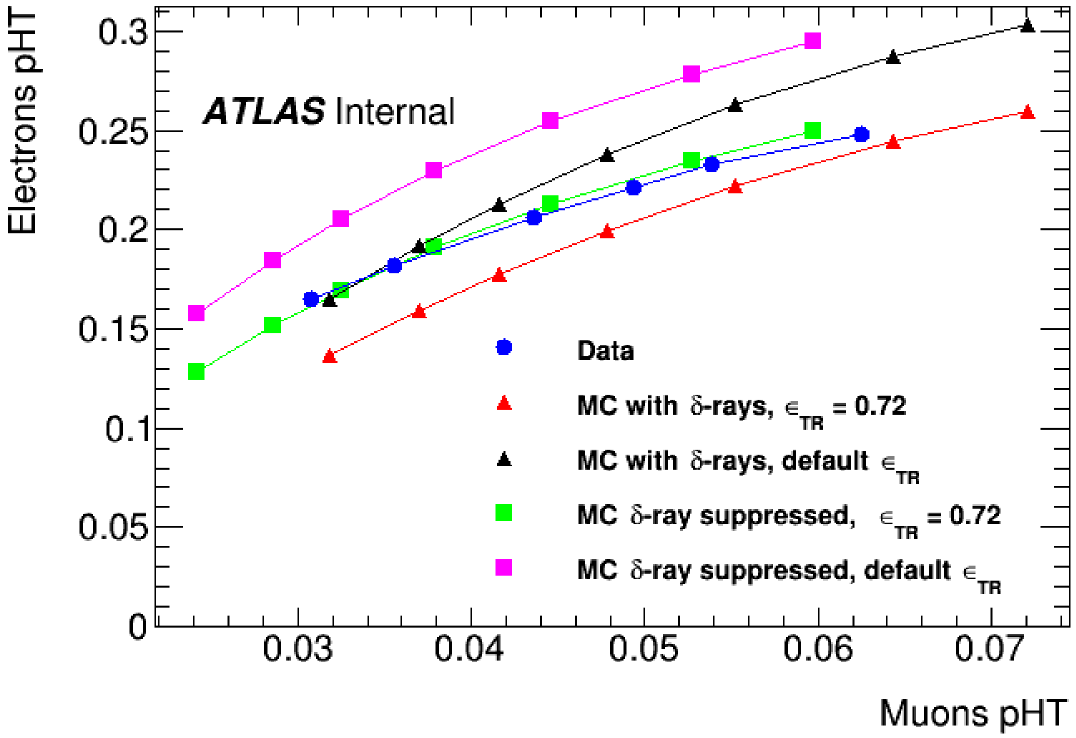

Figure 3.2: Electron pHT versus muons pHT in barrel long straws

For each region of the TRT, with a 1% TR efficiency step, MC and data were compared. This tuning method allowed us to determine a set of value for the TR efficiencies in the different regions. Respectively for the barrel, the ECA and ECB, 72%, 84% and 75%. The original ones being 95%, 100% and 100%. The agreement between MC and data is good and much better

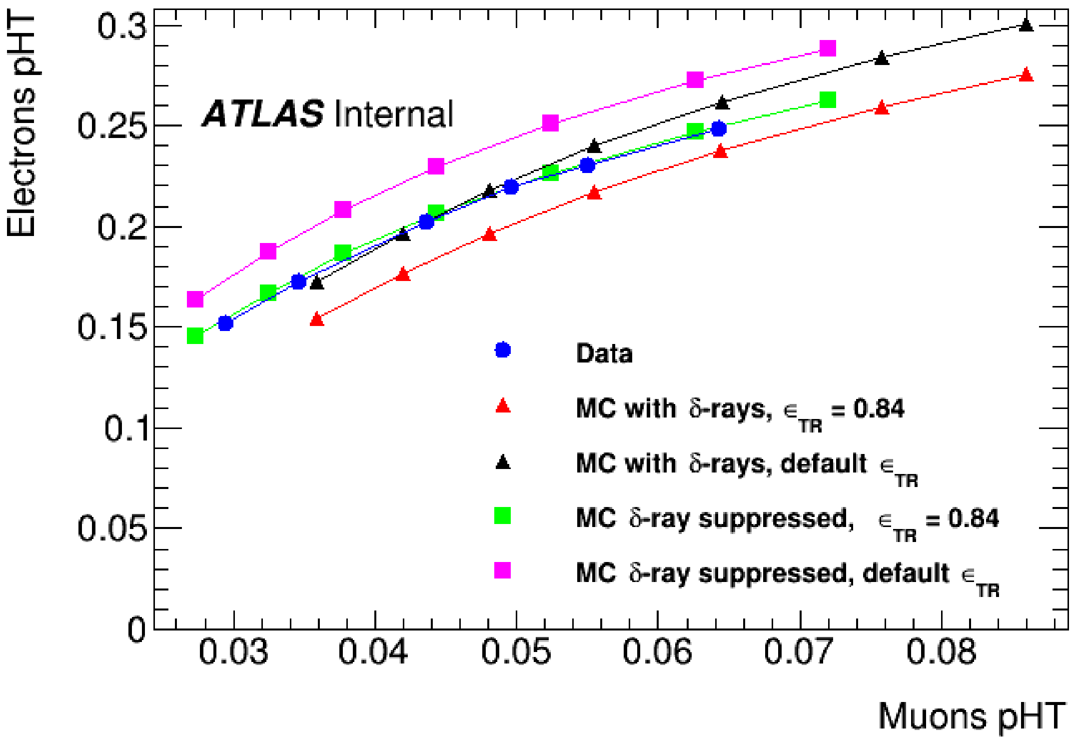

Figure 3.3: Electrons pHT versus muons pHT in ECA

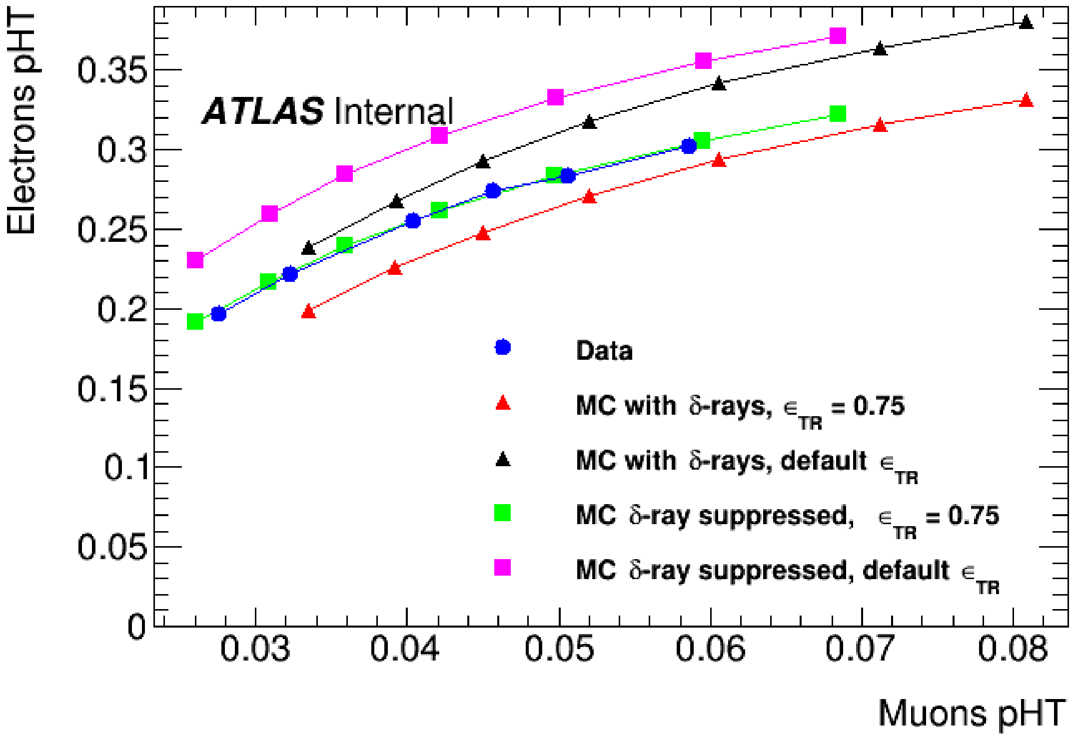

Figure 3.4: Electrons pHT versus muons pHT in ECB

than it was before as seen on figures 3.2, 3.3 and 3.4 by comparing default tune without δ-rays fixed MC to data.

In order to have a starting point for the fine tuning, the next step is to determine a rough set for the HT values. This was easily done by comparing the non-suppressed double counting δ-rays MC with the original set of TR efficiencies to the suppressed ones with the new set of TR efficiencies. Using pHT versus HT value plots (Figure 3.5 and 3.6) we could determine from the default HT tune the pHT for a muon sample for example and then using this pHT value on the δ-rays suppressed curve we can approximately determine the new HT value associated. The new set of HT values determined this way is 5.15 keV, 5.5 keV and 5.2 keV for respectively the barrel, ECA and ECB. The original ones being 6.02 keV, 6.39 keV and 6.07 keV.

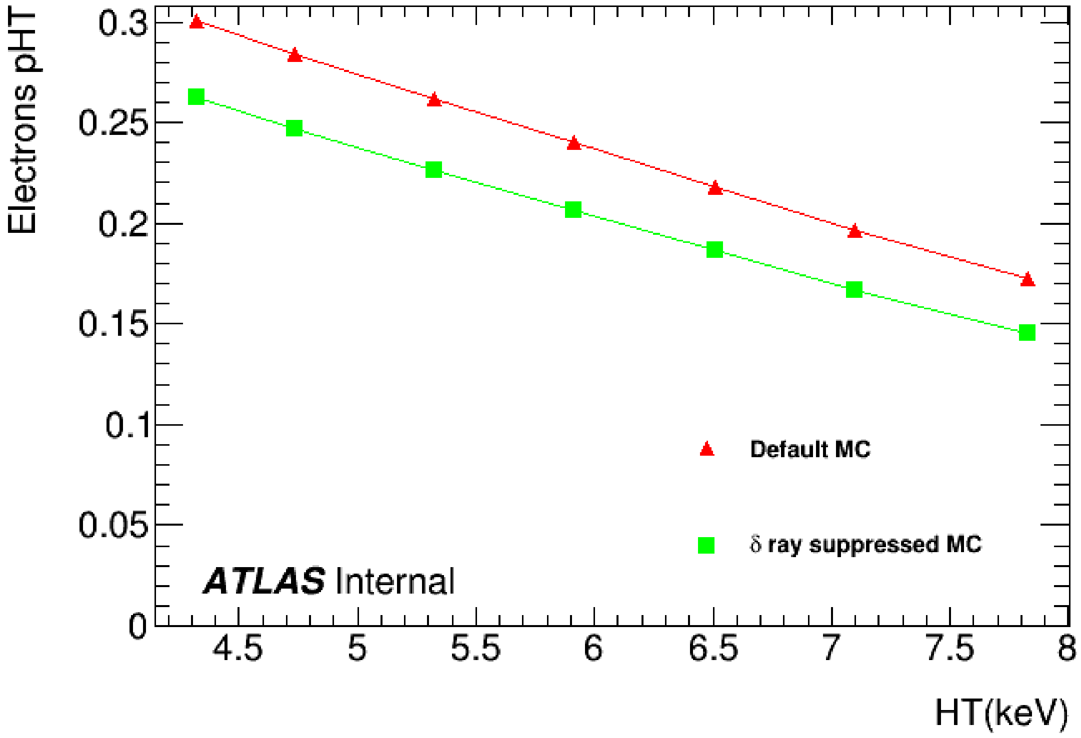

Figure 3.5: Electrons pHT vs HT value in end-caps A type wheels

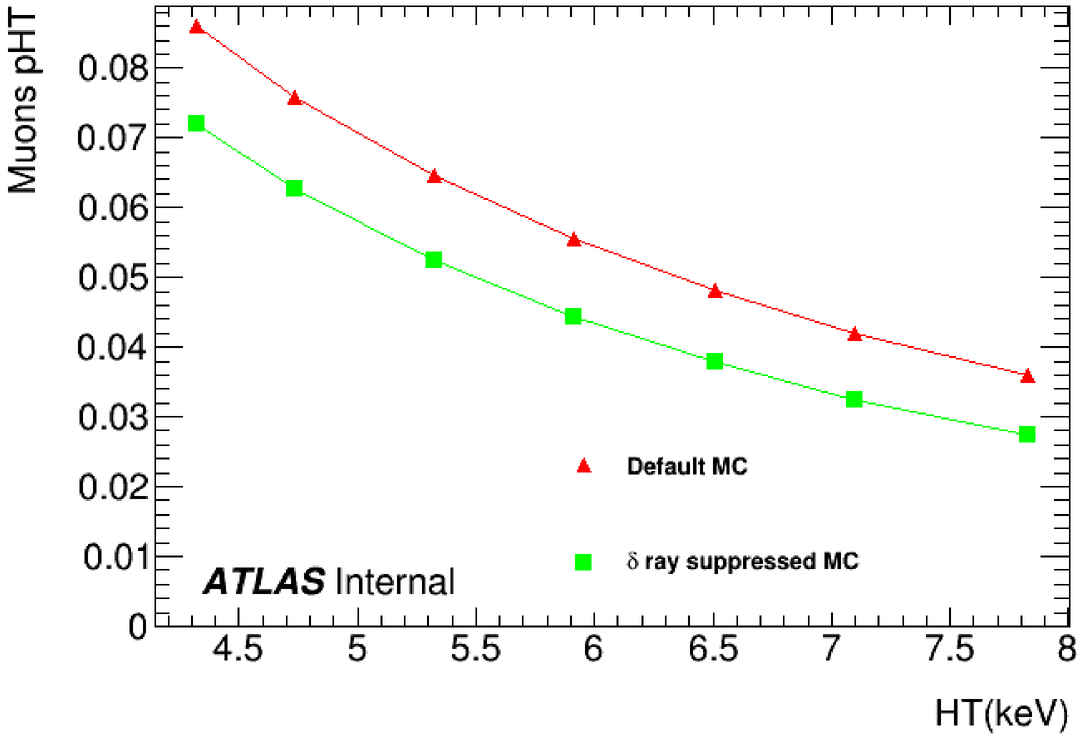

Figure 3.6: Muons pHT vs HT value in end-caps A type wheels

3.4 Fine tuning

To keep consistency with the work done for the argon tuning[62], the xenon HT tuning was done to 2013 p-Pb data which are the first runs including argon in the TRT. The TR efficiencies do not have very much impact on the muons pHT allowing the tuning to be split into two steps, first the fine tuning of HT values using muons samples and then the fine tuning of TR efficiencies using electrons samples.

The same configuration and selection as described in the previous section were used to generate in a first step samples with different HT values centred around the previously determined values and with fixed TR efficiencies values. The first layer of the barrel and two wheels of the end-caps which are containing argon were removed from the study as well as the end-caps fifty first straw layers since the data are using a special configuration in this region. With this configuration the HT set giving the best data/MC ratio in the different regions is 4.95 keV, 5.25 keV, 5.07 keV respectively in the barrel long straws, in ECA and ECB.

Based on this new HT tune, a new set of electrons samples with different TR efficiency values centred around the previous section values were generated. Using the same method than for the HT tuning, the fine tuned TR efficiency values set giving the best data/MC ratio was set to 77.4%, 93.2% and 83.0% respectively in the barrel long straws, in ECA and ECB.

Even though there should not be any xenon in the first layer of the barrel which contains all the short straws, the HT value for the barrel short straws was determined by applying a factor of 0.823 calculated thanks to the long straws HT values. The new HT value for short straws should then be 5.41 keV.

Using this new digitisation HT tune, the agreement between data and MC is very good (Figure 3.7, 3.8, 3.9 and 3.10). The Data/MC ratio values are for muons respectively in barrel, ECA and ECB, 1.002, 1.003 and 1.009. For the electrons samples the ratio values are respectively 1.004, 1.005 and 1.011.

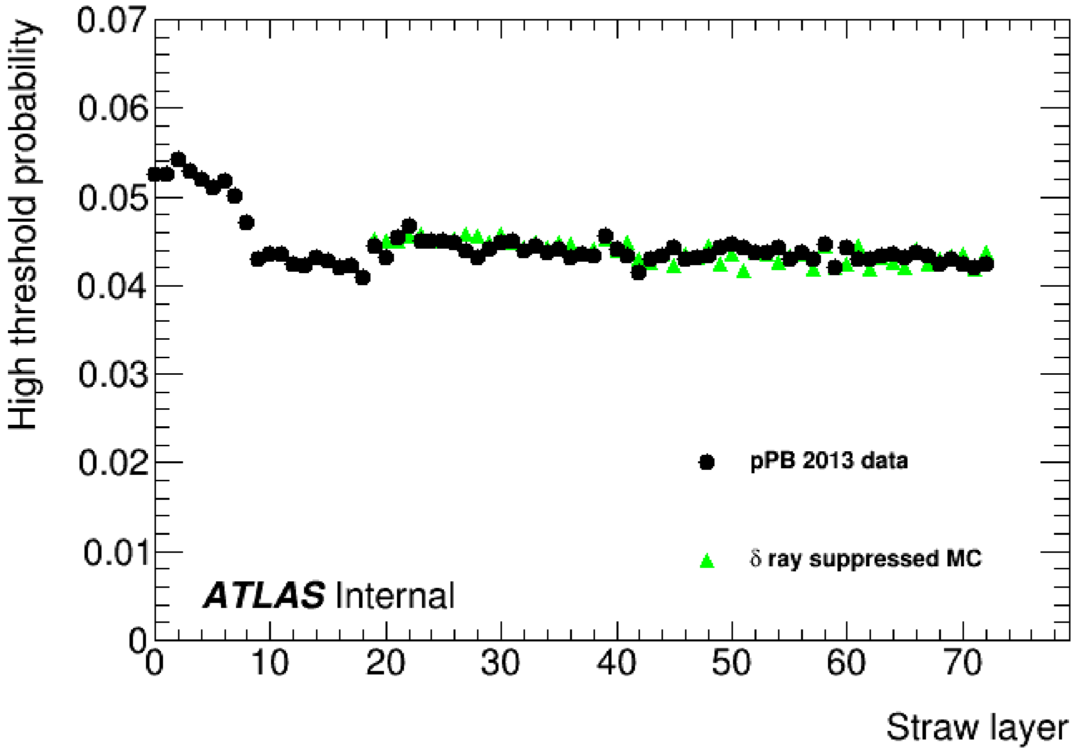

Figure 3.7: Muons pHT vs straw layer in the barrel. The first barrel layer being filled with argon no MC were computed in this region.

This double counting δ-rays suppressed tune was included into the TRT digitisation package

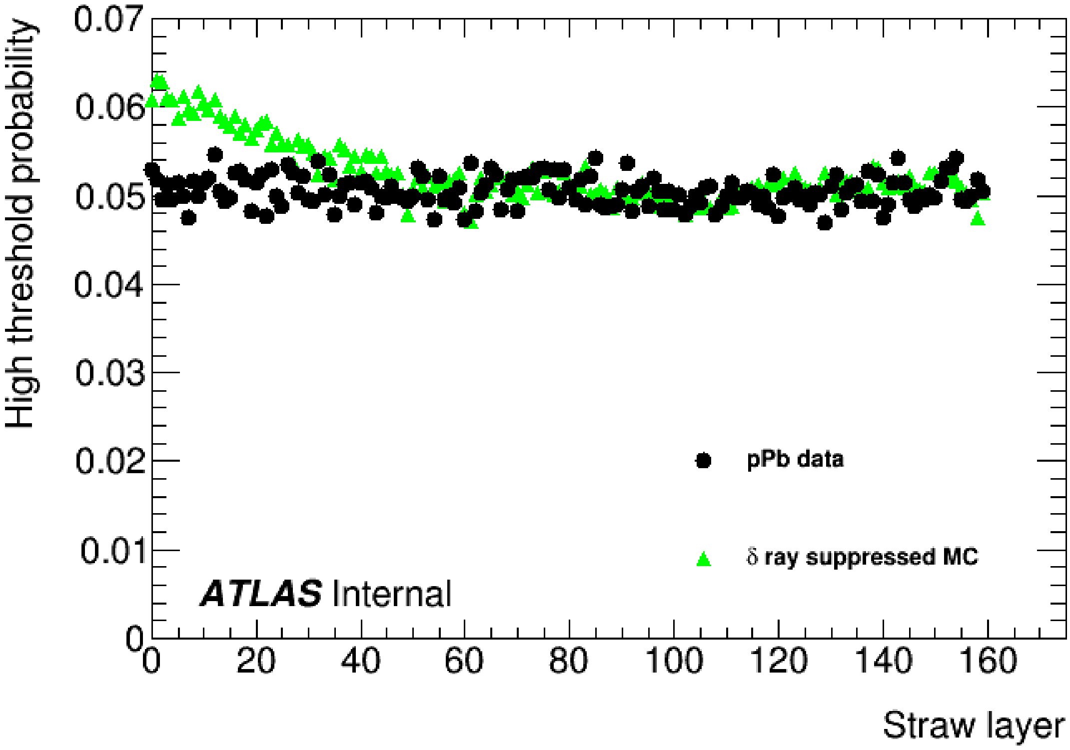

Figure 3.8: Muons pHT vs straw layer in the end-caps. The fifty first straw layers are removed from the comparison as the data are using a special configuration in this region

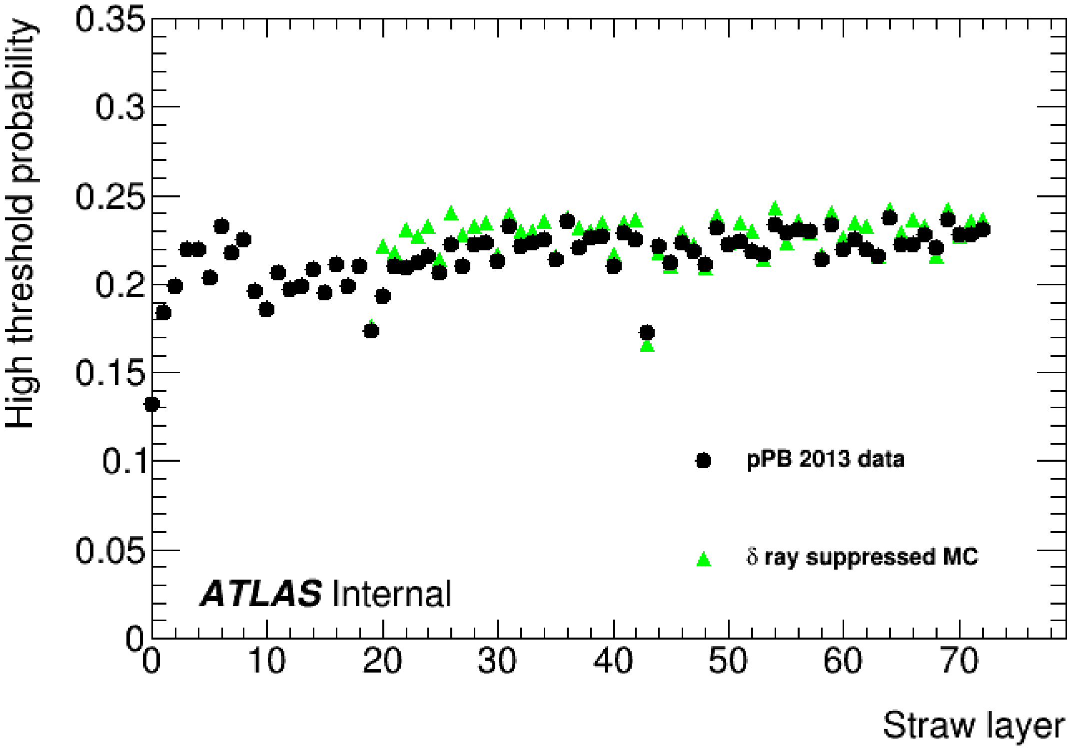

Figure 3.9: Electrons pHT vs straw layer in the barrel. The first barrel layer being filled with argon no MC were computed in this region.

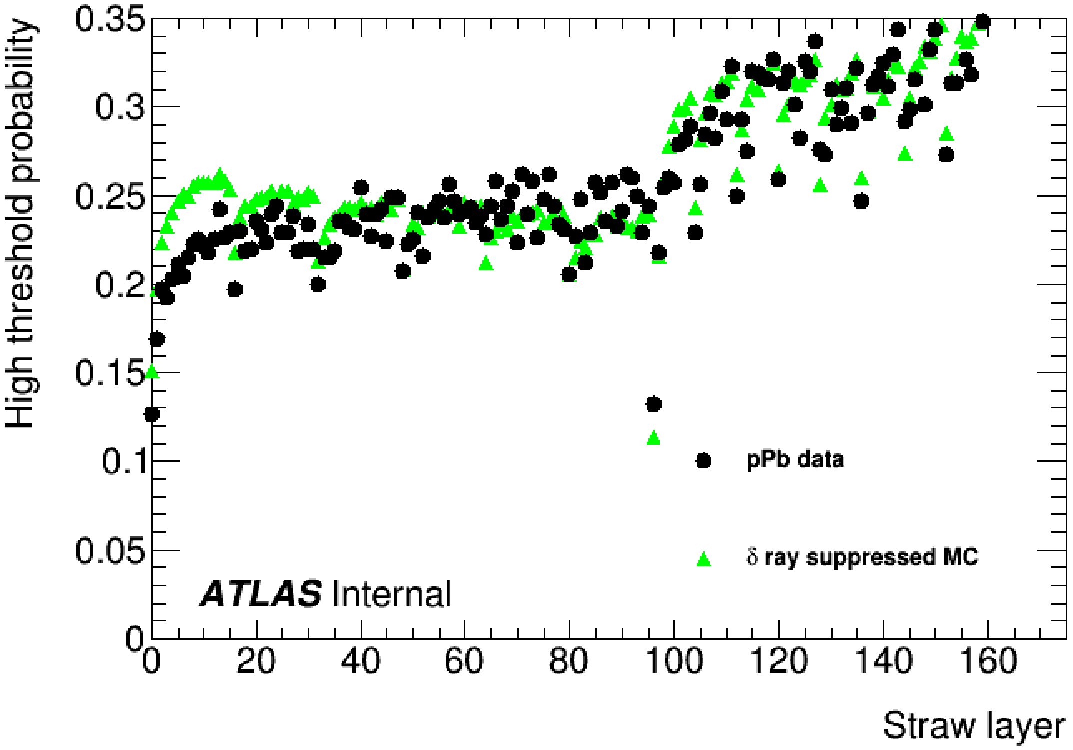

Figure 3.10: Electrons pHT vs straw layer in the end-caps. The fifty first straw layers are removed from the comparison as the data are using a special configuration in this region.

from tag TRT_Digitization-01-01-07. This tag is reading a flag added in the metadata of the HITS files at the simulation level from tag G4AtlasApps-00-09-01 to determine whether the δ-rays are double counted or not. It then automatically selects the corresponding tune. This feature was added to prevent any mismatch between simulation and digitisation parameters.

3.5 Study of double counting removal at higher pile-up

The whole study was realised at low pile-up. At high pile-up, the effect of the double counting of δ-rays fix is assumed to be increased. Some study at high pile-up would be required then and official MC samples including high pile-up and δ-rays fixed are presently in production.

3.6 Conclusion

Based on a low pile-up study a new digitisation tune corresponding to double counted δ-rays suppressed samples is now available :

	High threshold	TR efficiency
Barrel short	5.41 keV	0.774
Barrel long	4.95 keV	0.774
End-caps A	5.25 keV	0.932
End-caps B	5.07 keV	0.830

Chapter 4

The ATLAS Run 2 search

4.1 Data flow: Monte Carlo signal samples simulation and data reconstruction

The data recorded by the ATLAS detector in 2015 and 2016 used in this analysis requires many processing steps before reaching the desired analysis-ready flat ntuple as shown in the figure 4.1. In order to derive the analysis variables, core of the analysis strategy as described in the section 4.2, the recorded datasets as well as simulated signal datasets must undergo through several steps described in this section. The event generation, the simulation and the digitisation as described respectively in the sections 4.1.1, 4.1.2 and 4.1.3 are only relevant for the Monte-Carlo (MC) simulations, while the reconstruction as described in the section 4.1.4 is applicable to both data from the detector and MC samples.

Monte-Carlo simulations play an important role in High Energy Physics (HEP) analyses. They can be used for example to estimate the Standard Model expected backgrounds, the signal yield prediction of new physics process, variables allowing to discriminate signal from the background or systematic uncertainties.

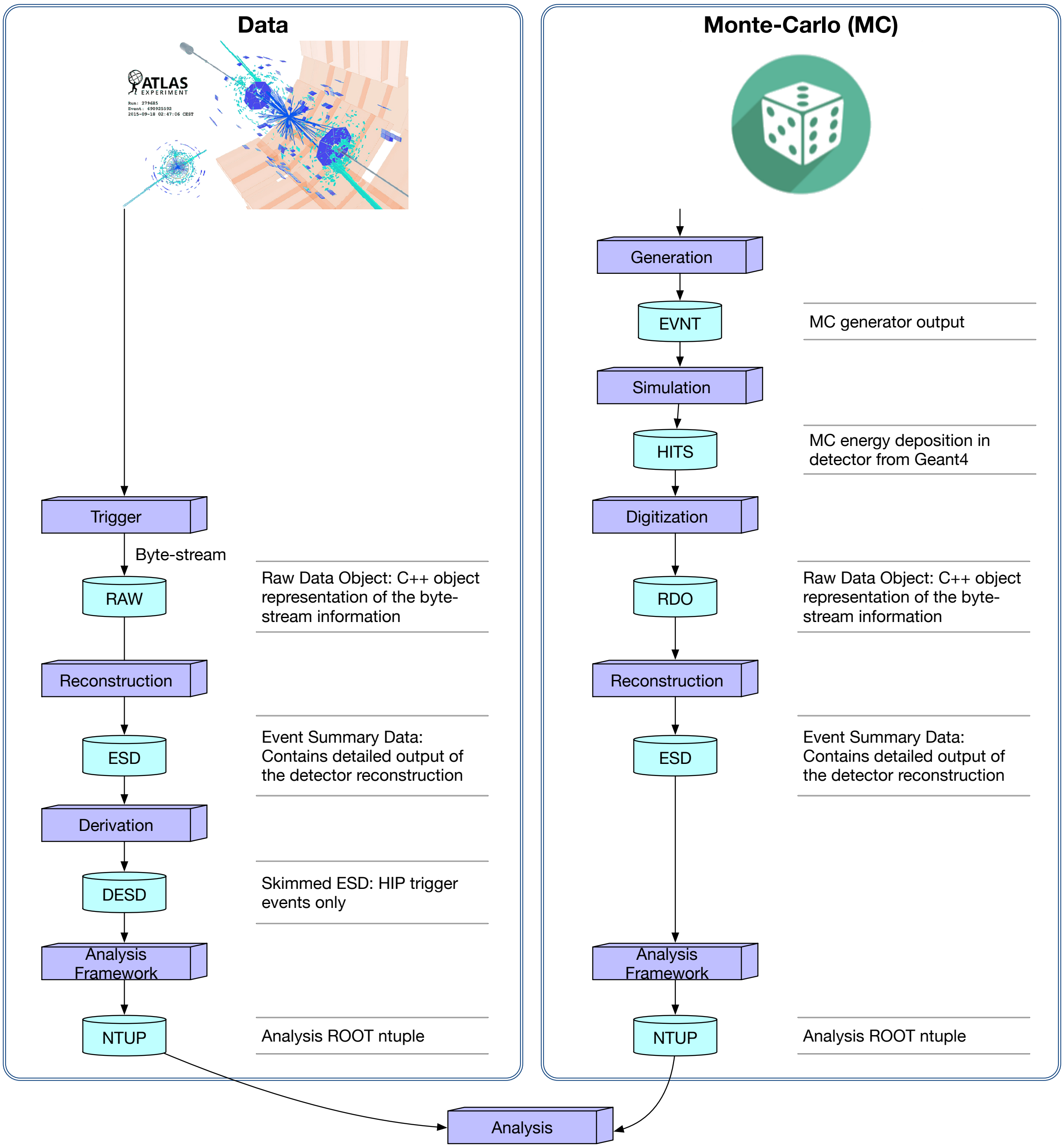

Figure 4.1: Data formats flow. Left diagram: Detector data processing flow. Right diagram: Monte-Carlo simulations data flow.

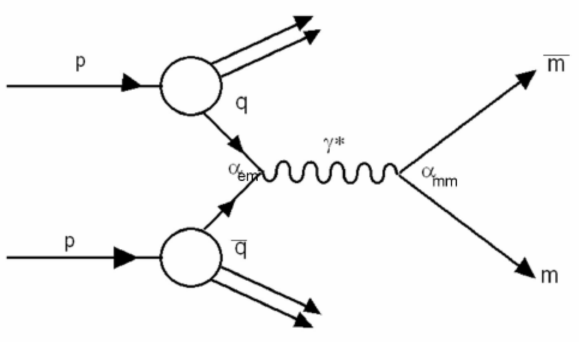

Figure 4.2: Feynman diagram for magnetic monopole production via the Drell-Yan mechanism. An analogous mechanism for HECO production is also used.

4.1.1 Event generation: Drell-Yan and Single Particle samples

The Highly Ionising Particles (HIP) production mechanism is not yet understood, the coupling to the photons of both the magnetic monopoles and the High Electric Charge Objects (HECO) being non-perturbative. Yet, it is a common practice to consider a Drell-Yan production mechanism, as shown in figure 4.2, allowing to derive mass limits serving as benchmarks for comparison with other experiments, such as for example MoEDAL. In addition to the Drell-Yan model assumption results, model independent efficiency maps are obtained allowing to derive cross-section limits for any model provided the production kinematics, based on the extrapolation method as discussed in the section 4.1.5. Two sets of MC simulations are thus needed, the Drell-Yan samples, as well as the model independent single particle samples.

Ten mass points are considered for monopoles and HECOs: 200, 500, 1000, 1500, 2000, 2500, 3000, 4000, 5000 and 6000 GeV. Magnetic monopoles of charge $|g| = 1g_D$, $2g_D$ and $3g_D$ are considered, as well as HECOs of charge $|z| = 20$, 40, 60, 80 and 100. HECOs with $|z| = 8$ and 10 were also studied but found that they had very low trigger efficiency due to the hadronic veto at level-1 as discussed in the section 4.2.1.

100 000 events per mass point were generated for single particle samples and 50 000 for Drell-Yan pair-produced samples.

Single Particle Events

The single particle samples are generated thanks to the Athena ParticleGun package. Each generated event consists in a HIP, or its anti-particle, with uniformly sampled kinetic energy in the range $10 < E_K < 6000$ GeV, η in the range $-2.0 < \eta < 2.0$ and ϕ in the full detector range.

Drell-Yan Events

This search considers the Drell-Yan model of pair production of spin-0 and spin-$\frac{1}{2}$ HIPs (see Fig. 4.2). The pair-produced samples are implemented in MadGraph5_aMC@NLO [64].

The MadGraph5_aMC@NLO generator [64] is used to compute the Drell-Yan production cross-sections and to generate the four-vectors of spin-0 and spin-$\frac{1}{2}$ pair-produced HIPs. A cut on the HIP transverse momentum is applied to both HIPs in the MadGraph samples at the generation stage to ensure that no CPU time is wasted on simulating particles not likely to penetrate to the EM calorimeter, a minimum requirement for firing the HIPTRT trigger. These p_T cuts are obtained for each mass-charge combination by determining the transverse momentum at which the HIPTRT trigger efficiency turns on (see Sec. 4.2.1).

Representative generator-level kinematic distributions for the Drell-Yan pair-produced events for various choices of HIP masses (after the generator-level p_T cuts are applied) are shown in Figs. 4.3–**??** for $g_D = 1$ spin-$\frac{1}{2}$, and spin-0 monopoles, respectively. These include transverse kinetic energy E_T^{kin}, pseudorapidity η, kinetic energy E_K, relativistic velocity β, transverse momentum p_T, and relativistic γ factor distributions. Similar distributions for HECOs are given in Appendix A.

For the Drell-Yan spin-$\frac{1}{2}$ HIP samples, the MadGraph four-vectors for the HIPs are subsequently processed in Athena by evgen, which implements the hadronisation and associated momentum smearing. PYTHIA8 [65, 66] with the A14N23LO PDF was used for the hadronisation.

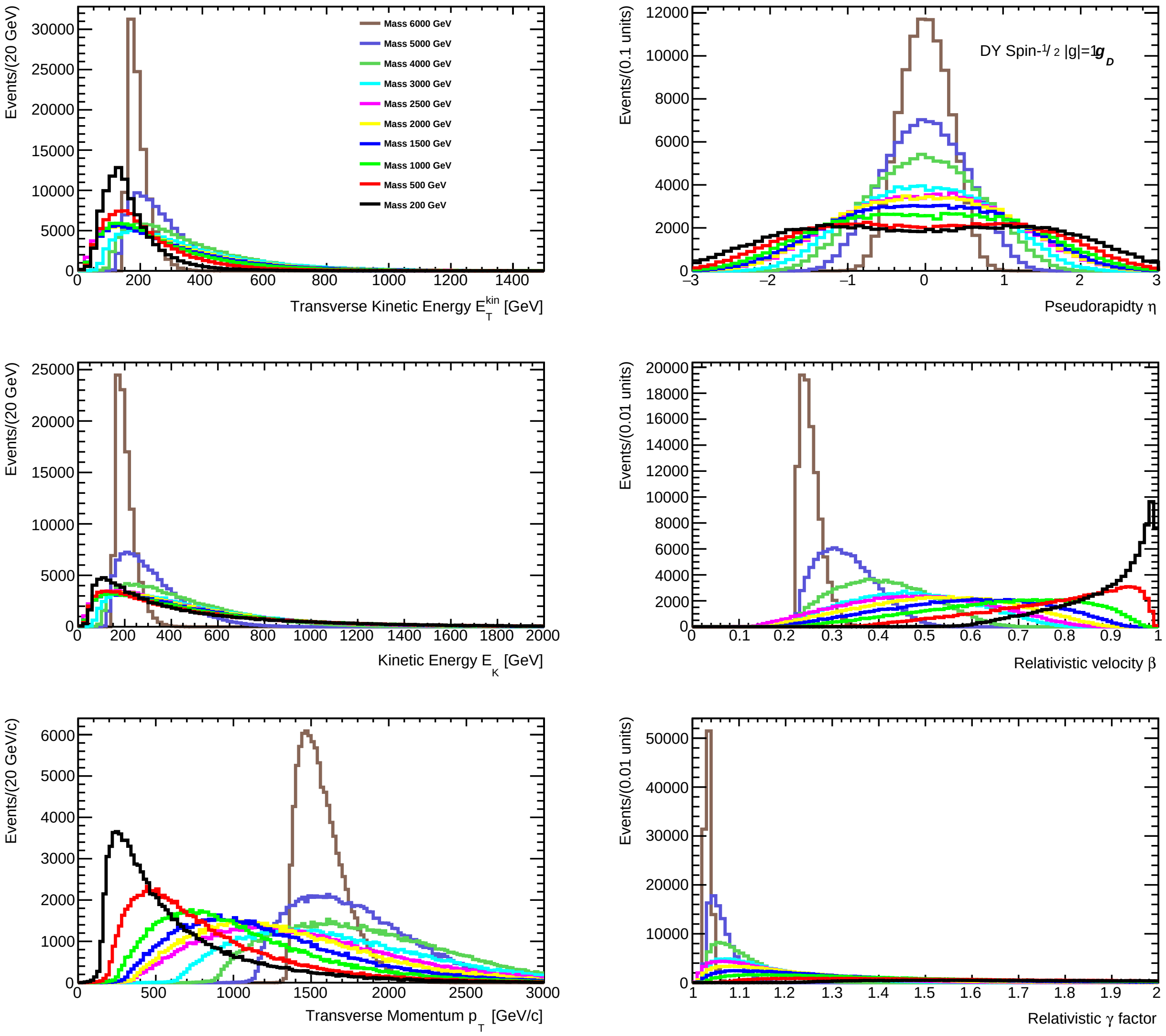

Figure 4.3: Generator-level transverse kinetic energy E_T^{kin}, pseudorapidity η, kinetic energy E_K, relativistic velocity β, transverse momentum p_T, and relativistic γ factor, distributions for Drell-Yan pair-produced charge $g_D = 1$ spin-$\frac{1}{2}$ monopoles with various masses (after a minimum p_T cut is applied).

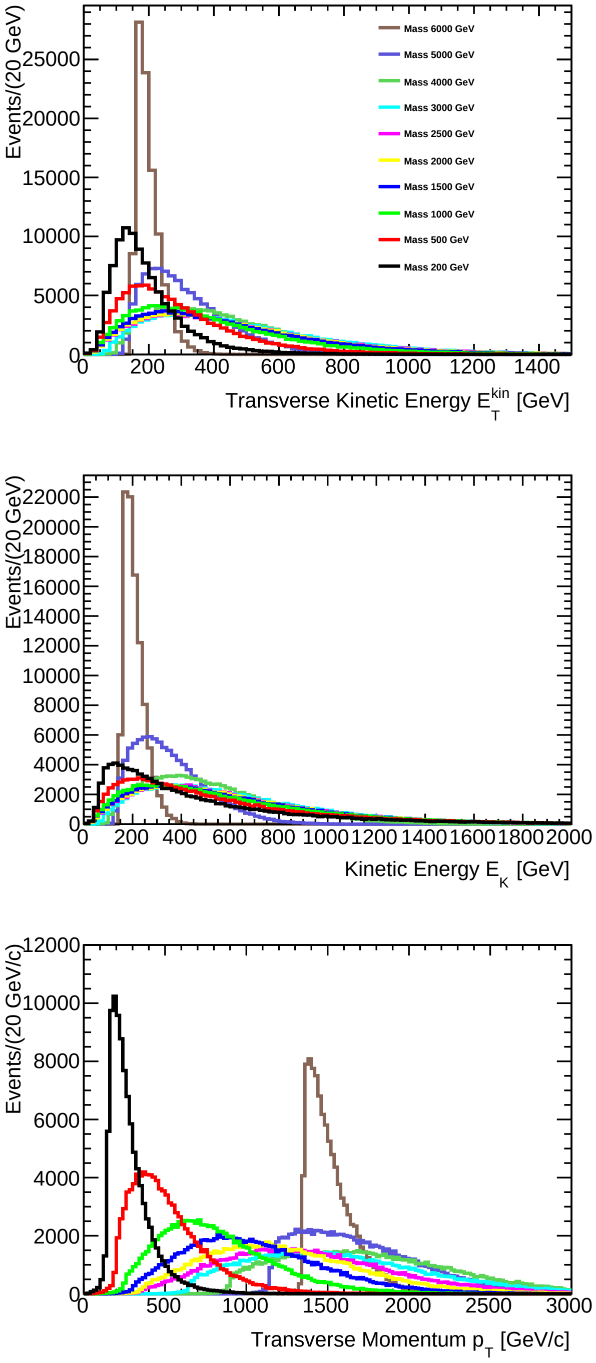

Figure 4.4: Generator-level transverse kinetic energy E_T^{kin}, pseudorapidity η, kinetic energy E_K, relativistic velocity β, transverse momentum p_T, and relativistic γ factor, distributions for Drell-Yan pair-produced charge $g_D = 1$ spin-0 monopoles with various masses (after a minimum p_T cut is applied).

Systematic uncertainties samples

In addition, various 10 000-events custom samples were produced to assess the systematic uncertainties in the final efficiency calculations as described in section 4.2.4.

4.1.2 Simulation of the events in the ATLAS detector with Geant4

The HIPs events being now generated, in order to estimate the signal selection efficiency of HIPs at ATLAS, the monopoles and HECOs interactions with the detector must be simulated. The simulated is done thanks to the GEANT4 package within the Athena framework. A dedicated HIP simulation package, `Simulation/G4Extensions/Monopole`, was developed and validated during the 2011 and 2012 HIPs searches as described in [20] and [67]. The validation of the simulation mostly focused on the HIP ionisation energy loss simulation, the δ-ray production mechanism for HIPs and the monopoles trajectory in the ATLAS magnetic field.

The simulation includes a special correction to Birks' Law in the LAr EM calorimeter. Birks' Law models the effect of electron-ion recombination as a function of dE/dx in LAr and is implemented in Athena as

$$E_{vis} = E_0 \frac{1 + A'k/E_D}{1 + k/(\rho E_D)dE/dx}, \tag{4.1}$$

where E_0 is the true deposited energy, E_{vis} is the visible energy, ρ is the LAr density, E_D is the electric field, k is Birks' constant and A' is a normalisation parameter. Birks' Law overestimates the recombination effects for particles with very large dE/dx, thus a HIP correction to Birks' Law was implemented, as described in Refs. [68, 20, 69].

Single particle samples and spin-$\frac{1}{2}$ Drell-Yan samples were fully simulated as part of the official MC15c production campaign. Due to limitations in computing resources, single and Drell-Yan monopole samples of charge $2g_D$, $3g_D$ and HECO samples of $|z| = 80$ finished with only a fraction of the requested events. It was impossible to finalize single particle samples of mass 6000 GeV monopoles for charges $2g_D$ or $3g_D$. Simulation of Drell-Yan samples of $3g_D$ monopole and $|z| = 100$ HECOs was not attempted due to frequent crashes in the digitisation stage. The efficiencies for those charge points were derived thanks to the extrapolation method as explained in section 4.1.5.

4.1.3 Digitisation with the ATHENA framework

The digitisation is the last step specific to the MC datasets production. It produces Raw Data Object (RDO) files, containing simulated digital signal corresponding to the previously simulated energy deposition and interactions in the detector, similar to the recorded data RAW files. The simulation of the pile-up conditions happens during the digitisation step. Additional collisions are overlaid to the HIPs events following the default MC15c pile-up profile. The default pile-up conditions are not aligned with the HIP trigger collected data conditions. Since collisions and simulated data do not have perfectly matching pileup profiles, a pileup reweighing is applied at analysis level together with an associated systematic uncertainty to account for these differences.

Most of the samples were produced with tag r7772 using release AtlasProd1 20.7.5.1.1, which contains the trigger menu with the HIPTRT trigger and is compatible with MC15c simulation production campaign. In order to fix PIXEL and SCT digitisation issues happening for high-charge samples, a new tag was created, tag r9862. This tag allowed to disable the PIXEL and SCT containers reconstructions which was causing fatal failures and are not used by the HIP analysis.

Monte Carlo samples were produced in Event Summary Data (ESD) and Analysis Objects Data (AOD) format.

4.1.4 Reconstruction with the ATHENA framework

Both digitised MC samples and data from the detector consist in ATLAS sub-detectors hits and energy deposition in calorimeter cells, in a C++ object representation of the detector byte-stream information. In order to be able to use this data, a full reconstruction of the physics objects involved in the events must be done event by event taking advantage of all the sub-detectors. The reconstruction can be split in two big steps, a first step reconstructing detailed information on the particles such as tracks, energy deposition clusters, stored in ESD files and a second part reconstructing the physics objects stored in AOD files or xAOD files for the Run 2 analysis. The HIP analysis being considered as an exotic analysis, the AODs do not contain monopole or HECO specific containers and the analysis variables must be derived at the analysis level. It is thus important for this analysis to store all datasets as ESDs which conserve all hits and calorimeter cells information and allow to derive relevant variables. As discussed in the section 4.2, this search event selection relies on two reconstructed objects: the TRT drift circles and the EM calorimeter clusters.

TRT hits and drift circles

The TRT pulses are digitised and recorded for each straw thanks to 27 bits. The binary message is split into 3 slices of 9 bits. For each slice the first bin is used as a High-Threshold (HT) hit flag and the 8 other bits contain the Low-Threshold (LT) hits information. Each bin represents about 3.125 ns and thus one slice covers 25 ns corresponding to one bunch spacing and one event thus covers 75 ns. The digitisation of a TRT pulse is shown in the figure 4.5. The bins are set to 0 when the signal is below the LT and to 1 when above the threshold. This allows to measure the time over threshold and the drift time. The drift time is measured as the time at which the pulse exceed the low threshold. That is because the electrons drifting velocity is orders of magnitude slower than the event particles. Thanks to a calibration the drift time allows to derive the drift-circle radius, the distance between the straw wire and the electrons produced at the point of closest approach to the wire, which is used by the tracking algorithm to reconstruct precise tracks. The parameter T_0 as described in the figure 4.5, take into account leading-edge time discrepancies between straws and was adjusted during the calibration. In order to suppress out-of-time pile-up, filters are applied on drift-circle leading-edge and trailing-edge. If a pulse has a too early trailing-edge it would be associated to the previous bunch crossing. Similarly a pulse with a late leading-edge would be suppressed as associated with the following bunch crossing.

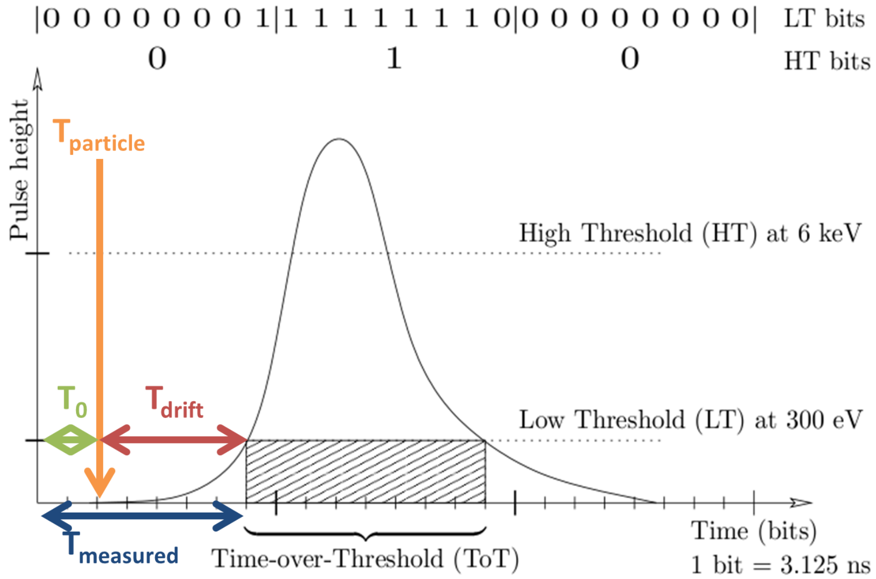

Figure 4.5: Digitization and timing of a TRT pulse [70]. The colored arrows are depicting different timings important for the reconstruction of a physical hit.

In this search, detailed drift-circles information is not required, the variables are indeed derived based on the number of HT and LT hits as discussed in the section 4.2.2.

Calorimeter topological clusters

ATLAS calorimeter clusters are usually used to measure the energy deposition of particles and jets. The HIPs energy loss in the inner detector, before reaching the calorimeter, is too important and it is not possible to reconstruct the HIPs energy based on the clusters. However, the shape of the energy deposition, ie the shape of the calorimeter clusters, in particular the lateral extent of the energy is a strong discriminant against the background in this search as shown in the section 4.2.2. The energy density-based approach of the topological clusters is thus relevant for this analysis. The topological clustering is split in two steps, the cluster maker and the cluster splitter. The cluster maker identifies cells with a high signal to noise ratio. The noise contributions being the external noise at a null luminosity and the noise coming from the pile-up or occupancy. Cells with a ratio above 4 as well as neighbouring cells with a ratio above 2 compose the clusters of the cluster maker algorithm. Once stable, all the neighbouring cell of each clusters are added to their respective cluster in order to keep the tails of EM cascades and jets. This algorithm would merge any sub-structure into a fat cluster and overlapping particles would be assigned to a single cluster. The cluster splitter algorithm attempts to break the previously defined clusters and overlapping particles. The algorithm identify the local maxima inside the clusters which would then be used as the seeds for another iteration of the cluster maker algorithm. The local maxima are defined as cells with an energy deposition $> 500\ MeV$ and the highest of a 4 or more cells cluster. The shared cells at the boundaries of the newly defined clusters have a weighted energy contribution to the clusters, avoiding a double counting of the energy deposition.

Trigger reconstruction

The triggers emulation for the MC simulations samples is done during the reconstruction step. It allows to estimate the signal efficiency of the trigger. The emulation was also made for enhanced-bias samples, allowing to derive the HIP trigger expected rate during the development phase. The signal efficiency, triggering rate and computation timing of a trigger are the key aspects to take into account when developing a trigger and it makes the trigger reconstruction a crucial step of the development.

4.1.5 Extrapolation method

Single particle samples are also used to obtain model-independent efficiency maps in the two-dimensional E_T^{kin} vs η plane. Here, E_T^{kin} is the transverse kinetic energy, that is, $E_T^{kin} = E_K \sin\theta$, where E_K is the kinetic energy and θ is the polar coordinate of the particle trajectory. Then, to obtain cross-section and mass limits for a realistic kinematic distribution, pair-produced samples of spin-0 and spin-$\frac{1}{2}$ HIPs are used in conjunction with the efficiency maps.

The Drell-Yan spin-$\frac{1}{2}$ HIP samples were fully simulated. Since the interaction of HIPs with the ATLAS detector is spin-independent, the spin-dependent differences in efficiency are determined by the production kinematic distributions alone and thus can be quantified at the Monte Carlo generator level. Therefore, it was not necessary to fully simulate the other pair-production model events. The efficiency maps from the single particle samples were used to infer the

HIP reconstruction efficiency for spin-0 Drell-Yan pair production as well as spin-$\frac{1}{2}$ Drell-Yan samples $3g_D$ monopole and $|z| = 100$ HECOs which could not be fully simulated due to frequent crashes in the digitisation stage. This “so-called” *extrapolation method* is described in Ref. [71].

The cross-sections for pair production of spin-0 HIPs are lower than that for the corresponding spin-$\frac{1}{2}$ HIPs due to angular momentum conservation considerations. Since the intermediate (virtual) photon (see Fig. 4.2) has spin-1, the production of spin-0 HIPs is suppressed near the phase-space threshold. This also results in differences in the kinematics distributions.

4.2 Highly Ionising Particles Run 2 Analysis

The analysis strategy relies on the definition of a signal region in the analysis variables plane were the signal efficiency must be high and the expected background low. A significant excess of observed events in the signal region compared to the expected background would yield to a discovery. A number of observed events compatible with the background only hypothesis would allow to infer cross-section upper limits and mass lower limits assuming a HIP production model. The HIPs production cross-section limits and the mass limits as described in the section 4.3.2 were derived using the signal region event selection efficiency, background rejection and associated uncertainties. The systematic uncertainties as described in the section 4.2.4 contribute to the signal efficiency uncertainty, together with the MC simulation statistical uncertainty. The background estimate uncertainty is derived thanks to the TRooABCD tool as described in the section 4.2.3, taking into account signal leakage, uncertainty on the transfer factor and statistics.

The event selection, aiming at discriminating HIP candidate events from the rest of the recorded collisions while keeping a high signal efficiency, is split in three steps: the HIP dedicated trigger deciding on which events to record for offline analysis as described in section 4.2.1, a coarse pre-selection cutting obvious background and regions with too low sensitivity as described in section 4.2.2 and the final selection based on the analysis discriminating variables as described in section 4.2.2.

4.2.1 Highly Ionising dedicated High-Level Trigger

As discussed in section 1.2.4, the HIPs have a big stopping power in the ATLAS detector material and may stop before going through all ATLAS sub-detectors layers. It is thus important to keep a high selection efficiency to trigger on information from the innermost sub-detectors of ATLAS. As the ATLAS trigger system had no capacity to trigger on particles tracks, this analysis relies on the EM calorimeters L1 triggers and HIPs candidates have to deposit energy in the EM calorimeter to fire the trigger. The Fast Tracker (FTK) recently developed would possibly provide a better triggering solution for future HIP analysis, however FTK was not available for the analysis presented in this work. The hardware-based triggering, level 1 trigger, was thus chosen to be the lowest unprescaled EM trigger available for run2.

None of the existing High Level Trigger (HLT) would have satisfying enough signal efficiency, the best candidates being the single electrons or photons EGamma triggers. Electrons triggers apply rules on discriminating variables based on particles tracks or TRT probability of high threshold hits, that cuts most of the HIP signal due to the high number of δ-electrons generated along the HIPs path. Photons triggers require that candidates EM clusters deposit energy in the second layer of the calorimeter. HIPs stopping before reaching the second layer of the calorimeter would not fire the trigger and the signal selection efficiency would be significantly affected. In addition, like the electrons triggers, the photons triggers use discriminating variables to identify photons, such as for example the ratio of energy deposited in the EM calorimeter over the energy deposited in the hadronic calorimeter. Even with loose identification criteria, HIPs with enough energy to reach the hadronic calorimeter are likely to be cut by the photons HLT.

Motivated by the inefficiencies mentioned above, a dedicated HIP HLT was developed, allowing to keep a high signal selection efficiency while maintaining a low rate.

Highly Ionising Particles High-Level Trigger algorithm

The HIP trigger algorithm was develloped in 2012 [72] for the previous ATLAS search for HIPs in Run 1, using data from pp collisions at $\sqrt{s} = 8\ TeV$ [42]. It allowed to recover events with

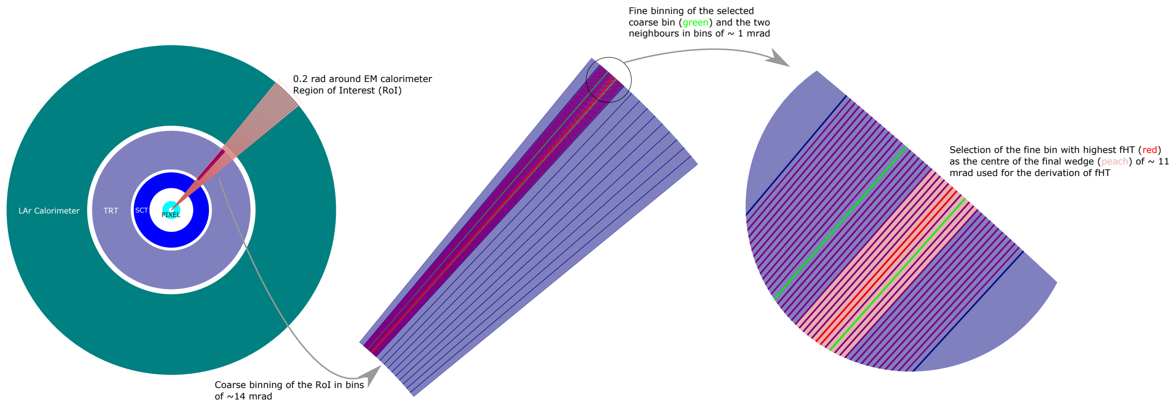

Figure 4.6: HIP High Level Trigger algorithm centring of the TRT wedge around the path of the particles.

HIPs stopping in the first layer or pre-sampler of the EM calorimeter and allowed to set better constraints on monopoles compared to the ATLAS search at $\sqrt{s} = 7\ TeV$ relying on electrons triggers, in the absence of a dedicated HIP trigger.

The HLT algorithm is seeded by the lowest unprescaled EM Level 1 (L1) trigger, the EM22VHI chain during 2015/2016 data taking period. The EM trigger reconstructs energy deposition in Region of Interests (RoI). In order to pass the L1 seed the energy deposition in the EM calorimeter must be above the threshold set to 22 GeV for the trigger EM22VHI. The L1 trigger also includes a so called Hadronic Veto (HV) and an EM Isolation (I) criteria. The EM isolation is not applied for L1 objects deposing more than 50 GeV in the calorimeter and have no impact on the HIP signal efficiency. The hadronic veto is rejecting events having an energy deposition in the hadronic calorimeter bigger than 1 GeV. This would suppress most HIPs candidates energetic enough to reach the hadronic calorimeter. Fortunately the Run 2 HV was revised to be only applicable for an energy deposit up to 50 GeV and would not be a limitation for HIPs detection as HIPs reaching the calorimeter are likely to deposit more than 50 GeV in it. The HV was a limitation for the Run 1 analysis and the new rule allows to probe for higher energy HIPs and lower electric charge HECOs. The Run 2 HV still impacts the lower charges HECOs as discussed later in this section.

The HIP trigger algorithm, TrigTRTHighTHitCounter, is a trigger hypothesis algorithm applying cuts on 2 variables, the number of TRT high threshold hits ($N_{HT,trig}$) and the fraction of TRT high threshold hits ($f_{HT,trig}$), reconstructed in a ∼11 mrad wedge centred around the HIP candidate RoI seeded by the Level 1 trigger. The first steps of the algorithm consist in identifying the RoI with highest $f_{HT,trig}$ and defining a wedge centred around the HIP candidate path in which the trigger variables are derived. The centring and size of the wedge as described in figure 4.6, were refined for the Run 2 in order to keep a low rate below 1 Hz with increased luminosity while maintaining a high signal efficiency. While the TRT would allow to cover an η range up to $|\eta| < 2$, the algorithm would only consider for the Run 2 RoI with $|\eta| < 1.7$, most of the background being in the forward region. This additional eta cut is having a minimal impact on signal efficiency, while allowing a significant rate decrease. The centring of the wedge is done in 2 steps, a first coarse binning of the 0.2 rad RoI wedge into 14 bins, and a second fine binning of the coarse bin with the highest $N_{HT,trig}$ and the two coarse neighbouring bins into 3 times 14 bins. The fine bin of about ∼1 mrad with the highest $N_{HT,trig}$ is the centre of the wedge defined by the central fine bin and its 10 neighbouring fine bins, highlighted in peach colour in figure 4.6, resulting in a ∼11 mrad wedge. The wedge's width in the TRT extends from ∼6 mm to ∼12 mm, to be compared to the TRT straws size of 4 mm. The trigger variables distributions reconstructed for one random run of 2016 are compared in the figure 4.7 to the ones of a representative monopole Drell-Yan sample and a QCD Monte-Carlo sample accounting for most of the background. The trigger selection was set for the Run 2 to $N_{HT,trig} > 30$ and $f_{HT,trig} > 0.5$. The recorded events that fire the trigger are in the tail of a falling distribution as shown in figure 4.7, making the trigger rate sensitive to the TRT occupancy.

HIP trigger performance

HIP trigger efficiency Comparing the Level 1 seed trigger efficiency turn-on curves, shown in figures 4.8 and 4.9, and the HIP HLT trigger efficiency turn-on curves, shown in figures 4.10 and 4.11, it can be observed that the HIP trigger efficiency is mostly driven by the Level 1 trigger efficiency. The Level 1 turn-on curves plateau around 1 after reaching the minimal energy

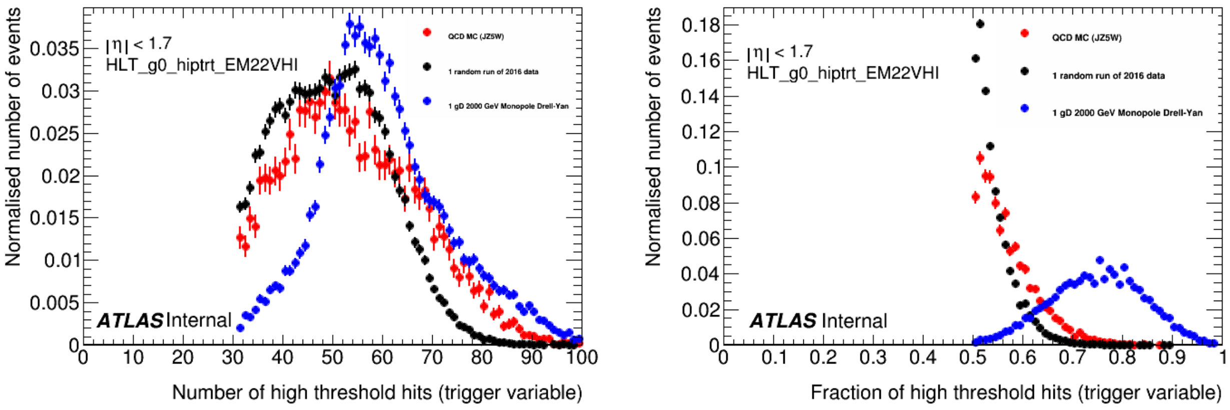

Figure 4.7: Left : $N_{HT,trig}$ distribution for candidates with $f_{HT,trig} > 0.5$. Right: $f_{HT,trig}$ distribution for candidates with $N_{HT,trig} > 20$. The samples used are one random run of 2016 data, a QCD MC (JZ5W), and a Drell-Yan MC with monopoles with mass 2000 GeV and charge $|g| = 1g_{\mathrm{D}}$. The distributions are normalised to the same number of candidates.

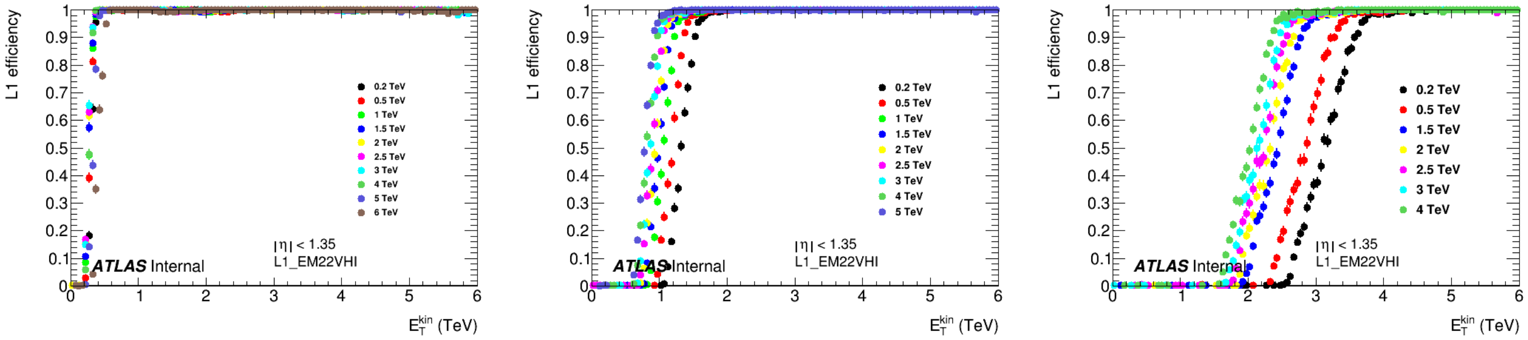

Figure 4.8: L1_EM22VHI trigger efficiencies for monopoles with charge $|g| = 1g_{\mathrm{D}}$ (left), $|g| = 2g_{\mathrm{D}}$ (middle) and $|g| = 3g_{\mathrm{D}}$ (right) and various masses, as a function of initial transverse kinetic energy, in the central region ($|\eta| < 1.35$). These plots are obtained using single-particle samples.

required for HIPs to reach the EM calorimeter. The $|z| = 20$ HECO presents an efficiency dip after the turn-on due to the hadronic veto as explained previously.

The figure 4.12 is comparing tunr-on curves of the HIP trigger with the 2016 lowest un-prescaled single photon and single electron triggers: `e_26_lhtight_nod0_ivar_loose` and `g140_loose`. As explained previously, the HIP trigger allows to recover candidates stopping in the first layer of the EM calorimeter or the pre-sampler. In addition the HIP trigger algorithm having no requirement on the hadronic calorimeter energy deposition, it allows to recover candidates cut by photon and electron triggers'discriminating variables conditions.

The HIP HLT algorithm efficiency with respect to Level 1 trigger acceptance is very high for

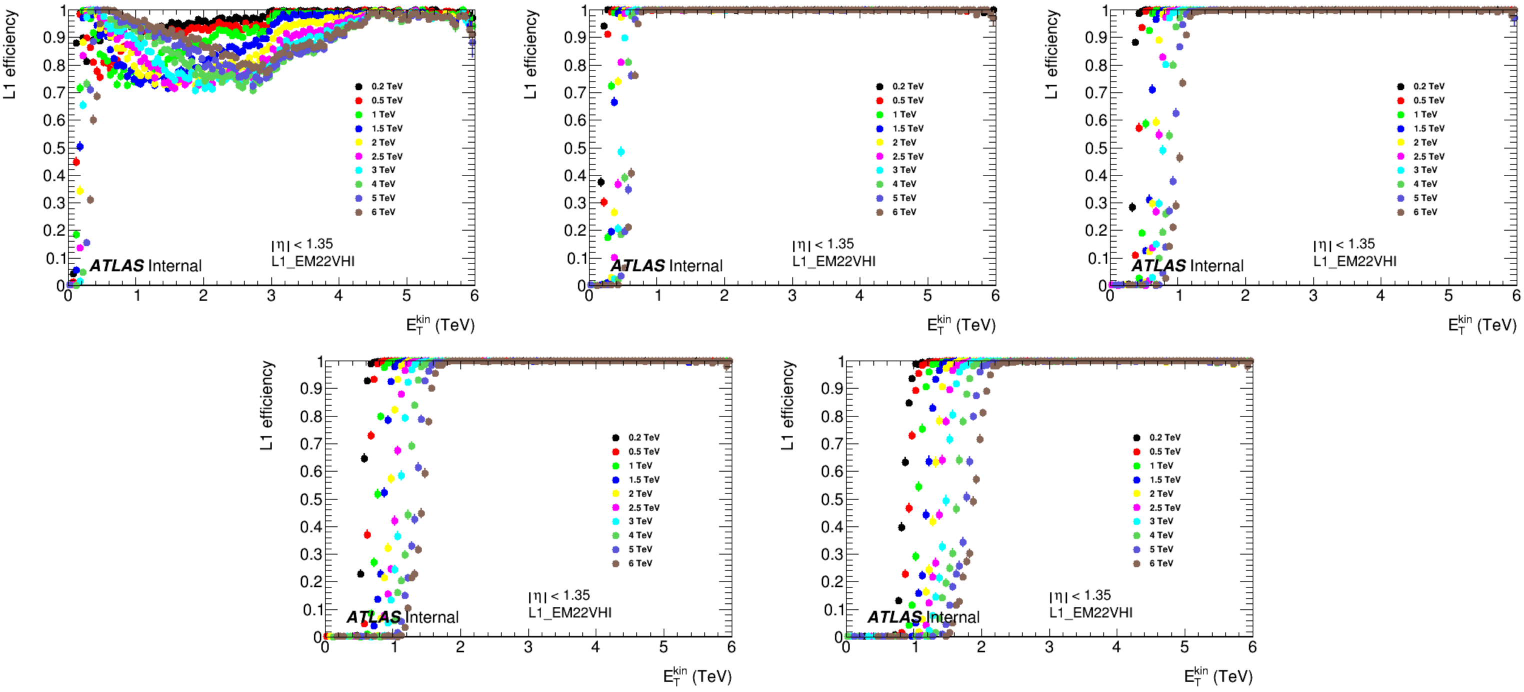

Figure 4.9: L1_EM22VHI trigger efficiencies for HECOs with charge $|z| = 20$ (top left), $|z| = 40$ (top middle), $|z| = 60$ (top right), $|z| = 80$ (bottom left), and $|z| = 100$ (bottom right) and various masses, as a function of initial transverse kinetic energy, in the central region ($|\eta| < 1.35$). These plots are obtained using single-particle samples.

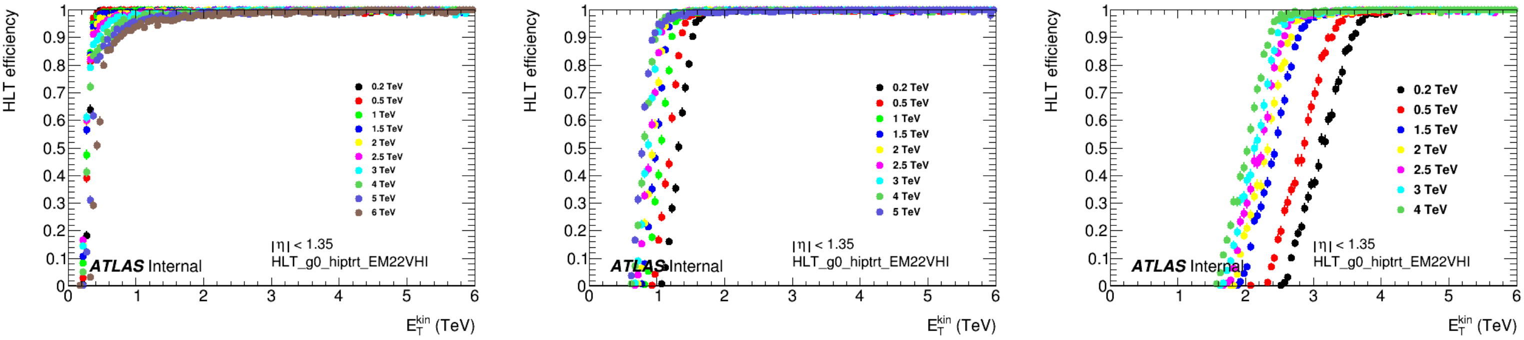

Figure 4.10: HIP HLT trigger efficiencies for monopoles with charge $|g| = 1g_{\mathrm{D}}$ (left), $|g| = 2g_{\mathrm{D}}$ (middle) and $|g| = 3g_{\mathrm{D}}$ (right) and various masses, as a function of initial transverse kinetic energy, in the central region ($|\eta| < 1.35$). These plots are obtained using single-particle samples.

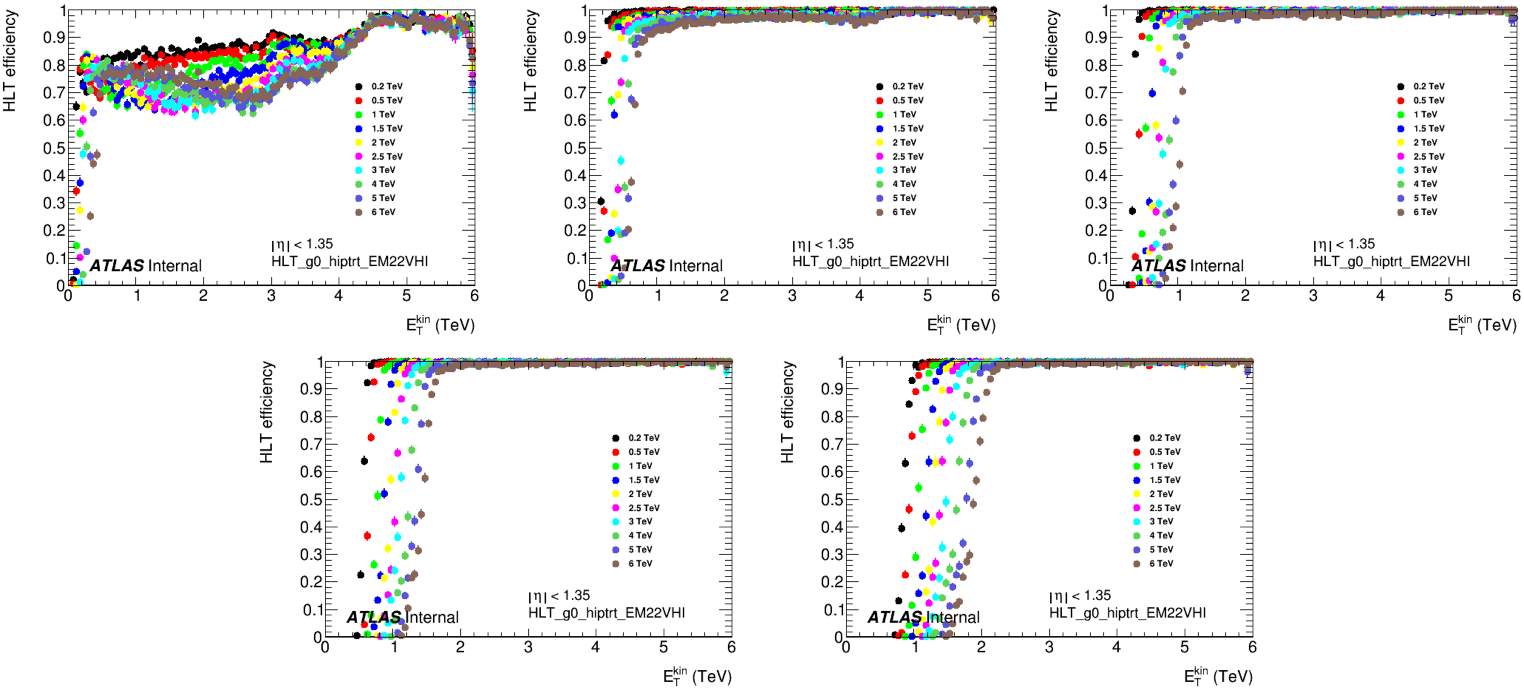

Figure 4.11: HIP HLT trigger efficiencies for HECOs with charge $|z| = 20$ (top left), $|z| = 40$ (top middle), $|z| = 60$ (top right), $|z| = 80$ (bottom left), and $|z| = 100$ (bottom right) and various masses, as a function of initial transverse kinetic energy, in the central region ($|\eta| < 1.35$). These plots are obtained using single-particle samples.

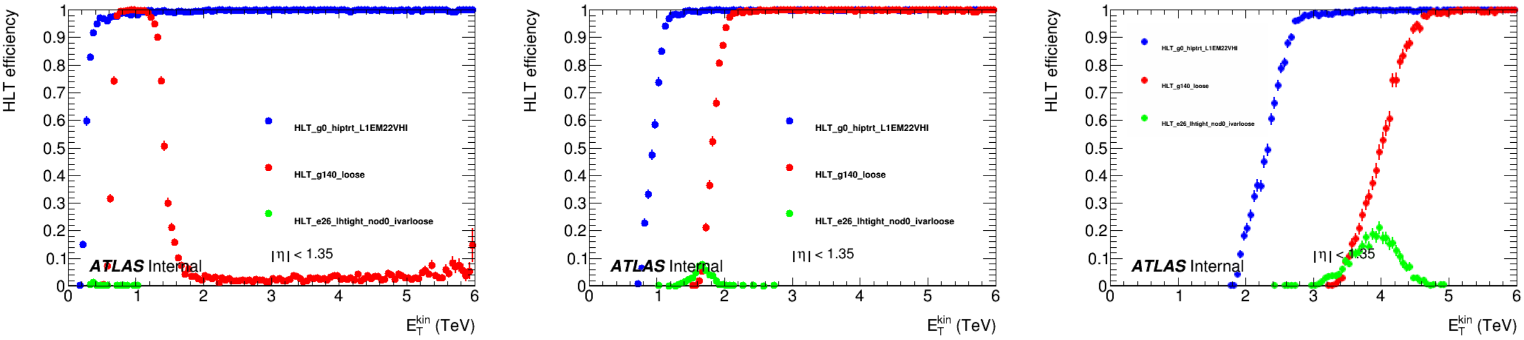

Figure 4.12: Trigger efficiencies for monopoles with charge $|g| = 1g_{\mathrm{D}}$ (left), $|g| = 2g_{\mathrm{D}}$ (middle) and $|g| = 3g_{\mathrm{D}}$ (right) with a mass of 2000 GeV, as a function of initial transverse kinetic energy, in the central region ($|\eta| < 1.35$). The HIP trigger is compared with the lowest-threshold electron and photon triggers that were unprescaled in 2016 runs. These plots are obtained using single-particle samples.

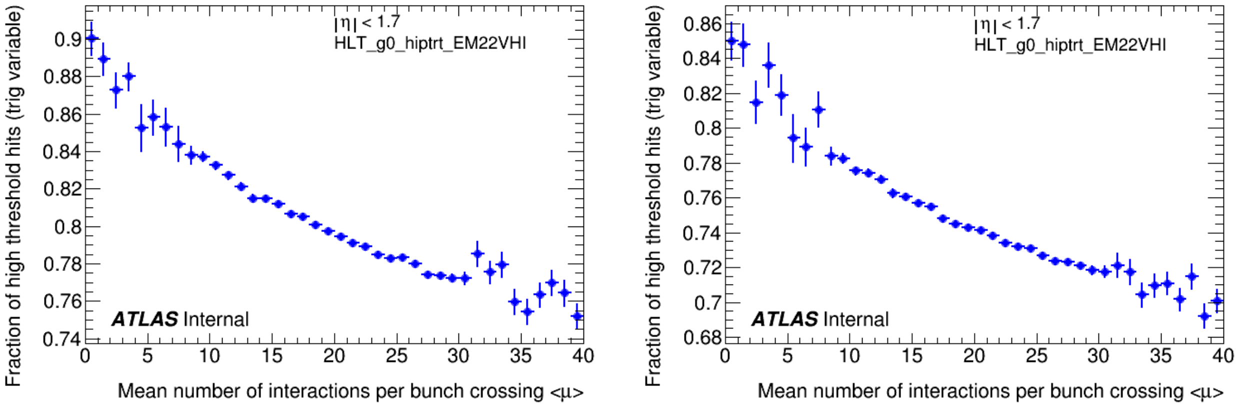

Figure 4.13: Profile histograms of the fraction of TRT HT hits from the HIP trigger $f_{HT,trig}$ as a function of pileup for a typical of monopole (left) and HECO (right) samples. All the entries in this figure come from events that fired the HIP trigger.

samples with high ionisation power. This is illustrated in figures 4.10 and 4.11 by a plateau value close from 1. Particles with a lower ionisation power, such as for example $|z| = 20$ HECOs, have a plateau value lower than 1 due to some HLT inefficiency. The efficiency loss is due to the tight $f_{HT,trig}$ cut, increased in Run 2 to limit the trigger rate. Indeed, at high pile-up, increasing the number of low threshold hits and thus decreasing the fraction of high threshold hits as shown in figure 4.13, the $f_{HT,trig}$ distribution extends below the threshold for lower charge HECOs and is responsible for the efficiency loss.

The overall dependence of the HIP trigger efficiency on the HIP pseudorapidity, η, and the transverse kinetic energy, E_T^{kin}, defines the HIP trigger efficiency maps, as shown in Figs. 4.14 and 4.15.

The structure in the efficiency maps reflects the detector geometry, as well as the HIP energy loss formulae. For example, the shape at the trigger turn-on energy reflects the fact that HIPs need sufficient kinetic energy at that pseudorapidity, taking into account dE/dx, to penetrate to the LAr calorimeter and deposit in excess of 22 GeV. So, depending on their direction, $|\eta|$, there are slight variations in the threshold E_T^{kin} value. Furthermore, the level-1 efficiency for some lower energy, low-charge HIPs is reduced when those HIPs punch through the crack in the hadronic calorimeter around $0.7 < |\eta| < 1.3$. If they deposit $1 < E_T < 50$ GeV in HCAL, they could be killed by the hadronic veto.

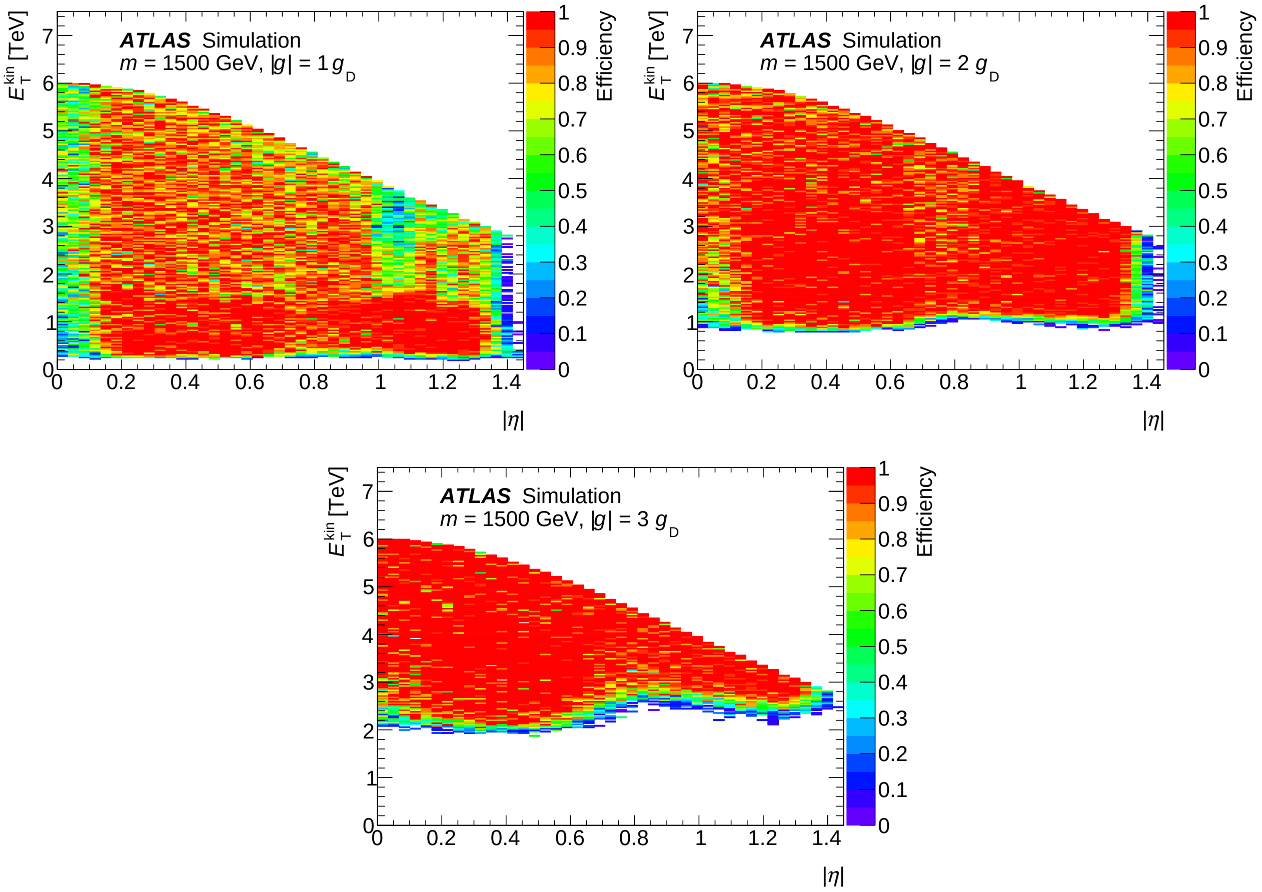

Figure 4.14: Left: HIP trigger efficiency map for monopoles with mass 1500 GeV and charge $|g| = 1g_{\mathrm{D}}$. Right: HIP trigger efficiency map for monopoles with mass 1500 GeV and charge $|g| = 2g_{\mathrm{D}}$. Bottom: HIP trigger efficiency map for monopoles with mass 1500 GeV and charge $|g| = 3g_{\mathrm{D}}$ These plots are obtained using single-particle samples.

Systematic uncertainties that can affect the trigger efficiency estimate are discussed in Section 4.2.4.

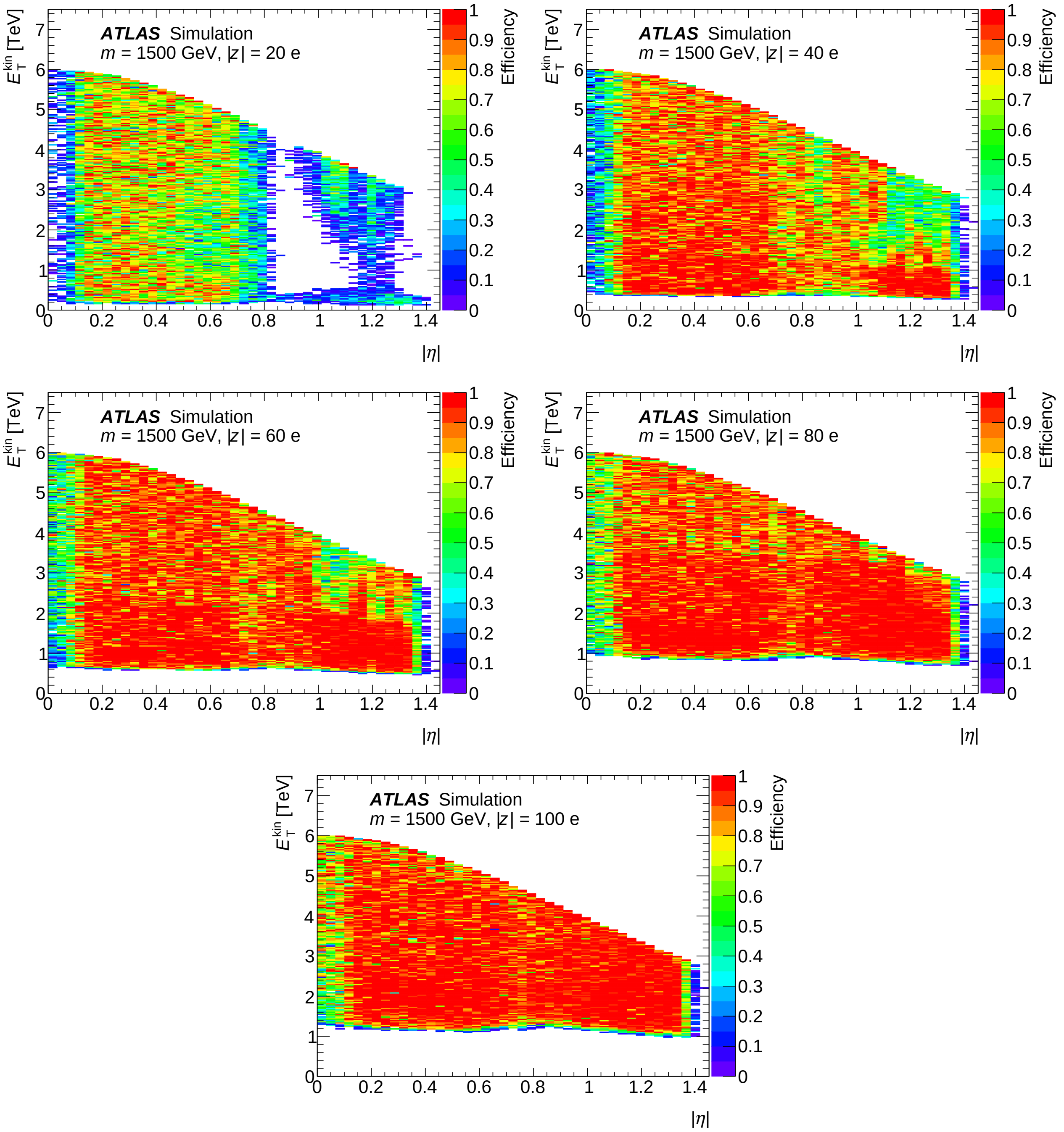

Figure 4.15: Top left: HIP trigger efficiency map for HECOs with mass 1500 GeV and charge $|z| = 20$. Top right: HIP trigger efficiency map for HECOs with mass 1500 GeV and charge $|z| = 40$. Middle left: HIP trigger efficiency map for HECOs with mass 1500 GeV and charge $|z| = 60$. Middle right: HIP trigger efficiency map for HECOs with mass 1500 GeV and charge $|z| = 80$. Bottom: HIP trigger efficiency map for HECOs with mass 1500 GeV and charge $|z| = 100$ These plots are obtained using single-particle samples.

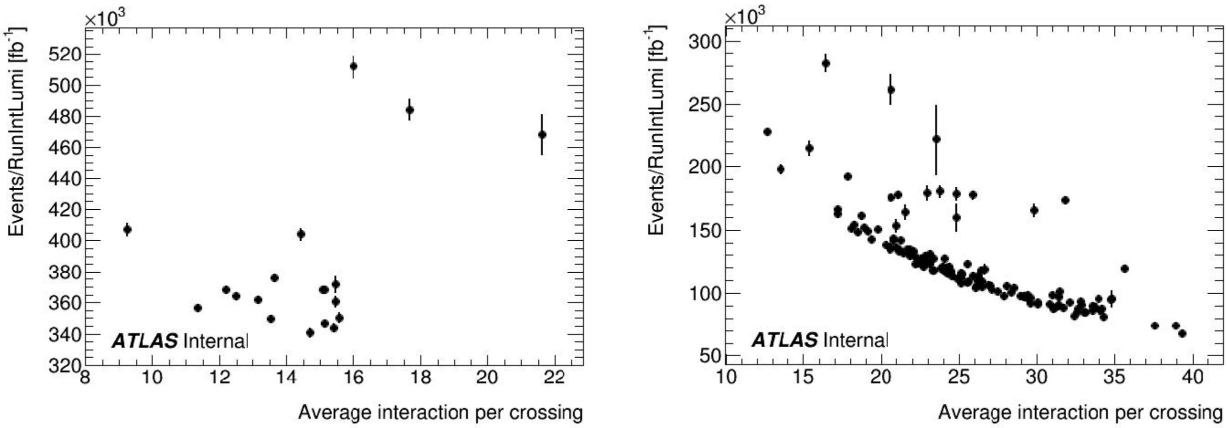

Figure 4.16: Event rate (normalised by luminosity) as a function of the mean number of interactions per bunch crossing $< \mu >$ for all the runs in the 2015 (left) and 2016 (right) datasets used in the analysis.

HIP trigger rate The Run 2 version of the HIP trigger was deployed on October 11, 2015 starting from run 281441 and its rate has remained below 2 Hz ever since. During the 2015 and 2016 periods, the trigger collected 1.58 fb^{-1} and 32.88 fb^{-1} of 13 TeV proton-proton collision data, respectively. Fig. 4.16 shows the event rate normalised by luminosity (events per fb^{-1}) as a function of the mean number of interactions per bunch crossing $< \mu >$ for all the runs in our dataset. The dependence on $< \mu >$ is a consequence of the pileup dependence of the $f_{HT,trig}$, and the fact that the runs cluster inside a narrow band illustrates the trigger stability from run to run. The lower rate at similar $< \mu >$ for 2016 data can be explained by the TRT gas mixture distribution. In 2016 additional straw layers of the TRT were filled with Argon instead of Xenon, lowering the probability of high threshold hits and thus the trigger rate. The impact on HIP signal efficiency was studied and is discussed in section 4.2.4.

4.2.2 Signal region

Preselection

The preselection applies a set of simple filters allowing to skim events and objects that can easily be discarded from the scope of the analysis. It consists in the following filters:

- Events that fire the HIP Trigger: the `DESDM_EXOTHIP` derivation applied on 2016 datasets is already filtering on the HIP trigger. However in 2015 the derivation used, `DESDM_RPVLL`, was not exclusive to the HIP analysis and additional trigger chains were included in the samples. An offline filter on the HIP trigger is thus applied.

- `CaloCalTopoCluster` calorimeter cluster candidate with $E_T > 18$ GeV: requirement on EM calo clusters energy below the Level 1 threshold of 22 GeV, allowing to focus on the RoI.
- $0 < |\eta| < 1.375$: The region $1.375 < |\eta| < 1.7$, included in the HIP trigger, is removed offline to ensure qualitative reconstructed analysis variables. The region $1.375 < |\eta| < 1.52$ correspond to the EM calorimeter barrel/end-cap transition region and is poorly instrumented, the region $1.52 < |\eta| < 1.7$ was not considered due to a correlation between the analysis variables as described in section 4.2.3.

Details about the topological cell clustering algorithm used to generate CaloCalTopoClusters are available in Ref. [73].

The algorithm used to produce the ntuples also include the Good Run List (GRL) selection tool and the Pile-up ReWeighting (PRW) tool. The first one allows us to ensure that the ntuples used contain only the runs and lumiblocks with fully functional detector and data quality checked. The PRW tool allows to set an event level weight for MC in order to match the average number of interactions distribution to data. The ntuples also include flags based on the EventInfo sub-detectors error bits and an incomplete events flag, allowing to veto those events with noise in a sub-detector or incomplete.

Final selection

The final selection is based on two independent powerful discriminants against the backgrounds: f_{HT} and w (described below).

The fraction of TRT high-threshold hits The offline f_{HT} variable described in this section is slightly different than the online one used by the HIP trigger (described in section 4.2.1). In addition to a different TRT hits container, using TRT_DriftCircles compared to TRT_TrigDriftCircles for the online one, the algorithm is handling the different regions in a way that was optimised during the Run 1 analysis. The centring of the TRT region corresponding to the ROI is done in a very similar way to the one done at trigger level, by localising the 0.8 mrad wedge with the highest number of high-threshold hits. But then the angle between the ROI and the centre of the TRT region of interest is computed by averaging the dphi of all high-threshold hits in a 20 mrad wedge centred around the previously localised 0.8 mrad wedge. Then a first rough selection is applied for ROI outside the central region, defined as $|\eta| < 0.1$, where we request all TRT hits to be on the same side of the detector than the ROI. In the barrel region, the algorithm is counting the number of TRT high and low threshold hits in a 8 mm road, which cannot be done in the end-caps as the radius information of a hit is not accessible due to the TRT geometry. In the end-caps we thus still have to use a 12 mrad wedge to count the hits. The size of the wedge is such that its width in the TRT is similar to the road size. The such defined offline f_{HT} variable is a powerful discriminant with a high separation power as showed in Fig. 4.17.

The w variable: a measure of the lateral energy dispersion of the EM cluster candidates The HIPs energy deposition in the calorimeters is very localised, as they do not induce showers in the calorimeters as opposed to the electrons, photons and hadrons. The energy dispersion in the EM calorimeter clusters is thus a strong discriminant against the background and is reconstructed in this analysis through the w variable. The w variable is the average of w_0, w_1 and w_2 variables reconstructed for the pre-sampler (EM0), the EM calorimeter layer 1 (EM1) and the EM calorimeter layer 2 (EM2) respectively. Only layers of the EM calorimeter with non trivial energy deposition are considered for the computation of the w variable, as they are the layers through which the HIP candidates actually pass, allowing to remove possible noise from pile-up tracks. However there is a minimal requirement that the energy deposition threshold is met for at least EM0 or EM1. The energy thresholds are 10 GeV for EM0 and EM1, and 5 GeV for EM2. The w_i variables are reconstructed in the layers with energy deposition above the thresholds as the ratio of energy deposition in the 2, 4 or 5 most

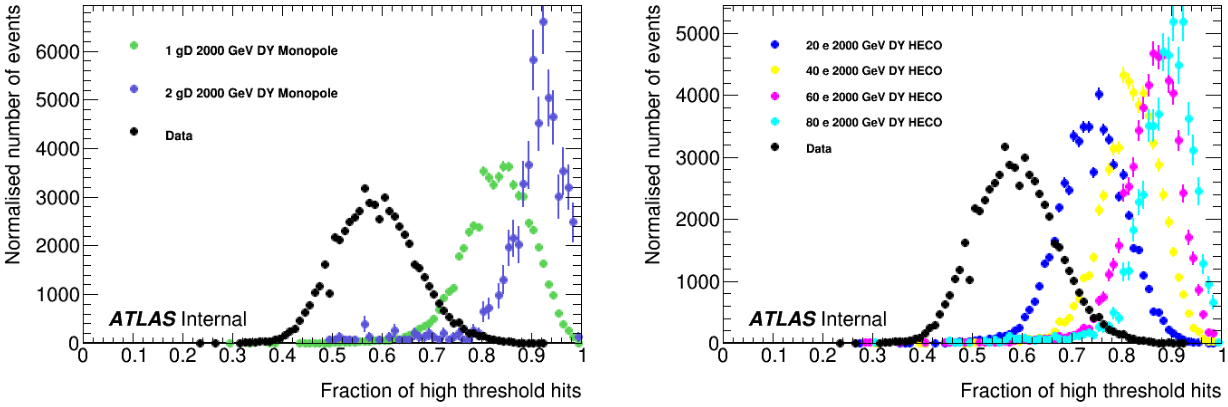

Figure 4.17: Discriminating power of f_{HT} for Drell-Yan produced HIPs with mass 2000 GeV and with different charges: (left) monopoles and (right) HECOs. Only 10% of the dataset is used for this plot.

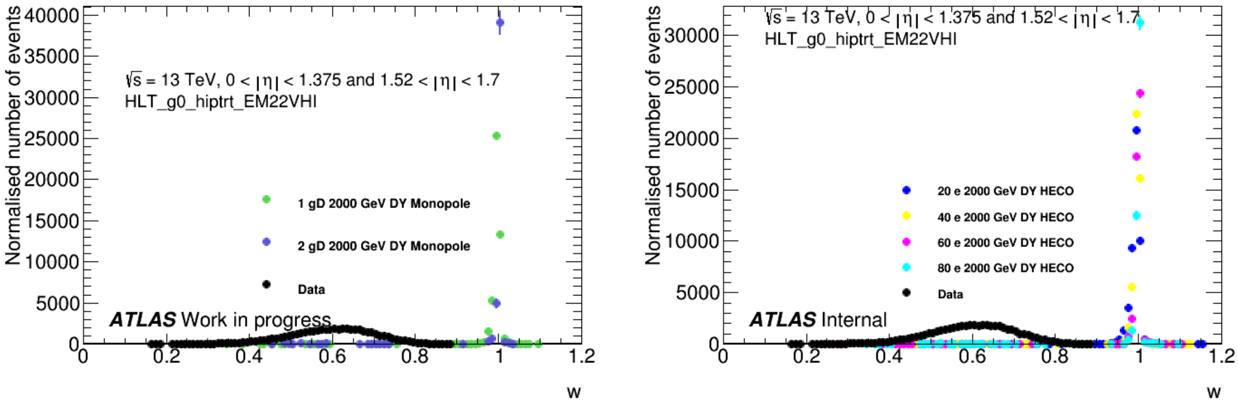

Figure 4.18: Discriminating power of w for Drell-Yan produced HIPs with mass 2000 GeV and with different charges: (left) monopoles and (right) HECOs. Only 10% of the dataset is used for this plot.

energetic cells, for the EM0, EM1 and EM2 layers respectively, over the total cluster energy deposition in the respective layer. The energy thresholds and number of cells parameters were optimised during the previous iteration of the analysis to maximise the signal efficiency while rejecting the background as described in [67].

The strong discriminating power of the w variable is evidenced in figure 4.18. While the signal samples w distribution is very narrow and peaks at 1, the data w distribution is very broad and peaks at a value of about 0.6. Background events with a high w value are on the tail of the distribution, hence with a very small occurrence.

Figure 4.19 shows that there is almost no dependence of w on pileup for various signal samples.

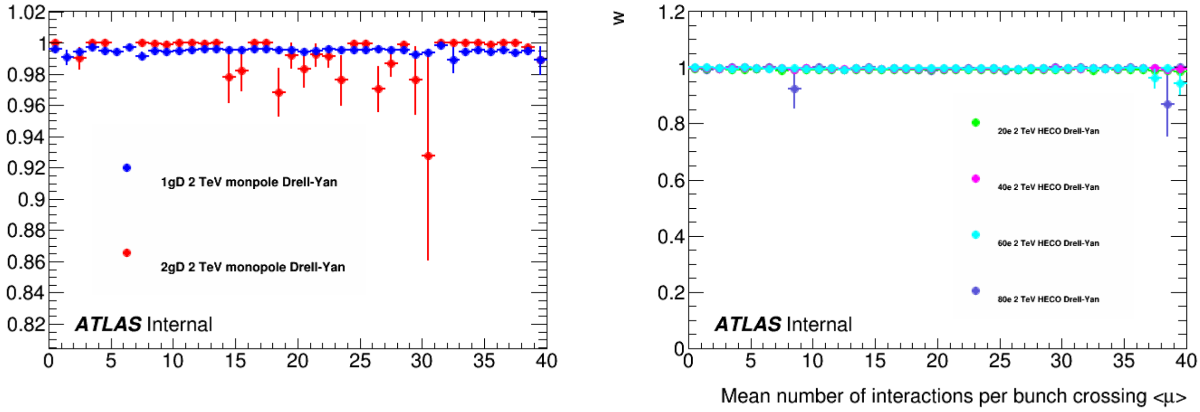

Figure 4.19: Dependence of w on the average number of interactions per bunch crossing, $<\mu>$, for Drell-Yan produced HIPs with mass 2000 GeV and with different charges: (left) monopoles and (right) HECOs.

	Data		$1g_{\mathrm{D}}$		$2g_{\mathrm{D}}$		$\lvert z\rvert = 20$		$\lvert z\rvert = 60$	
	events	rel. eff.	events	rel. eff.	events	rel. eff.	events	rel. eff.	events	rel. eff.
total	12840597	1	59221	1	67731	1	58654	1	91301	1
MadGraph p_T cut	-	-	50000	0.844	33200	0.490	50000	0.852	50000	0.548
L1	8954900	0.697	31921	0.638	6832	0.206	35688	0.714	16216	0.324
HLT	4575169	0.511	24663	0.773	1857	0.272	29426	0.825	8457	0.522
Preselection	443145	0.097	19961	0.809	1727	0.930	25217	0.857	6742	0.797
w	4	9.03×10^{-6}	19640	0.984	1669	0.966	23041	0.914	6678	0.991
f_{HT}	0	0	18774	0.956	1637	0.981	16893	0.733	6579	0.985

Table 4.1: Selection cut flow for data and a few typical Drell-Yan spin-$\frac{1}{2}$ signal MC samples for HIPs with a mass of 2000 GeV.

The final selection cuts were optimised by maximizing the sensitivity for most of the signal samples. The signal region was defined as $w \geq 0.96$ and $f_{HT} \geq 0.7$

4.2.3 Background estimate with the ABCD method

There are two sources of backgrounds that can occasionally produce high amounts of high-threshold hits in the TRT so as to pass our HIP trigger signature criteria: QCD jets, especially when the trajectories of several charged particles are close enough that their energy deposits overlap in the TRT straws; and high-energy electrons. Neither of these sources features EM calorimeter deposits with high values of w as defined by our signal region, but they have tails that may approach it. The former largely dominates due to a very large cross section. In this situation, where background events mostly come from very rare combinatorics among QCD processes with very large cross sections, it is computationally prohibitive to try to get

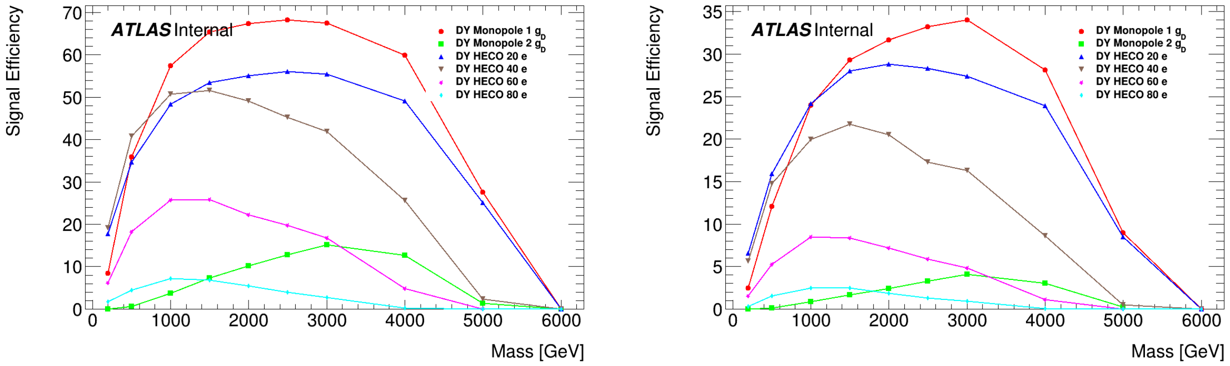

Figure 4.20: Overall efficiencies for Drell-Yan produced spin-0 (left) spin-$\frac{1}{2}$ (right) HIPs.

	Magnetic Charge		
Mass[GeV]	$\|g\| = 1g_D$	$\|g\| = 2g_D$	$\|g\| = 3g_D$
200	8.49 ± 0.72	0.03 ± 0.17	0.00 ± 0.00
500	35.97 ± 1.09	0.62 ± 0.30	0.00 ± 0.00
1000	57.45 ± 1.10	3.76 ± 0.53	0.01 ± 0.02
1500	65.46 ± 1.06	7.26 ± 0.64	0.04 ± 0.04
2000	67.34 ± 1.04	10.19 ± 0.73	0.08 ± 0.07
2500	68.22 ± 1.04	12.78 ± 0.77	0.13 ± 0.08
3000	67.44 ± 1.01	15.15 ± 0.90	0.10 ± 0.07
4000	60.00 ± 1.06	12.68 ± 0.78	0.00 ± 0.02
5000	27.56 ± 1.08	1.41 ± 0.35	0.00 ± 0.00
6000	0.03 ± 0.12	0.00 ± 0.00	0.00 ± 0.00

Table 4.2: Full selection efficiencies (in %) for Spin-0 Drell-Yan pair-produced monopoles. The efficiencies are extrapolated from the single-particle efficiency maps using the MC truth kinematics. Errors on the uncertainties are statistical.

	Magnetic Charge		
Mass[GeV]	$\|g\| = 1g_D$	$\|g\| = 2g_D$	$\|g\| = 3g_D$
200	2.45 ± 0.11	0.01 ± 0.05	0.00 ± 0.00
500	12.09 ± 0.18	0.14 ± 0.07	0.00 ± 0.00
1000	23.96 ± 0.21	0.85 ± 0.10	0.00 ± 0.01
1500	29.34 ± 0.22	1.64 ± 0.10	0.01 ± 0.02
2000	31.70 ± 0.22	2.42 ± 0.12	0.01 ± 0.02
2500	33.22 ± 0.22	3.30 ± 0.12	0.02 ± 0.03
3000	34.00 ± 0.23	4.06 ± 0.15	0.03 ± 0.04
4000	28.17 ± 0.22	3.02 ± 0.12	0.00 ± 0.00
5000	8.97 ± 0.19	0.23 ± 0.05	0.00 ± 0.00
6000	0.00 ± 0.02	0.00 ± 0.00	0.00 ± 0.00

Table 4.3: Full selection efficiencies (in %) for Spin-$\frac{1}{2}$ Drell-Yan pair-produced monopoles. The efficiencies are calculated from fully simulated Drell-Yan pair-produced samples, with the exception of charge $|g| = 3g_{\mathrm{D}}$, which is extrapolated from the single-particle efficiency maps using the MC truth kinematics. Errors on the uncertainties are statistical.

	Electric Charge				
Mass[GeV]	$\lvert z\rvert = 20$	$\lvert z\rvert = 40$	$\lvert z\rvert = 60$	$\lvert z\rvert = 80$	$\lvert z\rvert = 100$
200	17.7 ± 0.9	19.1 ± 0.9	6.2 ± 0.7	1.7 ± 0.5	1.1 ± 0.2
500	34.7 ± 1.1	40.8 ± 1.1	18.3 ± 0.9	4.4 ± 0.7	2.5 ± 0.3
1000	48.4 ± 1.1	50.7 ± 1.1	25.8 ± 1.0	7.2 ± 0.8	4.2 ± 0.4
1500	53.4 ± 1.1	51.6 ± 1.1	25.8 ± 1.0	6.8 ± 0.8	3.7 ± 0.4
2000	55.0 ± 1.1	49.2 ± 1.1	22.2 ± 1.0	5.4 ± 0.7	2.7 ± 0.4
2500	56.1 ± 1.1	45.3 ± 1.1	19.7 ± 1.0	3.9 ± 0.6	2.0 ± 0.3
3000	55.4 ± 1.1	41.9 ± 1.1	16.8 ± 0.9	2.8 ± 0.5	1.0 ± 0.2
4000	49.1 ± 1.1	25.7 ± 1.0	4.8 ± 0.5	0.3 ± 0.2	0.0 ± 0.0
5000	25.1 ± 1.0	2.4 ± 0.4	0.0 ± 0.0	0.0 ± 0.0	0.0 ± 0.0
6000	0.0 ± 0.1	0.0 ± 0.0	0.0 ± 0.0	0.0 ± 0.0	0.0 ± 0.0

Table 4.4: Full selection efficiencies (in %) for Spin-0 Drell-Yan pair-produced HECOs. The efficiencies are extrapolated from the single-particle efficiency maps using the MC truth kinematics. Errors on the uncertainties are statistical.

	Electric Charge				
Mass[GeV]	$\lvert z\rvert = 20$	$\lvert z\rvert = 40$	$\lvert z\rvert = 60$	$\lvert z\rvert = 80$	$\lvert z\rvert = 100$
200	6.5 ± 0.1	5.6 ± 0.1	1.6 ± 0.1	0.3 ± 0.1	0.8 ± 0.2
500	15.9 ± 0.2	14.7 ± 0.2	5.2 ± 0.1	1.5 ± 0.1	1.3 ± 0.2
1000	24.2 ± 0.2	19.9 ± 0.2	8.5 ± 0.2	2.5 ± 0.1	2.1 ± 0.3
1500	28.0 ± 0.2	21.8 ± 0.2	8.3 ± 0.2	2.4 ± 0.1	1.9 ± 0.3
2000	28.8 ± 0.2	20.5 ± 0.2	7.2 ± 0.2	1.9 ± 0.1	1.1 ± 0.2
2500	28.3 ± 0.2	17.3 ± 0.2	5.9 ± 0.1	1.3 ± 0.1	0.8 ± 0.2
3000	27.4 ± 0.2	16.3 ± 0.2	4.8 ± 0.1	0.9 ± 0.1	0.3 ± 0.1
4000	23.9 ± 0.2	8.6 ± 0.2	1.1 ± 0.1	0.1 ± 0.0	0.0 ± 0.0
5000	8.5 ± 0.2	0.5 ± 0.0	0.0 ± 0.0	0.0 ± 0.0	0.0 ± 0.0
6000	0.0 ± 0.0	0.0 ± 0.0	0.0 ± 0.0	0.0 ± 0.0	0.0 ± 0.0

Table 4.5: Full selection efficiencies (in %) for Spin-$\frac{1}{2}$ Drell-Yan pair-produced HECOs. The efficiencies are calculated from fully simulated Drell-Yan pair-produced samples, with the exception of charge $|z| = 100$, which is extrapolated from the single-particle efficiency maps using the MC truth kinematics. Errors on the uncertainties are statistical.

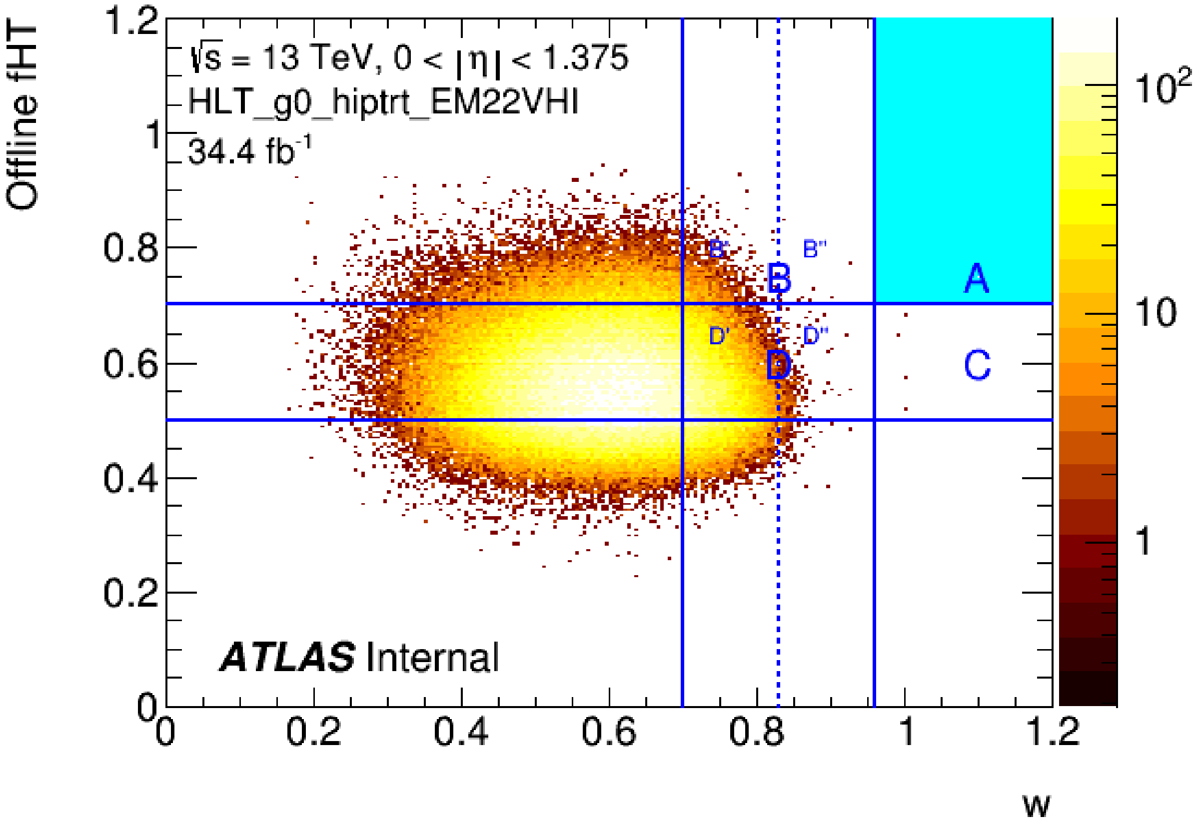

Figure 4.21: Distribution of the offline f_{HT} versus w after preselection in data. The signal region (A) is blinded in the data. The control regions used for the background estimate and background validation check are also indicated.

a background estimate from simulations. Luckily, there is a robust method for obtaining a data-driven background estimate.

Data-driven background estimate

The background is estimated using the so-called ABCD method [74], which relies on the two variables we use as discriminators (f_{HT} and w) being independent. Figure 4.21 shows the 2D plot of the two variables after preselection for the full dataset considered in this analysis. The four regions, the signal region A and the control regions B, C and D, are defined on this plane as shown in the plot:

- Region A (signal region): high $w > 0.96$ and $f_{HT} > 0.7$

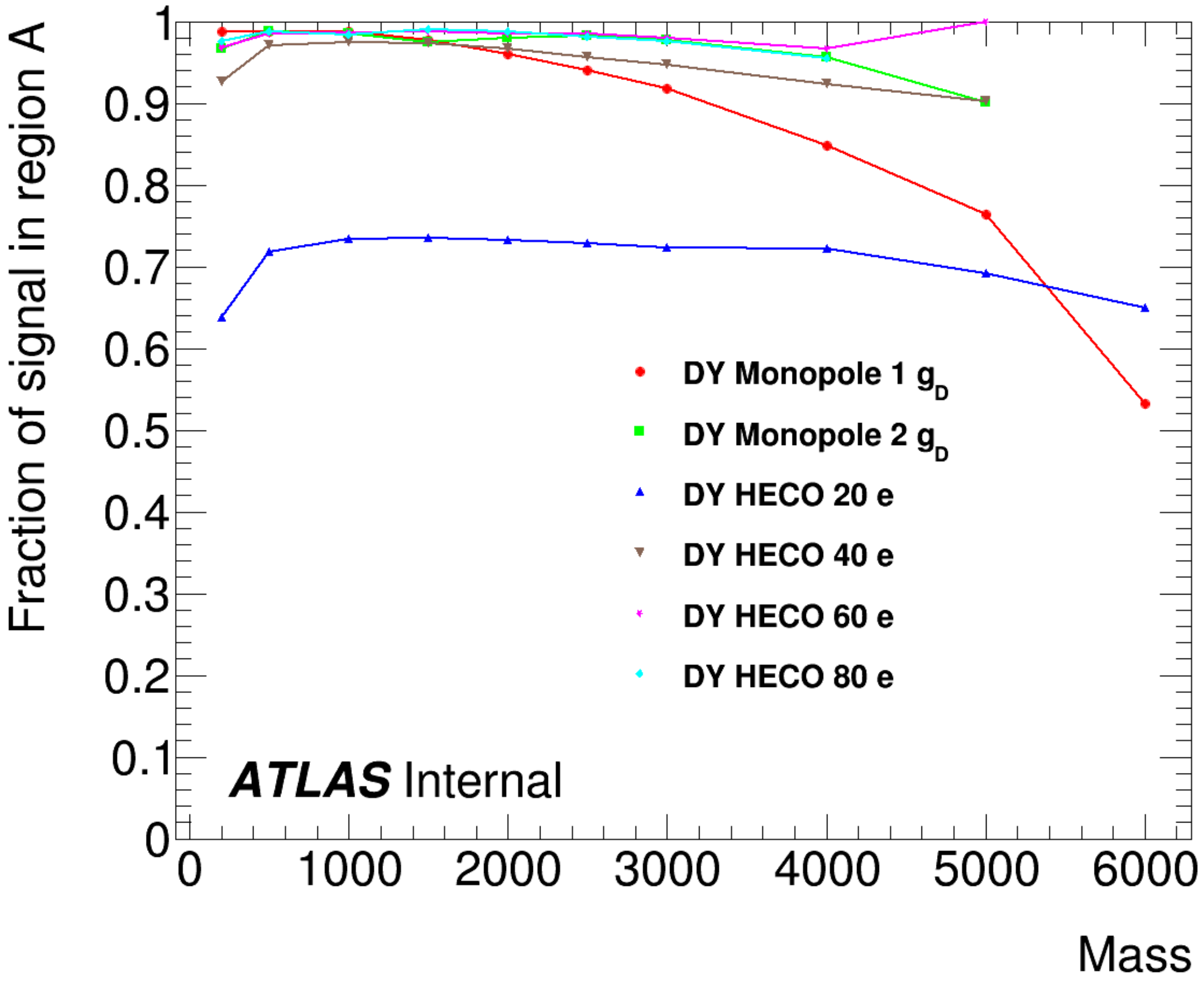

Figure 4.22: Fraction of signal in region A defined as A/(A+B+C+D) per mass for Drell-Yan signal samples.

- Region B: $0.7 < w < 0.96$ and $f_{HT} > 0.7$
- Region C: $w > 0.96$ and $0.5 < f_{HT} < 0.7$
- Region D: $0.7 < w < 0.96$ and $0.5 < f_{HT} < 0.7$.

Four further regions D', D", B' and B", subsets of regions D and B, were defined, used for the validation as described in section 4.2.3.

The signal region was chosen to maximise background rejection while maintaining a high signal efficiency. A signal region definition that would ensure a very high signal efficiency for all samples would have a poor rejection power and thus it was decided to reject more background

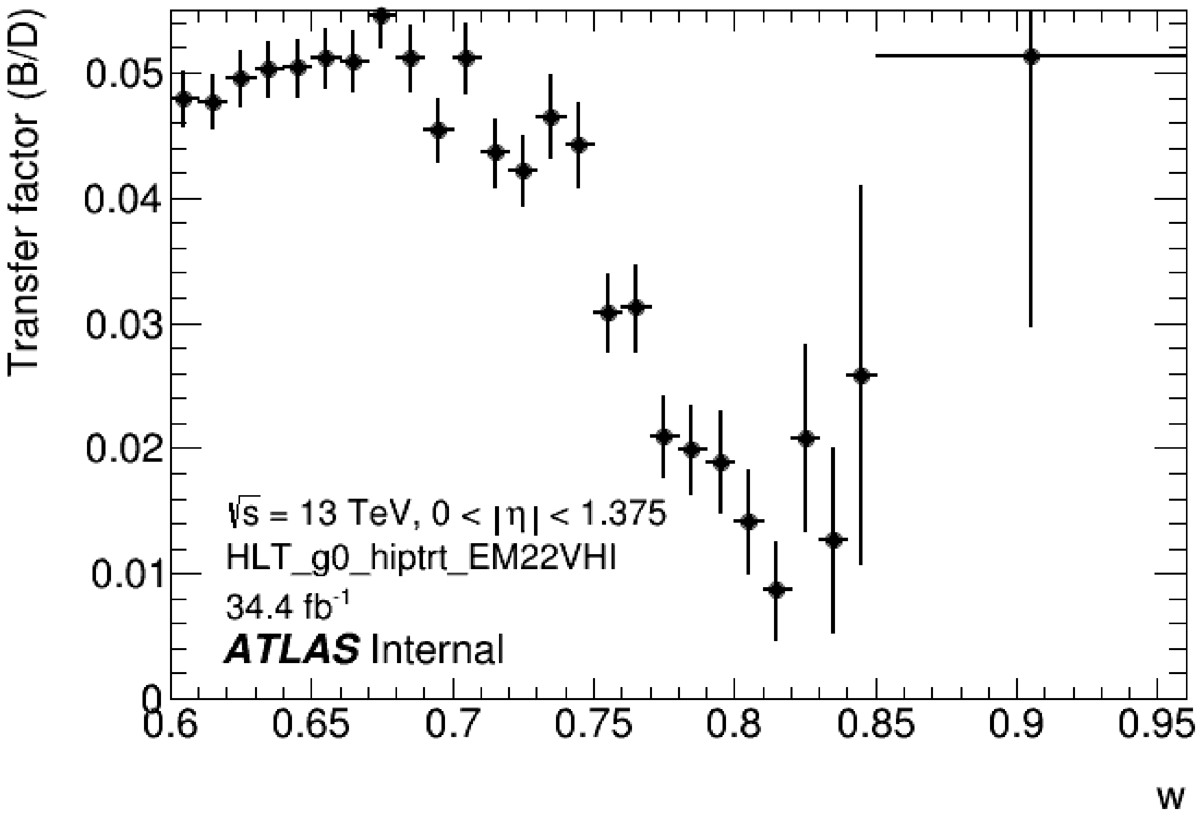

Figure 4.23: Transfer factors as a function of w.

knowing that signal leakage in the control region would be significant for a few samples, as shown in Table 1 and Fig. 4.22. A simultaneous ABCD fit is used in order to accommodate any signal region into the control regions. The fit is realised with the TRooABCD application of the TRooFit toolkit [75] based on the RooFit data analysis framework.

Figure 4.23 shows the *transfer factor*, defined as the number of events in region B over the number of events in region D, for finely binned in w sub-regions. The key idea behind the ABCD method is that the transfer factor is assumed to be identical between the control region and the signal region, a result of the uncorrelated nature of the two variables in the ABCD plane. The non-uniformity of the transfer factor over a wide w range is highlighting the correlation of the f_{HT} and w variables for different regions. The variable correlation study was done in the previous iteration of the analysis (see the study made in Ref. [67]) and the variables were found to be uncorrelated at high w, where the control region was defined. A new feature of the transfer factor when considering the full η range up to $|\eta| = 1.7$, thus not studied in Run 1

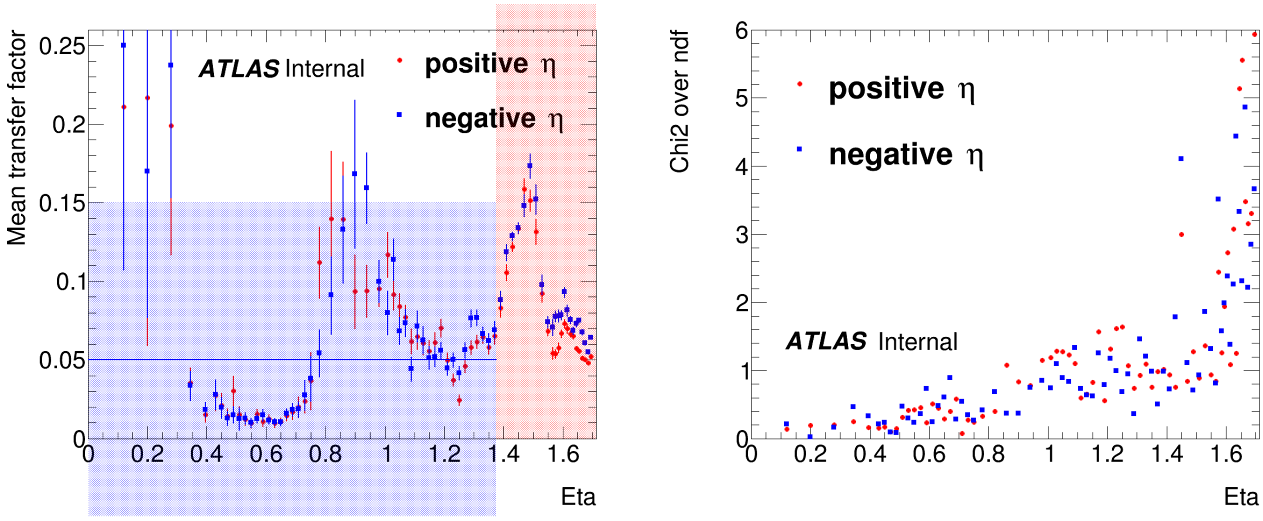

(a) Mean transfer factor (b) Associated χ^2

Figure 4.24: Study of the mean transfer factor as a function of η. The mean value of the transfer factor per bin is estimmated from the transfer factor as a function of w histogram for events in an η range corresponding to the associated bin. The χ^2 associated to each bin mean factor is a marker of the uniformity of the transfer factor as a function of w. The horizontal blue line in 4.24a represent the integrated mean transfer factor up to $\eta = 1.375$, to which we assigned a 200% systematic uncertainty. The red band is the high η excluded region.

and unexpected, appears at $w = 0.87$ where its value jumps to a plateau. The cause for this discontinuity is not understood. In order to keep a uniform transfer factor, a correlation study was made for different η regions as showned on figure 4.24.

The study of the mean factor as a function of η allow us to defined sub-regions were the transfer factor is consistent with a flat assumption. We defined a total of 8 regions:

- $|\eta| < 0.32$: lower statistic region.
- $0.32 < |\eta| < 0.77$: TRT barrel only.
- $0.77 < |\eta| < 1.06$:TRT barrel/EC transition region.
- $1.06 < |\eta| < 1.21$.
- $1.21 < |\eta| < 1.29$.
- $1.29 < |\eta| < 1.375$.

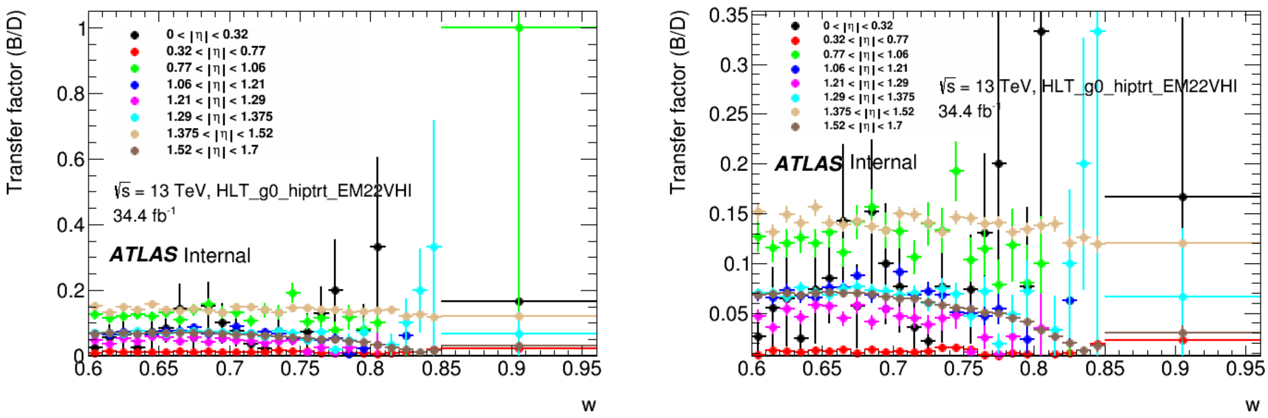

(a) Mean transfer factor

(b) Associated χ^2

Figure 4.25: Transfer factor as a function of w for all the η regions.

- $1.375 < |\eta| < 1.52$:LAr calorimeter barrel/EC transition region.
- $1.52 < |\eta| < 1.7$.

The last two regions are rejected from the analysis. The calorimeter transition region, as explained in the previous section, is a region where the definition of w is uncertain. The last region region was rejected due to a too important correlation between the two variables. Indeed we can see from the χ^2 in this region shown in figure 4.24b, or in figure 4.25a, that the tranfer factor is non-uniform, attesting of a strong correlation. At the same time, it appeared that the jump in transfer factor mentionned earlier is happening only in this region.

In order to take into account both the correlation and the dependance in η, a large 200% systematic uncertainty was added to a unique mean transfer factor. This allow us to perform the analysis on a single η region, $0 < |\eta| < 1.375$, while maintaining a conservative almost null expected background.

Sample	A	B	C	D	B′	B″	D′	D″
Data	blinded	1528	4	30375	1516	12	30023	352

Table 4.6: Observed number of events in the different regions.

The observed numbers of events in each region are reported in Table 4.6. The background-only fit using the observed number of events in the control regions yields a background estimate of

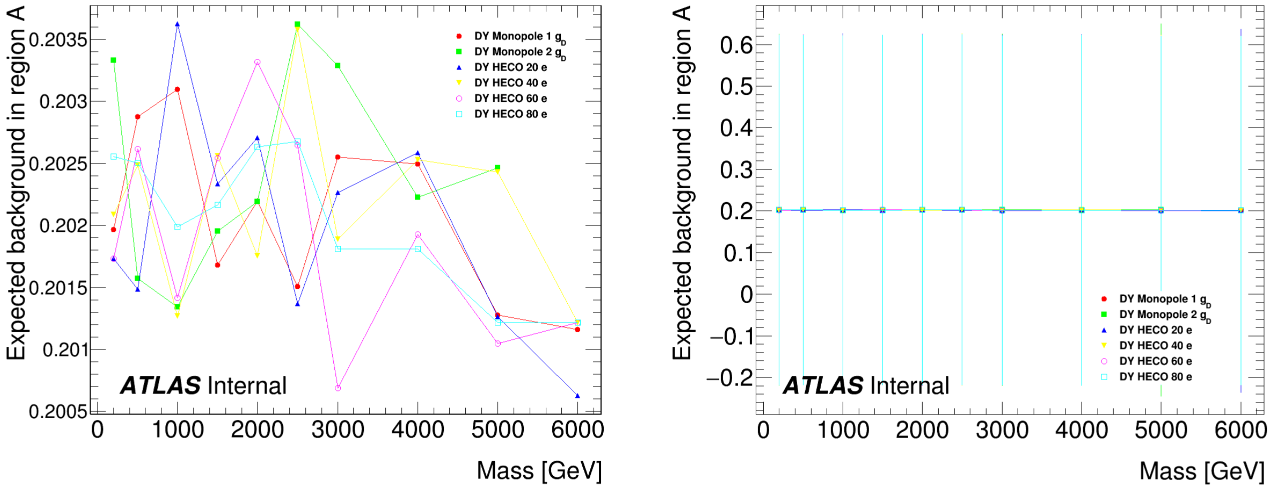

(a) Without erros ploted

(b) With errors ploted

Figure 4.26: Graph of the background estimate results for all Drell-Yan signal samples with assumed number of observed events in region A corresponding to the background-only fit yield that is 0.20 ± 0.42.

$\mathrm{A}_{est} = \frac{BC}{D} = 0.20 \pm 0.11$. To which we have to add the transfer factor uncertainty and get: $\mathrm{A}_{est} = \frac{BC}{D} = 0.20 \pm 0.42$. This estimate assumes that there is no signal leakage into the control regions. It is used as the pre-unblinding observed number of events in the signal region for the simultaneous fit with a signal of an unknown strength. The background estimate results for each signal sample are summarised in Fig. 4.26. The blinded prediction of background in the signal region appears to be not dependent on the signal. The expected background stays close from the background-only fit, even for low charge HECO samples, which have a more significant signal leakage. That is because the shapes of the background and signal distributions are well separated, as shown in Fig. 4.27 and Fig. 4.28, respectively, for a low signal leakage sample and for a higher signal leakage one. The TRooABCD fit results, before applying the transfer factor uncertainty, are shown for a representative $|z| = 20$ HECO sample with a mass of 2000 GeV in Fig. 4.29.

Table 4.7 compares the background yield in the signal region for both low- and high-signal-contamination samples, for different numbers of observed events in the signal region. It appears that the post-unblinding background yield assuming a handful of observed events would significantly change only for the samples with the most signal leakage.

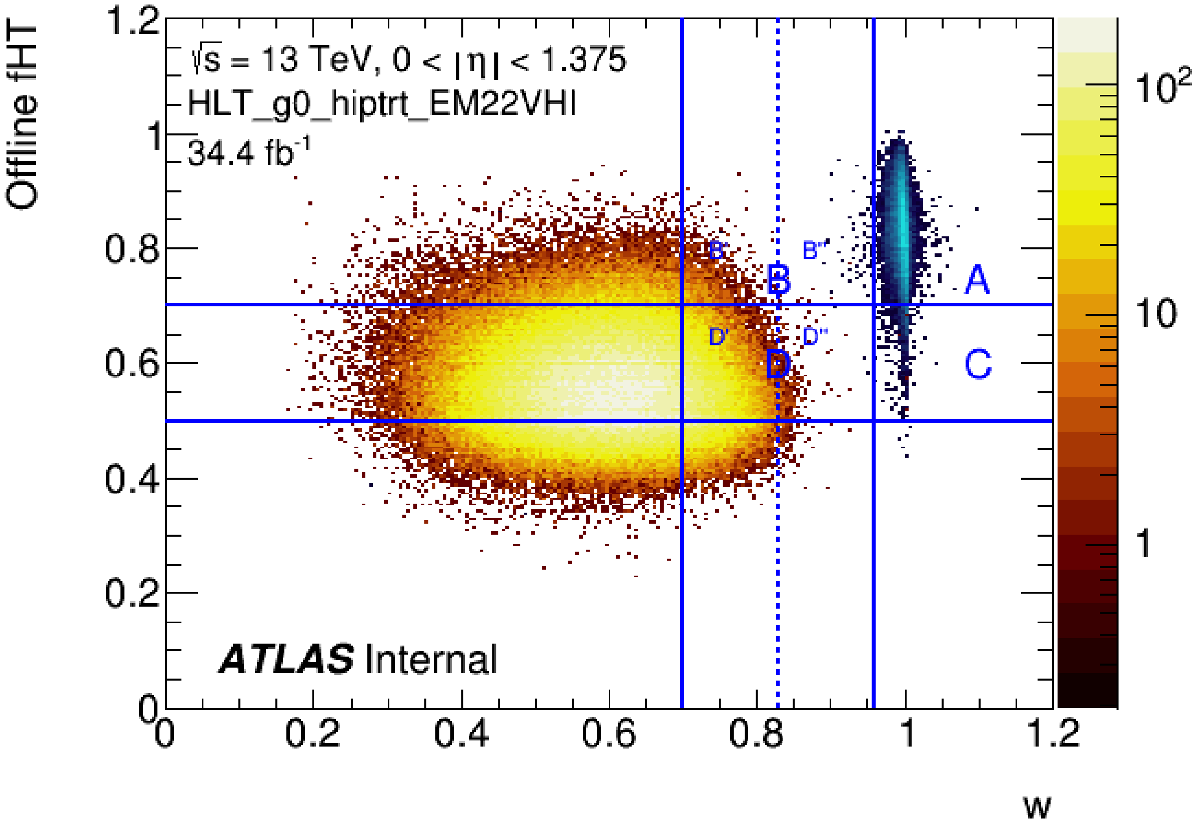

Figure 4.27: Distribution of the offline f_{HT} versus w after preselection in data and a 1 g_{D} 2-TeV DY signal.

Nb. of events in SR	Background in signal region for $\|z\| = 20$ DY	Background in signal region for 1 g_{D} DY
0	$0.1910 \pm 0.1130 \pm 0.0009$	$0.1924 \pm 0.1117 \pm 0.0008$
0.20	$0.2027 \pm 0.1135 \pm 0.0003$	$0.2022 \pm 0.1139 \pm 0.0001$
1	$0.1893 \pm 0.1197 \pm 0.0484$	$0.1999 \pm 0.1181 \pm 0.0377$
2	$0.1702 \pm 0.1231 \pm 0.1173$	$0.2001 \pm 0.1160 \pm 0.0863$
3	$0.1543 \pm 0.1233 \pm 0.1805$	$0.1958 \pm 0.1182 \pm 0.1395$

Table 4.7: Background in signal region after simultaneous fit ABCD method assuming 0, 0.20, 1, 2 and 3 observed events in signal region for a HECO DY sample with a charge of $|z| = 20$ and mass of 2000 GeV and a sample with a charge of 1 g_D and mass of 2000 GeV. The first uncertainty is statistical, the second is systematic. The systematic uncertainty associated to the signal strength was determined thanks to TRooABCD as the difference between the background-only fit and a fit with a high signal contribution. The 200% transfer factor uncertainty is not applied

Validation of the ABCD method

The validation is done by comparing the expected number of events, results from the background-only fit, to the actual observed number of events in relevant regions of the ABCD plane, regions B'B"D'D", being defined as:

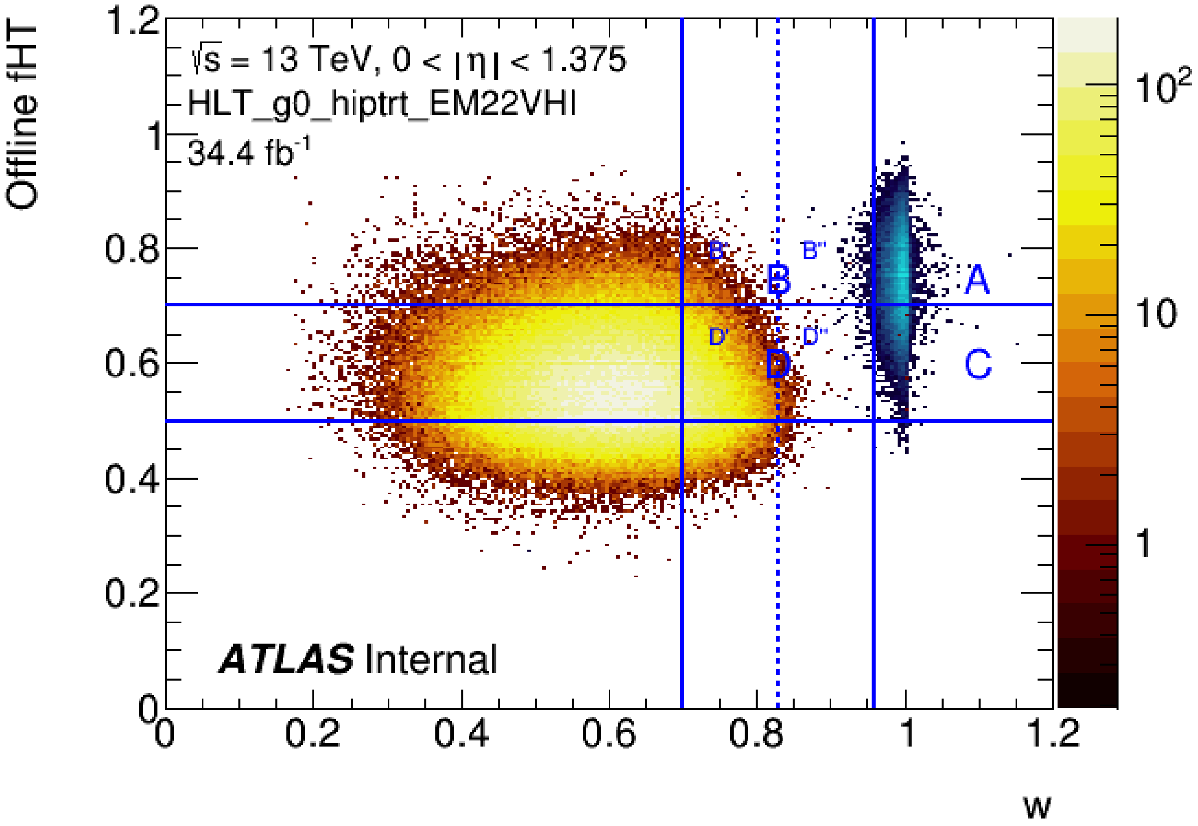

Figure 4.28: Distribution of the offline f_{HT} versus w after preselection in data and a $|z| = 20$ 2-TeV DY signal. Representative example of signal samples with a significant signal contamination in region C.

- Region B': $0.7 < w < 0.83$ and $f_{HT} > 0.7$
- Region B": $0.83 < w < 0.96$ and $f_{HT} > 0.7$
- Region D': $0.7 < w < 0.83$ and $0.5 < f_{HT} < 0.7$.
- Region D": $0.83 < w < 0.96$ and $0.5 < f_{HT} < 0.7$.

The background-only fit expected number of events are B"$_{est} = \frac{B'D''}{D'} = 17.77 \pm 1.06$, To which we have to add the transfer factor uncertainty and get: B"$_{est} = \frac{B'D''}{D'} = 17.77 \pm 35.56$, which is compatible with the observed value $B''_{obs} = 12$.

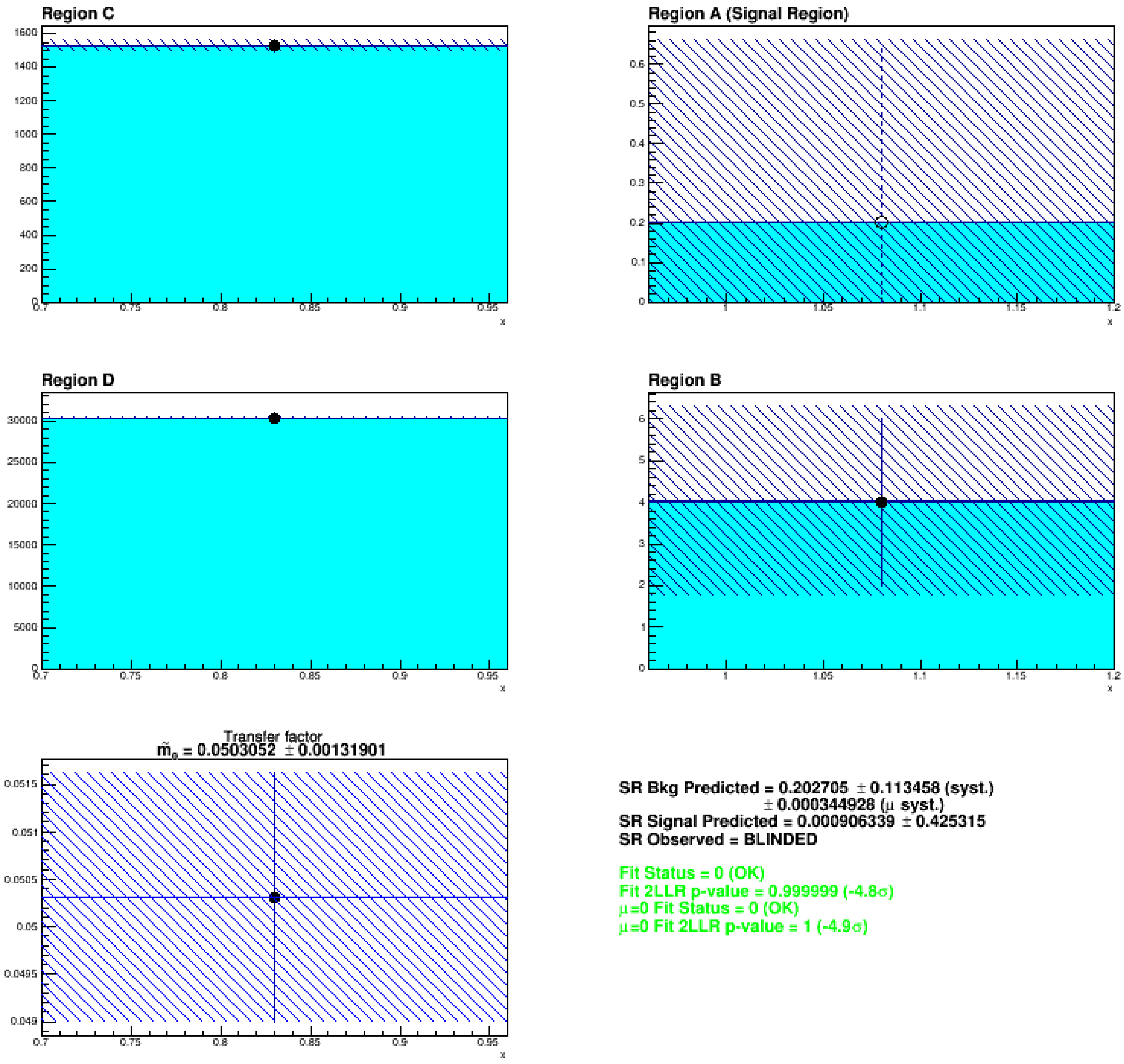

Figure 4.29: Signal and background yield obtained with a simultaneous fit ABCD method using TRooFit for HECO with charge $|z| = 20$ with a mass of 2000 GeV, assuming 0.20 observed event in the signal region corresponding to the nominal ABCD expected background and without the 200% transfer factor uncertainty.

4.2.4 Systematic uncertainties

The signal selection efficiencies, as described in the section 4.2.2, are fully derived from Monte-Carlo simulations and are subject, in addition to statistical uncertainties, to systematics uncertainties on the simulation. The systematic uncertainties can be estimated for the known effects that are relevant for HIPS. The effects that this analysis is taking into account are:

- Detector material
- Energy loss calculation
- Range cut for propagation of δ-rays
- Correction to Birks' Law
- TRT occupancy
- Cross talk in EM calorimeter cells
- Calorimeter signal arrival time
- Precision of the extrapolation method
- TRT gas distribution
- Pile-up reweighting
- LHC luminosity

The systematic uncertainties can be split in two, based on the derivation method used in this analysis: the first 4 in the above list are linked to the simulation of the HIPs in the detector and happen at an early stage of the MC production chain, handled by the GEANT4 package, the rest of the systematic uncertainties can be estimated from the analysis ntuples. Additional single particles MC samples of 10 000 events for each HIPs charges with a mass of 1.5 TeV were requested with alternate assumptions for all 4 effects requiring a full GEANT4 simulation. While the HIPs efficiency is mass dependant, only a central 1.5 TeV mass sample was requested for each charge in order to limit the number of samples. This approximation was tested and validated for extreme mass points. The uncertainties on efficiencies for DY generated samples were derived from the single particle samples using the extrapolation method [71]. The uncertainties derived at the analysis were estimated for all charge and mass points independently as no additional samples were required.

Each systematic uncertainties are assessed separately and the overall effect is taken as the quadratic sum of all the contributions. Each systematic uncertainty contribution is described in this section and the average over all mass and charges is provided as an indication for comparison purpose. The systematic uncertainties used for the cross-section limits calculation in section 4.3.1 are summarised in appendixF.

Detector material The accuracy of the ATLAS detector material description in GEANT4 is determining in the simulation of the HIPs interaction with the detector. Due to the highly ionising nature of HIPs, their interaction simulation is sensitive to small uncertainties on the detector material. In addition the HIP trigger and the analysis selection variables have requirements on the EM calorimeter energy deposition and thus the HIPs minimal energy to reach the calorimeter is dependant on the energy deposition in the previous sub-detector, in turn dependant on the accuracy of the detector material description.

The associated systematic uncertainties were derived by simulating the interaction of HIPs through the detector with an alternative more conservative detector description. The alternative detector description includes the following:

- Increase Pixel (including IBL) services by 10%
- Increase SCT services by 10%
- +7.5% X0 SCT/TRT endcap
- +7.5% X0 ID endplate
- +5% X0 radial barrel cryo

- +5% X0 radial PS-Layer1 barrel
- +5% X0 PS-Layer1 end-cap
- Transition distortion

The average systematic uncertainty associated to the detector material description uncertainty was found to be ∼7%.

Energy loss calculation The energy loss calculation for HIPs, as described in section 1.2.4, has in the velocity regime relevant for HIPs propagation an uncertainty of about 3% [16, 76]. The energy loss calculation impact the analysis on two aspects: the penetrating power of the HIPs, being determining for the Level 1 trigger efficiency, and the δ-rays production mechanism affecting the analysis variables f_{HT} and w, and thus the signal selection efficiency.

The uncertainty associated to the energy loss calculation uncertainty was assessed by suppressing the number of produced δ-rays by 3% in Geant4. The uncertainty was assessed only in one direction and taken as symmetric.

The average systematic uncertainty associated to the energy loss calculation uncertainty was found to be ∼4%.

Range cut for propagation of δ-rays The TRT simulation package is not simulating low energy δ-electrons, in order to limit the required computational resources. The energy loss associated to those δ-electrons is added to the HIPs energy losses. The energy threshold is set in the TRT Geant4 simulation package as a range cut [77] allowing the δ-rays for electrons with a penetration power higher than the selected range and thus effectively equivalent to setting up a lower limit on the electrons' energy. The default range cut in the TRT simulation package is set to 50 μm. The smaller the range cut, the more precise the simulation is. The double counting of delta electrons described in section 3.2 is not relevant here as the HIP digitisation is not using the PAI model responsible for the double counting. The range cut affects the number of δ-electrons and thus both the trigger and offline f_{HT} variable.

To estimate the effect of the δ-rays range cut on the HIP selection efficiency, a samples with an alternative range cut of 25 μm were generated.

The average systematic uncertainty associated to the TRT range cut for propagation of δ-rays was found to be ∼4%.

Correction to Birks' law As described in section 4.1.2, the fraction of visible energy in the LAr calorimeter is estimated thanks to the empirical Birks'Law formula. The formula as implemented in Geant4 is overestimating the electron-ion recombination effect at very high $\mathrm{d}E/\mathrm{d}x$. A correction to the Birks'Law was implemented in Geant4 for HIPs based on the experimental heavy ions data, as described in [69, 68, 67]. The accuracy of the correction is thus limited by the heavy ions data available and thus for very high $\mathrm{d}E/\mathrm{d}x$ a residual systematic uncertainty on the fraction of visible energy remains. This uncertainty affects the calculation of the energy deposition in the calorimeter and thus the Level 1 trigger efficiency.

In order to estimate the systematic uncertainty, additional HIPs MC samples were requested with conservative estimates of the lowest and highest fraction of visible energy as a function of $\mathrm{d}E/\mathrm{d}x$.

The average systematic uncertainty associated to the correction to Birks'Law was found to be ∼4% for the lower bound, and ∼6% for the upper bound.

TRT occupancy The global TRT occupancy is defined as the ratio of the number of TRT low threshold hits over the total number of possible hits, ie the number of straws. The higher the pile-up, the higher the TRT occupancy both variables being fully correlated. The accuracy of the TRT occupancy in the MC simulations is important for this analysis as both the trigger and the final selection are using the fraction of TRT high-threshold hits f_{HT} dependant on the number of TRT hits.

The TRT occupancy accuracy in MC15c samples was estimated by comparing data and MC for a $Z \rightarrow e^+e^-$ sample as shown in the figure 4.30. The occupancies ratio was applied as a scale factor on the HIP signal samples number of TRT low threshold hits when deriving the

f_{HT} variable. The resulting signal efficiencies were compared to the baseline calculations and the differences were accounted as a systematic uncertainty.

The average systematic uncertainty associated to the TRT occupancy was found to be ∼5%.

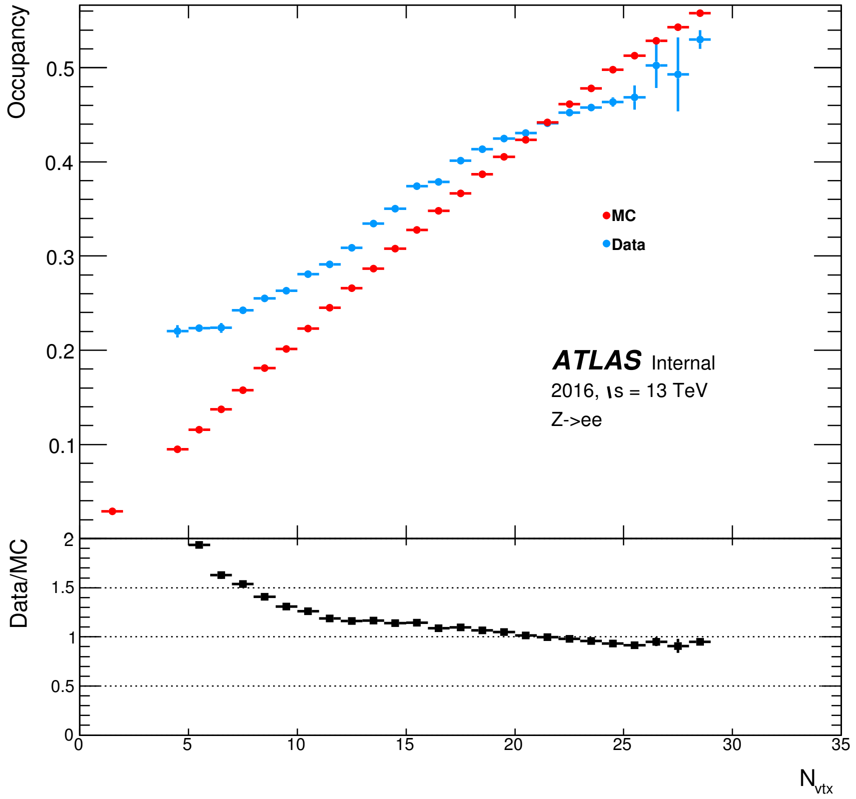

Figure 4.30: Comparison of the TRT occupancy as a function of the number of reconstructed vertices for data (blue) and simulation (red). The samples used are two runs of 2016 data and $Z \to e^+e^-$ MC events.

Crosstalk in EM calorimeter cells In electronics, the crosstalk is the phenomenon where the signal in one channel creates an undesired effect in other channels. In the EM calorimeter the crosstalk effect adds energy deposition signal in a particular cell from the signal in neighbouring cells. There are three types of crosstalk in the EM calorimeter: inductive, resistive and capacitive crosstalk, in both ϕ and η directions. The EM calorimeter crosstalk effects were studied and implemented in Geant4 [78]. However the middle-to-middle inductive crosstalk in the ϕ direction, of order 1.8%, was unfortunately not implemented in Geant4.

The nature of the w variable makes the analysis sensitive to crosstalk in the ϕ direction and the non-simulated effect would result in an inaccuracy of the reconstructed w variable and thus the selection efficiency. This inaccuracy was estimated at analysis level and treated as a systematic uncertainty. The signal efficiencies taking into account the crosstalk correction were derived by adding to each cell in the EM clusters 1.8% of the energy of the two neighbouring cells in ϕ. This additional effect slightly spread the energy deposition, thus decrease the w value and finally decrease the signal efficiency. The efficiency drop for spin-$\frac{1}{2}$ Drell-Yan samples is shown in figure 4.31.

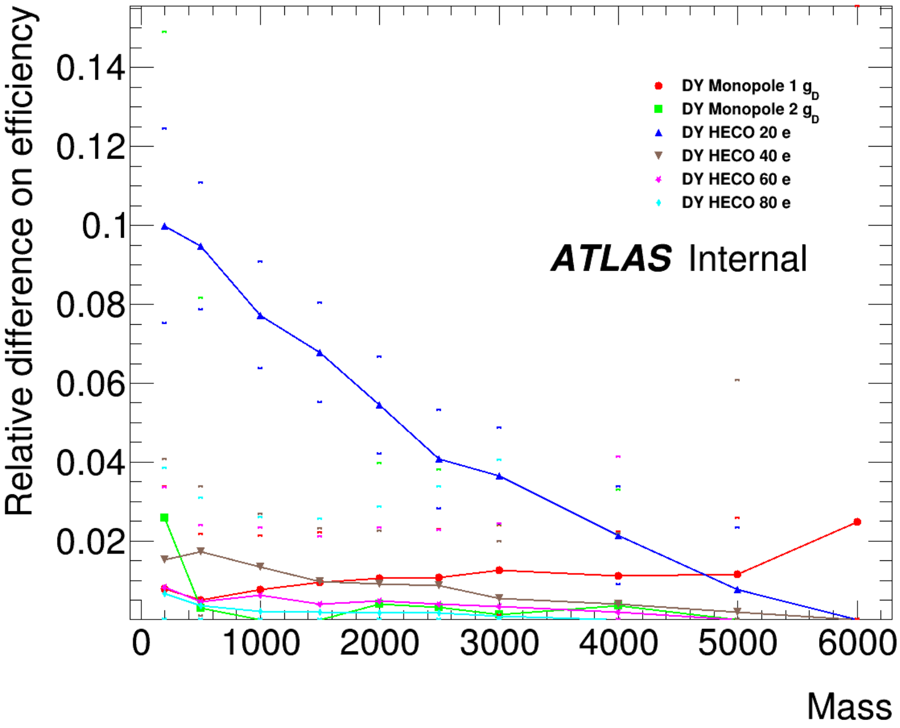

Figure 4.31: The relative difference in efficiency associated to cross-talk applied to spin-$\frac{1}{2}$ Drell-Yan events.

The average systematic uncertainty associated to the crosstalk in the EM calorimeter cells was found to be ∼2%.

Calorimeter signal arrival time A delayed arrival time in the calorimeter higher than 10 ns can affect the L1 trigger efficiency. Indeed the cluster would have an increased probability to be assigned to the next bunch crossing, the period being only 25 ns. HIPs slow down mostly toward the end of their trajectory and thus it is a valid approximation to consider candidates firing the trigger having a constant speed until reaching the EM calorimeter. With such an approximation a 10 ns arrival time corresponds to a transverse β of 0.37. In order to assess the effect of the calorimeter signal arrival time on the selection efficiency for DY HIP samples, an additional cut was added to the cut flow at generator level discarding events with $\beta > 0.37$. The relative efficiency drop compared to the baseline MC simulations was accounted for as a systematic uncertainty.

The average systematic uncertainty associated to the calorimeter signal arrival time was found to be $\sim$6%.

Precision of the extrapolation method The extrapolation method [71] accuracy relies on the precision of the efficiency maps and thus depends on the binning. In order to estimate the accuracy of the extrapolation method, extrapolated signal selection efficiencies for spin-$\frac{1}{2}$ were compared to the one derived from the fully simulated MC samples, as shown in table 4.8. The relative efficiency differences were accounted for as a systematic uncertainty.

The average systematic uncertainty associated to the precision of the extrapolation method was found to be $\sim$1%.

TRT Gas Distribution The TRT straws were filled during the LHC Run 1 with a Xenon gas mixture, chosen for its high absorbance of TR photons. Due to a gas leak affecting some layers of the sub-detector and to the high cost of Xenon, the most critical straws were filled with Argon for Run 2. The Argon/Xenon gas distribution changed between 2015 and 2016 as described in the figure 4.32. While most of the luminosity for this analysis was collected in 2016, the MC samples were generated under the MC15c campaign considering the 2015 TRT gas distribution. The additional Argon layers in 2016 are thus not accurately simulated, which

Monopole Spin 1/2 Efficiencies				
Charge[g_D]	Mass[GeV]	Simulation Efficiency[%]	Extrapolation Efficiency[%]	Discrepancy [%]
1	200	2.45 ± 0.04	2.61 ± 0.21	-0.16 ± 0.22
1	500	12.09 ± 0.12	13.27 ± 0.57	-1.18 ± 0.58
1	1000	23.96 ± 0.17	26.78 ± 0.84	-2.82 ± 0.85
1	1500	29.34 ± 0.18	32.34 ± 0.90	-3.00 ± 0.92
1	2000	31.70 ± 0.18	34.28 ± 0.93	-2.58 ± 0.94
1	2500	33.22 ± 0.19	34.78 ± 0.98	-1.56 ± 1.00
1	3000	34.00 ± 0.17	35.22 ± 0.78	-1.21 ± 0.80
1	4000	28.17 ± 0.14	29.25 ± 0.69	-1.08 ± 0.70
1	5000	8.97 ± 0.07	9.03 ± 0.35	-0.06 ± 0.36
1	6000	0.00 ± 0.00	0.00 ± 0.00	0.00 ± 0.00
2	200	0.01 ± 0.00	0.01 ± 0.00	0.00 ± 0.00
2	500	0.14 ± 0.01	0.13 ± 0.02	0.01 ± 0.02
2	1000	0.85 ± 0.03	0.87 ± 0.08	-0.01 ± 0.09
2	1500	1.64 ± 0.05	1.76 ± 0.16	-0.12 ± 0.16
2	2000	2.42 ± 0.06	2.45 ± 0.19	-0.03 ± 0.20
2	2500	3.30 ± 0.08	3.36 ± 0.27	-0.05 ± 0.28
2	3000	4.06 ± 0.06	4.14 ± 0.25	-0.07 ± 0.25
2	4000	3.02 ± 0.06	3.18 ± 0.24	-0.16 ± 0.24
2	5000	0.23 ± 0.01	0.25 ± 0.05	-0.02 ± 0.05

Table 4.8: Full selection efficiencies for Drell-Yan pair-produced spin-$\frac{1}{2}$ monopoles. The efficiencies extrapolated from the single-particle efficiency maps using the MC truth kinematics are compared to the efficiencies obtained from the full GEANT4 simulation for the same events. The errors on the efficiencies and discrepancy are statistical.

HECO Spin 1/2 Efficiencies				
Charge $\|z\|$	Mass[GeV]	Simulation Efficiency[%]	Extrapolation Efficiency[%]	Discrepancy [%]
20	200	6.53 ± 0.11	7.57 ± 0.59	-1.04 ± -0.60
20	500	15.91 ± 0.16	17.61 ± 0.80	-1.70 ± -0.81
20	1000	24.17 ± 0.18	26.62 ± 0.94	-2.44 ± -0.96
20	1500	28.03 ± 0.19	30.08 ± 0.94	-2.05 ± -0.96
20	2000	28.80 ± 0.18	31.03 ± 0.92	-2.23 ± -0.93
20	2500	28.31 ± 0.18	30.34 ± 0.87	-2.03 ± -0.89
20	3000	27.39 ± 0.16	28.87 ± 0.80	-1.48 ± -0.81
20	4000	23.91 ± 0.15	25.03 ± 0.75	-1.12 ± -0.77
20	5000	8.51 ± 0.08	8.88 ± 0.40	-0.36 ± -0.40
20	6000	0.00 ± 0.00	0.01 ± 0.00	-0.00 ± -0.00
40	200	5.62 ± 0.10	6.81 ± 0.53	-1.19 ± -0.53
40	500	14.74 ± 0.14	17.68 ± 0.74	-2.94 ± -0.75
40	1000	19.93 ± 0.15	22.45 ± 0.76	-2.51 ± -0.78
40	1500	21.76 ± 0.15	23.32 ± 0.78	-1.56 ± -0.80
40	2000	20.49 ± 0.15	21.36 ± 0.75	-0.86 ± -0.76
40	2500	17.31 ± 0.13	18.01 ± 0.68	-0.71 ± -0.69
40	3000	16.31 ± 0.13	16.71 ± 0.65	-0.40 ± -0.67
40	4000	8.61 ± 0.10	8.70 ± 0.48	-0.08 ± -0.49
40	5000	0.47 ± 0.02	0.46 ± 0.10	0.01 ± -0.10
40	6000	0.00 ± 0.00	0.00 ± 0.00	0.00 ± 0.00
60	200	1.56 ± 0.03	1.77 ± 0.13	-0.21 ± -0.13
60	500	5.24 ± 0.06	5.76 ± 0.33	-0.51 ± -0.34
60	1000	8.51 ± 0.09	8.81 ± 0.44	-0.30 ± -0.45
60	1500	8.33 ± 0.09	8.52 ± 0.43	-0.19 ± -0.44
60	2000	7.21 ± 0.08	7.24 ± 0.41	-0.03 ± -0.42
60	2500	5.90 ± 0.07	6.01 ± 0.35	-0.12 ± -0.35
60	3000	4.83 ± 0.06	4.88 ± 0.31	-0.05 ± -0.32
60	4000	1.11 ± 0.03	1.14 ± 0.15	-0.02 ± -0.16
60	5000	0.00 ± 0.00	0.00 ± 0.00	-0.00 ± -0.00
60	6000	0.00 ± 0.00	0.00 ± 0.00	0.00 ± 0.00
80	200	0.32 ± 0.01	0.34 ± 0.04	-0.02 ± -0.04
80	500	1.53 ± 0.03	1.55 ± 0.14	-0.02 ± -0.14
80	1000	2.49 ± 0.04	2.54 ± 0.18	-0.05 ± -0.18
80	1500	2.45 ± 0.04	2.43 ± 0.18	0.02 ± -0.18
80	2000	1.88 ± 0.03	1.85 ± 0.16	0.02 ± -0.16
80	2500	1.32 ± 0.03	1.33 ± 0.14	-0.01 ± -0.14
80	3000	0.90 ± 0.02	0.92 ± 0.12	-0.02 ± -0.12
80	4000	0.07 ± 0.01	0.06 ± 0.03	0.00 ± -0.03
80	5000	0.00 ± 0.00	0.00 ± 0.00	0.00 ± 0.00
80	6000	0.00 ± 0.00	0.00 ± 0.00	0.00 ± 0.00

Table 4.9: Full selection efficiencies for Drell-Yan pair-produced spin-$\frac{1}{2}$ HECOs. The efficiencies extrapolated from the single-particle efficiency maps using the MC truth kinematics are compared to the efficiencies obtained from the full Geant4 simulation for the same events. The errors on the efficiencies and discrepancy are statistical.

could have an impact on the selection efficiency due to the Argon lower transition radiation absorption probability.

The TRT particle identification relies on the distinct probability of generating TR photons for electrons and muons. The low and high thresholds were tuned so that the particles ionisation energy deposition would create low threshold hits, a Minimum Ionising Particle (MIP) deposing about 2 keV, and the TR photons would create high threshold hits, typically deposing 6-15 keV. The high threshold was thus set to $\sim$6 keV for Xenon gas mixture straws. Electrons would have a higher TR efficiency and thus generate a higher number of HT hits than muons or pions. The fraction of high threshold hits in the TRT was thus a good discriminant between electrons and muons.

The Argon high threshold was tuned so that the probability of high threshold hit of muons is aligned to the one of Xenon filled straws in the same area of the detector. The high threshold was thus set to $\sim$2 keV for Argon gas mixture straws. The electrons probability of high threshold hit in Argon is lower than in Xenon, reducing the particle identification power of the TRT.

The high f_{HT} of HIPs is due to the high number of generated δ-rays. Indeed each δ-electron would deposit $\sim$2 keV in a straw and overlapping δ-rays would generate a high threshold hit. While the $\mathrm{d}E/\mathrm{d}x$ of a MIP is $\sim$2.7 times lower in Argon than in Xenon, the high threshold was set $\sim$3 times lower in Argon than in Xenon. The probability for δ-rays to generate high threshold hits is thus higher in Argon. The MC15c f_{HT} is thus underestimated, as well as the selection efficiency.

The limit derived are thus conservative and no systematic uncertainty associated to the TRT gas distribution was deemed necessary.

Pile-up reweighting The pile-up reweighting (PRW) is applying weights to MC samples events in order to adjust the $< \mu >$ distribution to the one of the data. Due to known mismodelling in the MC of the level of activity being produced at central eta values during non-diffractive interactions, a scale factor is applied on the data $< \mu >$ distribution before deriving the pile-up weights. The data scale factor is thus a parameter of the PRW tool and

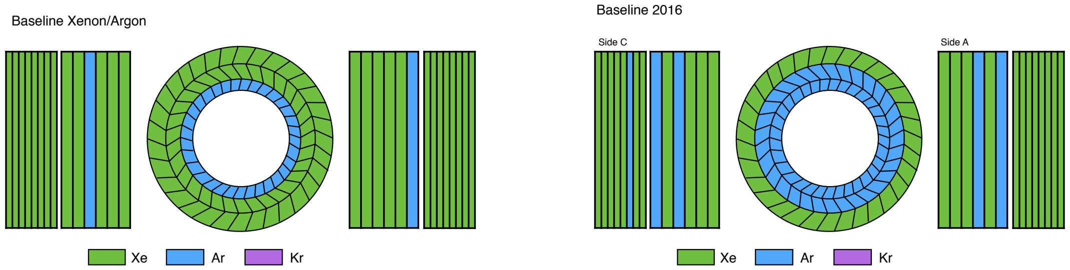

Figure 4.32: The TRT baseline gas distribution for 2015 shown on the left, and for 2016 shown on the right. The sections of the Transition Radiation Tracker filled with Argon in 2016 but not in 2015 account for roughly a third of the portion of the detector used in this analysis.

an associated systematic uncertainty was derived.

The nominal scale factor was set for the MC15c campaign to 1/1.09. As recommended by expert the uncertainty on the efficiency was estimated by using a scale factor of 1 for the upper bound, and 1/1.18 for the lower bound.

The average systematic uncertainty associated to the pile-up reweighting scale factor was found to be ∼3% for the lower bound, and ∼2% for the upper bound.

Summary of systematics

The uncertainty in the combined 2015+2016 integrated luminosity is 2.2% [79]. This is added in quadrature to the uncertainties listed in Tables 5–17.[1]

---

[1] Note that the 2015 dataset represents 1.58 fb^{-1}, or 37.5% of the 4.216 fb^{-1} integrated luminosity recorded by ATLAS in 2015, due to the fact that the HIP trigger started collecting data on October 11, 2015.

Spin-$\frac{1}{2}$ $1g_{\text{D}}$	eff.	MC Stat.	Det. material	G4 range cut	Birks High	Birks Low	δ-ray Prod.	TRT Occ.	LAr x-talk	Calo Arrival	Extrap.	Weight Up	Weight Down	total Up	total Down
200GeV	2	±2	± 2	12	22	9	±13	8	6	-8	0	6	7	33	16
500GeV	12	±1	± 6	10	19	2	±12	9	10	-6	0	10	10	31	14
1000GeV	24	±1	± 6	10	19	2	±12	12	12	-3	0	12	12	34	14
1500GeV	29	±1	± 6	10	19	2	±12	7	10	-6	0	10	11	31	14
2000GeV	32	±1	± 6	10	19	2	±12	4	8	-10	0	8	9	29	17
2500GeV	33	±1	± 6	10	19	2	±12	-1	5	-17	0	4	6	26	21
3000GeV	34	±1	± 6	10	19	2	±12	-5	3	-24	0	2	5	26	28
4000GeV	28	±1	± 6	10	19	2	±12	-7	4	-40	0	2	6	26	43
5000GeV	9	±1	± 3	-7	-8	-6	±9	-18	1	-66	0	-2	4	11	70
6000GeV	0	±11	± 6	10	19	2	±12	0	0	0	0	0	0	25	13

Table 4.10: Relative uncertainties on the signal efficiencies in percentages for Drell-Yan produced spin-$\frac{1}{2}$ monopoles of charge $|g| = 1g_{\text{D}}$. The total relative uncertainties are calculated as quadratic sums of the individual relative uncertainties including the 2.2% uncertainty on the luminosity measurement. Note that the δ-ray and material density uncertainties are taken as symmetric, as described in the text.

Spin-0 $1g_{\text{D}}$	eff.	MC Stat.	Det. material	G4 range cut	Birks High	Birks Low	δ-ray Prod.	TRT Occ.	LAr x-talk	Calo Arrival	Extrap.	Weight Up	Weight Down	total Up	total Down
200GeV	8	±1	± 7	4	13	2	±6	-1	0	0	-0.02	0	0	17	10
500GeV	36	±1	± 3	0	4	-5	±0	-1	0	0	-0.07	0	0	5	6
1000GeV	57	±0	± 3	0	4	-5	±0	-1	0	0	-0.10	0	0	5	6
1500GeV	65	±0	± 3	0	4	-5	±0	-2	0	-2	-0.09	0	0	5	7
2000GeV	67	±0	± 3	0	4	-5	±0	-3	0	-5	-0.07	0	1	5	8
2500GeV	68	±0	± 3	0	4	-5	±0	-4	0	-7	-0.04	-1	1	5	10
3000GeV	67	±0	± 3	0	4	-5	±0	-6	0	-11	-0.03	-1	1	5	13
4000GeV	60	±0	± 3	0	4	-5	±0	-9	0	-22	-0.02	-1	2	5	25
5000GeV	28	±1	± 1	-8	-8	-5	±8	-17	0	-52	0.00	-3	3	9	57
6000GeV	0	±8	± 3	0	4	-5	±0	0	0	0	0.00	0	0	5	6

Table 4.11: Relative uncertainties on the signal efficiencies in percentages for Drell-Yan produced spin-0 monopoles of charge $|g| = 1g_{\text{D}}$. The total relative uncertainties are calculated as quadratic sums of the individual relative uncertainties including the 2.2% uncertainty on the luminosity measurement. Note that the δ-ray and material density uncertainties are taken as symmetric, as described in the text.

Spin-$\frac{1}{2}$ 40e	eff.	MC Stat.	Det. material	G4 range cut	Birks High	Birks Low	δ-ray	TRT Occ.	LAr x-talk	Calo Arrival	Weight Up	Weight Down	total Up	total Down
200GeV	6	±2	± 3	9	9	10	±5	10	20	-10	20	22	41	12
500GeV	15	±1	± 3	9	9	10	±5	15	19	-5	20	21	41	8
1000GeV	20	±1	± 3	9	9	10	±5	8	12	-3	12	13	29	7
1500GeV	22	±1	± 3	9	9	10	±5	3	7	-3	7	8	21	7
2000GeV	20	±1	± 3	9	9	10	±5	-1	4	-5	4	5	19	8
2500GeV	17	±1	± 3	9	9	10	±5	-2	4	-8	3	5	19	10
3000GeV	16	±1	± 3	9	9	10	±5	-4	3	-10	2	3	18	12
4000GeV	9	±1	± 3	9	9	10	±5	-5	1	-11	0	2	17	14
5000GeV	0	±4	± 3	9	9	10	±5	-8	-2	-2	-4	0	17	11
6000GeV	0	±0	± 3	9	9	10	±5	0	0	0	0	0	17	6

Table 4.12: Relative uncertainties on the signal efficiencies in percentages for Drell-Yan produced spin-$\frac{1}{2}$ HECOs of charge $|z| = 40$. The total relative uncertainties are calculated as quadratic sums of the individual relative uncertainties including the 2.2% uncertainty on the luminosity measurement. Note that the δ-ray and material density uncertainties are taken as symmetric, as described in the text.

Spin-0	eff.	MC	Det.	G4	Birks	Birks	δ-ray	TRT	LAr	Calo	Extrap.	Weight	Weight	total	total
40e		Stat.	material	range cut	High	Low	Prod.	Occ.	x-talk	Arrival		Up	Down	Up	Down
200GeV	19	±1	± 3	0	0	1	±2	-8	-1	0	-0.19	-1	1	5	9
500GeV	41	±1	± 3	0	0	1	±2	-3	-1	0	-0.16	0	0	5	6
1000GeV	51	±0	± 3	0	0	1	±2	-3	0	0	-0.09	-1	0	5	5
1500GeV	52	±0	± 3	0	0	1	±2	-3	0	-1	-0.05	0	0	5	6
2000GeV	49	±0	± 3	0	0	1	±2	-4	0	-3	-0.03	0	0	5	7
2500GeV	45	±0	± 3	0	0	1	±2	-4	0	-6	-0.03	-1	1	5	9
3000GeV	42	±1	± 3	0	0	1	±2	-5	0	-7	-0.02	0	0	5	10
4000GeV	26	±1	± 3	0	0	1	±2	-5	0	-6	-0.01	-1	1	5	9
5000GeV	2	±3	± 3	0	0	1	±2	-7	0	-2	0.01	-2	1	5	9
6000GeV	0	±0	± 3	0	0	1	±2	0	0	0	0.00	0	0	4	4

Table 4.13: Relative uncertainties on the signal efficiencies in percentages for Drell-Yan produced spin-0 HECOs of charge $|z| = 40$. The total relative uncertainties are calculated as quadratic sums of the individual relative uncertainties including the 2.2% uncertainty on the luminosity measurement. Note that the δ-ray and material density uncertainties are taken as symmetric, as described in the text.

4.3 Results

4.3.1 Final yield

No events were observed in the data in the signal region delineated by $w > 0.96$ and $f_{HT} > 0.7$ in Fig. 4.21.

4.3.2 Cross-section limits on HIP production and lower mass limits assuming a Drell-Yan pair production model

The limits on the number of HIPs produced are derived using Histfitter. The inputs for the calculation are:

- the selection efficiency (Section 4.2.2);
- the statistical and systematic uncertainties in selection efficiency (Section 4.2.4);
- the number of expected background events with uncertainties (Section 4.2.3);
- the number of observed events;
- the integrated luminosity with uncertainties (34.4 fb^{-1} with 2.2% relative uncertainty).

The limits are then translated into production cross-sections limits, and 95% CL upper limits in the measured monopole cross section assuming Drell-Yan kinematic distributions are shown in figures 4.33 and 4.34, for spin-0 and spin-1/2, respectively. Similarly, the respective HECO cross section limits are shown in Figs. 4.35 and 4.36.

Histfitter is used to compute limits in the number of produced HIP events for each mass and charge point. The calculation is performed in the frequentist profile likelihood test statistic using 20 000 toys. These limits are then translated into limits in the HIP production cross section. For a given mass and charge, the inputs to those calculations are:

- the selection efficiency (see Section 4.2.2);
- the statistical and systematic uncertainties in selection efficiency (see Section 4.2.4);
- the number of expected background events with uncertainties (see Section 4.2.3);
- the number of observed events;
- the integrated luminosity with uncertainties (34.4 fb^{-1} with 2.2% relative uncertainty).

In order to understand the effects of the systematic uncertainties on the calculated limits, the cross section upper limits were derived considering only the statistical uncertainties in the selection efficiency. These limits are presented in Appendix G.

Drell-Yan mass limits

For a given charge, the mass at which the upper cross-section limit crosses the theoretical cross-section, corresponds to a lower mass limit. The mass limits are listed in the table 4.14. Due to the uncertainty on the theoretical cross-section, those values are indicative and used for comparison with other experiments.

Drell-Yan Lower Mass Limits [GeV]							
	$\lvert g\rvert = 1g_{\mathrm{D}}$	$\lvert g\rvert = 2g_{\mathrm{D}}$	$\lvert z\rvert = 20$	$\lvert z\rvert = 40$	$\lvert z\rvert = 60$	$\lvert z\rvert = 80$	$\lvert z\rvert = 100$
Spin-0	1840	1715	1355	1605	1620	1485	1385
Spin-1/2	2365	2125	1820	2040	2005	1860	1645

Table 4.14: Lower mass limits (in GeV) at 95% confidence level in models of spin-0 and spin-1/2 leading-order DY HIP pair production.

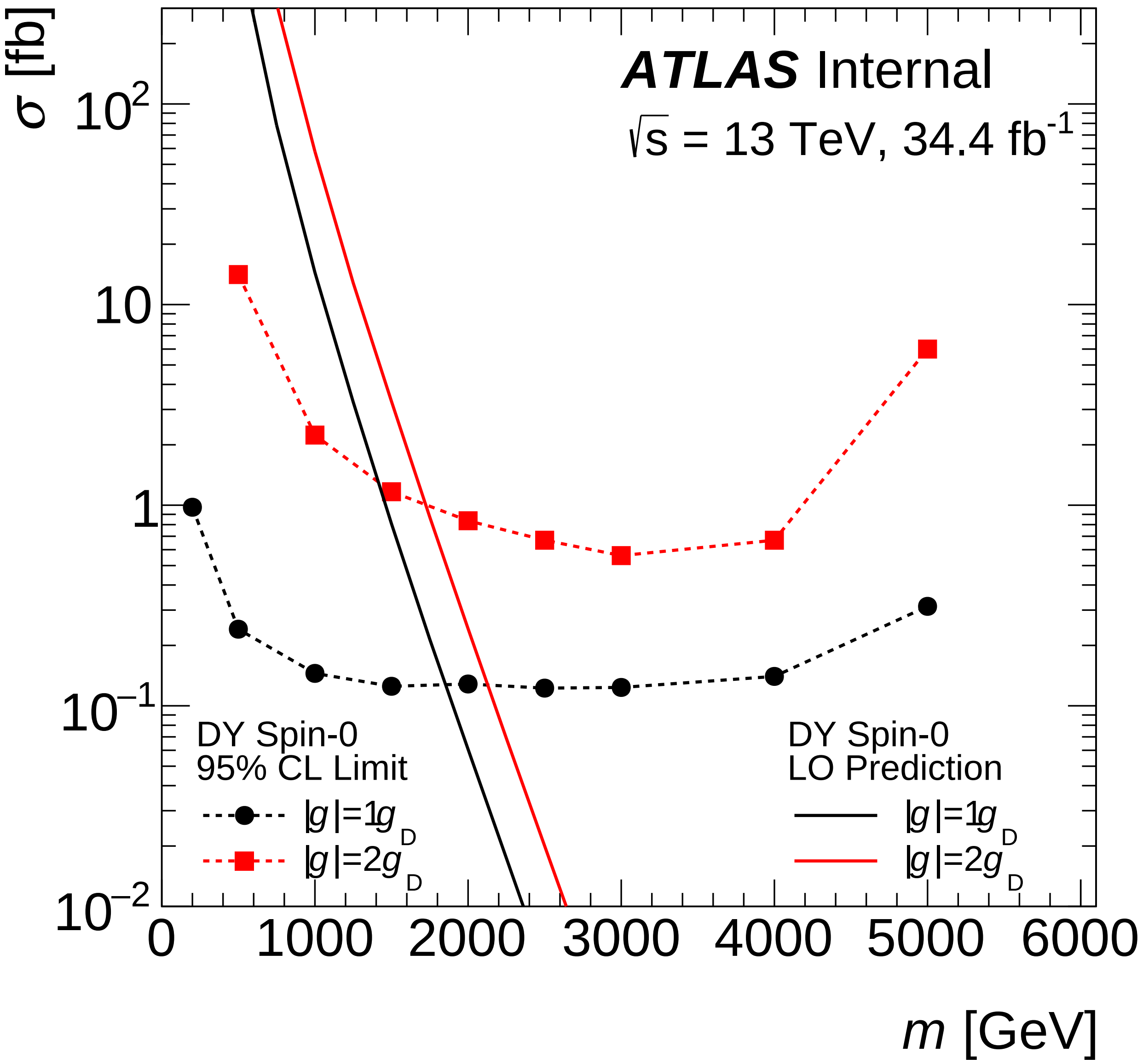

Figure 4.33: Observed 95% CL upper limits for Drell-Yan spin-0 monopoles as a function of HIP mass in various scenarios (dashed lines with markers). Overlaid on the plots are the theoretical cross-sections (solid lines).

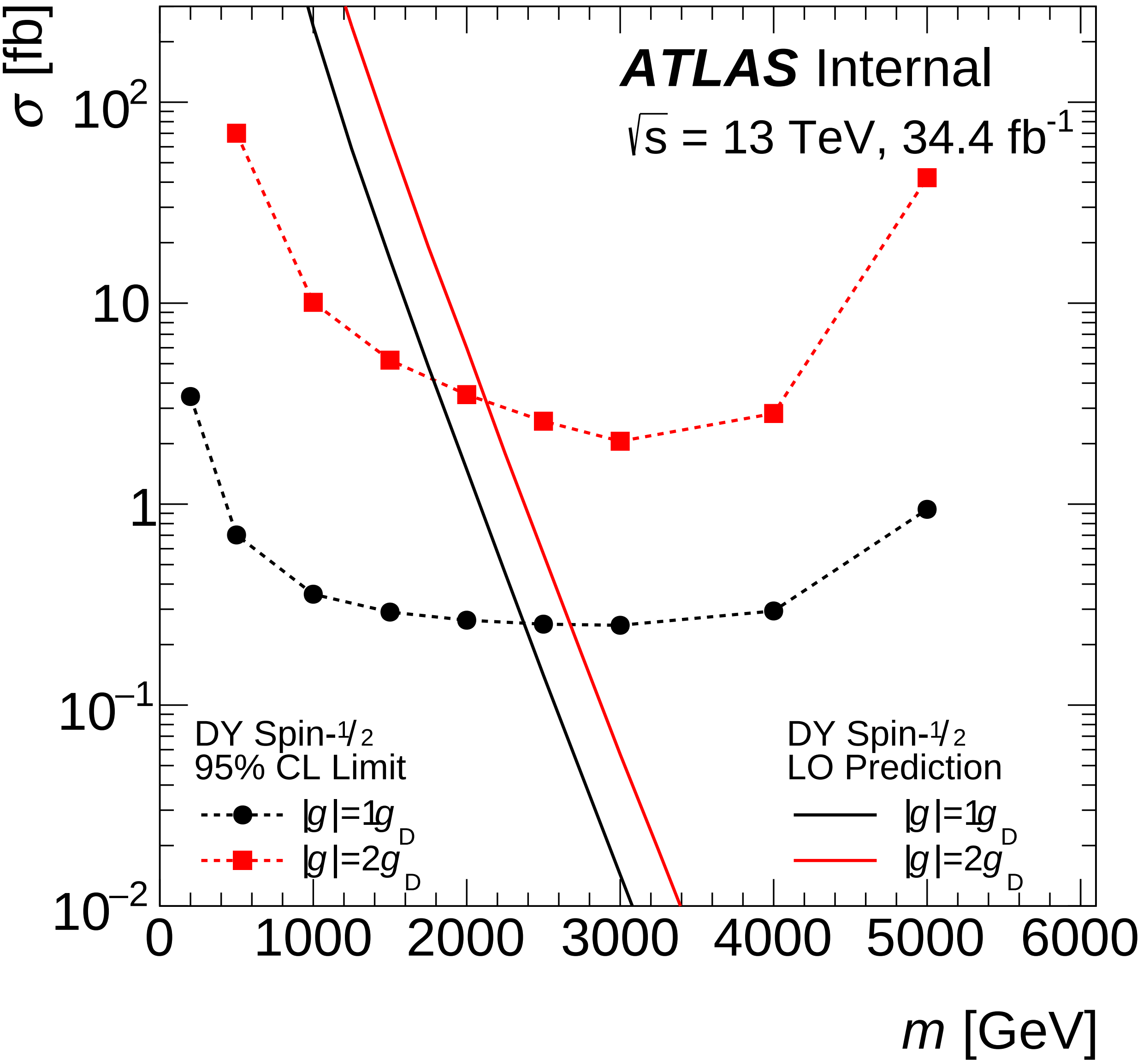

Figure 4.34: Observed 95% CL upper limits for Drell-Yan spin-$\frac{1}{2}$ monopoles as a function of HIP mass in various scenarios (dashed lines with markers). Overlaid on the plots are the theoretical cross-sections (solid lines).

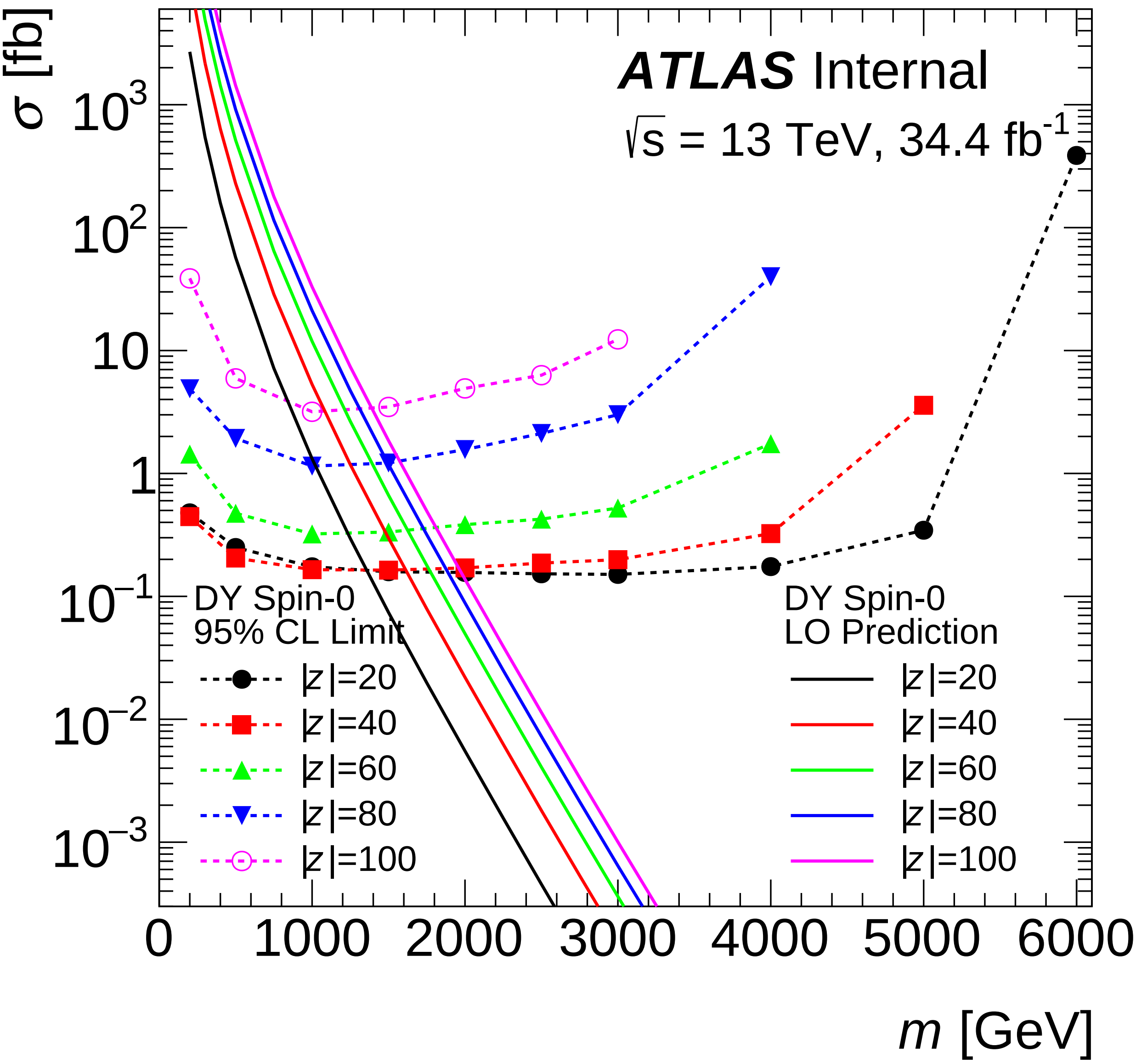

Figure 4.35: Observed 95% CL upper limits for Drell-Yan spin-0 HECOs as a function of HIP mass in various scenarios (dashed lines with markers). Overlaid on the plots are the theoretical cross-sections (solid lines).

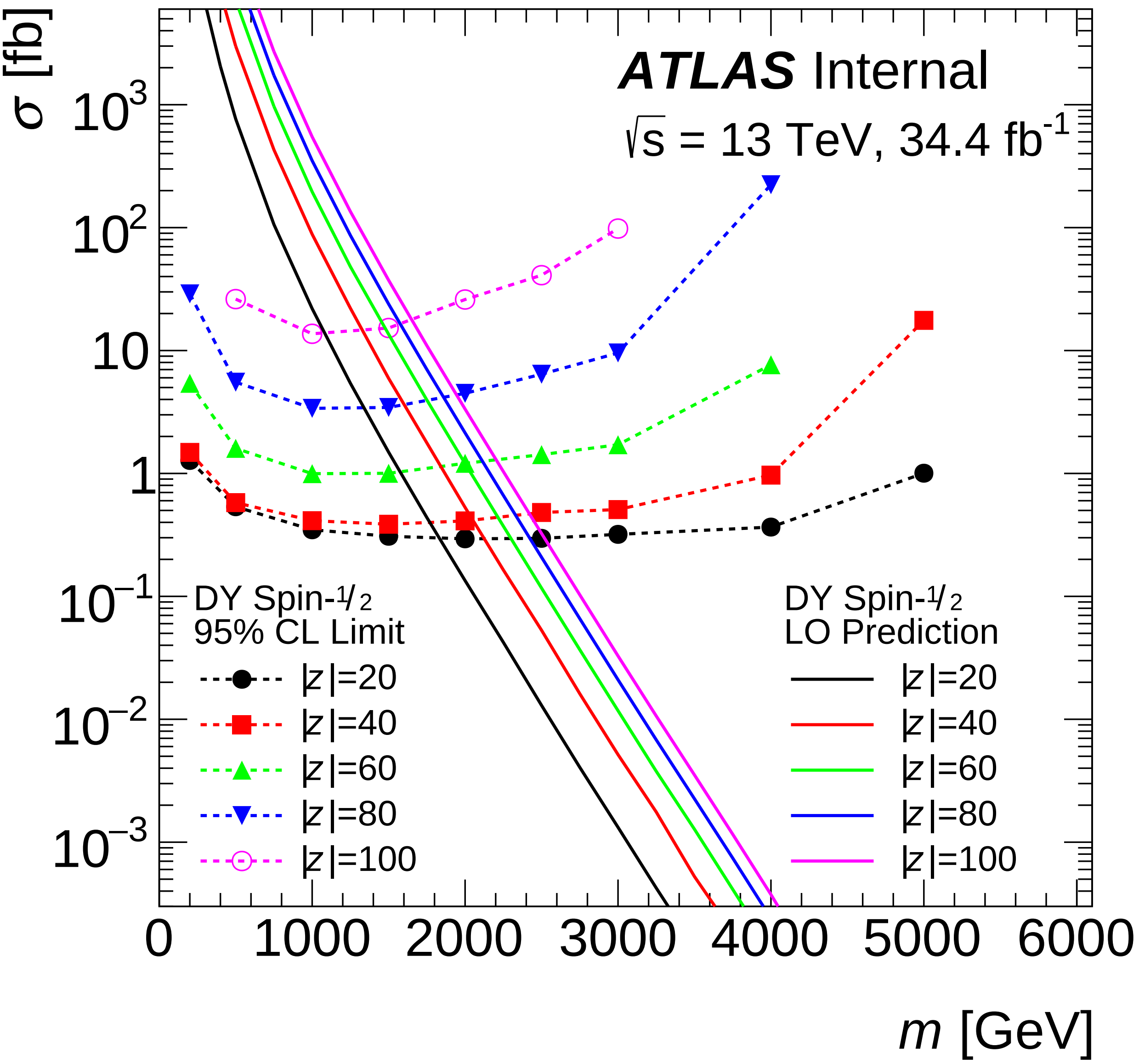

Figure 4.36: Observed 95% CL upper limits for Drell-Yan spin-$\frac{1}{2}$ HECOs as a function of HIP mass in various scenarios (dashed lines with markers). Overlaid on the plots are the theoretical cross-sections (solid lines).

Chapter 5

MoEDAL trapping detector analysis

The dedicated experiment can enjoy a new energy regime opened at the LHC allowing direct probes of magnetic monopoles at the TeV scale for the first time. MoEDAL pioneered a technique in which monopoles would be slowed down in a dedicated aluminium array and the presence of trapped monopoles is probed by analysing the samples with a superconducting magnetometer. High ionisation from magnetic monopoles is one of the signatures used by experimental searches around the world. Another main signature that free magnetic charges would have in nature is to induce a persistent current when passed through superconducting loops. The Monopole and Exotics Detector at the LHC (MoEDAL) [80] is combining NTD arrays and trapping array consisting in aluminium volumes in which the magnetic monopoles could stop in and then be scanned thanks to an induction technique.

This work presents the analysis of the magnetometer data collected from the trapping detector array exposed to 13 TeV proton-proton collisions during the Run 2 of the LHC.

5.1 The magnetometer data

The magnetic field inside the MoEDAL forward trapping detector exposed to LHC collisions was measured in the Laboratory for Natural Magnetism (LNM) located on the magnetically quiet

Adlisberg in the outskirts of Zürich. The measurements were done thanks to a Superconducting Quantum Interference Device (SQUID) magnetometer allowing to reach a precision smaller than the Dirac charge. In addition to be far from sources of electromagnetic fields, the device is shielded in a Faraday cage allowing to hide from the Earth magnetic field and to reduce the background noise. For the MoEDAL purpose, a calibration step was required to express the calorimeter outputs in Dirac charges equivalent and to study the monopoles expected signal in the calorimeter.

5.1.1 Independent calibrations of the calorimeter output to Dirac charges equivalent

Two independent calibration approaches were used, agreeing within 10%, considered as the uncertainty on the calibration. The first method is using a calibration sample with a known dipole moment, allowing with a convolution method to estimate the magnetometer response to a monopole. The second method is a more direct approach using a long solenoid whose ends can be used to emulate monopoles.

The convolution method [81]

The calibration sample consists in a 14 mm long needle with a 1 mm diameter made from a floppy disk material trapped in a non-magnetic plastic disk. The needle was magnetised such that the longitudinal dipole moment is $\mu = 3.02\ 10^{-6}$ Am^2. The figure 5.1 shows the measured current along the calibration sample, calibrated such that the plateau corresponds to the sample dipole moment. The superposition principle for magnetic fields applied to the situation, allows to consider the calibration sample dipole as a chain of smaller dipoles. The magnetometer response to a pseudopole is thus emulated by summing the measurements of the calibration sample by steps of 1 mm. The plateau in figure 5.2 allows to set the calibration constant to $9.15\ 10^5$ $\mathrm{g_D}$.

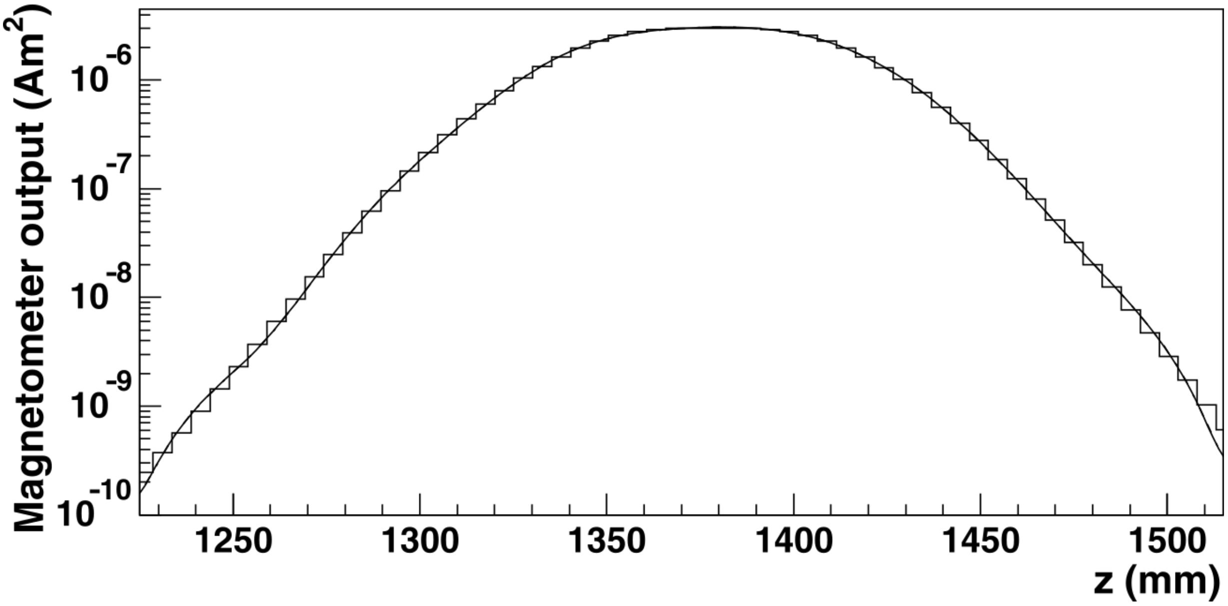

Figure 5.1: The measured current from the calibration sample as a function of z. A smoothed form of the spectrum is overlaid. The data are expressed in units of magnetic moment since the magnetometer calibration is such that the plateau value returns the value of the sample dipole moment

Direct approach: the solenoid method

The long solenoid, as shown in figure 5.3, can be considered as having two opposite sign poles, referred to as pseudopoles. Knowing the characteristics of the solenoid, the pseudopoles' charges were calculated to be $\sim$ 32.4 $g_D/$. The calorimeter response was measured for several current intensities and compared to the expected response derived thanks to the calibration constant set up with the calibration sample. The agreement as shown in figure 5.4 allows to estimate the uncertainty on the calibration to be within 10%.

Monopole signal emulation

SQUID magnetometer are able to measure extremely small magnetic fields variation and the Laboratory for Natural Magnetism at ETHZ's SQUID sensitivity allow us to probe particles with a magnetic charge higher or equal to 1. The signature of a monopole passing through a superconducting coil is a non-zero persistent current (Figure 5.5) that would be induced by the magnetic charge but not cancelled by the corresponding opposite pole as it would be the case for a dipole. This feature is proper to magnetic monopoles making those measurements fully

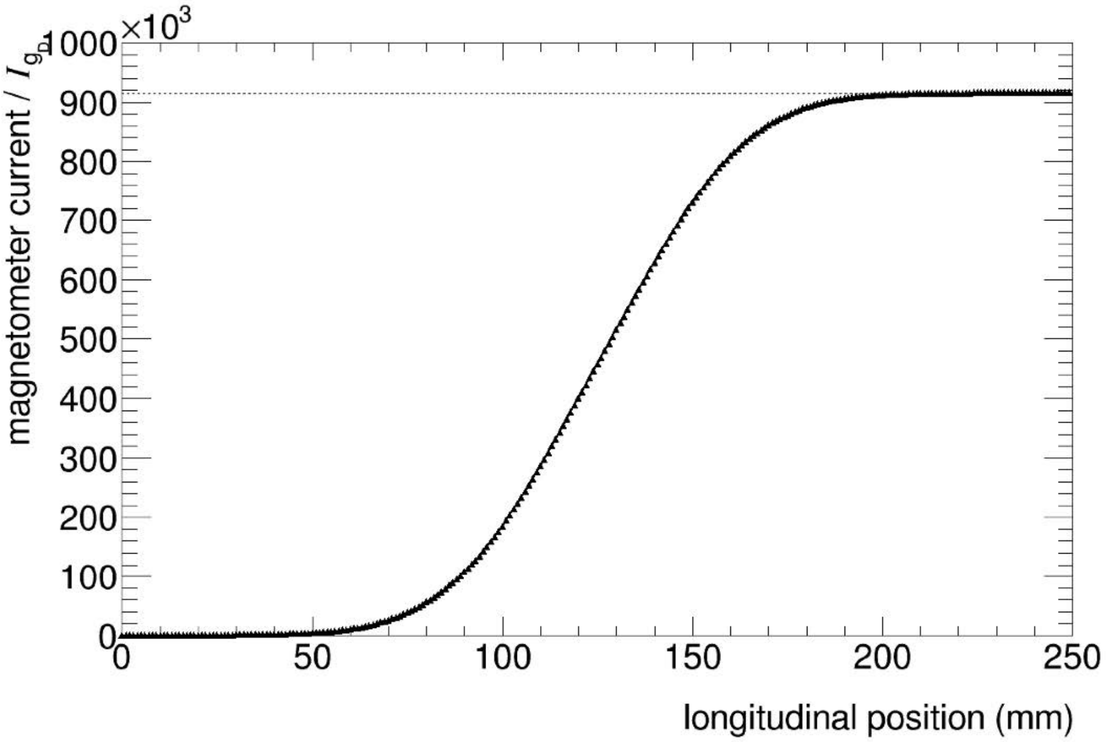

Figure 5.2: Measurement of the calibration sample with a dipole magnetic moment $\mu = 3.0210^{-6}\mathrm{Am}^2$. The sample was measured at 250 positions in steps of 1 mm. Calibration constant tuned for plateau at 9.15 10^5 $\mathrm{g_D}$

background free. One could even pass several times a candidate bar through the coils, observing as many increments in the persistent current corresponding to the magnetic charge in the sample. In addition thanks to a calibration realised on dipoles with a known magnetisation we can derive from the persistent current the magnetic charge associated. The expected signature of a monopole passing through the SQUID magnetometer is represented on figure 5.5.

5.1.2 Measurements of the forward trapping detector array

The aluminium bars of the MoEDAL trapping array are scanned and pass through superconducting coils of a SQUID magnetometer (Figures 5.6 and 5.7). Each of the 672 aluminium bars of the forward trapping array was scanned and had the associated persistent current measured, as shown in figure 5.8. The samples with a persistent current above 0.4were set aside as candidates and remeasured several times, as shown in figure 5.8. The re-measurements of those candidates ruled out the monopole hypothesis and monopoles with a charge higher than

Figure 5.3: Solenoid used for the calibration with poles equivalent to 32.4 $\mathrm{g_D}/\mu\mathrm{A}$

1 g_D were excluded from all the samples. The spurious fluctuation observed in the first passage distribution, creating a fake signal at $\sim \pm 1.8\ g_D$, can happen for samples containing magnetic dipoles impurities. It was observed that the offset probability is increased for increased magnetisation samples. The effect is also increased with increasing tray transport speed as shown in figure 5.9. While true signal was excluded from the data thanks to additional measurements of the candidates, false negatives could occur if the response to a monopole in the first passage was cancelled by a spurious fluctuation. The false-negative probability was estimated from the samples persistent current distribution in figure 5.8. The distribution was fitted by four Gaussians (two for the central pic and two for each pics at $\sim \pm 1.8\ g_D$) and the probability was assessed as the normalised integral of the distribution in $\pm 0.4\ g_D$ windows around integer Dirac charges. The probability was found to be 0.02% for $\pm 1 g_\mathrm{D}$ charges, 1.5% for $\pm 2 g_\mathrm{D}$ charges and negligible for charges above. The detector efficiency was conservatively set to 98% in the limit calculation to take into account this effect.

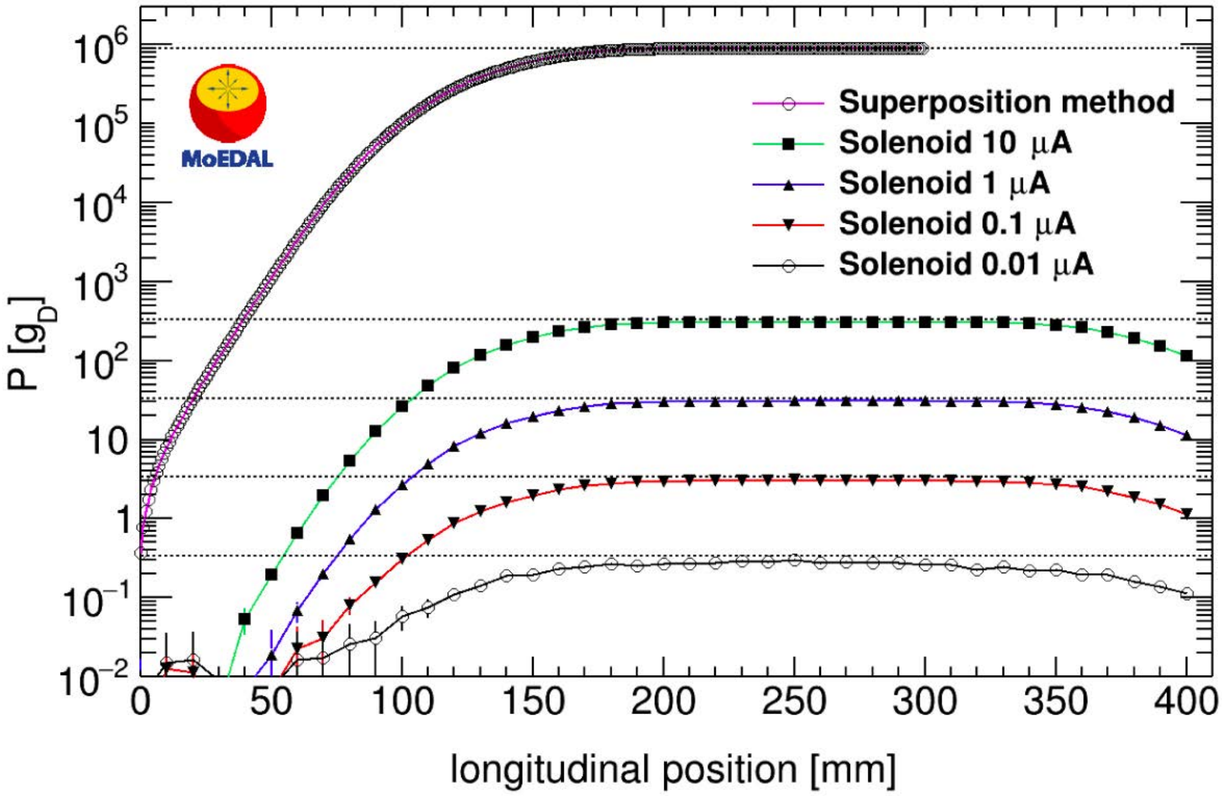

Figure 5.4: Results of the calibration measurements with the superposition method using a magnetic dipole sample and the solenoid method with $P = 32.4 g_D/\mu\text{A}$ and various currents. The dashed lines represent the expected plateau values in units of Dirac charge. The calibration constant is tuned using the measurement from the superposition method.

5.2 Simulation and analysis

The interpretation of the results requires to derive the detector acceptance. A clear description of the detector geometry was designed in order to simulate via GEANT4 the interaction of the simulated monopoles with the LHCb material and the MoEDAL trapping array. The LHCb material description was redesigned for MoEDAL, as the zone of interest for MoEDAL being mostly outside from the LHCb acceptance, the existing description was not detailed enough. The detector acceptance is also highly dependent on the production model, as the kinematics distributions (Figure 5.10) determine the probability for a monopole to be trapped in the array.

Drell-Yan production samples were generated via MadGraph5 at leading order for spin 0, $\frac{1}{2}$and 1 monopoles, with both β-independent coupling and β-dependant coupling to the photon in which g was substituted by βg. The samples were then simulated through the detector via GEANT4. The use of several production models allows to sense how the uncertainty on the

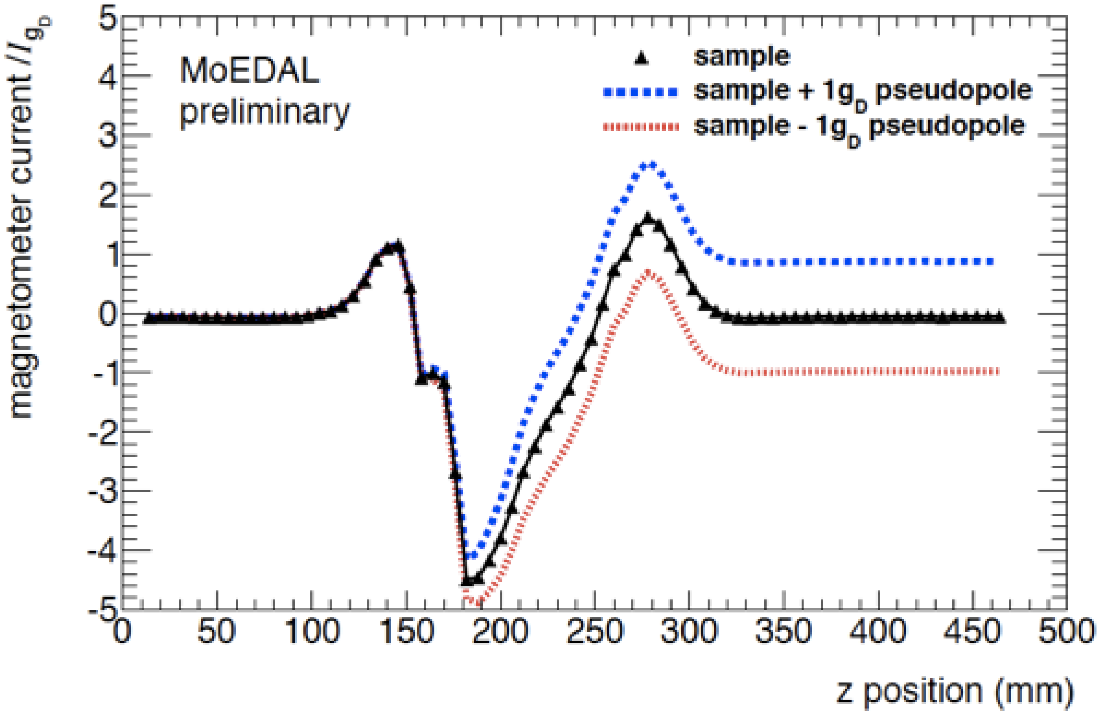

Figure 5.5: Response of the magnetometer current at 76 different positions for a single sample passing through the magnetometer. The dashed blue and red lines show the response of the magnetometer to a sample emulating respectively a 1 g_D charge and a -1 g_D charge

production mechanism affects the search acceptance.

5.3 Results

5.3.1 2016 exposure

No magnetic monopole was observed in the forward trapping detector exposed to 2.11 fb^{-1} of LHC interactions, allowing to set constraints on magnetic monopole production cross-section and mass assuming a Drell-Yan production mechanism, as shown in figure 5.11. Those results probe the TeV regime for charges up to 5 g_D with first limits at LHC for 5 g_D monopoles. They are the best limits at LHC for charges higher than 2 g_D as shown in the table 5.1.

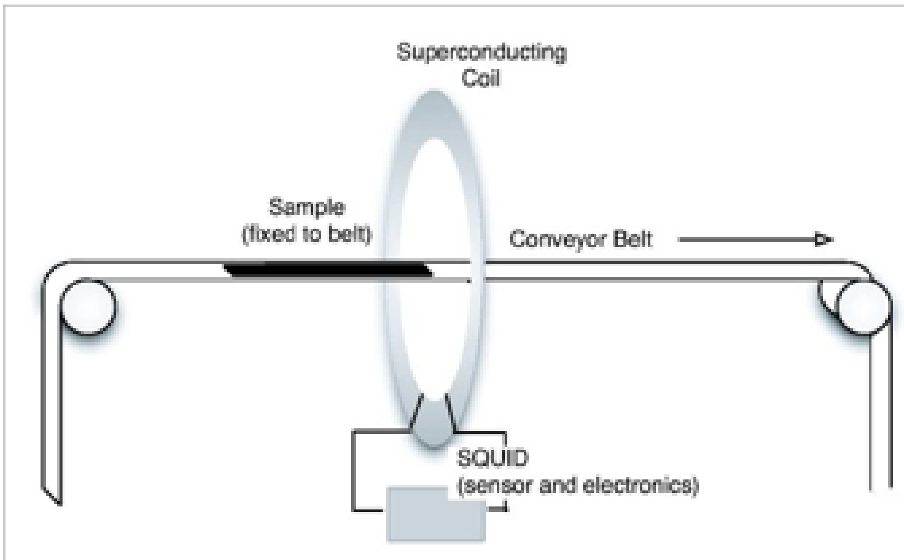

Figure 5.6: Schematic of the scanning of MMT aluminium bars through SQUID's superconducting coils

5.3.2 Recent iteration of the analysis

The analysis was re-run in 2018 with the full trapping array, and thus an increased acceptance, exposed to 4.0 fb^{-1} of 13 TeV proton-proton collisions [86]. The analysis also introduces an additional photon fusion production model in the interpretation of the measurements. No monopole candidate was observed and more constraining limits were set as shown in table 5.2.

MoEDAL is a cost-efficient passive detector dedicated for searching for new charged long-lived particles. The trapping detector array can yield to competitive results quickly and with no background ambiguities. The limits already surpass existing constraints for charges higher than 2 g_D. The analysis is complementary to the ATLAS search and allows to probe higher charges. The beam pipes of LHC experiments that were removed during the first long shutdown are also planned to be scanned the same way, making it possible to probe particles with very high ionising power, e.g. with high Dirac charges.

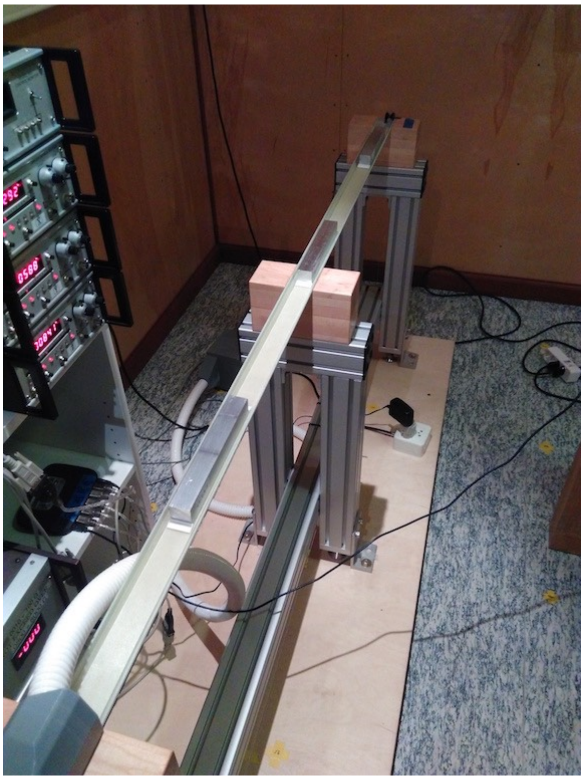

Figure 5.7: SQUID magnetometer tray with three aluminium bars ready to be scanned.

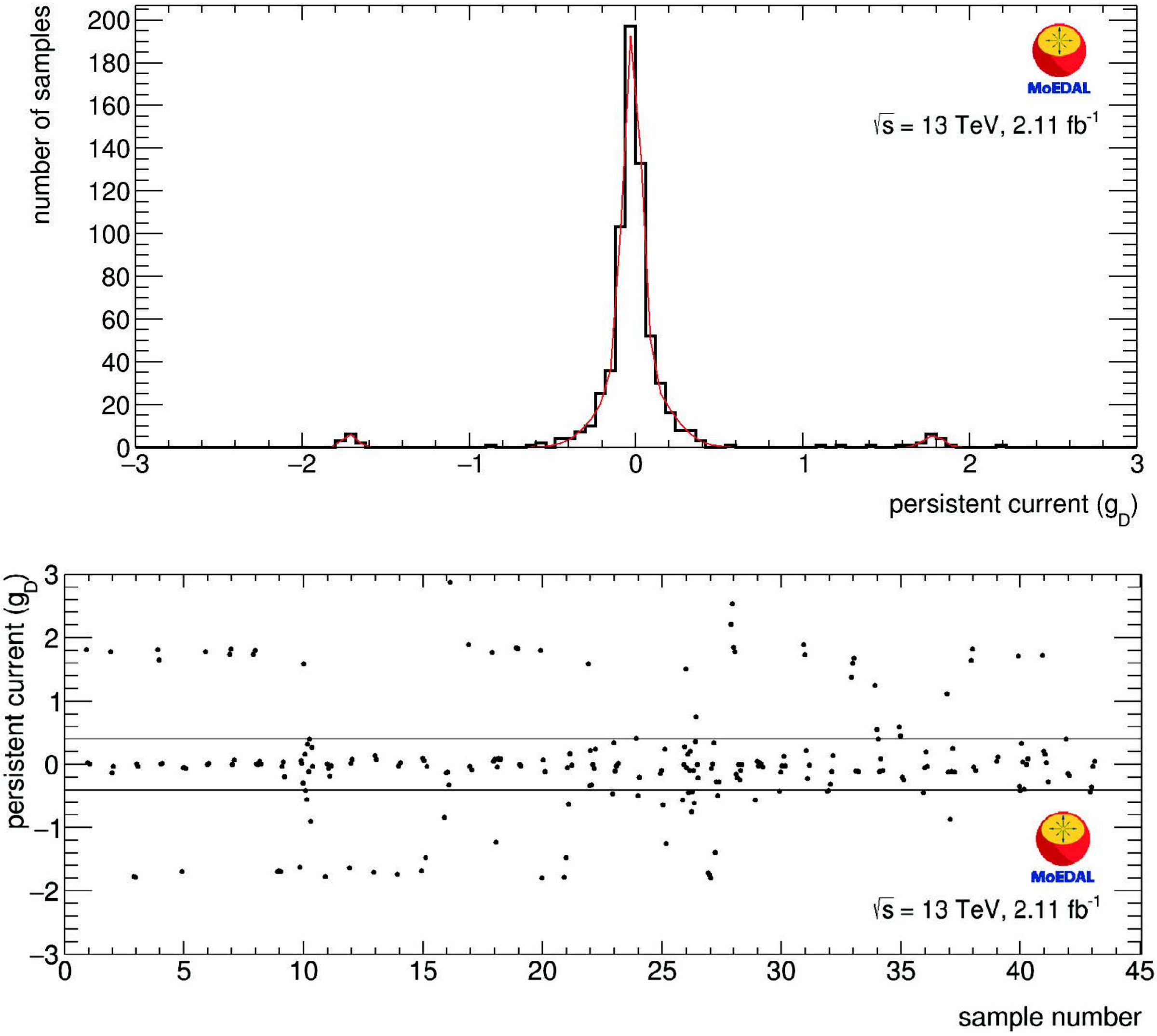

Figure 5.8: Top: persistent current (in units of gD after application of a calibration constant) after first passage through the magnetometer for all samples. The red curve shows a fit of the measured distribution using a sum of four Gaussian functions. Bottom: results of repeated measurements of candidate samples with absolute measured values in excess of $0.4 g_{\mathrm{D}}$.

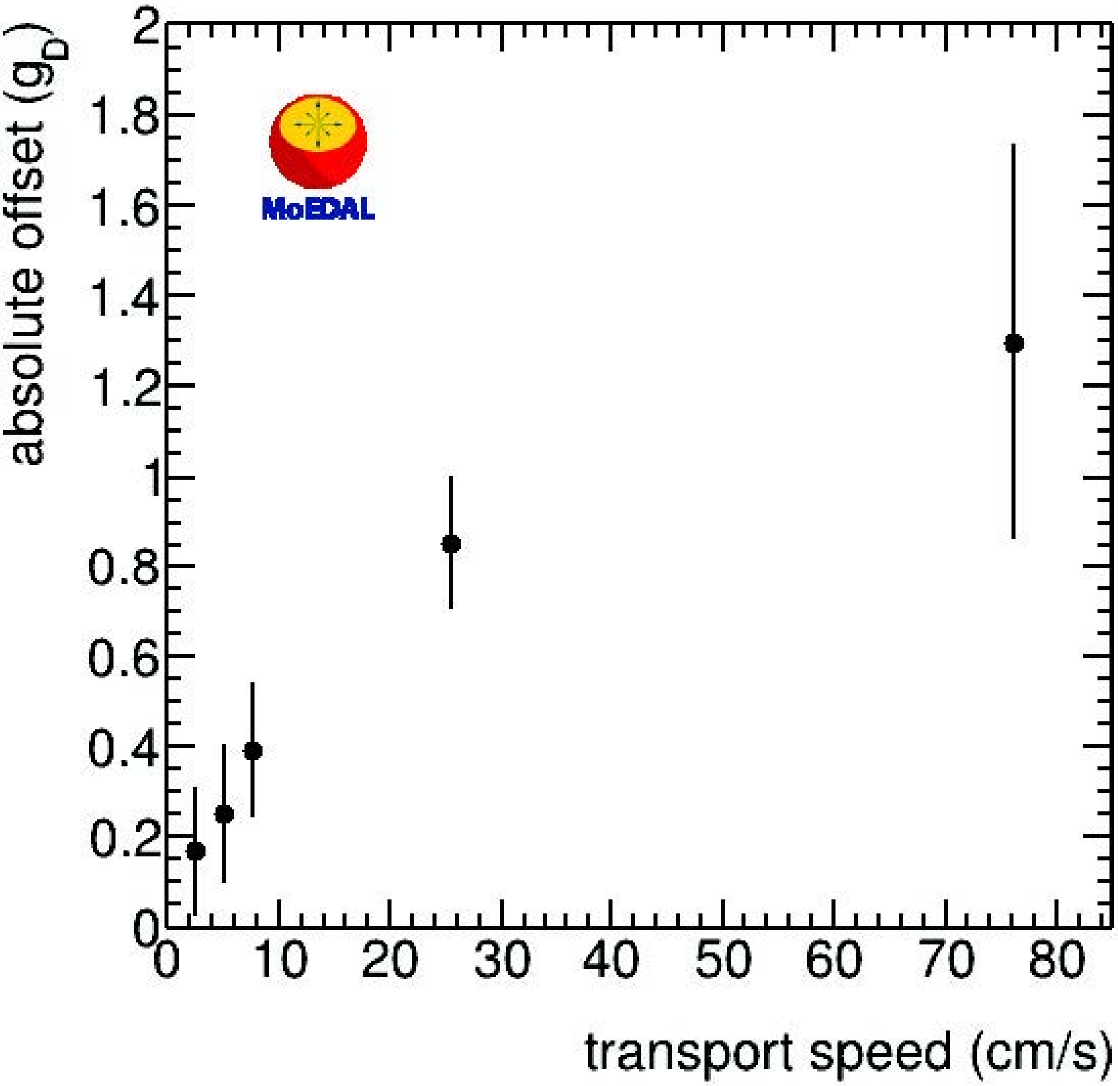

Figure 5.9: Absolute value of the average persistent current offset measured with magnetised calibration samples as a function of speed of transport through the magnetometer sensing region. The offset values are lower than during the MMT scanning as this study was done after an upgrade of the magnetometer aiming at reducing all possible source of noise, in particular from static charge accumulated on the tray thanks to an anti-static brush installed along the sample holder track.

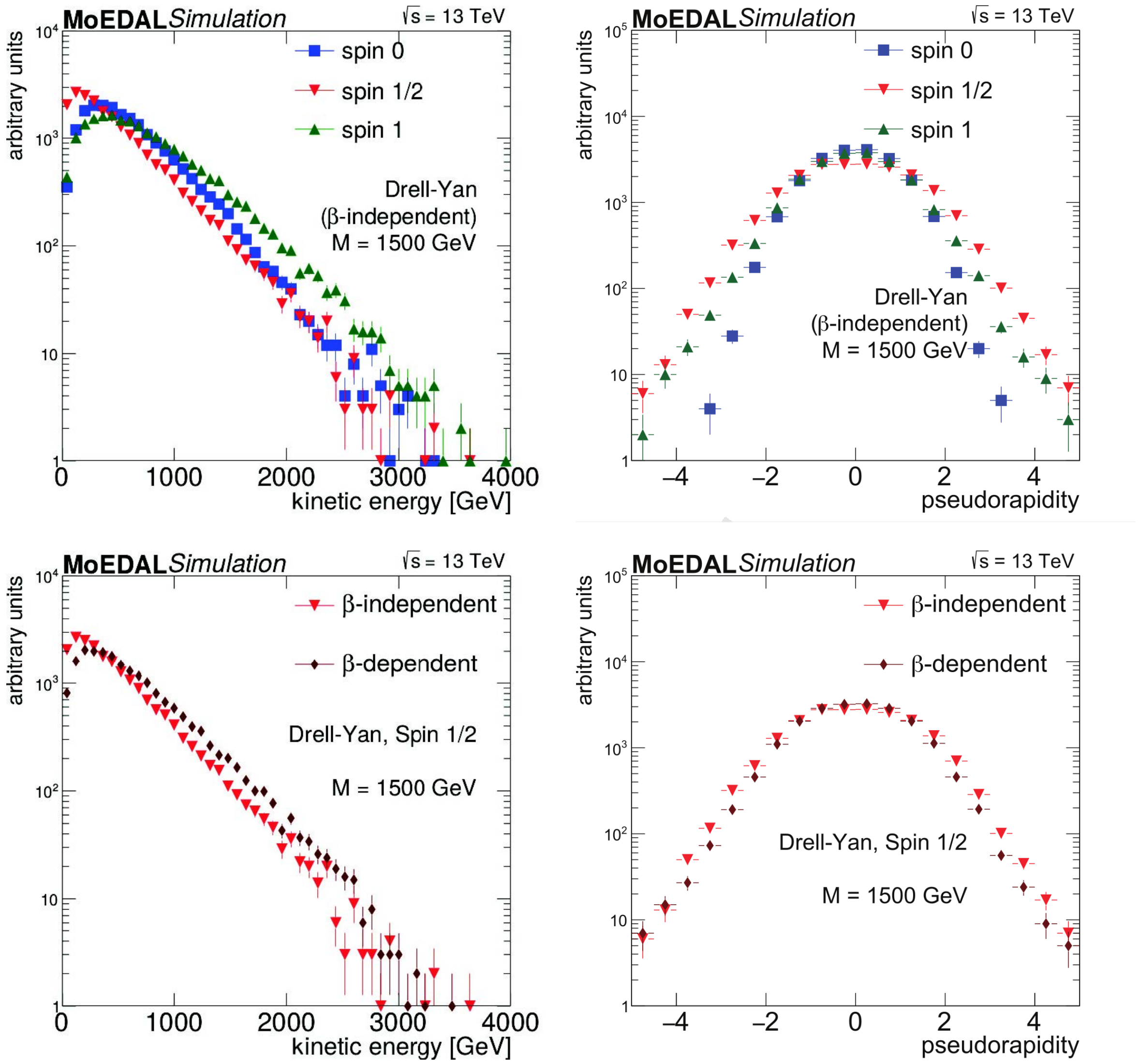

Figure 5.10: Distributions of kinetic energy (left) and pseudorapidity (right) for monopoles with mass 1500 GeV in models of Drell-Yan pair production generated by MadGraph. The top plots show the standard β- independent coupling with different spin values (0, $\frac{1}{2}$, 1) superimposed; and the bottom plots show spin-$\frac{1}{2}$with two types of couplings (β-independent and β-dependent) superimposed.

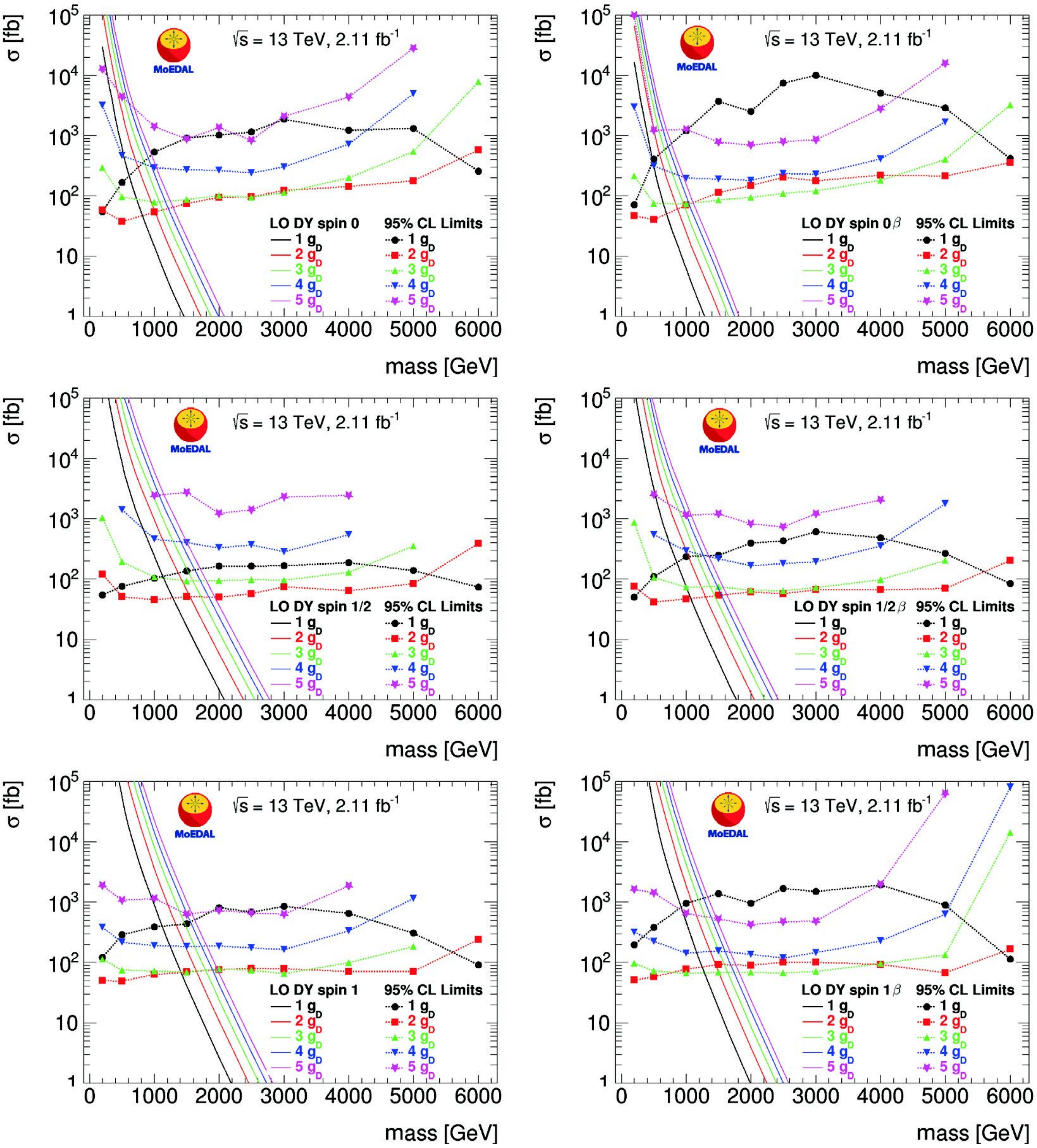

Figure 5.11: Cross-section upper limits at 95% confidence level for the DY monopole pair production model with β-independent (left) and β-dependent (right) couplings in 13 TeV pp collisions as a function of mass for spin-0 (top), spin-$\frac{1}{2}$(middle) and spin-1 (bottom) monopoles. The colours correspond to different monopole charges. Acceptance loss is dominated by monopoles punching through the trapping volume for $|g| = g_{\mathrm{D}}$ while it is dominated by stopping in upstream material for higher charges, explaining the shape difference. The solid lines are cross-section calculations at leading order (LO).

Mass limits [GeV]	$1g_\mathrm{D}$	$2g_\mathrm{D}$	$3g_\mathrm{D}$	$4g_\mathrm{D}$	$5g_\mathrm{D}$
MoEDAL 13 TeV (2016 exposure) [82]					
DY spin-0	600	1000	1080	950	690
DY spin- $\frac{1}{2}$	1110	1540	1600	1400	–
DY spin-1	1110	1640	1790	1710	1570
DY spin-0 β -dep.	490	880	960	890	690
DY spin- $\frac{1}{2}\beta$ -dep.	850	1300	1380	1250	1070
DY spin-1 β -dep.	930	1450	1620	1600	1460
MoEDAL 13 TeV (2015 exposure) [83]					
DY spin-0	460	760	800	650	–
DY spin- $\frac{1}{2}$	890	1250	1260	1100	–
MoEDAL 8 TeV [84]					
DY spin-0	420	600	560	–	–
DY spin- $\frac{1}{2}$	700	920	840	–	–
ATLAS 8 TeV [42]					
DY spin-0	1050	–	–	–	–
DY spin- $\frac{1}{2}$	1340	–	–	–	–
ATLAS 13 TeV [85]					
DY spin-0	1840	1715	–	–	–
DY spin- $\frac{1}{2}$	2365	2125	–	–	–

Table 5.1: 95% confidence level mass limits in models of spin-0, spin-$\frac{1}{2}$and spin-1 monopole pair production in LHC pp collisions. The present results (after 2016 exposure) are interpreted for Drell- Yan production with both β-independent and β- dependent couplings. These limits are based upon cross sections computed at leading order and are only indicative since the monopole coupling to the photon is too large to allow for perturbative calculations.

		Magnetic charge (g_D)				
		1	2	3	4	5
Process/coupling	Spin	95% C.L. mass limits (GeV)				
DY	0	790	1150	1210	1130	...
DY	1/2	1320	1730	1770	1640	...
DY	1	1400	1840	1950	1910	1800
DY β dep.	0	670	1010	1080	1040	900
DY β dep.	1/2	1050	1450	1530	1450	...
DY β dep.	1	1220	1680	1790	1780	1710
DY $+\gamma\gamma$	0	2190	2930	3120	3090	...
DY $+\gamma\gamma$	1/2	2420	3180	3360	3340	...
DY $+\gamma\gamma$	1	2920	3620	3750	3740	...
DY $+\gamma\gamma$ β dep.	0	1500	2300	2590	2640	...
DY $+\gamma\gamma$ β dep.	1/2	1760	2610	2870	2940	2900
DY $+\gamma\gamma$ β dep.	1	2120	3010	3270	3300	3270

Table 5.2: 95% C.L. mass limits [86] in models of spin-0, spin-$\frac{1}{2}$, and spin-1 monopole pair direct production in LHC pp collisions. The present results are interpreted for Drell-Yan and combined DY and photon-fusion production with both β- independent and β-dependent couplings.

Chapter 6

Conclusion

First hypothesised by Pierre Curie in 1894, and included in a quantum theory by Paul Dirac in 1931, the magnetic monopole has been hunted for decades and subject to many dedicated experiments. While the Dirac theory would give an explanation to the electric charge quantisation, monopoles arising as topological defects in Grand Unified Theories or monopoles in recent electro-weak theories with mass in the TeV scale reachable in colliders, give an additional motivation for dedicated searches.

The searches presented in this work with the ATLAS and MoEDAL detectors are using LHC proton-proton collisions with an energy at the centre of mass of 13 TeV, allowing to probe a new regime of masses and charges surpassing all previous searches at colliders. Recent theoretical developments on the so called electro-weak monopoles are predicting monopoles mass within a range attainable at LHC.

The ATLAS search discussed in this thesis is a continuation of the Run 1 search performed on 8 TeV collisions data, and relies on the same analysis strategy. The analysis is based on the magnetic monopoles highly ionising properties and is thus extended to all Highly Ionising Particles, that is in addition to magnetic monopoles, High Electric Charge Objects. Benefiting from a dedicated High Level Trigger and two discriminating variables reconstructed from the TRT and EM calorimeter sub-detectors, the search reaches high efficiencies.

With no observed event in the 34.4 fb^{-1} of 13 TeV collisions data analysed, stringent cross-section upper-limits were set assuming a Drell-Yan production mechanism for both spin-0 and spin-$\frac{1}{2}$HIPs. They are the best limits to date for monopoles searches at colliders of charges $g \leq 2g_D$.

While the MoEDAL experiment is also sensitive to both magnetic monopoles and HECOs, the MoEDAL search detailed in this document is focusing on the trapping detector alone and thus relevant for magnetic monopoles. The MoEDAL magnetic monopoles trapping detector is the first collider experiment using an induction detection method. Magnetic monopoles produced at the LHCb interaction point would be bind to the trapping detector aluminium bars and then detected thanks to a SQUID magnetometer. This approach is limited by the LHCb received luminosity and the MoEDAL acceptance, smaller than the ATLAS one, but however allows to probe charges higher than the one ATLAS is sensitive to.

In the latest trapping detector analysis, published after this work, no magnetic monopoles was observed in the material exposed to 4.0 fb^{-1} of 13 TeV collisions. Cross-sections and mass limits were set assuming Drell-Yan and Photon Fusion production models for magnetic monopoles with a charge up to $5g_D$. The limits surpass existing constraints for charges higher than $2g_D$.

The ATLAS and MoEDAL searches for magnetic monopoles are complementary searches, covering together both lower and higher magnetic charges. An extension to the MoEDAL trapping detector search, using the same induction method on the LHC detectors material and beam-pipe, was started, allowing to probe for magnetic monopoles with very high charges, that would be trapped in the detector material close from the beam or directly in the beam pipe.

Bibliography

[1] S. L. Glashow. “Partial Symmetries of Weak Interactions”. In: *Nucl. Phys.* 22 (1961), pp. 579–588. DOI: `10.1016/0029-5582(61)90469-2`.

[2] Steven Weinberg. “A Model of Leptons”. In: *Phys. Rev. Lett.* 19 (1967), pp. 1264–1266. DOI: `10.1103/PhysRevLett.19.1264`.

[3] Abdus Salam. “Weak and Electromagnetic Interactions”. In: *Conf. Proc.* C680519 (1968), pp. 367–377.

[4] R. Aaij et al. “Observation of $J/\psi p$ Resonances Consistent with Pentaquark States in $\Lambda_b^0 \to J/\psi K^- p$ Decays”. In: *Phys. Rev. Lett.* 115 (7 Aug. 2015), p. 072001. DOI: `10.1103/PhysRevLett.115.072001`. URL: `https://link.aps.org/doi/10.1103/PhysRevLett.115.072001`.

[5] P. Curie. “On the possible existence of magnetic conductivity and free magnetism”. In: *Seances Sic. Phys. (Paris)* (1894), p. 76.

[6] P.A.M. Dirac. “Quantised Singularities in the Electromagnetic Field”. In: *Proc. Roy. Soc.* A 133 (1931), p. 60.

[7] P.A.M. Dirac. “The Theory of Magnetic Poles”. In: *Phys. Rev.* 74 (1948), p. 817. DOI: `10.1103/PhysRev.74.817`.

[8] Y. Aharonov and D. Bohm. “Significance of electromagnetic potentials in the quantum theory”. In: *Phys. Rev.* 115 (1959). [,95(1959)], pp. 485–491. DOI: `10.1103/PhysRev.115.485`.

[9] Julian S. Schwinger. “Magnetic charge and quantum field theory”. In: *Phys. Rev.* 144 (1966), p. 1087. DOI: `10.1103/PhysRev.144.1087`.

[10] Y.M. Cho and D. Maison. “Monopole configuration in Weinberg-Salam model”. In: *Phys. Lett. B* 391 (1997), p. 360. DOI: `10.1016/S0370-2693(96)01492-X`. arXiv: `9601028 [hep-th]`.

[11] Kyoungtae Kimm, J. H. Yoon, and Y. M. Cho. “Finite energy electroweak dyon”. In: *The European Physical Journal C* 75.2 (Feb. 2015). ISSN: 1434-6052. DOI: `10.1140/epjc/s10052-015-3290-3`. URL: `http://dx.doi.org/10.1140/epjc/s10052-015-3290-3`.

[12] G. ’t Hooft. “Magnetic Monopoles in Unified Gauge Theories”. In: *Nucl. Phys. B* 79 (1974), p. 276. DOI: `10.1016/0550-3213(74)90486-6`.

[13] A.M. Polyakov. “Particle Spectrum in the Quantum Field Theory”. In: *JETP Lett.* 20 (1974), p. 194.

[14] Yakov M. Shnir. *Magnetic Monopoles.* Text and Monographs in Physics. Berlin/Heidelberg: Springer, 2005. ISBN: 9783540252771, 9783540290827. DOI: `10.1007/3-540-29082-6`.

[15] Yoichi Kazama, Chen Ning Yang, and Alfred S. Goldhaber. “Scattering of a Dirac particle with charge Ze by a fixed magnetic monopole”. In: *Phys. Rev. D* 15 (8 Apr. 1977), pp. 2287–2299. DOI: `10.1103/PhysRevD.15.2287`. URL: `https://link.aps.org/doi/10.1103/PhysRevD.15.2287`.

[16] S.P. Ahlen. “Stopping-power formula for magnetic monopoles”. In: *Phys. Rev. D* 17 (1978), p. 229.

[17] S.P. Ahlen and K. Kinoshita. “Calculation of the stopping power of very-low-velocity magnetic monopoles”. In: *Phys. Rev. D* 26 (1982), p. 2347. DOI: `10.1103/PhysRevD.26.2347`.

[18] A. De Roeck et al. “Sensitivity of LHC experiments to exotic highly ionising particles”. In: *Eur. Phys. J. C* 72 (2012), p. 1985. DOI: `10.1140/epjc/s10052-012-1985-2`. arXiv: `1112.2999 [hep-ph]`.

[19] John David Jackson. *Classical electrodynamics.* 3rd ed. New York, NY: Wiley, 1999. ISBN: 9780471309321. URL: `http://cdsweb.cern.ch/record/490457`.

[20] S. Burdin, A. Firan, and W. Taylor. "A Search for Magnetic Monopoles at ATLAS". In: *ATL-COM-PHYS-2012-367, https://cds.cern.ch/record/1435748/* (2012).

[21] S. Burdin et al. "Non-collider searches for stable massive particles". In: *Phys. Rept.* 582 (2015), p. 1. DOI: `10.1016/j.physrep.2015.03.004`. arXiv: `1410.1374 [hep-ph]`.

[22] E.N. Parker. In: *Astrophys. J.* 163 (1970), p. 224.

[23] Michael S. Turner, Eugene N. Parker, and T. J. Bogdan. "Magnetic Monopoles and the Survival of Galactic Magnetic Fields". In: *Phys. Rev.* D26 (1982), p. 1296. DOI: `10.1103/PhysRevD.26.1296`.

[24] MACRO Collaboration. "Final results of magnetic monopole searches with the MACRO experiment". In: *Eur. Phys. J. C* 25 (2002), p. 511. DOI: `10.1140/epjc/s2002-01046-9`. arXiv: `hep-ex/0207020 [hep-ex]`.

[25] D. P. Hogan et al. "Relativistic Magnetic Monopole Flux Constraints from RICE". In: *Phys. Rev. D* 78 (2008), p. 075031. DOI: `10.1103/PhysRevD.78.075031`. arXiv: `0806.2129 [astro-ph]`.

[26] ANITA-II Collaboration. "Ultra-Relativistic Magnetic Monopole Search with the ANITA-II Balloon-borne Radio Interferometer". In: *Phys. Rev. D* 83 (2011), p. 023513. DOI: `10.1103/PhysRevD.83.023513`. arXiv: `1008.1282 [astro-ph]`.

[27] ANTARES Collaboration. "Search for Relativistic Magnetic Monopoles with the ANTARES Neutrino Telescope". In: *Astropart. Phys.* 35 (2012), p. 634. DOI: `10.1016/j.astropartphys.2012.02.007`. arXiv: `1110.2656 [astro-ph]`.

[28] IceCube Collaboration. "Search for Relativistic Magnetic Monopoles with IceCube". In: *Phys. Rev. D* 87 (2013), p. 022001. DOI: `10.1103/PhysRevD.87.022001`. arXiv: `1208.4861 [astro-ph.HE]`.

[29] K. Ueno. "Search for GUT monopoles at Super-Kamiokande". In: *Nucl. Phys. Proc. Suppl.* 229-232 (2012), pp. 540–540. DOI: `10.1016/j.nuclphysbps.2012.09.177`.

[30] J.M. Kovalik and J.L. Kirschvink. "New Superconducting Quantum Interface Device Based Constraints on the Abundance of Magnetic Monopoles Trapped in Matter: An Investigation of Deeply Buried Rocks". In: *Phys. Rev. A* 33 (1986), p. 1183. DOI: `10.1103/PhysRevA.33.1183`.

[31] H. Jeon and M.J. Longo. "Search for Magnetic Monopoles Trapped in Matter". In: *Phys. Rev. Lett.* 75 (1995), p. 1443. DOI: `10.1103/PhysRevLett.75.1443`. arXiv: `9508003 [hep-ex]`.

[32] M. Acciarri et al. "Search for anomalous Z –¿ gamma gamma gamma events at LEP". In: *Phys. Lett.* B345 (1995), pp. 609–616. DOI: `10.1016/0370-2693(95)01612-T`.

[33] K. Kinoshita et al. "Search for highly ionizing particles in e^+e^- annihilations at sqrt(s) = 91.1 GeV". In: *Phys. Rev. D* 46 (1992), p. 881. DOI: `10.1103/PhysRevD.46.R881`.

[34] S. D. Drell and Tung-Mow Yan. "Massive Lepton Pair Production in Hadron-Hadron Collisions at High-Energies". In: *Phys. Rev. Lett.* 25 (1970). [Erratum: Phys. Rev. Lett.25,902(1970)], pp. 316–320. DOI: `10.1103/PhysRevLett.25.316,10.1103/PhysRevLett.25.902.2`.

[35] J.L. Pinfold et al. "A Search for highly ionizing particles produced at the OPAL intersection point at LEP". In: *Phys. Lett. B* 316 (1993), p. 407. DOI: `10.1016/0370-2693(93)90346-J`.

[36] OPAL Collaboration. "Search for Dirac magnetic monopoles in e^+e^- collisions with the OPAL detector at LEP2". In: *Phys. Lett. B* 663 (2008), p. 37. DOI: `10.1016/j.physletb.2008.03.057`. arXiv: `0707.0404 [hep-ex]`.

[37] D0 Collaboration. "Search for Heavy Pointlike Dirac Monopoles". In: *Phys. Rev. Lett.* 81 (1998), p. 524. DOI: `10.1103/PhysRevLett.81.524`. arXiv: `9803023 [hep-ex]`.

[38] G.R. Kalbfleisch et al. "Limits on production of magnetic monopoles utilizing samples from the D0 and CDF detectors at the Tevatron". In: *Phys. Rev. D* 69 (2004), p. 052002. DOI: `10.1103/PhysRevD.69.052002`. arXiv: `0306045 [hep-ex]`.

[39] CDF Collaboration. "Direct search for Dirac magnetic monopoles in $p\bar{p}$ collisions at $\sqrt{s} =$ 1.96 TeV". In: *Phys. Rev. Lett.* 96 (2006), p. 201801. DOI: `10.1103/PhysRevLett.96.201801`. arXiv: `0509015 [hep-ex]`.

[40] H1 Collaboration. "A direct search for stable magnetic monopoles produced in positron-proton collisions at HERA". In: *Eur. Phys. J. C* 41 (2005), p. 133. DOI: `10.1140/epjc/s2005-02201-6`. arXiv: `0501039 [hep-ex]`.

[41] ATLAS Collaboration. "Search for magnetic monopoles in sqrt(s) = 7 TeV pp collisions with the ATLAS detector". In: *Phys. Rev. Lett.* 109 (2012), p. 261803. DOI: `10.1103/PhysRevLett.109.261803`. arXiv: `1207.6411 [hep-ex]`.

[42] ATLAS Collaboration. "Search for magnetic monopoles and stable particles with high electric charges in 8 TeV *pp* collisions with the ATLAS detector". In: *Phys. Rev. D* 93.5 (2016), p. 052009. DOI: `10.1103/PhysRevD.93.052009`. arXiv: `1509.08059 [hep-ex]`.

[43] K. Bendtz et al. "Search in 8 TeV proton-proton collisions with the MoEDAL monopole-trapping test array". In: *Proceedings of the 14th ICATPP Conference* (2014). arXiv: `1311.6940 [physics.ins-det]`.

[44] G. Aad et al. "The ATLAS Experiment at the CERN Large Hadron Collider". In: *JINST* 3 (2008), S08003. DOI: `10.1088/1748-0221/3/08/S08003`.

[45] S. Chatrchyan et al. "The CMS Experiment at the CERN LHC". In: *JINST* 3 (2008), S08004. DOI: `10.1088/1748-0221/3/08/S08004`.

[46] K. Aamodt et al. "The ALICE experiment at the CERN LHC". In: *JINST* 3 (2008), S08002. DOI: `10.1088/1748-0221/3/08/S08002`.

[47] M Capeans et al. *ATLAS Insertable B-Layer Technical Design Report.* Tech. rep. CERN-LHCC-2010-013. ATLAS-TDR-19. Sept. 2010. URL: `https://cds.cern.ch/record/1291633`.

[48] Pierfrancesco Butti. *Advanced alignment of the ATLAS tracking system.* Tech. rep. ATL-PHYS-PROC-2014-231. Geneva: CERN, Oct. 2014. DOI: `10.1016/j.nuclphysbps.2015.09.449`. URL: `https://cds.cern.ch/record/1957194`.

[49] C. Patrignani et al. "Review of Particle Physics". In: *Chin. Phys.* C40.10 (2016), p. 100001. DOI: `10.1088/1674-1137/40/10/100001`.

[50] Christian W. Fabjan and Fabiola Gianotti. “Calorimetry for particle physics”. In: *Rev. Mod. Phys.* 75 (4 Oct. 2003), pp. 1243–1286. DOI: `10.1103/RevModPhys.75.1243`. URL: `https://link.aps.org/doi/10.1103/RevModPhys.75.1243`.

[51] Zhaoxia Meng. “Performance of the ATLAS liquid argon calorimeter”. In: *Physics at the LHC2010. Proceedings, 5th Conference, PLHC2010, Hamburg, Germany, June 7-12, 2010.* 2010, pp. 406–408. DOI: `10.3204/DESY-PROC-2010-01/meng`.

[52] J E Mdhluli, B Mellado, and E Sideras-Haddad. “Neutron irradiation and damage assessment of plastic scintillators of the Tile Calorimeter”. In: *Journal of Physics: Conference Series* 802 (Jan. 2017), p. 012008. DOI: `10.1088/1742-6596/802/1/012008`. URL: `https://doi.org/10.1088%2F1742-6596%2F802%2F1%2F012008`.

[53] F Carrió et al. “The sROD module for the ATLAS Tile Calorimeter Phase-II Upgrade Demonstrator”. In: *Journal of Instrumentation* 9.02 (Feb. 2014), pp. C02019–C02019. DOI: `10.1088/1748-0221/9/02/c02019`. URL: `https://doi.org/10.1088%2F1748-0221%2F9%2F02%2Fc02019`.

[54] A Artamonov et al. “The ATLAS Forward Calorimeter”. In: *Journal of Instrumentation* 3.02 (Feb. 2008), P02010–P02010. DOI: `10.1088/1748-0221/3/02/p02010`. URL: `https://doi.org/10.1088%2F1748-0221%2F3%2F02%2Fp02010`.

[55] Giordano Cattani and. “The Resistive Plate Chambers of the ATLAS experiment: performance studies”. In: *Journal of Physics: Conference Series* 280 (Feb. 2011), p. 012001. DOI: `10.1088/1742-6596/280/1/012001`. URL: `https://doi.org/10.1088%2F1742-6596%2F280%2F1%2F012001`.

[56] Koichi Nagai. “Thin gap chambers in ATLAS”. In: *Nuclear Instruments and Methods in Physics Research Section A: Accelerators, Spectrometers, Detectors and Associated Equipment* 384.1 (1996). BEAUTY ’96, pp. 219–221. ISSN: 0168-9002. DOI: `https://doi.org/10.1016/S0168-9002(96)01065-0`. URL: `http://www.sciencedirect.com/science/article/pii/S0168900296010650`.

[57] S. Majewski et al. “A thin multiwire chamber operating in the high multiplication mode”. In: *Nuclear Instruments and Methods in Physics Research* 217.1 (1983), pp. 265–271.

ISSN: 0167-5087. DOI: `https://doi.org/10.1016/0167-5087(83)90146-1`. URL: `http://www.sciencedirect.com/science/article/pii/0167508783901461`.

[58] Morad Aaboud et al. “Performance of the ATLAS Trigger System in 2015”. In: *Eur. Phys. J.* C77.5 (2017), p. 317. DOI: `10.1140/epjc/s10052-017-4852-3`. arXiv: `1611.09661 [hep-ex]`.

[59] MoEDAL Collaboration. “The Physics Programme Of The MoEDAL Experiment At The LHC”. In: *Int. J. Mod. Phys. A* 29 (2014), p. 1430050. DOI: `10.1142/S0217751X14300506`. arXiv: `1405.7662 [hep-ph]`.

[60] LHCb Collaboration. “The LHCb Detector at the LHC”. In: *JINST* 3 (2008), S08005. DOI: `10.1088/1748-0221/3/08/S08005`.

[61] *Particle Identification Performance of the ATLAS Transition Radiation Tracker.* Tech. rep. ATLAS-CONF-2011-128. Geneva: CERN, Sept. 2011. URL: `http://cds.cern.ch/record/1383793`.

[62] A Maevskiy. *Implementation of Argon-Based Gas in the TRT Simulation.* Tech. rep. Geneva: CERN, June 2015. URL: `https://dl.dropboxusercontent.com/u/8760566/ArgonAthenaSimulation2014-3.pdf`.

[63] S Fratina and E Klinkby. *The Geometry of the ATLAS Transition Radiation Tracker.* Tech. rep. ATL-COM-INDET-2010-002. Geneva: CERN, Jan. 2010. URL: `https://cds.cern.ch/record/1232064`.

[64] J. Alwall et al. “The automated computation of tree-level and next-to-leading order differential cross sections, and their matching to parton shower simulations”. In: *JHEP* 7 (2014), p. 79. DOI: `10.1007/JHEP07(2014)079`. arXiv: `1405.0301 [hep-ph]`.

[65] T. Sjostrand, S. Mrenna, and P. Skands. “PYTHIA 6.4 Physics and Manual”. In: *JHEP* 05 (2006), p. 026. DOI: `10.1088/1126-6708/2006/05/026`. arXiv: `0603175 [hep-ph]`.

[66] T. Sjostrand, S. Mrenna, and P. Skands. “A brief introduction to PYTHIA 8.1”. In: *Comput. Phys. Commun.* 178 (2008), p. 852. DOI: `10.1016/j.cpc.2008.01.036`. arXiv: `0710.3820 [hep-ph]`.

[67] ATLAS Collaboration. “A Search for Magnetic Monopoles and Exotic Long-lived Particles with Large Electric Charge at ATLAS”. In: *ATL-COM-PHYS-2014-538, https://cds.cern.ch/record/1* (2015).

[68] S. Burdin and W. Taylor. “A Correction to Birks’ Law in LAr for Highly Ionizing Particles”. In: *ATL-COM-LARG-2011-001* ().

[69] S. Burdin, M. Horbatsch, and W. Taylor. “A correction to Birks’ Law in liquid argon ionization chamber simulations for highly ionizing particles”. In: *Nucl. Instrum. Meth. A* 664 (2012), p. 111. DOI: `10.1016/j.nima.2011.10.044`.

[70] S. Schaepe. “Commissioning and performance of the ATLAS Transition Radiation Tracker with first high energy pp and Pb-Pb collisions at LHC”. In: (2011). DOI: `10.1109/ANIMMA.2011.6172828`.

[71] R. Koniuk, E. Noordeh, and W. Taylor. “Extension of the Magnetic Monopole Search to Include Scalar Monopoles”. In: *ATL-COM-PHYS-2014-1417, https://cds.cern.ch/record/1966026/* (2014).

[72] S. Burdin et al. “Level-2 Trigger for Highly Ionising Particle Searches”. In: *ATLAS-COM-DAQ-2013-008* ().

[73] ATLAS Collaboration. “Topological cell clustering in the ATLAS calorimeters and its performance in LHC Run 1”. In: *Eur. Phys. J. C* 77 (2017), p. 490. DOI: `10.1140/epjc/s10052-017-5004-5`. arXiv: `1603.02934 [hep-ex]`.

[74] Read, A. “ABCD Method”. In: *https://twiki.cern.ch/twiki/pub/AtlasProtected/ATLASStatisticsFAQ* ().

[75] Buttinger, W. “https://gitlab.cern.ch/will/TRooFit”. In: ().

[76] S.P. Ahlen. “Theoretical and experimental aspects of the energy loss of relativistic heavily ionizing particles”. In: *Rev. Mod. Phys.* 52 (1980), p. 121.

[77] Geant4 Collaboration. “Geant4 developments and applications”. In: *IEEE Trans. Nucl. Sci.* 53 (2006), p. 270. DOI: `10.1109/TNS.2006.869826`.

[78] J. Labbé and R. Ishmukhametov. In: *ATL-LARG-INT-2009-004* ().

[79] "Luminosity determination in *pp* collisions at $\sqrt{s} = 13$ TeV using the ATLAS detector at the LHC". In: (June 2019).

[80] MoEDAL Collaboration. *Technical Design Report of the Moedal Experiment.* Tech. rep. 2009.

[81] A. De Roeck et al. "Development of a magnetometer-based search strategy for stopped monopoles at the Large Hadron Collider". In: *The European Physical Journal C* 72.12 (2012), p. 2212. DOI: `10.1140/epjc/s10052-012-2212-x`. URL: `https://doi.org/10.1140/epjc/s10052-012-2212-x`.

[82] B. Acharya et al. "Search for magnetic monopoles with the MoEDAL forward trapping detector in 2.11 fb^{-1} of 13 TeV proton-proton collisions at the LHC". In: *Phys. Lett. B* 782 (2018), pp. 510–516. DOI: `10.1016/j.physletb.2018.05.069`. arXiv: `1712.09849 [hep-ex]`.

[83] MoEDAL Collaboration. "Search for magnetic monopoles with the MoEDAL forward trapping detector in 13 TeV proton-proton collisions at the LHC". In: *Phys. Rev. Lett.* 118.6 (2017), p. 061801. DOI: `10.1103/PhysRevLett.118.061801`. arXiv: `1611.06817 [hep-ex]`.

[84] MoEDAL Collaboration. "Search for magnetic monopoles with the MoEDAL prototype trapping detector in 8 TeV proton-proton collisions at the LHC". In: *JHEP* 08 (2016), p. 067. DOI: `10.1007/JHEP08(2016)067`. arXiv: `1604.06645 [hep-ex]`.

[85] G. Aad et al. "Search for Magnetic Monopoles and Stable High-Electric-Charge Objects in 13 TeV Proton-Proton Collisions with the ATLAS Detector". In: *Physical Review Letters* 124.3 (Jan. 2020). ISSN: 1079-7114. DOI: `10.1103/physrevlett.124.031802`. URL: `http://dx.doi.org/10.1103/PhysRevLett.124.031802`.

[86] B. Acharya et al. "Magnetic Monopole Search with the Full MoEDAL Trapping Detector in 13 TeV pp Collisions Interpreted in Photon-Fusion and Drell-Yan Production". In: *Phys. Rev. Lett.* 123.2 (2019), p. 021802. DOI: `10.1103/PhysRevLett.123.021802`. arXiv: `1903.08491 [hep-ex]`.

Auxiliary material

A Kinematic Distributions for Drell-Yan Pair-Produced HIPs

Generator-level kinematic distributions for Drell-Yan pair-produced events for various choices of HIP masses (after the generator-level p_T cuts are applied) are shown in Figs. 1–3 for $|z| = 20$ spin-$\frac{1}{2}$, spin-0 and spin-1 HECOs, respectively.

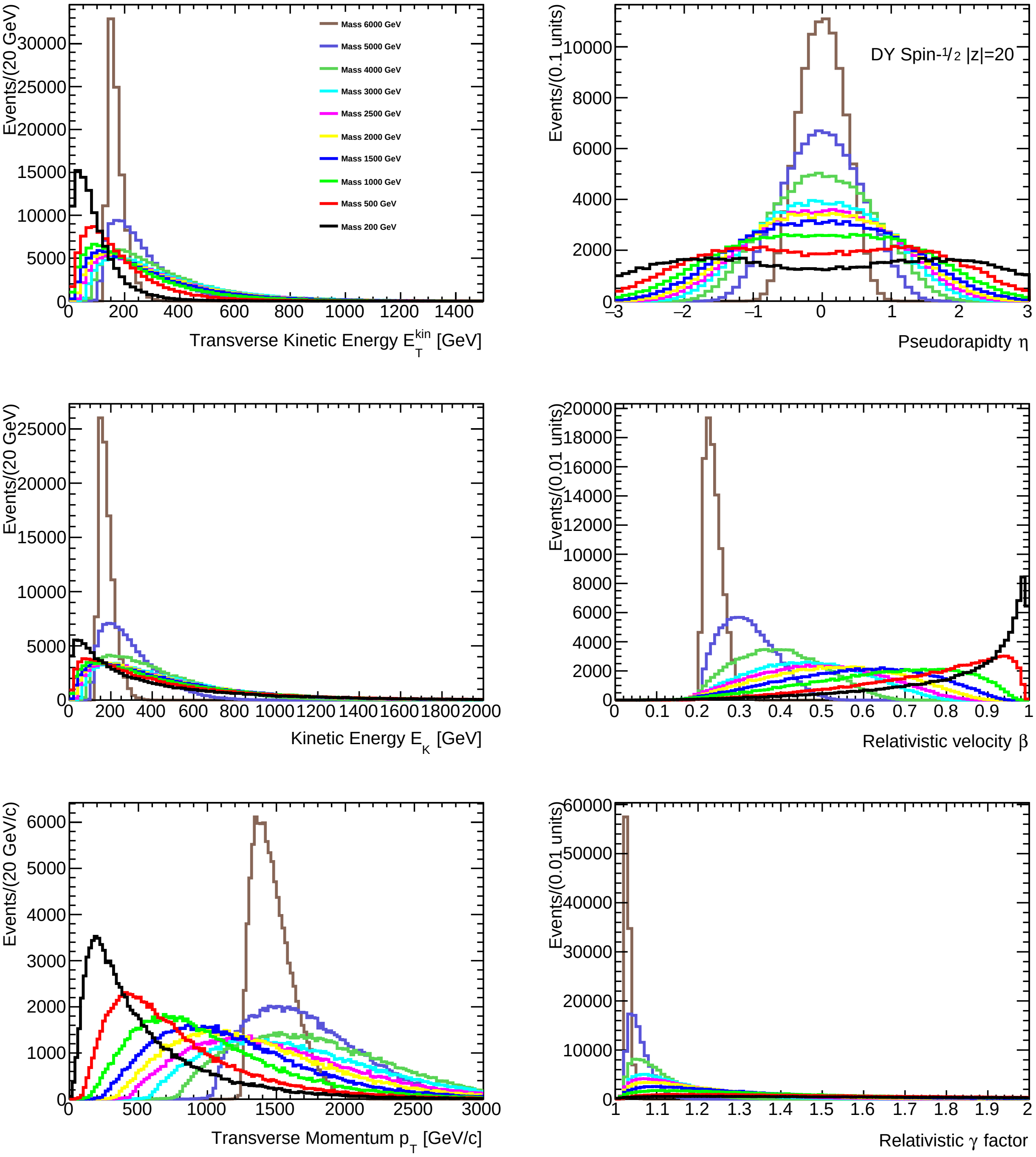

Figure 1: Generator-level transverse kinetic energy E_T^{kin}, pseudorapidity η, kinetic energy E_K, relativistic velocity β, transverse momentum p_T, and relativistic γ factor, distributions for Drell-Yan pair-produced charge $|z| = 20$ spin-$\frac{1}{2}$ HECOs with various masses (after a minimum p_T cut is applied).

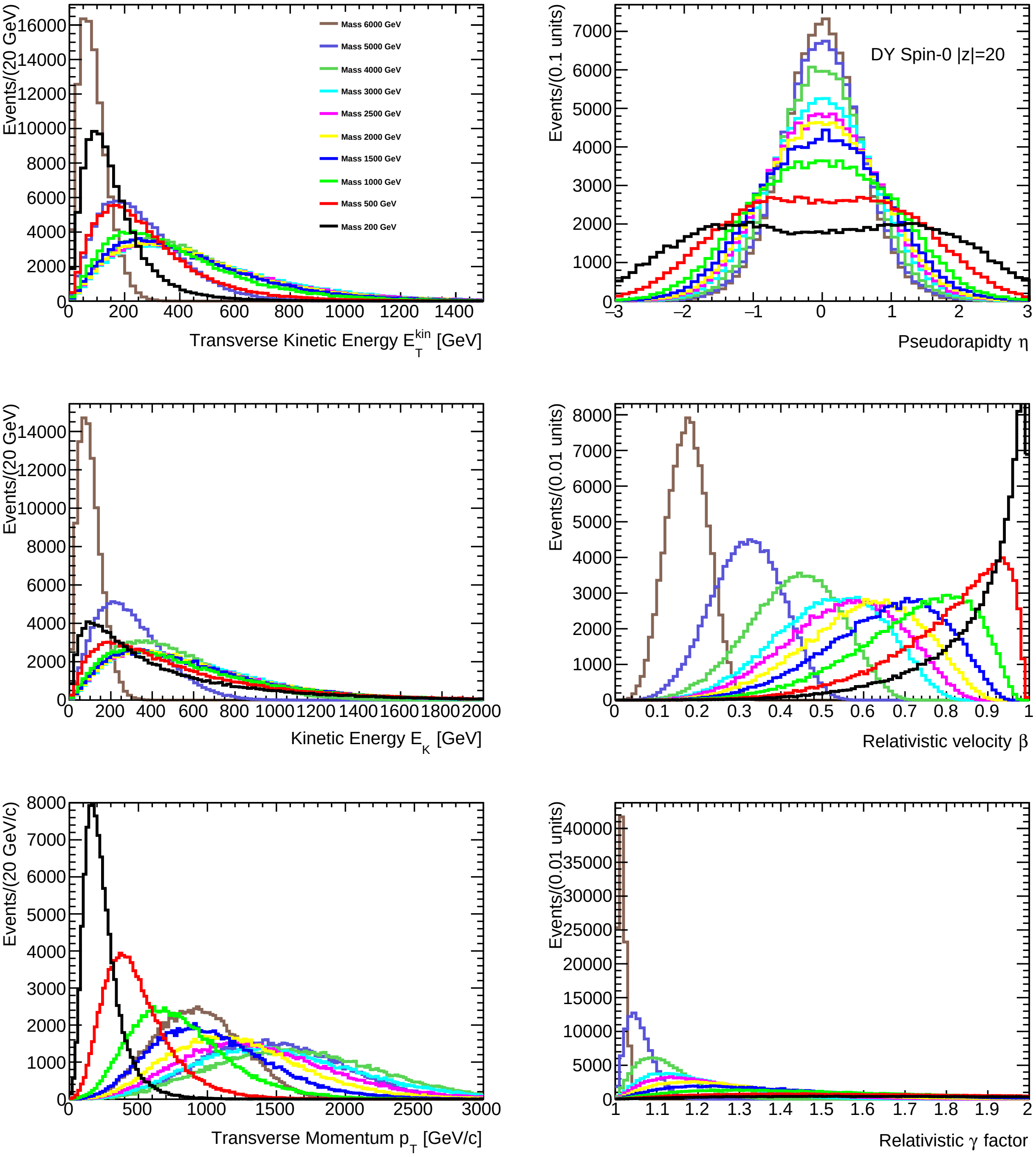

Figure 2: Generator-level transverse kinetic energy E_T^{kin}, pseudorapidity η, kinetic energy E_K, relativistic velocity β, transverse momentum p_T, and relativistic γ factor, distributions for Drell-Yan pair-produced charge $|z| = 20$ spin-0 HECOs with various masses (after a minimum p_T cut is applied).

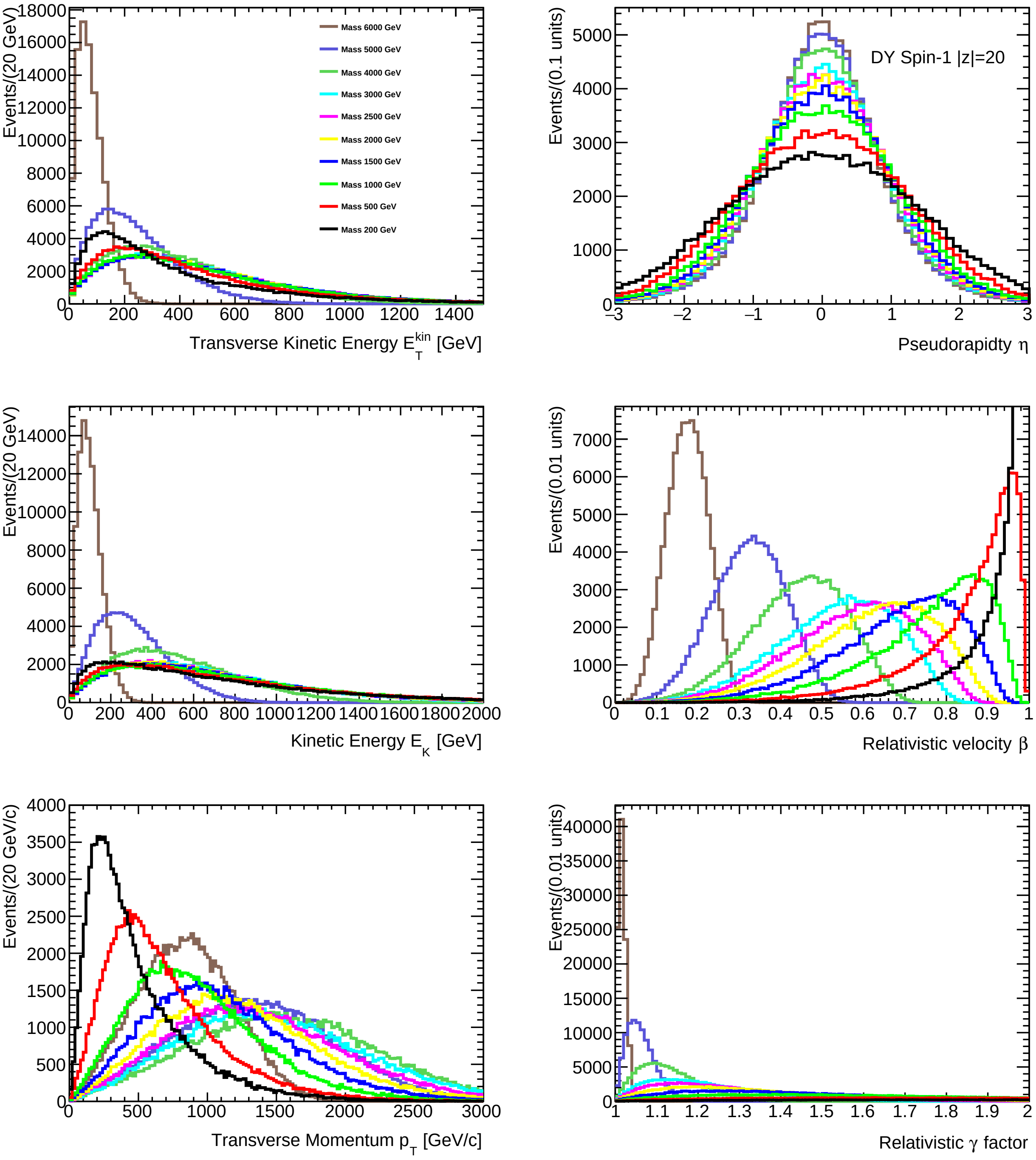

Figure 3: Generator-level transverse kinetic energy E_T^{kin}, pseudorapidity η, kinetic energy E_K, relativistic velocity β, transverse momentum p_T, and relativistic γ factor, distributions for Drell-Yan pair-produced charge $|z| = 20$ spin-1 HECOs with various masses (after a minimum p_T cut is applied).

B Signal leakage for Drell-Yan samples in regions B, C and D

Sample	A	B	C	D	A+B+C+D	Total
$\lvert g\rvert = 1\ g_\mathrm{D}$						
M = 200 GeV	2933	8	32	0	2973	42000
M = 500 GeV	9056	36	72	0	9164	46000
M = 1000 GeV	14991	46	136	0	15173	47000
M = 1500 GeV	18278	59	349	1	18687	48000
M = 2000 GeV	20322	79	726	3	21130	50000
M = 2500 GeV	19846	82	1126	10	21064	50000
M = 3000 GeV	23506	90	1916	12	25524	47000
M = 4000 GeV	23678	111	3889	33	27711	50000
M = 5000 GeV	12706	74	3608	33	16421	50000
M = 6000 GeV	90	3	65	1	159	50000
$\lvert g\rvert = 2\ g_\mathrm{D}$						
M = 1500 GeV	152	0	3	0	155	4000
M = 2000 GeV	866	1	17	0	884	18000
M = 2500 GeV	414	0	6	0	420	8000
M = 3000 GeV	1655	2	34	0	1691	16000
M = 4000 GeV	922	1	39	0	962	14500
M = 5000 GeV	406	1	37	0	444	39500
$\lvert z\rvert = 20$						
M = 200 GeV	3526	186	1709	64	5485	50000
M = 500 GeV	9285	411	3090	98	12884	49000
M = 1000 GeV	13962	431	4457	110	18960	50000
M = 1500 GeV	16767	373	5455	120	22715	50000

Continued on next page

Table 1: Number of Drell-Yan signal events in the different regions.

Sample	A	B	C	D	A+B+C+D	Total
M = 2000 GeV	18010	340	6039	92	24481	50000
M = 2500 GeV	17543	257	6014	111	23925	48000
M = 3000 GeV	18637	221	6647	84	25589	48000
M = 4000 GeV	17755	108	6427	54	24344	50000
M = 5000 GeV	10000	27	4194	12	14233	50000
M = 6000 GeV	50	0	23	0	73	50000
$\|z\| = 40$						
M = 200 GeV	4254	30	302	0	4586	50000
M = 500 GeV	10975	41	268	0	11284	48000
M = 1000 GeV	16182	31	374	2	16589	50000
M = 1500 GeV	16801	34	416	1	17252	50000
M = 2000 GeV	15674	27	511	1	16213	50000
M = 2500 GeV	14130	19	608	1	14758	50000
M = 3000 GeV	12766	22	668	2	13458	49000
M = 4000 GeV	7369	8	584	1	7962	50000
M = 5000 GeV	575	0	55	0	630	50000
$\|z\| = 60$						
M = 200 GeV	4348	17	119	0	4484	48000
M = 500 GeV	7640	10	109	0	7759	50000
M = 1000 GeV	9200	10	101	2	9313	49000
M = 1500 GeV	9043	14	97	0	9154	50000
M = 2000 GeV	7298	9	93	1	7401	50000
M = 2500 GeV	6892	2	100	0	6994	50000
M = 3000 GeV	5300	5	97	0	5402	48000
M = 4000 GeV	1351	1	41	1	1394	50000
M = 5000 GeV	4	0	0	0	4	50000

Continued on next page

Table 1: Number of Drell-Yan signal events in the different regions.

Sample	A	B	C	D	A+B+C+D	Total
M = 6000 GeV	0	0	0	0	0	50000
$\|z\| = 80$						
M = 200 GeV	2437	6	48	0	2491	50000
M = 500 GeV	3261	2	35	0	3298	49000
M = 1000 GeV	4252	6	57	0	4315	45000
M = 1500 GeV	4233	4	34	0	4271	47000
M = 2000 GeV	3070	2	31	0	3103	47000
M = 2500 GeV	2107	1	34	0	2142	49000
M = 3000 GeV	1315	2	29	0	1346	48000
M = 4000 GeV	127	0	5	1	133	49000
M = 5000 GeV	0	0	0	0	0	50000
M = 6000 GeV	0	0	0	0	0	50000

Table 1: Number of Drell-Yan signal events in the different regions.

C Transfer factor study for different eta slices and link to analysis variables

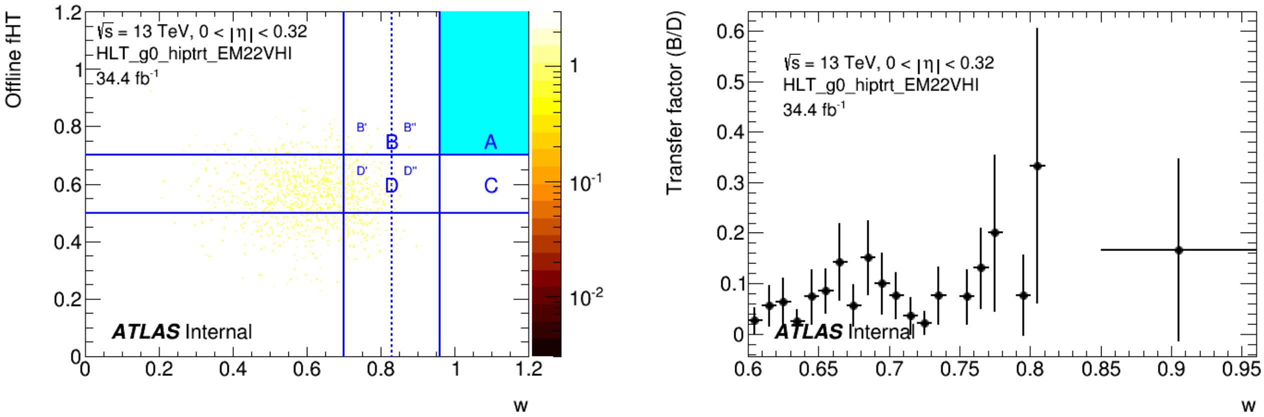

(a) fHT vs w

(b) Transfer factor.

Figure 4: Transfer factor for region $|\eta| < 0.32$.

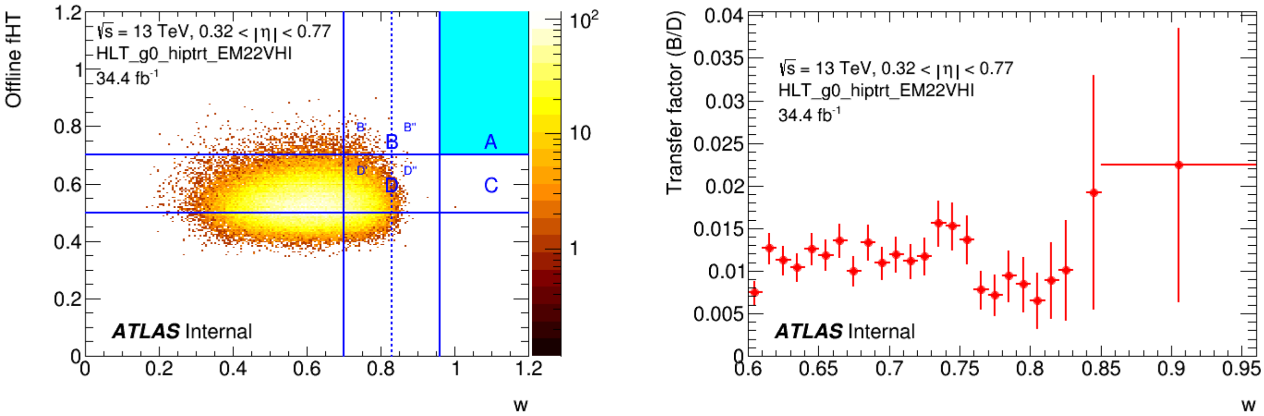

(a) fHT vs w

(b) Transfer factor.

Figure 5: Transfer factor for region $0.32 < |\eta| < 0.77$.

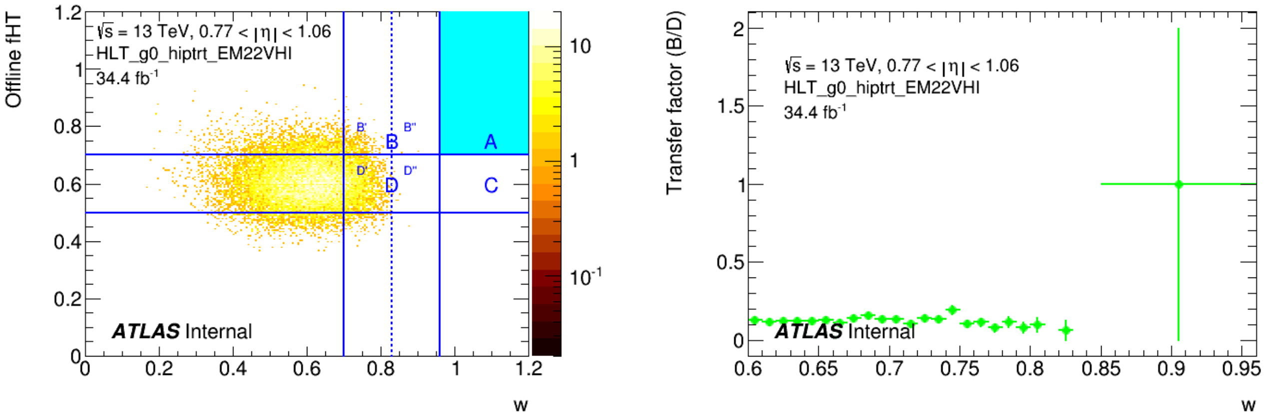

(a) fHT vs w

(b) Transfer factor.

Figure 6: Transfer factor for region $0.77 < |\eta| < 1.06$.

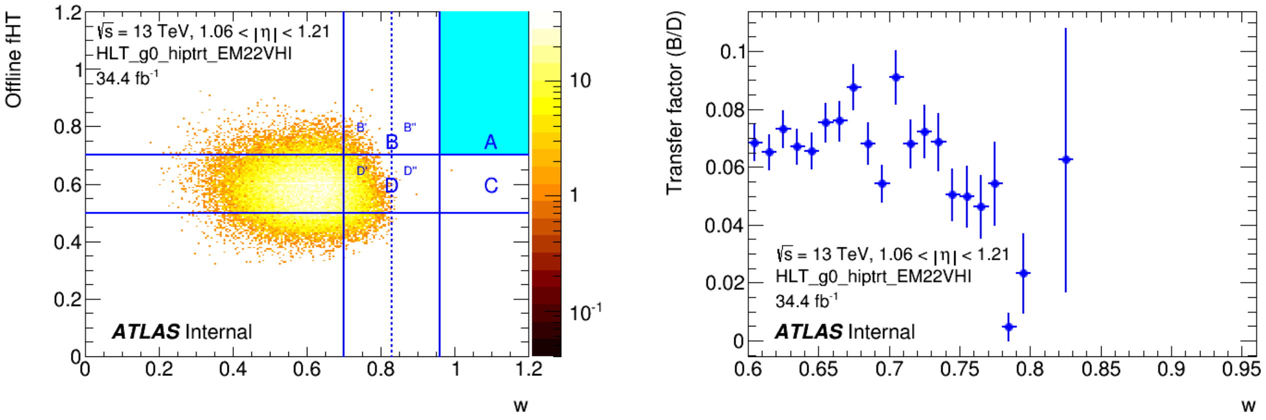

(a) fHT vs w

(b) Transfer factor.

Figure 7: Transfer factor for region $1.06 < |\eta| < 1.21$.

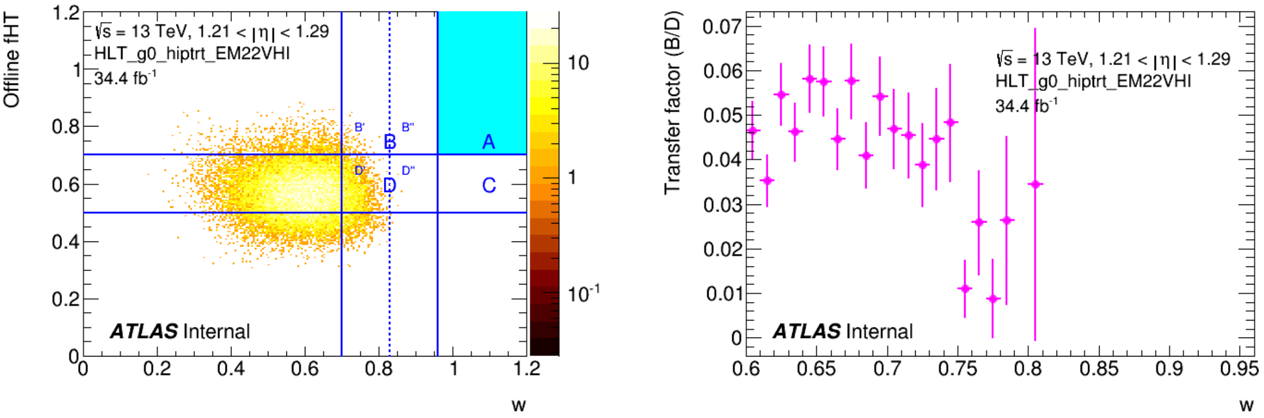

(a) fHT vs w (b) Transfer factor.

Figure 8: Transfer factor for region $1.21 < |\eta| < 1.29$.

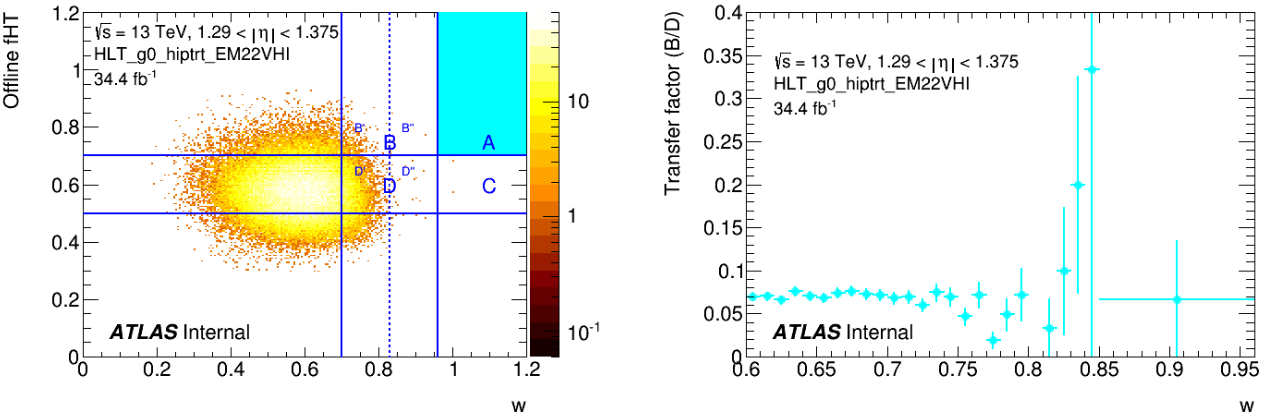

(a) fHT vs w (b) Transfer factor.

Figure 9: Transfer factor for region $1.29 < |\eta| < 1.375$.

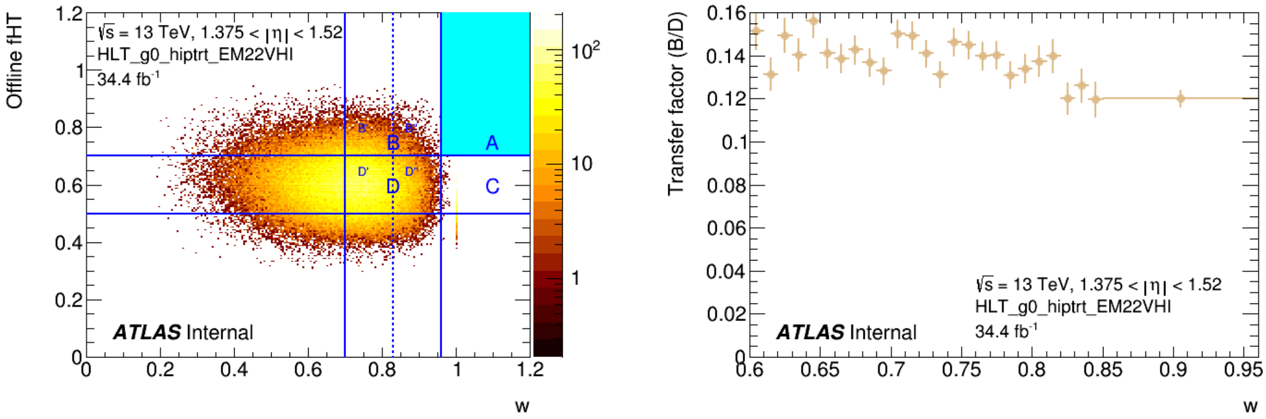

(a) fHT vs w

(b) Transfer factor.

Figure 10: Transfer factor for region $1.375 < |\eta| < 1.52$.

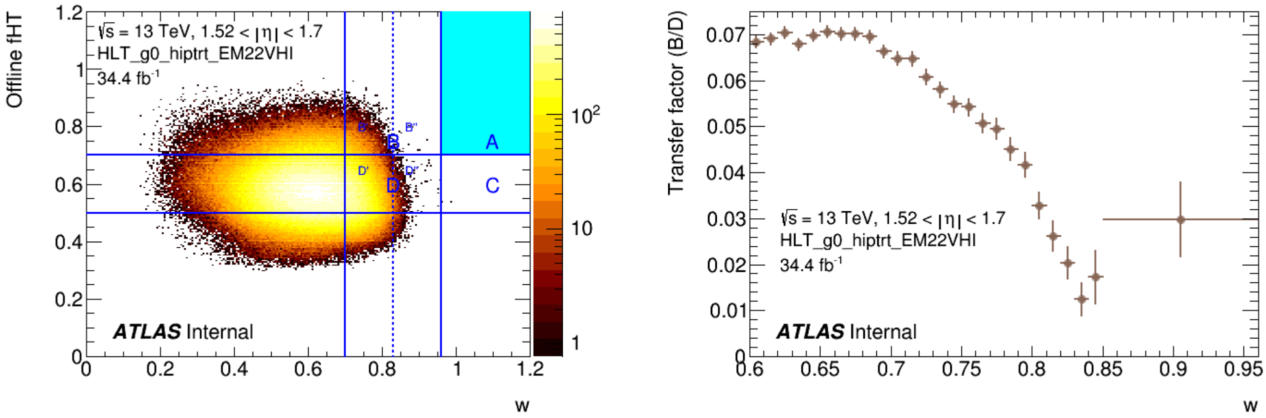

(a) fHT vs w

(b) Transfer factor.

Figure 11: Transfer factor for region $1.52 < |\eta| < 1.7$.

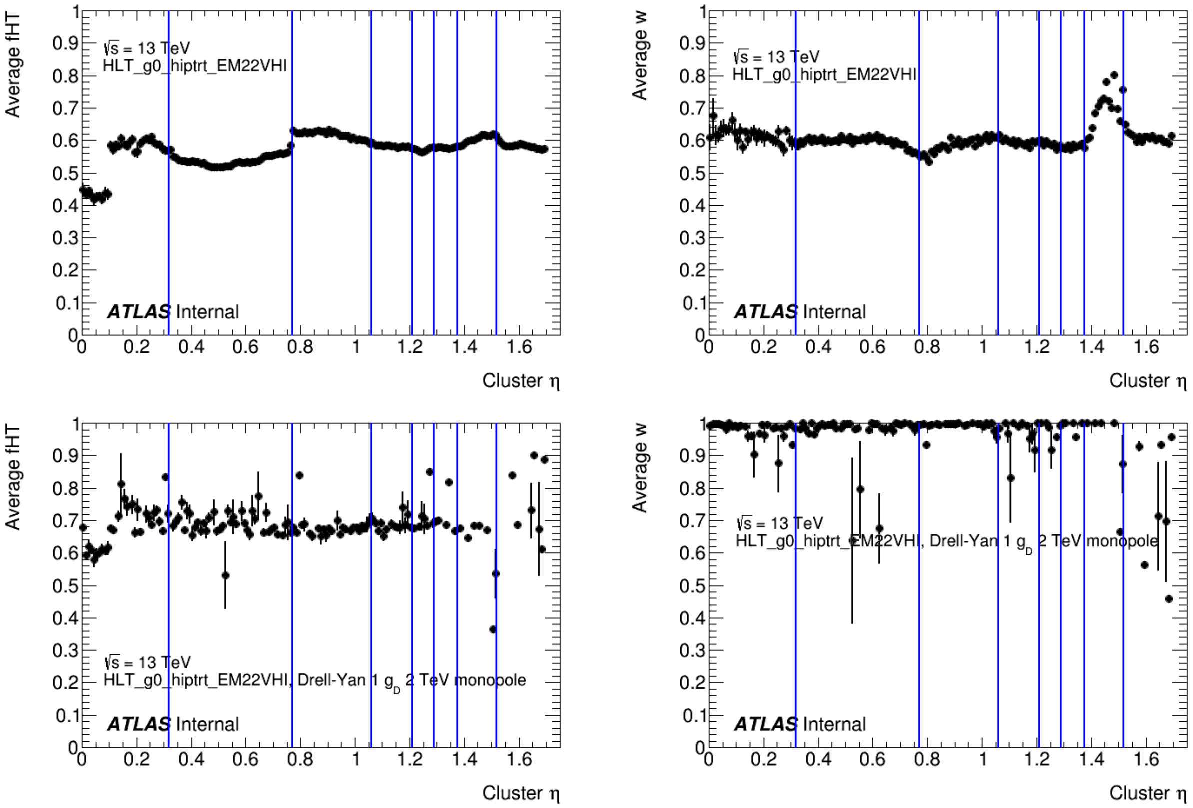

Figure 12: Profile histograms of f_{HT} and w versus $|\eta|$

D Complete set of efficiency maps

Below are presented the complete set of efficiency maps vs transverse kinetic energy and pseudo rapidity. The maps were made using the fully simulated Monte Carlo single particle samples described in Section 4.1.1, for HECO and monopoles of all mass and charge points. Selection cuts were applied with the criteria described in Section 4.2.

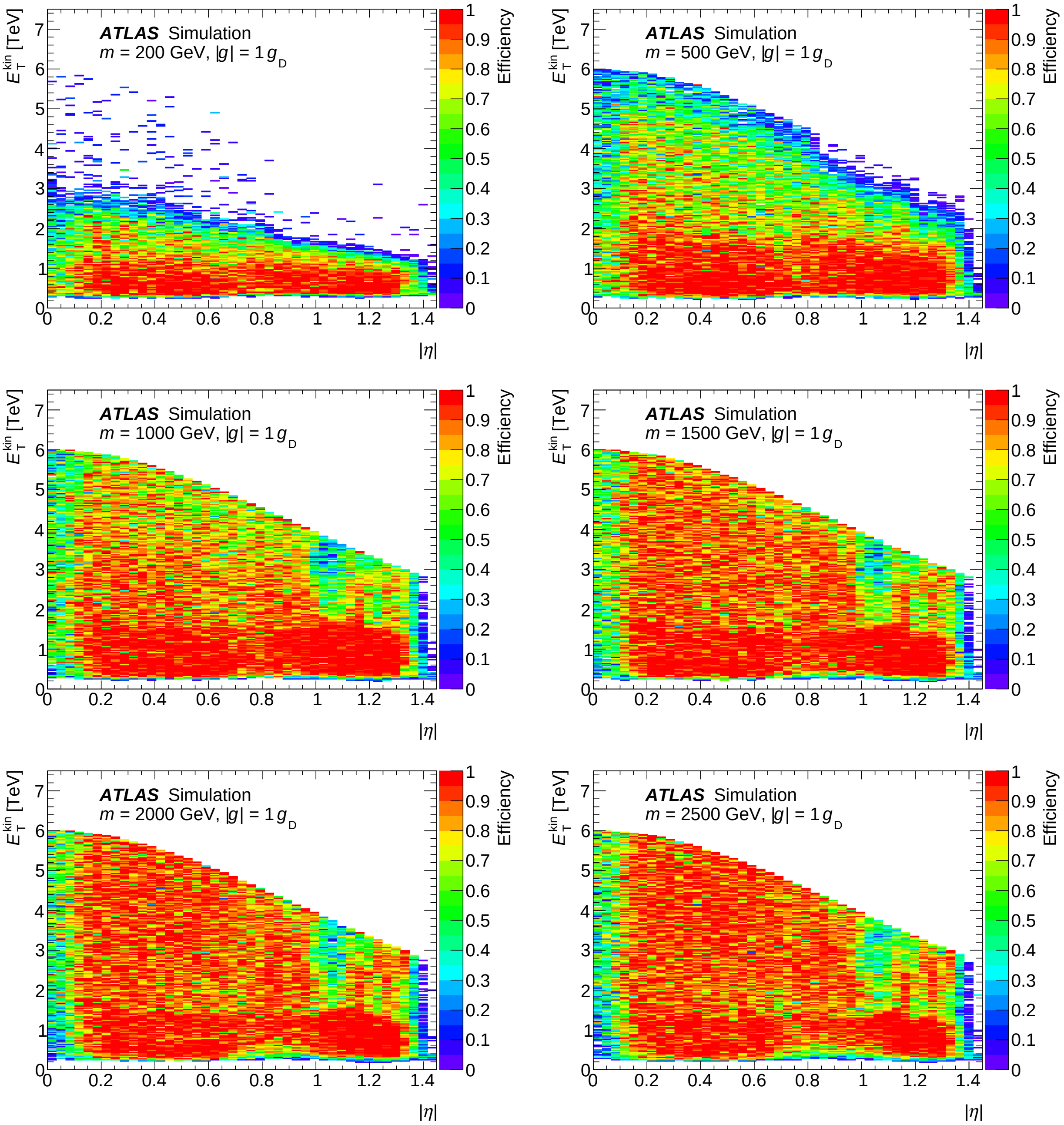

Figure 13: Selection efficiency as a function of transverse kinetic energy E_T^{kin} and pseudorapidity η for $g_{\mathrm{D}} = 1$ monopoles.

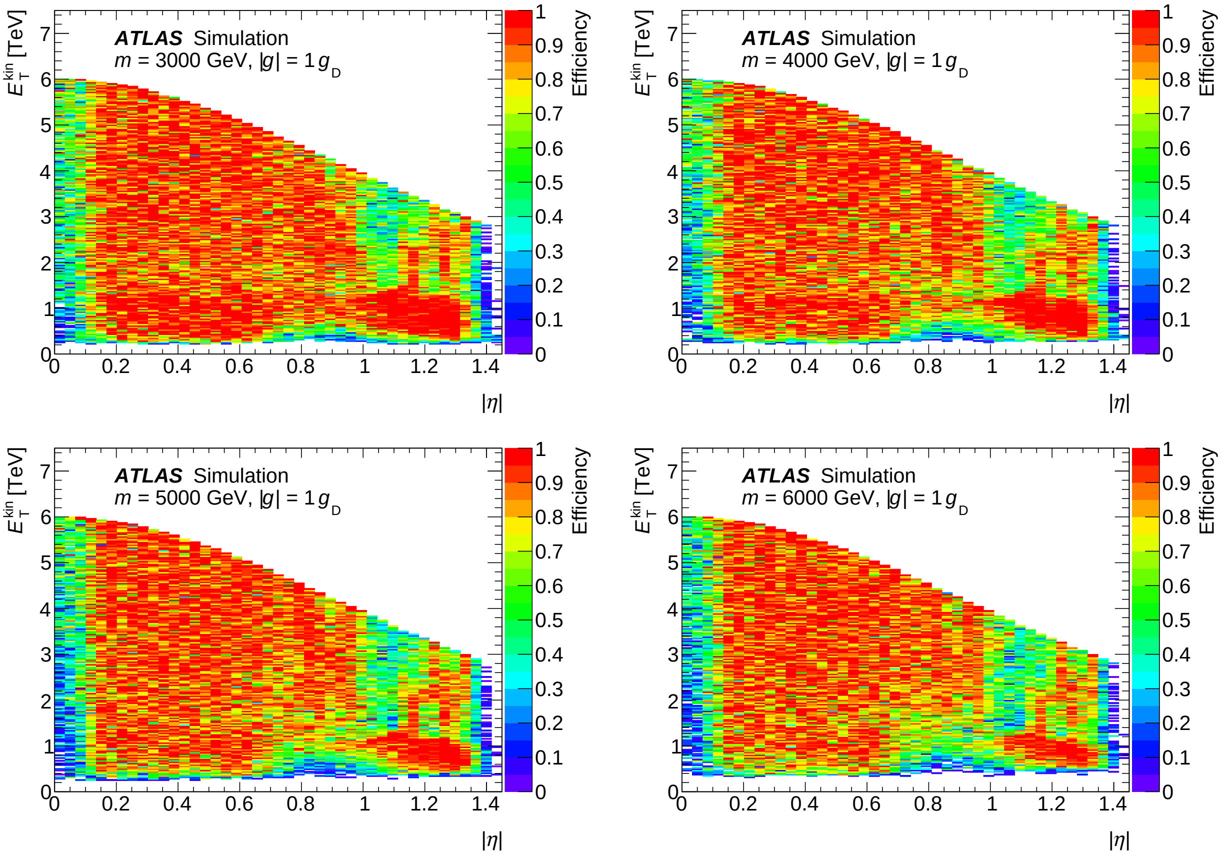

Figure 13 continued.

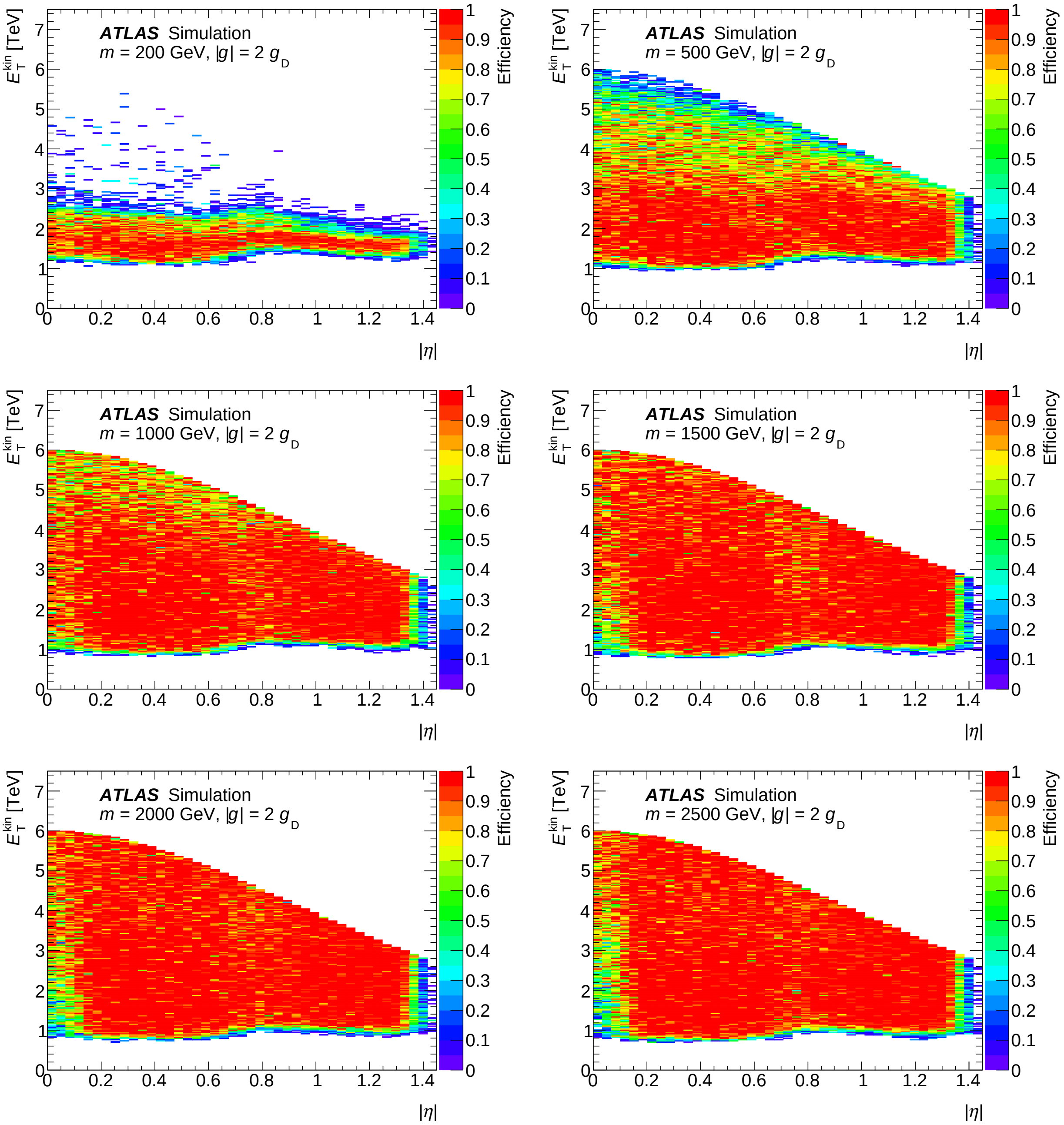

Figure 14: Selection efficiency as a function of transverse kinetic energy E_T^{kin} and pseudorapidity η for $g_{\mathrm{D}} = 2$ monopoles.

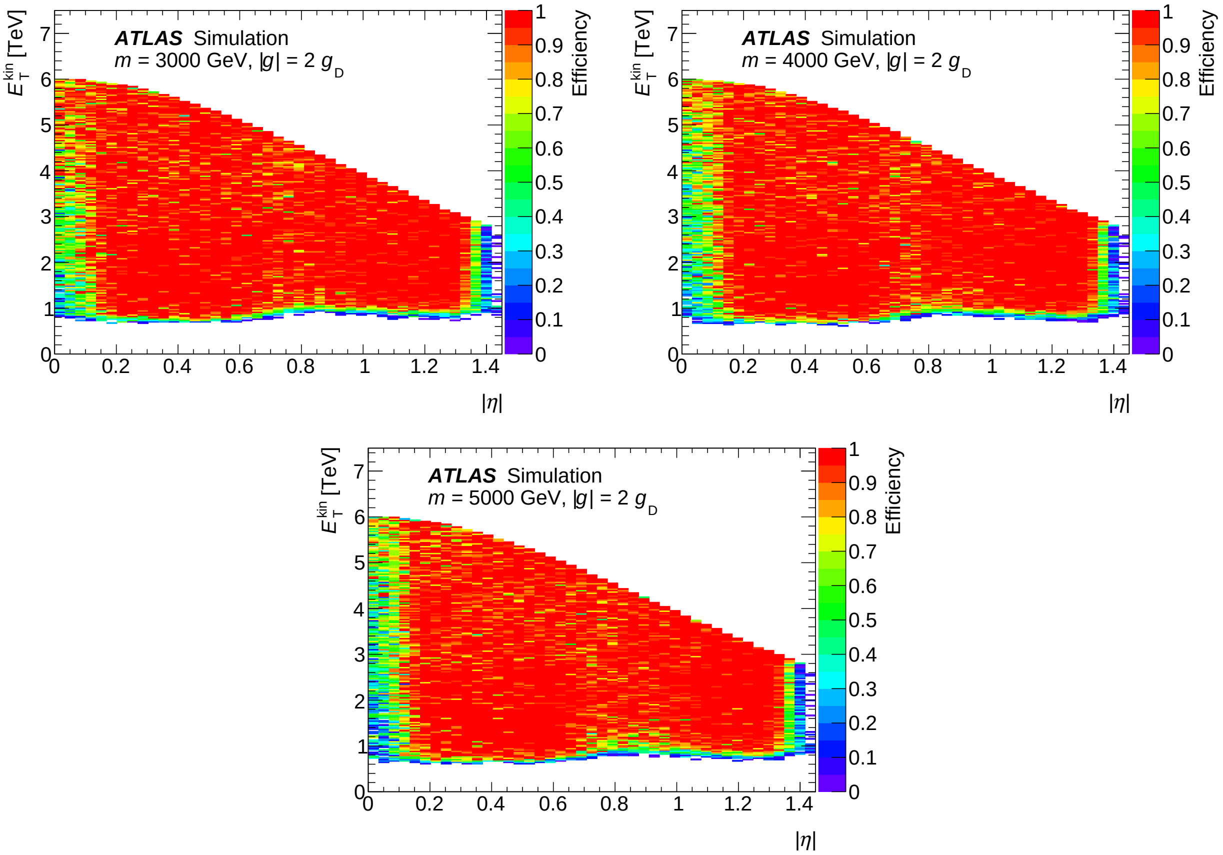

Figure 14 continued.

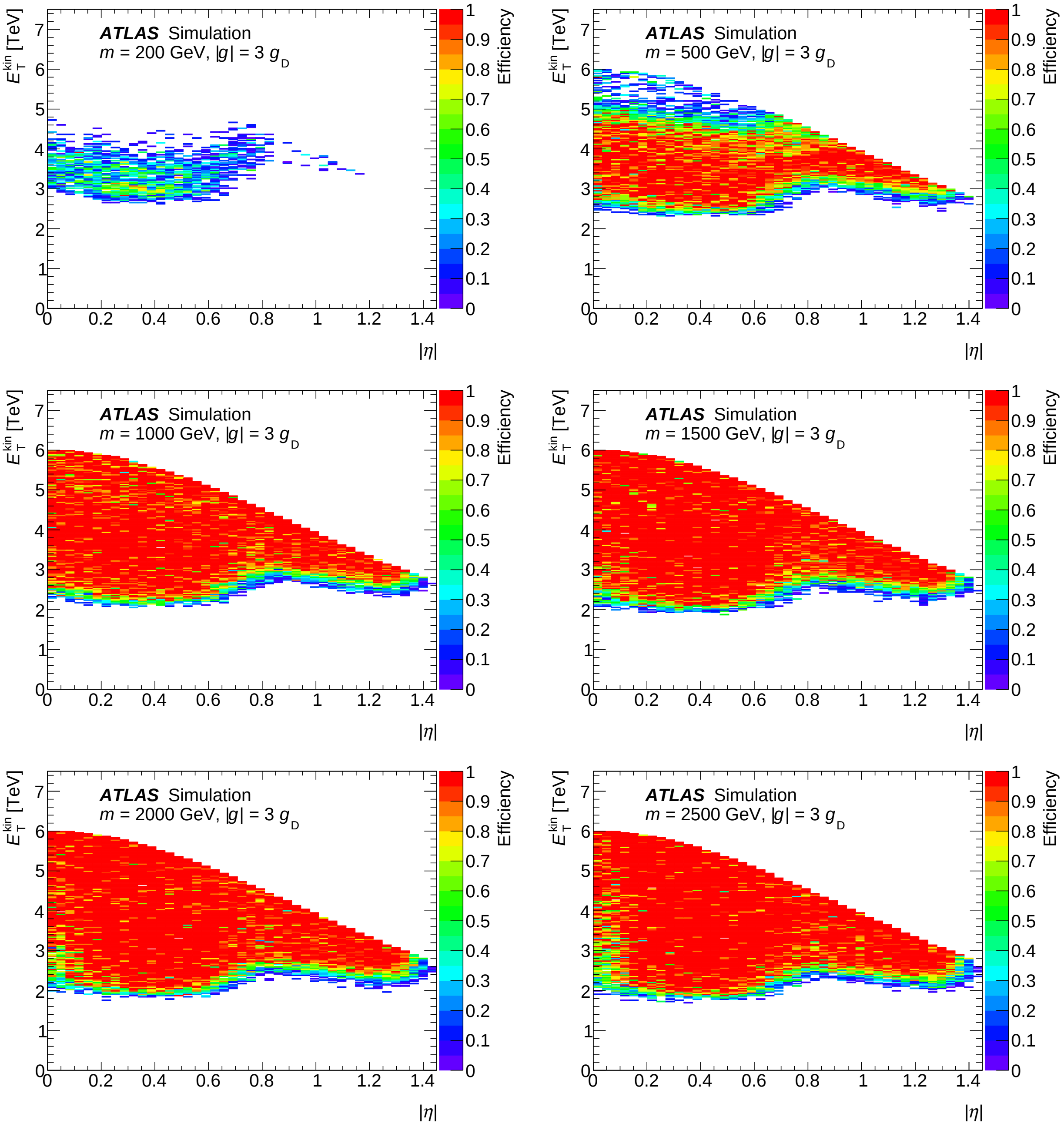

Figure 15: Selection efficiency as a function of transverse kinetic energy E_T^{kin} and pseudorapidity η for $g_{\mathrm{D}} = 3$ monopoles.

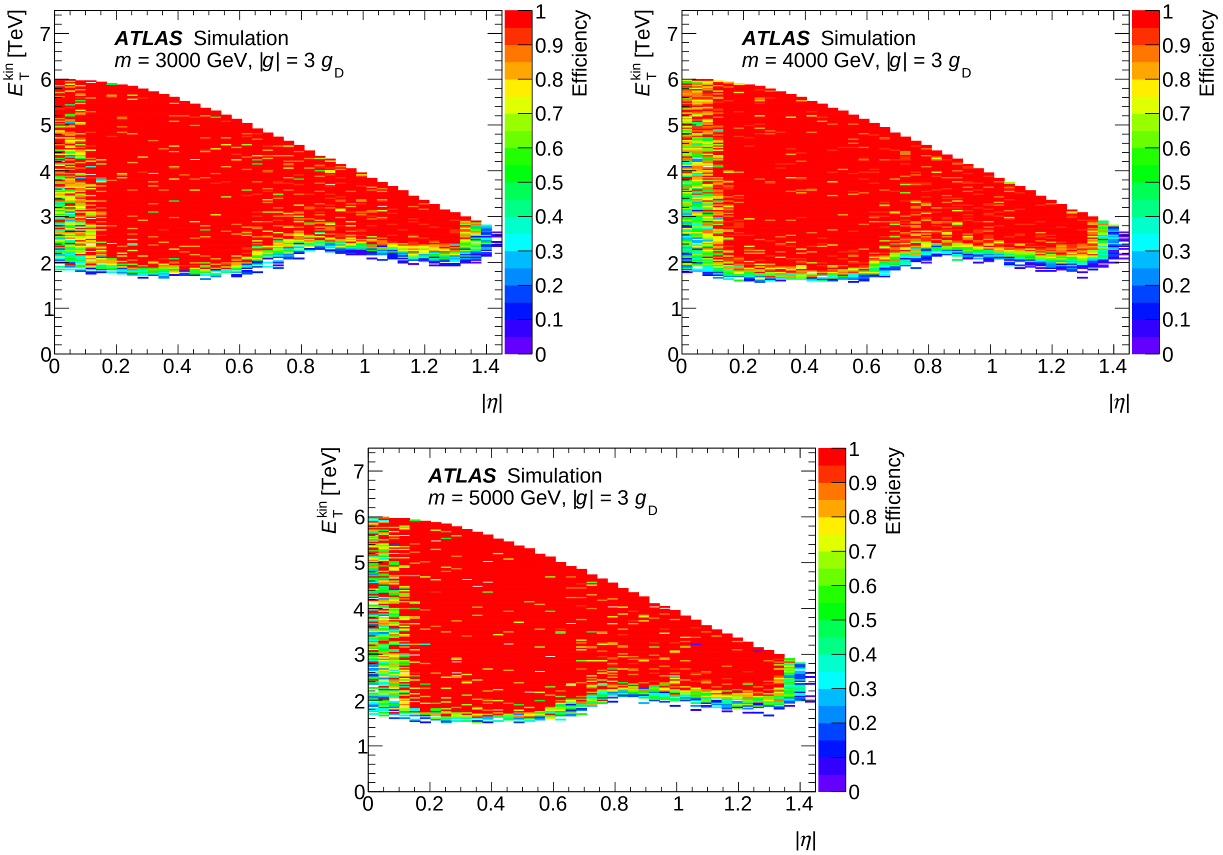

Figure 15 continued.

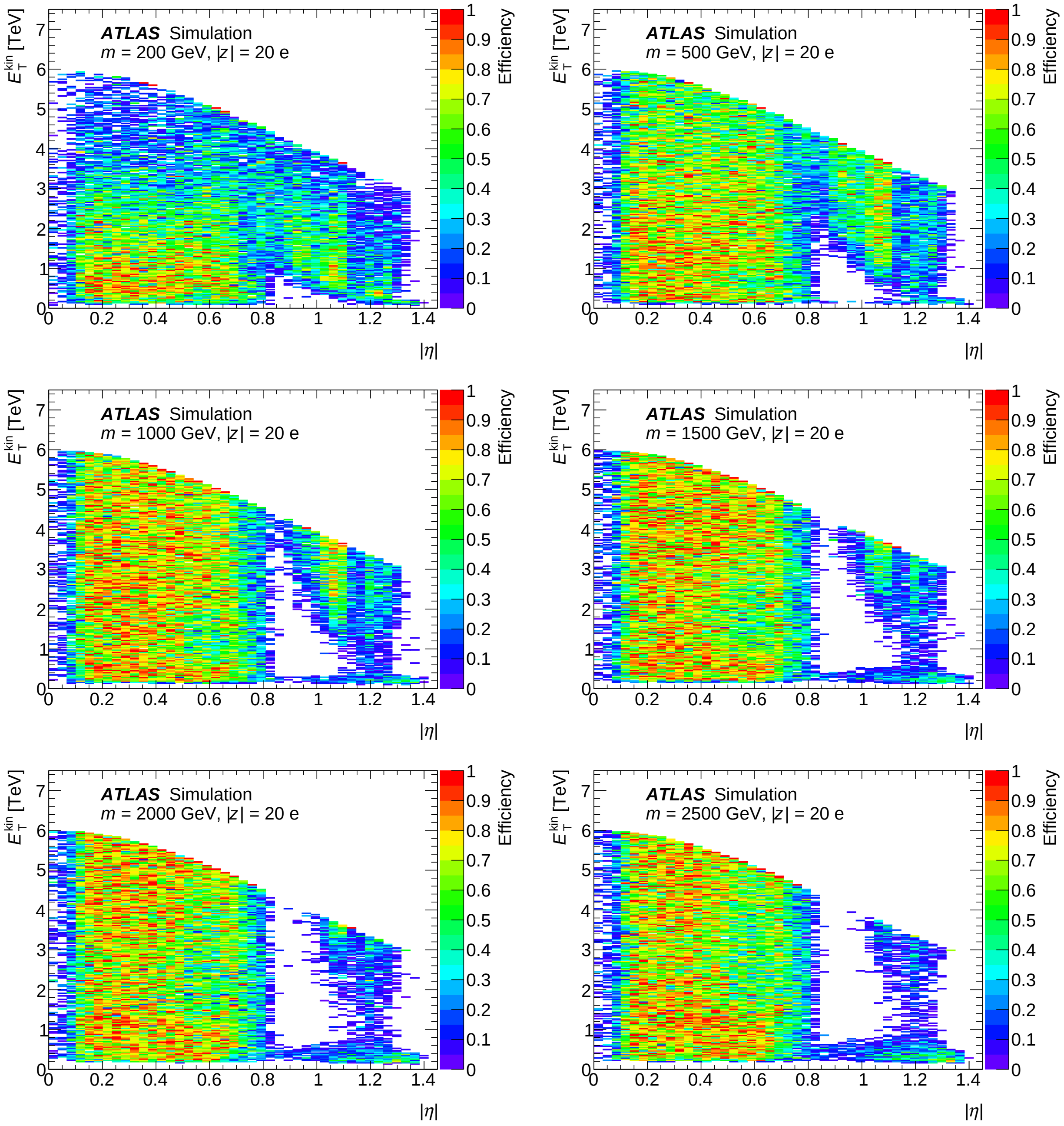

Figure 16: Selection efficiency as a function of transverse kinetic energy E_T^{kin} and pseudorapidity η for HECOs of charge $|z| = 20$.

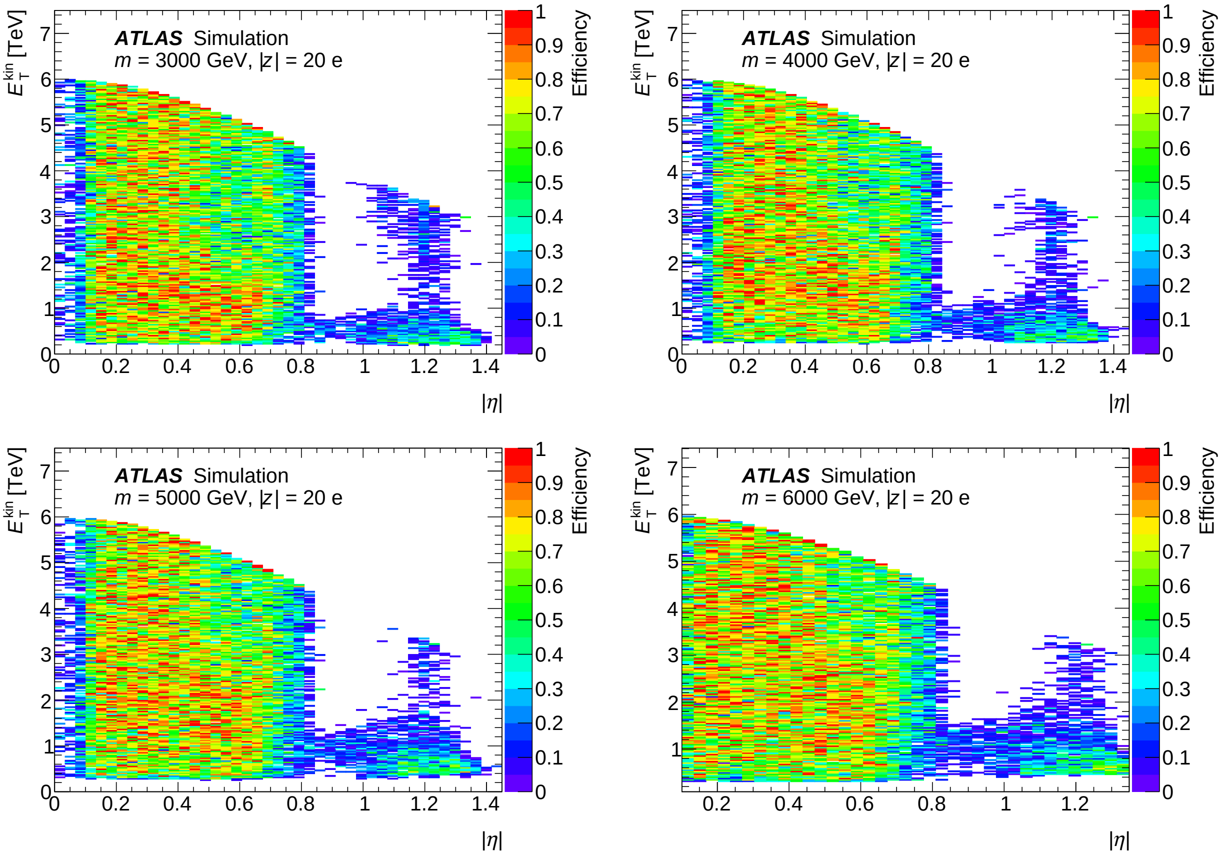

Figure 16 continued.

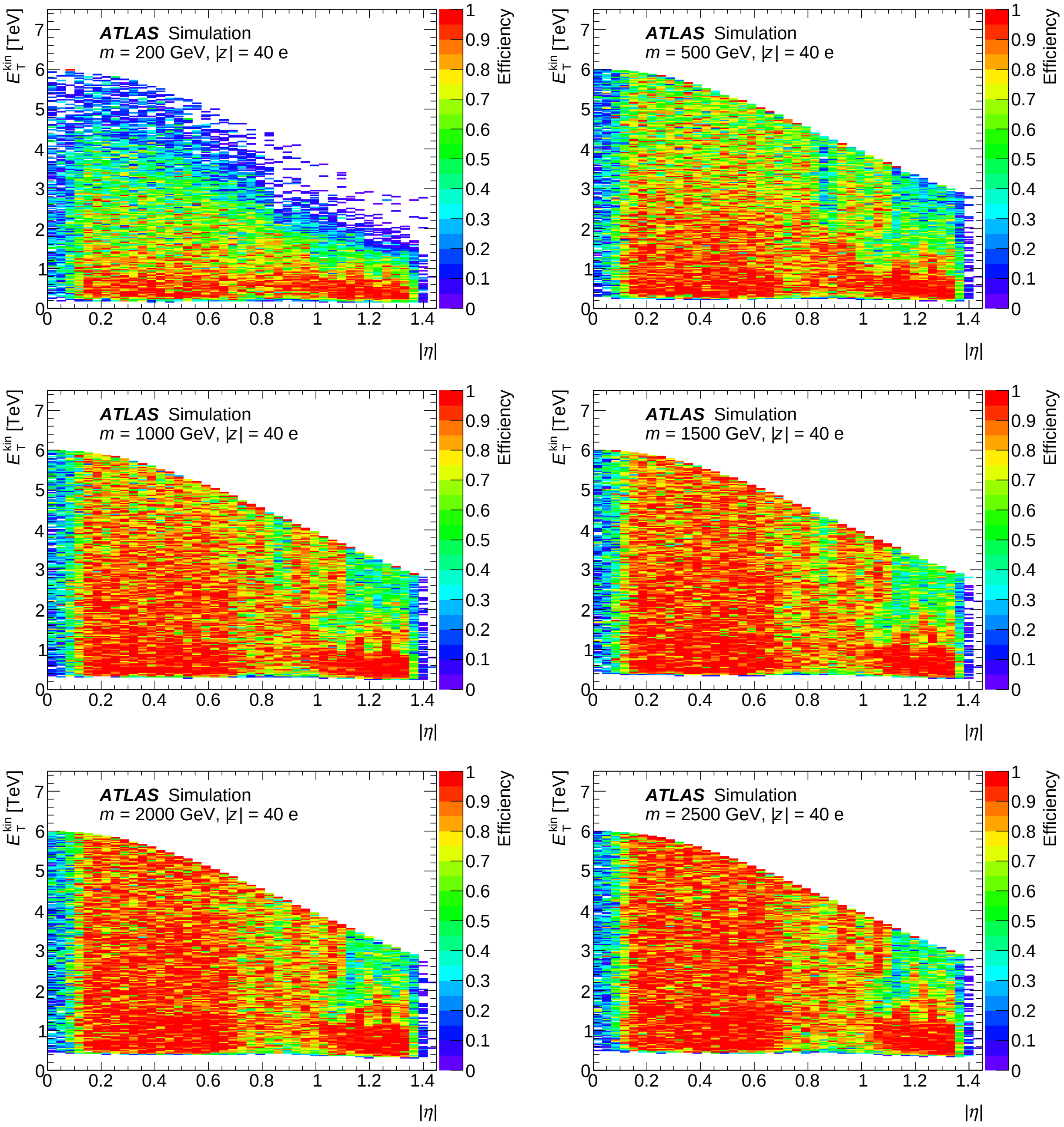

Figure 17: Selection efficiency as a function of transverse kinetic energy E_T^{kin} and pseudorapidity η for HECOs of charge $|z| = 40$.

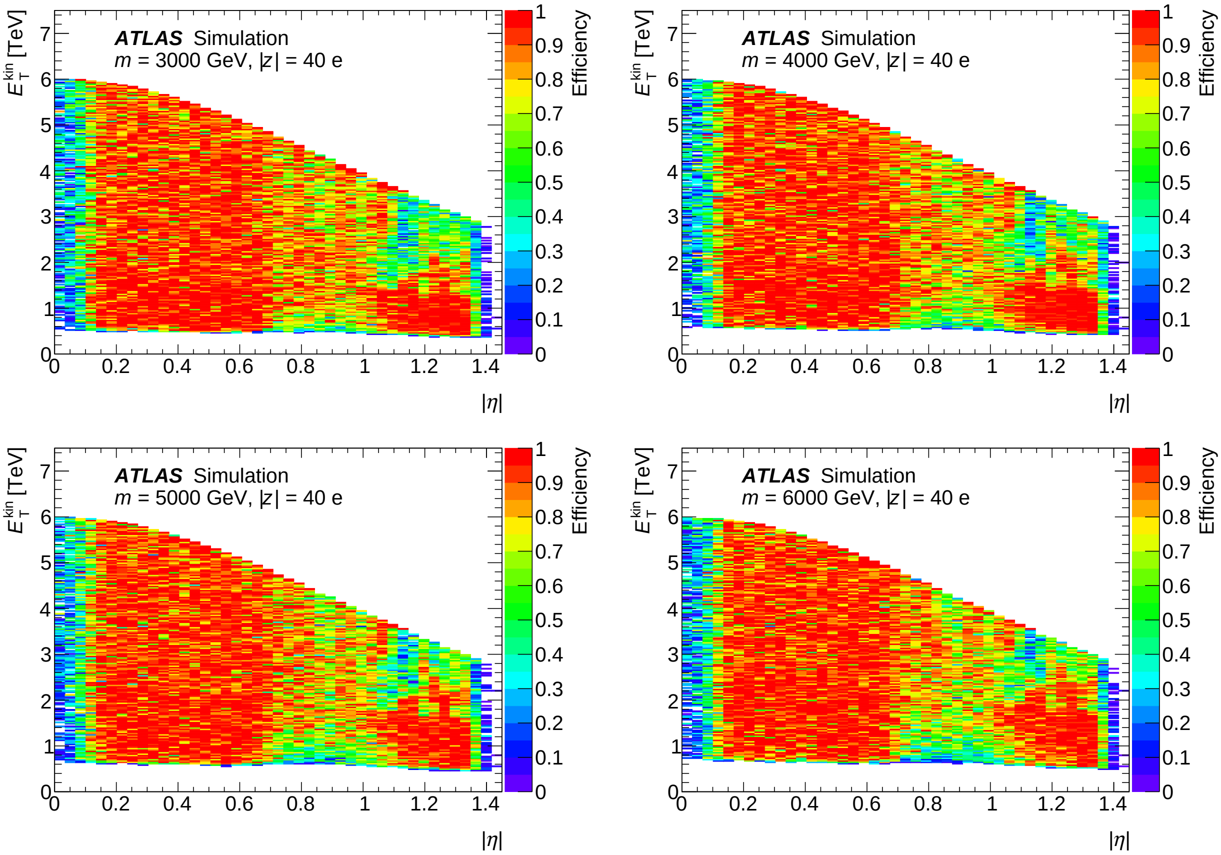

Figure 17 continued.

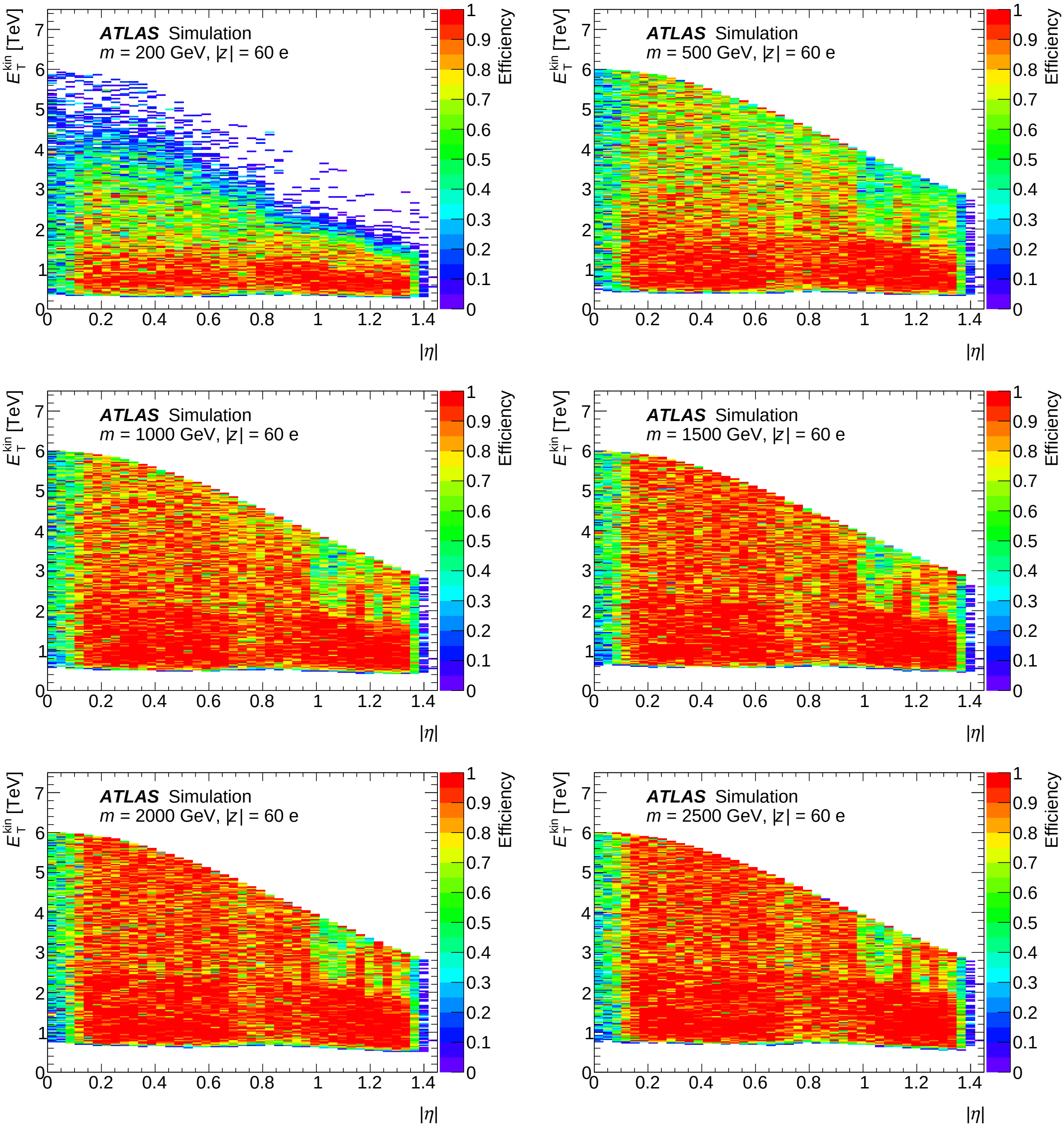

Figure 18: Selection efficiency as a function of transverse kinetic energy E_T^{kin} and pseudorapidity η for HECOs of charge $|z| = 60$.

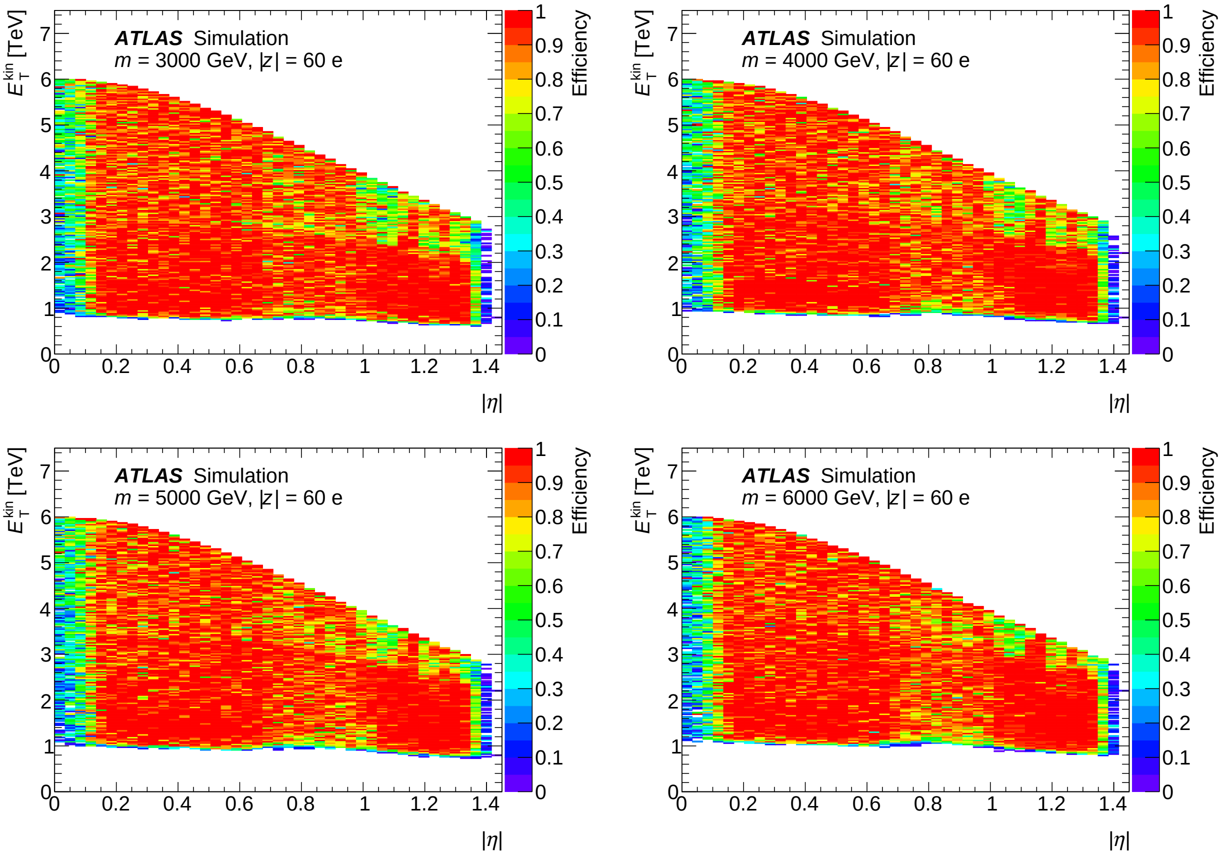

Figure 18 continued.

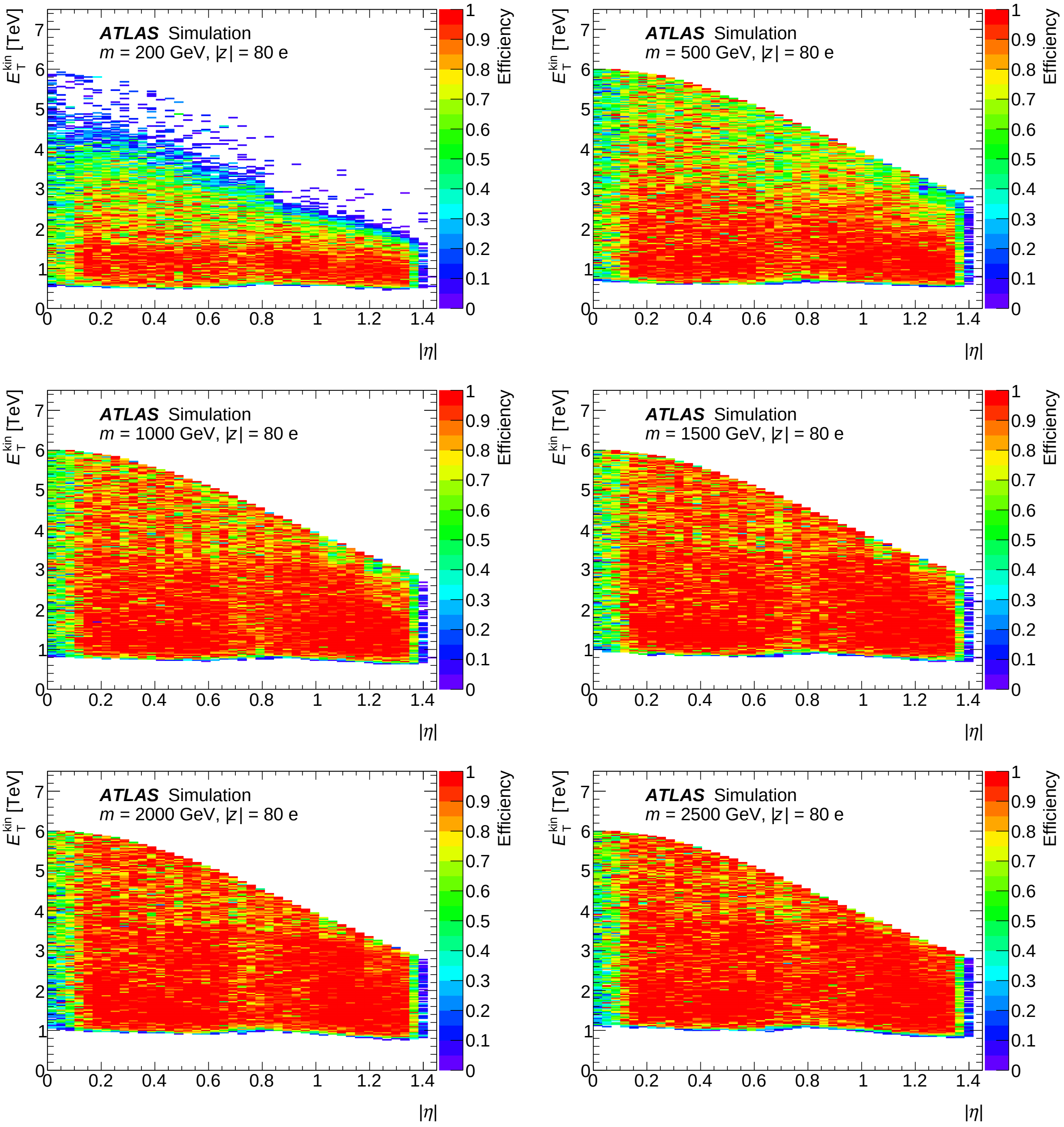

Figure 19: Selection efficiency as a function of transverse kinetic energy E_T^{kin} and pseudorapidity η for HECOs of charge $|z| = 80$.

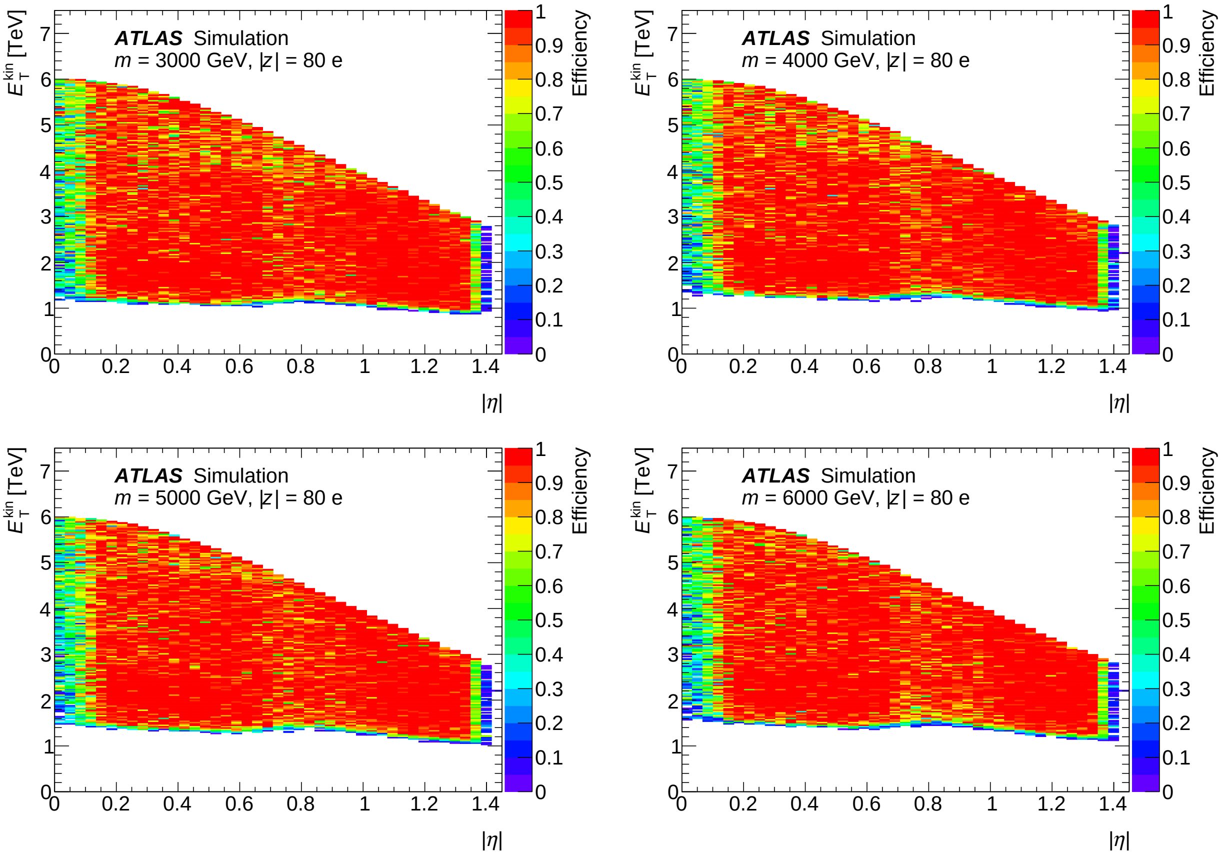

Figure 19 continued.

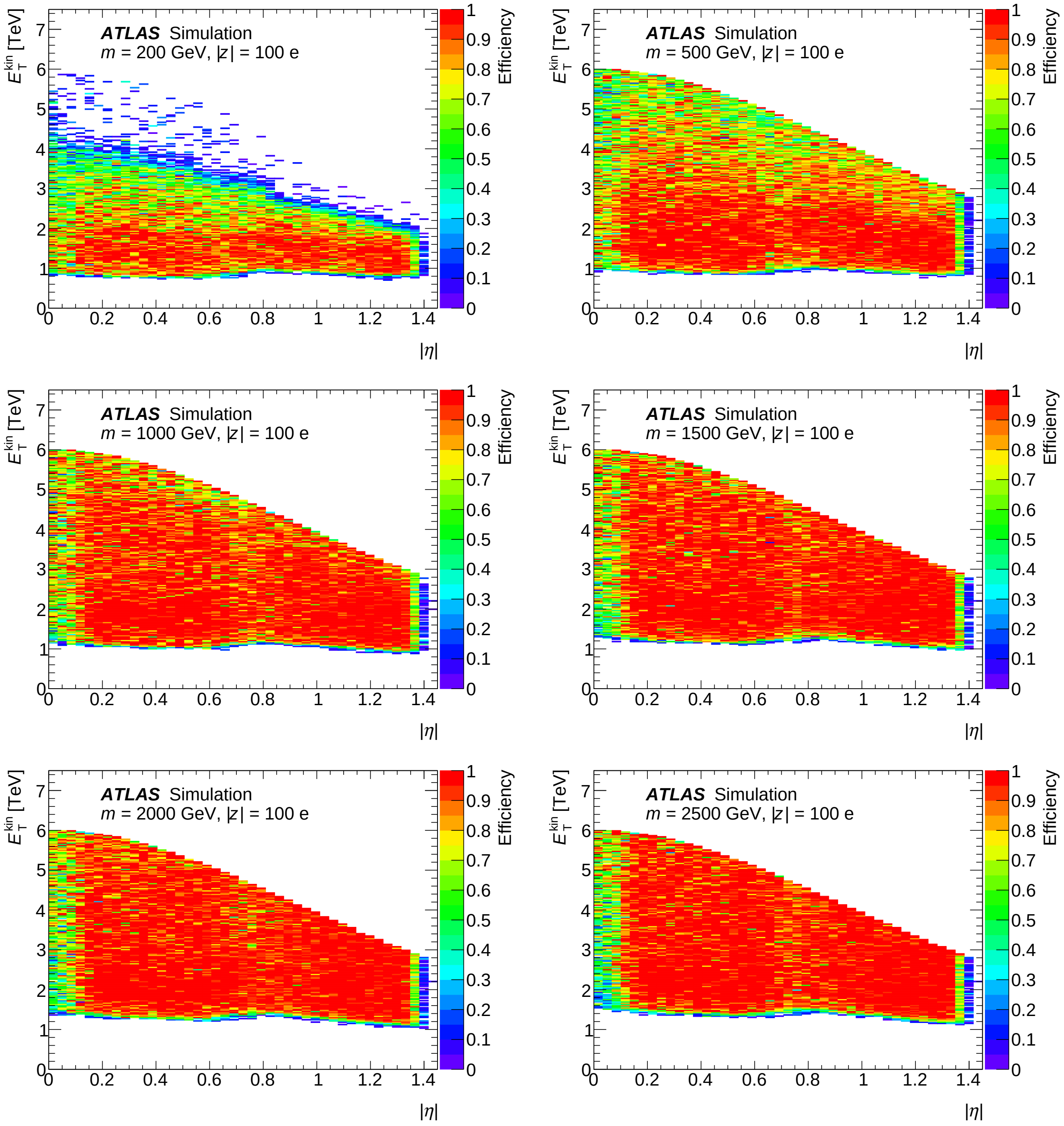

Figure 20: Selection efficiency as a function of transverse kinetic energy E_T^{kin} and pseudorapidity η for HECOs of charge $|z| = 100$.

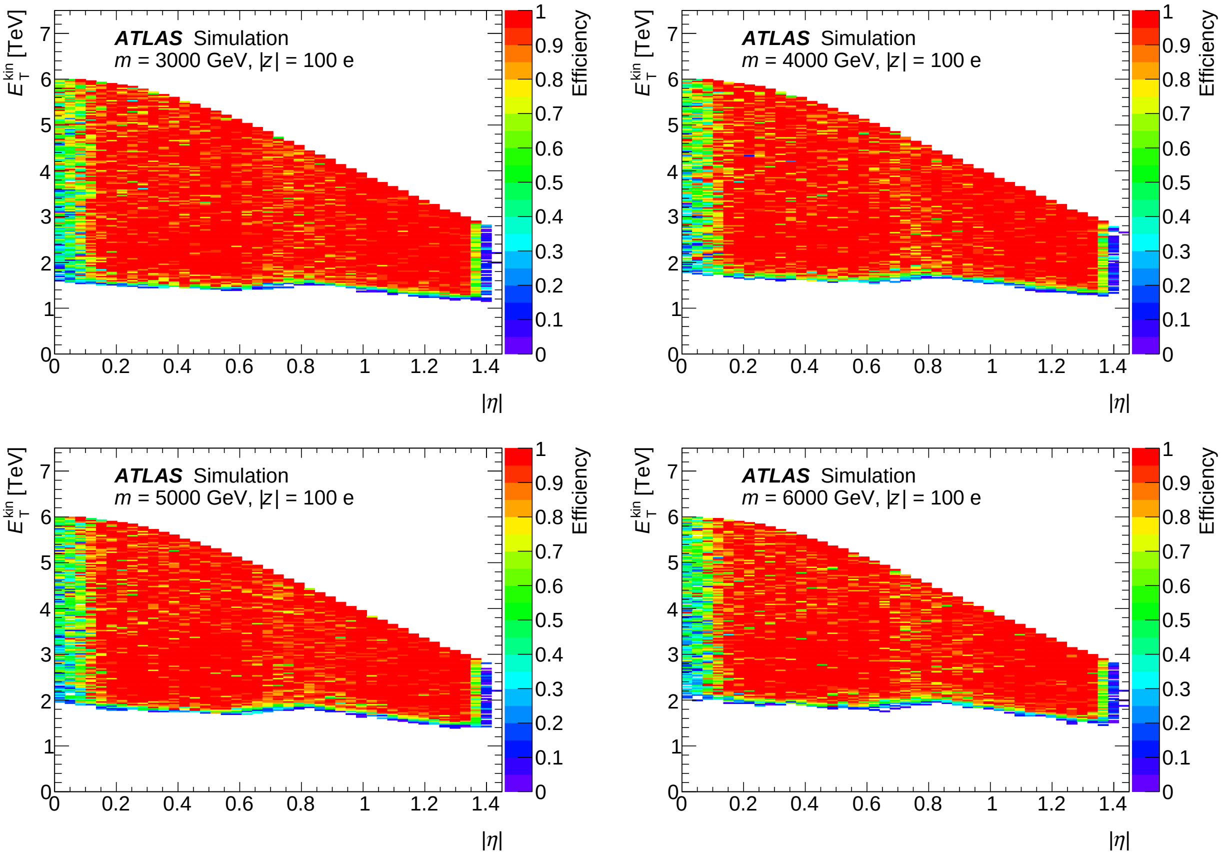

Figure 20 continued.

E Full efficiency cut flow

The following include cut-flow tables for single particle and DY-$\frac{1}{2}$samples as well as cut-flow plots for DY spin-$\frac{1}{2}$(figs. 21-22).

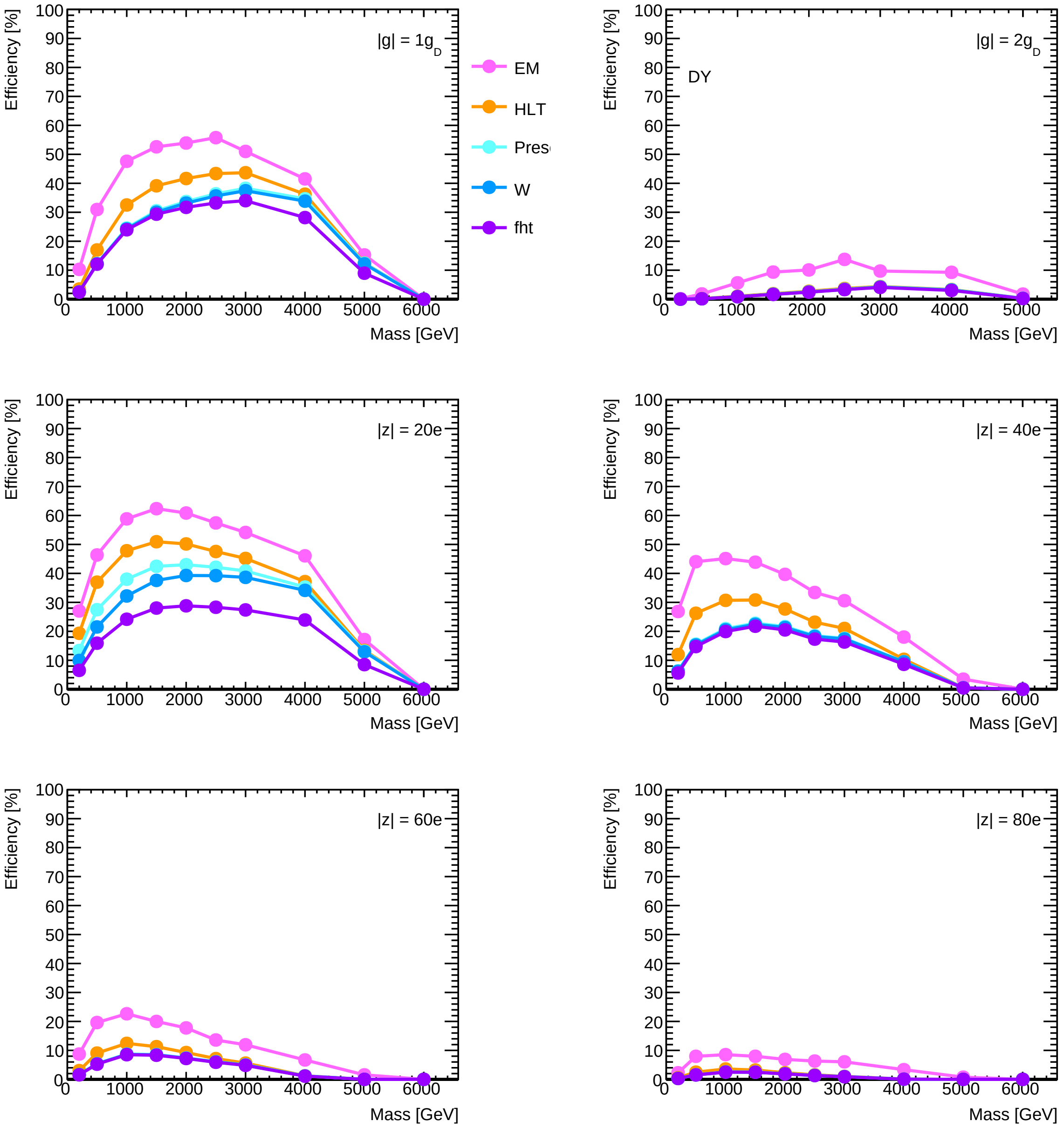

Figure 21: Full selection efficiency cut flow for DY spin-$\frac{1}{2}$including pT efficiency.

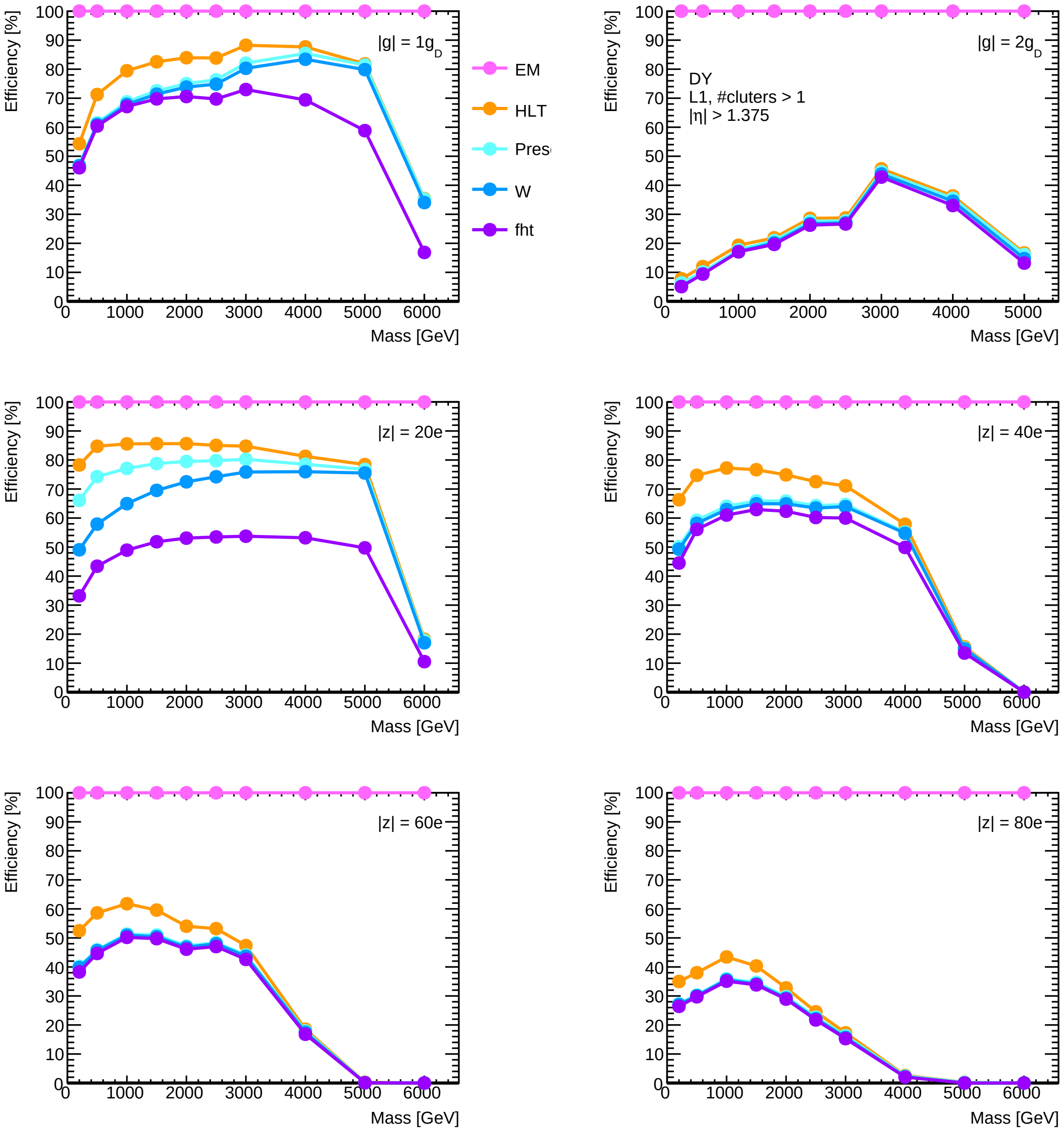

Figure 22: Full selection efficiency cut flow for DY spin-$\frac{1}{2}$including pT efficiency, for particles in the central region $|\eta| < 1.375$ which pass the L1 EM trigger.

Mass 200GeV	$\vert g\vert = 1g_D$		$\vert g\vert = 2g_D$		$\vert z\vert = 20$		$\vert z\vert = 40$		$\vert z\vert = 60$		$\vert z\vert = 80$	
	Events	eff. [%]	Events	eff.[%]	Events	eff.[%]	Events	eff.[%]	Events	eff.[%]	Events	eff.[%]
Total	258708	100	8257543	100	100000	100	114169	100	447160	100	1295400	100
pT Cut	99000	38	99800	1	100000	100	100449	88	100000	22	100000	8
HIP Trigger	79940	31	56821	1	57668	58	83941	74	80498	18	75467	6
Preselection	63550	25	47992	1	57120	57	65936	58	63365	14	59491	5
w Selection	20363	8	12360	0	24741	25	30710	27	29439	7	29652	2
fHT Selection	19198	7	12237	0	20730	21	26830	24	27043	6	28093	2

Mass 500GeV	$\vert g\vert = 1g_D$		$\vert g\vert = 2g_D$		$\vert z\vert = 20$		$\vert z\vert = 40$		$\vert z\vert = 60$		$\vert z\vert = 80$	
	Events	eff. [%]	Events	eff.[%]	Events	eff.[%]	Events	eff.[%]	Events	eff.[%]	Events	eff.[%]
Total	150635	100	841841	100	109752	100	121736	100	229283	100	375218	100
pT Cut	100000	66	99700	12	100000	91	100000	82	100000	44	100000	27
HIP Trigger	81297	54	60086	7	55999	51	82345	68	78832	34	73663	20
Preselection	64628	43	50369	6	55295	50	64799	53	62392	27	58574	16
w Selection	44224	29	41903	5	33866	31	49820	41	51008	22	50139	13
fHT Selection	41740	28	41503	5	27836	25	44986	37	47469	21	47703	13

Mass 1000GeV	$\vert g\vert = 1g_D$		$\vert g\vert = 2g_D$		$\vert z\vert = 20$		$\vert z\vert = 40$		$\vert z\vert = 60$		$\vert z\vert = 80$	
	Events	eff. [%]	Events	eff.[%]	Events	eff.[%]	Events	eff.[%]	Events	eff.[%]	Events	eff.[%]
Total	121691	100	304663	100	107775	100	133370	100	186115	100	336502	100
pT Cut	100000	82	91500	30	100000	93	99000	74	100000	54	100000	30
HIP Trigger	81237	67	57389	19	53854	50	79984	60	76877	41	71069	21
Preselection	64595	53	47941	16	52991	49	62995	47	61118	33	56952	17
w Selection	54411	45	45887	15	33723	31	52742	40	54743	29	52913	16
fHT Selection	51795	43	45165	15	27133	25	48204	36	51322	28	50417	15

Mass 1500GeV	$\vert g\vert = 1g_D$		$\vert g\vert = 2g_D$		$\vert z\vert = 20$		$\vert z\vert = 40$		$\vert z\vert = 60$		$\vert z\vert = 80$	
	Events	eff. [%]	Events	eff.[%]	Events	eff.[%]	Events	eff.[%]	Events	eff.[%]	Events	eff.[%]
Total	117587	100	204618	100	111918	100	132323	100	189710	100	333033	100
pT Cut	99000	84	97500	48	100000	89	100000	76	100000	53	100000	30
HIP Trigger	80545	68	62619	31	52486	47	79447	60	75079	40	69081	21
Preselection	64141	55	52009	25	51384	46	62621	47	59617	31	55421	17
w Selection	55839	47	51054	25	32616	29	53752	41	54378	29	52583	16
fHT Selection	53183	45	49906	24	25559	23	49396	37	51279	27	50146	15

Mass 2000GeV	$\vert g\vert = 1g_D$		$\vert g\vert = 2g_D$		$\vert z\vert = 20$		$\vert z\vert = 40$		$\vert z\vert = 60$		$\vert z\vert = 80$	
	Events	eff. [%]	Events	eff.[%]	Events	eff.[%]	Events	eff.[%]	Events	eff.[%]	Events	eff.[%]
Total	118443	100	201970	100	117309	100	135142	100	182602	100	322373	100
pT Cut	100000	84	99000	49	100000	85	100000	74	100000	55	98000	30
HIP Trigger	81299	69	64698	32	51295	44	78307	58	73658	40	65875	20
Preselection	64594	55	53619	27	50152	43	61866	46	58717	32	52999	16
w Selection	56702	48	52859	26	31648	27	53499	40	53806	29	50572	16
fHT Selection	53916	46	51563	26	24242	21	49542	37	50987	28	48348	15

Mass 2500GeV	$\vert g\vert = 1g_D$		$\vert g\vert = 2g_D$		$\vert z\vert = 20$		$\vert z\vert = 40$		$\vert z\vert = 60$		$\vert z\vert = 80$	
	Events	eff. [%]	Events	eff.[%]	Events	eff.[%]	Events	eff.[%]	Events	eff.[%]	Events	eff.[%]
Total	111561	100	148236	100	121932	100	144622	100	216375	100	311614	100
pT Cut	100000	90	99500	67	100000	82	100000	69	100000	46	100000	32
HIP Trigger	81328	73	65757	44	50317	41	77329	53	72192	33	65375	21
Preselection	64688	58	54452	37	49151	40	61064	42	57740	27	52792	17
w Selection	56663	51	53661	36	31252	26	53249	37	53236	25	50620	16
fHT Selection	53580	48	52157	35	23414	19	49172	34	50472	23	48414	16

Mass 3000 GeV	$\|g\| = 1g_D$		$\|g\| = 2g_D$		$\|z\| = 20$		$\|z\| = 40$		$\|z\|= 60$		$\|z\|= 80$	
	Events	eff. [%]	Events	eff.[%]	Events	eff.[%]	Events	eff.[%]	Events	eff.[%]	Events	eff.[%]
Total	138960	100	248916	100	133935	100	143377	100	216669	100	300460	100
pT Cut	100000	72	99000	40	100000	75	99000	69	100000	46	100000	33
HIP Trigger	80795	58	66315	27	50040	37	75737	53	71093	33	64210	21
Preselection	64315	46	54831	22	48880	36	60009	42	56909	26	51981	17
w Selection	55929	40	53972	22	31385	23	52506	37	52621	24	50065	17
fHT Selection	52744	38	52270	21	23176	17	48514	34	49826	23	47827	16

Mass 4000 GeV	$\|g\| = 1g_D$		$\|g\| = 2g_D$		$\|z\| = 20$		$\|z\| = 40$		$\|z\|= 60$		$\|z\|= 80$	
	Events	eff. [%]	Events	eff.[%]	Events	eff.[%]	Events	eff.[%]	Events	eff.[%]	Events	eff.[%]
Total	162462	100	205990	100	141749	100	164212	100	236842	100	386946	100
pT Cut	100000	62	99000	48	100000	71	100449	61	100000	42	100000	26
HIP Trigger	79465	49	67326	33	49410	35	75176	46	68827	29	61362	16
Preselection	63618	39	55352	27	48200	34	59334	36	55183	23	49870	13
w Selection	54747	34	54441	26	31940	23	52389	32	51436	22	48267	12
fHT Selection	51077	31	52280	25	22892	16	48147	29	48688	21	46029	12

Mass 5000 GeV	$\|g\| = 1g_D$		$\|g\| = 2g_D$		$\|z\| = 20$		$\|z\| = 40$		$\|z\|= 60$		$\|z\|= 80$	
	Events	eff. [%]	Events	eff.[%]	Events	eff.[%]	Events	eff.[%]	Events	eff.[%]	Events	eff.[%]
Total	272600	100	443531	100	225172	100	247582	100	446849	100	817883	100
pT Cut	100000	37	99500	22	100000	44	100000	40	100000	22	100000	12
HIP Trigger	77872	29	68206	15	49700	22	73444	30	67085	15	58900	7
Preselection	62717	23	55965	13	48223	21	58103	23	53840	12	48057	6
w Selection	53593	20	54943	12	33231	15	51965	21	50613	11	46781	6
fHT Selection	49431	18	52442	12	23333	10	47512	19	47690	11	44564	5

Mass 6000 GeV	$\|g\| = 1g_D$		$\|g\| = 2g_D$		$\|z\| = 20$		$\|z\| = 40$		$\|z\|= 60$		$\|z\|= 80$	
	Events	eff. [%]	Events	eff.[%]	Events	eff.[%]	Events	eff.[%]	Events	eff.[%]	Events	eff.[%]
Total	3518202	100	0	100	2131227	100	1997848	100	18942145	100	172130088	100
pT Cut	100000	3	-	-	100000	5	100000	5	100000	1	98000	0
HIP Trigger	75767	2	-	-	49736	2	71985	4	65261	0	55958	0
Preselection	61298	2	-	-	47982	2	57236	3	52602	0	45825	0
w Selection	51807	1	-	-	34015	2	51670	3	49901	0	44771	0
fHT Selection	47493	1	-	-	23451	1	46857	2	46962	0	42475	0

Table 2: Full selection efficiency cut flow for single particle samples.

Mass 200 GeV	$\|g\| = 1g_D$		$\|g\| = 2g_D$		$\|z\| = 20$		$\|z\| = 40$		$\|z\| = 60$		$\|z\| = 80$	
	Events	eff. [%]	Events	eff.[%]	Events	eff.[%]	Events	eff.[%]	Events	eff.[%]	Events	eff.[%]
Total	129093	100	1894767	100	50000	100	56829	100	214637	100	647700	100
pT Cut	49400	38	22900	1	50000	100	50000	88	48000	22	50000	8
HIP Trigger	4524	4	222	0	9660	19	6807	12	6486	3	3603	1
Preselection	3223	2	164	0	6687	13	3601	6	3524	2	2117	0
w Selection	3209	2	132	0	4968	10	3536	6	3490	2	2097	0
fHT Selection	3164	2	131	0	3267	7	3196	6	3344	2	2049	0

Mass 500 GeV	$\|g\| = 1g_D$		$\|g\| = 2g_D$		$\|z\| = 20$		$\|z\| = 40$		$\|z\| = 60$		$\|z\| = 80$	
	Events	eff. [%]	Events	eff.[%]	Events	eff.[%]	Events	eff.[%]	Events	eff.[%]	Events	eff.[%]
Total	69292	100	228825	100	53779	100	58433	100	114642	100	183857	100
pT Cut	46000	66	27100	12	49000	91	48000	82	50000	44	49000	27
HIP Trigger	11771	17	451	0	19886	37	15335	26	10403	9	4581	2
Preselection	8527	12	352	0	14773	27	9104	16	6187	5	2869	2
w Selection	8450	12	328	0	11569	22	8941	15	6141	5	2848	2
fHT Selection	8376	12	326	0	8556	16	8615	15	6012	5	2814	2

Mass 1000 GeV	$\|g\| = 1g_D$		$\|g\| = 2g_D$		$\|z\| = 20$		$\|z\| = 40$		$\|z\| = 60$		$\|z\| = 80$	
	Events	eff. [%]	Events	eff.[%]	Events	eff.[%]	Events	eff.[%]	Events	eff.[%]	Events	eff.[%]
Total	57195	100	90233	100	53887	100	67358	100	91197	100	151426	100
pT Cut	47000	82	27100	30	50000	93	50000	74	49000	54	45000	30
HIP Trigger	18594	33	918	1	25768	48	20670	31	11323	12	5425	4
Preselection	14049	25	801	1	20470	38	14105	21	7940	9	3856	3
w Selection	13865	24	773	1	17350	32	13841	21	7876	9	3818	3
fHT Selection	13706	24	767	1	13026	24	13426	20	7762	9	3766	2

Mass 1500 GeV	$\|g\| = 1g_D$		$\|g\| = 2g_D$		$\|z\| = 20$		$\|z\| = 40$		$\|z\| = 60$		$\|z\| = 80$	
	Events	eff. [%]	Events	eff.[%]	Events	eff.[%]	Events	eff.[%]	Events	eff.[%]	Events	eff.[%]
Total	57012	100	64009	100	55959	100	66162	100	94855	100	156525	100
pT Cut	48000	84	30500	48	50000	89	50000	76	50000	53	47000	30
HIP Trigger	22311	39	1220	2	28502	51	20394	31	10712	11	5034	3
Preselection	17401	31	1126	2	23749	42	15082	23	8109	9	3934	3
w Selection	17119	30	1081	2	21027	38	14849	22	8012	8	3870	2
fHT Selection	16728	29	1051	2	15687	28	14394	22	7905	8	3834	2

Mass 2000 GeV	$\|g\| = 1g_D$		$\|g\| = 2g_D$		$\|z\| = 20$		$\|z\| = 40$		$\|z\| = 60$		$\|z\| = 80$	
	Events	eff. [%]	Events	eff.[%]	Events	eff.[%]	Events	eff.[%]	Events	eff.[%]	Events	eff.[%]
Total	59221	100	67731	100	58654	100	67571	100	91301	100	154608	100
pT Cut	50000	84	33200	49	50000	85	50000	74	50000	55	47000	30
HIP Trigger	24663	42	1857	3	29426	50	18723	28	8457	9	3525	2
Preselection	19961	34	1727	3	25217	43	14631	22	6742	7	2985	2
w Selection	19640	33	1669	2	23041	39	14414	21	6678	7	2938	2
fHT Selection	18774	32	1637	2	16893	29	13847	20	6579	7	2901	2

Mass 2500 GeV	$\|g\| = 1g_D$		$\|g\| = 2g_D$		$\|z\| = 20$		$\|z\| = 40$		$\|z\| = 60$		$\|z\| = 80$	
	Events	eff. [%]	Events	eff.[%]	Events	eff.[%]	Events	eff.[%]	Events	eff.[%]	Events	eff.[%]
Total	55780	100	51994	100	58527	100	72311	100	108187	100	152691	100
pT Cut	50000	90	34900	67	48000	82	50000	69	50000	46	49000	32
HIP Trigger	24186	43	1917	4	27833	48	16739	23	7746	7	2378	2
Preselection	20283	36	1786	3	24650	42	13369	18	6565	6	2106	1
w Selection	19880	36	1744	3	22955	39	13193	18	6512	6	2059	1
fHT Selection	18530	33	1717	3	16571	28	12516	17	6380	6	2015	1

Mass 3000GeV	$\vert g\vert = 1g_D$		$\vert g\vert = 2g_D$		$\vert z\vert = 20$		$\vert z\vert = 40$		$\vert z\vert = 60$		$\vert z\vert = 80$	
	Events	eff. [%]	Events	eff.[%]	Events	eff.[%]	Events	eff.[%]	Events	eff.[%]	Events	eff.[%]
Total	65311	100	102835	100	64289	100	70965	100	104001	100	144221	100
pT Cut	47000	72	40900	40	48000	75	49000	69	48000	46	48000	33
HIP Trigger	28506	44	4492	4	29033	45	14903	21	5838	6	1500	1
Preselection	25003	38	4360	4	26250	41	12475	18	5203	5	1384	1
w Selection	24444	37	4284	4	24833	39	12328	17	5153	5	1338	1
fHT Selection	22208	34	4179	4	17608	27	11573	16	5027	5	1301	1

Mass 4000GeV	$\vert g\vert = 1g_D$		$\vert g\vert = 2g_D$		$\vert z\vert = 20$		$\vert z\vert = 40$		$\vert z\vert = 60$		$\vert z\vert = 80$	
	Events	eff. [%]	Events	eff.[%]	Events	eff.[%]	Events	eff.[%]	Events	eff.[%]	Events	eff.[%]
Total	81231	100	80939	100	70875	100	81739	100	118421	100	189603	100
pT Cut	50000	62	38900	48	50000	71	50000	61	50000	42	49000	26
HIP Trigger	29434	36	2702	3	26336	37	8451	10	1457	1	165	0
Preselection	28150	35	2632	3	25007	35	7789	10	1403	1	152	0
w Selection	27491	34	2556	3	24198	34	7731	9	1369	1	136	0
fHT Selection	22881	28	2445	3	16946	24	7041	9	1317	1	129	0

Mass 5000GeV	$\vert g\vert = 1g_D$		$\vert g\vert = 2g_D$		$\vert z\vert = 20$		$\vert z\vert = 40$		$\vert z\vert = 60$		$\vert z\vert = 80$	
	Events	eff. [%]	Events	eff.[%]	Events	eff.[%]	Events	eff.[%]	Events	eff.[%]	Events	eff.[%]
Total	136300	100	201929	100	112586	100	123790	100	223425	100	408938	100
pT Cut	50000	37	45300	22	50000	44	50000	40	50000	22	50000	12
HIP Trigger	17025	12	592	0	15132	13	672	1	10	0	8	0
Preselection	16930	12	566	0	14793	13	651	1	6	0	7	0
w Selection	16600	12	517	0	14557	13	641	1	4	0	0	0
fHT Selection	12230	9	462	0	9586	9	581	0	4	0	0	0

Mass 6000GeV	$\vert g\vert = 1g_D$		$\vert g\vert = 2g_D$		$\vert z\vert = 20$		$\vert z\vert = 40$		$\vert z\vert = 60$		$\vert z\vert = 80$	
	Events	eff. [%]	Events	eff.[%]	Events	eff.[%]	Events	eff.[%]	Events	eff.[%]	Events	eff.[%]
Total	1759101	100	-	-	1065197	100	998857	100	9467989	100	87754274	100
pT Cut	50000	3	-	-	49980	5	49997	5	49984	1	49962	0
HIP Trigger	179	0	-	-	81	0	0	0	0	0	0	0
Preselection	178	0	-	-	79	0	0	0	0	0	0	0
w Selection	172	0	-	-	75	0	0	0	0	0	0	0
fHT Selection	85	0	-	-	47	0	0	0	0	0	0	0

Table 3: Full selection efficiency cut flow for Drell-Yann spin-$\frac{1}{2}$ samples.

F Complete Systematic Uncertainty tables

Spin-0 $1g_{\text{D}}$	eff.	MC Stat.	Det. material	G4 range cut	Birks High	Birks Low	δ-ray prod.	TRT Occ.	LAr x-talk	Calo Arrival	Extrap	Weight Up	Weight Down	total Up	total Down
200GeV	8	±1	± 7	4	13	2	±6	-1	0	0	-0.02	0	0	17	10
500GeV	36	±1	± 3	0	4	-5	±0	-1	0	0	-0.07	0	0	5	6
1000GeV	57	±0	± 3	0	4	-5	±0	-1	0	0	-0.10	0	0	5	6
1500GeV	65	±0	± 3	0	4	-5	±0	-2	0	-2	-0.09	0	0	5	7
2000GeV	67	±0	± 3	0	4	-5	±0	-3	0	-5	-0.07	0	1	5	8
2500GeV	68	±0	± 3	0	4	-5	±0	-4	0	-7	-0.04	-1	1	5	10
3000GeV	67	±0	± 3	0	4	-5	±0	-6	0	-11	-0.03	-1	1	5	13
4000GeV	60	±0	± 3	0	4	-5	±0	-9	0	-22	-0.02	-1	2	5	25
5000GeV	28	±1	± 1	-8	-8	-5	±8	-17	0	-52	0.00	-3	3	9	57
6000GeV	0	±8	± 3	0	4	-5	±0	0	0	0	0.00	0	0	5	6

Table 4: Relative uncertainties on the signal efficiencies in percentages for Drell-Yan produced spin-0 monopoles of charge $|g| = 1g_{\text{D}}$. The errors on the uncertainties are statistical. The total relative uncertainties are calculated as quadratic sums of the individual relative uncertainties including the 2.2% uncertainty on the luminosity measurement. Note that the δ-ray and material density uncertainties are taken as symmetric, as described in the text.

Spin$-\frac{1}{2}$ $1g_{\text{D}}$	eff.	MC Stat.	Det. material	G4 range cut	Birks High	Birks Low	δ-ray	TRT Occ.	LAr x-talk	Calo Arrival	Weight Up	Weight Down	total Up	total Down
200GeV	2	±2	± 2	12	22	9	±13	8	6	-8	6	7	33	16
500GeV	12	±1	± 6	10	19	2	±12	9	10	-6	10	10	31	14
1000GeV	24	±1	± 6	10	19	2	±12	12	12	-3	12	12	34	14
1500GeV	29	±1	± 6	10	19	2	±12	7	10	-6	10	11	31	14
2000GeV	32	±1	± 6	10	19	2	±12	4	8	-10	8	9	29	17
2500GeV	33	±1	± 6	10	19	2	±12	-1	5	-17	4	6	26	21
3000GeV	34	±1	± 6	10	19	2	±12	-5	3	-24	2	5	26	28
4000GeV	28	±1	± 6	10	19	2	±12	-7	4	-40	2	6	26	43
5000GeV	9	±1	± 3	-7	-8	-6	±9	-18	1	-66	-2	4	11	70
6000GeV	0	±11	± 6	10	19	2	±12	0	0	0	0	0	25	13

Table 5: Relative uncertainties on the signal efficiencies in percentages for Drell-Yan produced spin-$\frac{1}{2}$ monopoles of charge $|g| = 1g_{\text{D}}$. The errors on the uncertainties are statistical. The total relative uncertainties are calculated as quadratic sums of the individual relative uncertainties including the 2.2% uncertainty on the luminosity measurement. Note that the δ-ray and material density uncertainties are taken as symmetric, as described in the text.

Spin-0 $2g_{\text{D}}$	eff.	MC Stat.	Det. material	G4 range cut	Birks High	Birks Low	δ-ray prod.	TRT Occ.	LAr x-talk	Calo Arrival	Extrap	Weight Up	Weight Down	total Up	total Down
200GeV	0	±6	± 16	1	-2	-2	±1	0	-1	0	0.00	1	0	16	16
500GeV	1	±3	± 16	1	-2	-2	±1	0	0	0	0.01	0	0	16	16
1000GeV	4	±2	± 16	1	-2	-2	±1	-1	0	0	-0.01	0	0	16	16
1500GeV	7	±1	± 16	1	-2	-2	±1	0	0	0	-0.04	0	-0	16	16
2000GeV	10	±1	± 16	1	-2	-2	±1	-1	0	0	-0.01	0	0	16	16
2500GeV	13	±1	± 16	1	-2	-2	±1	0	0	0	-0.01	0	0	16	16
3000GeV	15	±1	± 16	1	-2	-2	±1	-1	0	0	-0.01	0	0	16	16
4000GeV	13	±1	± 16	1	-2	-2	±1	-3	0	0	-0.03	-1	1	16	16
5000GeV	1	±3	± 16	1	-2	-2	±1	-4	0	0	-0.02	0	-0	16	17
6000GeV	0	±0	± 16	1	-2	-2	±1	0	0	0	-0.02	0	0	16	16

Table 6: Relative uncertainties on the signal efficiencies in percentages for Drell-Yan produced spin-0 monopoles of charge $|g| = 2g_{\text{D}}$. The errors on the uncertainties are statistical. The total relative uncertainties are calculated as quadratic sums of the individual relative uncertainties including the 2.2% uncertainty on the luminosity measurement. Note that the δ-ray and material density uncertainties are taken as symmetric, as described in the text.

Spin−$\frac{1}{2}$ $2g_{\mathrm{D}}$	eff.	MC Stat.	Det. material	G4 range cut	Birks High	Birks Low	δ-ray	TRT Occ.	LAr x-talk	Calo Arrival	Weight Up	Weight Down	total Up	total Down
200GeV	0	±9	± 9	11	8	7	±11	-14	-10	0	-7	-7	21	24
500GeV	0	±6	± 9	11	8	7	±11	0	-8	0	-9	-8	21	20
1000GeV	1	±4	± 9	11	8	7	±11	-5	2	0	1	2	21	15
1500GeV	2	±3	± 9	11	8	7	±11	10	7	0	8	7	27	14
2000GeV	2	±2	± 9	11	8	7	±11	2	1	0	1	2	21	14
2500GeV	3	±2	± 9	11	8	7	±11	2	2	0	2	1	21	14
3000GeV	4	±2	± 9	11	8	7	±11	1	2	0	2	2	21	14
4000GeV	3	±2	± 9	11	8	7	±11	-2	5	0	4	6	23	14
5000GeV	0	±5	± 9	11	8	7	±11	11	8	0	8	7	27	14
6000GeV	0	±0	± 15	3	1	0	±3	0	0	0	0	0	16	16

Table 7: Relative uncertainties on the signal efficiencies in percentages for Drell-Yan produced spin-$\frac{1}{2}$ monopoles of charge $|g| = 2g_{\mathrm{D}}$. The errors on the uncertainties are statistical. The total relative uncertainties are calculated as quadratic sums of the individual relative uncertainties including the 2.2% uncertainty on the luminosity measurement. Due to lack of Drell-Yan sample for mass 6000 GeV the efficiency, TRT occ, LAr Cross Talk and Calorimeter Arrival systematics have been extrapolated from single particle efficiency maps. Note that the δ-ray and material density uncertainties are taken as symmetric, as described in the text.

Spin-0 20e	eff.	MC Stat.	Det. material	G4 range cut	Birks High	Birks Low	δ-ray prod.	TRT Occ.	LAr x-talk	Calo Arrival	Extrap	Weight Up	Weight Down	total Up	total Down
200GeV	18	±1	± 6	-7	1	-9	±10	-21	-9	0	-0.16	-2	2	12	28
500GeV	35	±1	± 1	0	4	-9	±6	-17	-9	0	-0.10	-2	1	8	22
1000GeV	48	±0	± 1	0	4	-9	±6	-14	-7	-2	-0.09	-2	1	8	19
1500GeV	53	±0	± 1	0	4	-9	±6	-16	-6	-3	-0.07	-2	2	8	21
2000GeV	55	±0	± 1	0	4	-9	±6	-17	-4	-5	-0.07	-2	2	8	21
2500GeV	56	±0	± 1	0	4	-9	±6	-18	-3	-8	-0.06	-2	2	8	23
3000GeV	55	±0	± 1	0	4	-9	±6	-18	-2	-11	-0.04	-3	3	8	24
4000GeV	49	±0	± 1	0	4	-9	±6	-21	-1	-22	-0.03	-3	4	8	33
5000GeV	25	±1	± 8	-7	-3	-4	±8	-22	0	-56	-0.02	-5	5	12	62
6000GeV	0	±10	± 1	0	4	-9	±6	0	0	0	0.00	0	0	8	11

Table 8: Relative uncertainties on the signal efficiencies in percentages for Drell-Yan produced spin-0 HECOs of charge $|z| = 20$. The errors on the uncertainties are statistical. The total relative uncertainties are calculated as quadratic sums of the individual relative uncertainties including the 2.2% uncertainty on the luminosity measurement. Note that the δ-ray and material density uncertainties are taken as symmetric, as described in the text.

Spin-$\frac{1}{2}$ 20e	eff.	MC Stat.	Det. material	G4 range cut	Birks High	Birks Low	δ-ray	TRT Occ.	LAr x-talk	Calo Arrival	Weight Up	Weight Down	total Up	total Down
200GeV	7	±2	± 12	12	25	7	±6	-11	6	-8	13	18	39	19
500GeV	16	±1	± 6	7	14	-4	±2	-12	2	-8	8	13	23	16
1000GeV	24	±1	± 6	7	14	-4	±2	-9	4	-10	8	12	23	16
1500GeV	28	±1	± 6	7	14	-4	±2	-14	3	-14	4	11	21	21
2000GeV	29	±1	± 6	7	14	-4	±2	-14	5	-17	5	11	21	24
2500GeV	28	±1	± 6	7	14	-4	±2	-15	5	-23	4	10	21	29
3000GeV	27	±1	± 6	7	14	-4	±2	-18	4	-28	1	9	20	34
4000GeV	24	±1	± 6	7	14	-4	±2	-19	4	-39	1	9	20	44
5000GeV	9	±1	± 3	1	6	3	±2	-20	5	-68	-1	10	13	71
6000GeV	0	±15	± 6	7	14	-4	±2	0	0	0	0	0	17	8

Table 9: Relative uncertainties on the signal efficiencies in percentages for Drell-Yan produced spin-$\frac{1}{2}$ HECOs of charge $|z| = 20$. The errors on the uncertainties are statistical. The total relative uncertainties are calculated as quadratic sums of the individual relative uncertainties including the 2.2% uncertainty on the luminosity measurement. Note that the δ-ray and material density uncertainties are taken as symmetric, as described in the text.

Spin-0 40e	eff.	MC Stat.	Det. material	G4 range cut	Birks High	Birks Low	δ-ray prod.	TRT Occ.	LAr x-talk	Calo Arrival	Extrap	Weight Up	Weight Down	total Up	total Down
200GeV	19	±1	± 3	0	0	1	±2	-8	-1	0	-0.19	-1	1	5	9
500GeV	41	±1	± 3	0	0	1	±2	-3	-1	0	-0.16	0	0	5	6
1000GeV	51	±0	± 3	0	0	1	±2	-3	0	0	-0.09	-1	0	5	5
1500GeV	52	±0	± 3	0	0	1	±2	-3	0	-1	-0.05	0	0	5	6
2000GeV	49	±0	± 3	0	0	1	±2	-4	0	-3	-0.03	0	0	5	7
2500GeV	45	±0	± 3	0	0	1	±2	-4	0	-6	-0.03	-1	1	5	9
3000GeV	42	±1	± 3	0	0	1	±2	-5	0	-7	-0.02	0	0	5	10
4000GeV	26	±1	± 3	0	0	1	±2	-5	0	-6	-0.01	-1	1	5	9
5000GeV	2	±3	± 3	0	0	1	±2	-7	0	-2	0.01	-2	1	5	9
6000GeV	0	±0	± 3	0	0	1	±2	0	0	0	0.00	0	0	4	4

Table 10: Relative uncertainties on the signal efficiencies in percentages for Drell-Yan produced spin-0 HECOs of charge $|z| = 40$. The errors on the uncertainties are statistical. The total relative uncertainties are calculated as quadratic sums of the individual relative uncertainties including the 2.2% uncertainty on the luminosity measurement. Note that the δ-ray and material density uncertainties are taken as symmetric, as described in the text.

Spin-$\frac{1}{2}$ 40e	eff.	MC Stat.	Det. material	G4 range cut	Birks High	Birks Low	δ-ray	TRT Occ.	LAr x-talk	Calo Arrival	Weight Up	Weight Down	total Up	total Down
200GeV	6	±2	± 3	9	9	10	±5	10	20	-10	20	22	41	12
500GeV	15	±1	± 3	9	9	10	±5	15	19	-5	20	21	41	8
1000GeV	20	±1	± 3	9	9	10	±5	8	12	-3	12	13	29	7
1500GeV	22	±1	± 3	9	9	10	±5	3	7	-3	7	8	21	7
2000GeV	20	±1	± 3	9	9	10	±5	-1	4	-5	4	5	19	8
2500GeV	17	±1	± 3	9	9	10	±5	-2	4	-8	3	5	19	10
3000GeV	16	±1	± 3	9	9	10	±5	-4	3	-10	2	3	18	12
4000GeV	9	±1	± 3	9	9	10	±5	-5	1	-11	0	2	17	14
5000GeV	0	±4	± 3	9	9	10	±5	-8	-2	-2	-4	0	17	11
6000GeV	0	±0	± 3	9	9	10	±5	0	0	0	0	0	17	6

Table 11: Relative uncertainties on the signal efficiencies in percentages for Drell-Yan produced spin-$\frac{1}{2}$ HECOs of charge $|z| = 40$. The errors on the uncertainties are statistical. The total relative uncertainties are calculated as quadratic sums of the individual relative uncertainties including the 2.2% uncertainty on the luminosity measurement. Note that the δ-ray and material density uncertainties are taken as symmetric, as described in the text.

Spin-0 60e	eff.	MC Stat.	Det. material	G4 range cut	Birks High	Birks Low	δ-ray prod.	TRT Occ.	LAr x-talk	Calo Arrival	Extrap	Weight Up	Weight Down	total Up	total Down
200GeV	6	±1	± 2	0	1	1	±1	-1	0	0	-0.03	0	-0	3	3
500GeV	18	±1	± 2	0	1	1	±1	-1	0	0	-0.04	0	0	3	3
1000GeV	26	±1	± 2	0	1	1	±1	-1	0	0	-0.02	0	0	3	3
1500GeV	26	±1	± 2	0	1	1	±1	-1	0	0	-0.01	0	0	3	3
2000GeV	22	±1	± 2	0	1	1	±1	-1	0	0	0.00	0	0	3	3
2500GeV	20	±1	± 2	0	1	1	±1	-1	0	0	-0.01	0	0	3	3
3000GeV	17	±1	± 2	0	1	1	±1	-2	0	-1	0.00	0	0	3	3
4000GeV	5	±2	± 2	0	1	1	±1	-2	0	-1	-0.01	0	1	3	4
5000GeV	0	±29	± 2	0	1	1	±1	0	0	0	0.00	0	0	3	3
6000GeV	0	±0	± 2	0	1	1	±1	0	0	0	0.00	0	0	3	3

Table 12: Relative uncertainties on the signal efficiencies in percentages for Drell-Yan produced spin-0 HECOs of charge $|z| = 60$. The errors on the uncertainties are statistical. The total relative uncertainties are calculated as quadratic sums of the individual relative uncertainties including the 2.2% uncertainty on the luminosity measurement. Note that the δ-ray and material density uncertainties are taken as symmetric, as described in the text.

Spin-$\frac{1}{2}$ 60e	eff.	MC Stat.	Det. material	G4 range cut	Birks High	Birks Low	δ-ray	TRT Occ.	LAr x-talk	Calo Arrival	Weight Up	Weight Down	total Up	total Down
200GeV	2	±2	± 0	3	5	4	±4	12	13	-5	13	13	27	7
500GeV	5	±1	± 0	3	5	4	±4	9	10	-2	9	10	21	5
1000GeV	9	±1	± 0	3	5	4	±4	3	3	-1	3	4	10	5
1500GeV	8	±1	± 0	3	5	4	±4	1	2	-1	2	2	9	4
2000GeV	7	±1	± 0	3	5	4	±4	-1	0	-1	0	1	8	4
2500GeV	6	±1	± 0	3	5	4	±4	1	2	-1	2	2	9	4
3000GeV	5	±1	± 0	3	5	4	±4	-1	1	-2	1	1	8	5
4000GeV	1	±3	± 0	3	5	4	±4	0	2	-1	2	3	9	4
5000GeV	0	±53	± 0	3	5	4	±4	0	0	0	0	0	8	4
6000GeV	0	±0	± 0	3	5	4	±4	0	0	0	0	0	8	4

Table 13: Relative uncertainties on the signal efficiencies in percentages for Drell-Yan produced spin-$\frac{1}{2}$ HECOs of charge $|z| = 60$. The errors on the uncertainties are statistical. The total relative uncertainties are calculated as quadratic sums of the individual relative uncertainties including the 2.2% uncertainty on the luminosity measurement. Note that the δ-ray and material density uncertainties are taken as symmetric, as described in the text.

Spin-0 80e	eff.	MC Stat.	Det. material	G4 range cut	Birks High	Birks Low	δ-ray prod.	TRT Occ.	LAr x-talk	Calo Arrival	Extrap	Weight Up	Weight Down	total Up	total Down
200GeV	2	±2	± 7	4	5	5	±4	-1	0	0	0.00	0	-0	11	8
500GeV	4	±1	± 7	4	5	5	±4	-1	0	0	0.00	0	0	11	8
1000GeV	7	±1	± 7	4	5	5	±4	-1	0	0	-0.01	0	0	11	8
1500GeV	7	±1	± 7	4	5	5	±4	-1	0	0	0.00	0	-0	11	8
2000GeV	5	±1	± 7	4	5	5	±4	-1	0	0	0.00	0	-0	11	8
2500GeV	4	±1	± 7	4	5	5	±4	-1	0	0	0.00	0	0	11	8
3000GeV	3	±2	± 7	4	5	5	±4	-1	0	0	-0.01	0	0	11	8
4000GeV	0	±6	± 7	4	5	5	±4	-1	0	0	0.00	0	0	11	8
5000GeV	0	±0	± 7	4	5	5	±4	0	0	0	0.00	0	0	11	8
6000GeV	0	±0	± 7	4	5	5	±4	0	0	0	0.00	0	0	11	8

Table 14: Relative uncertainties on the signal efficiencies in percentages for Drell-Yan produced spin-0 HECOs of charge $|z| = 80$. The errors on the uncertainties are statistical. The total relative uncertainties are calculated as quadratic sums of the individual relative uncertainties including the 2.2% uncertainty on the luminosity measurement. Note that the δ-ray and material density uncertainties are taken as symmetric, as described in the text.

Spin-$\frac{1}{2}$ 80e	eff.	MC Stat.	Det. material	G4 range cut	Birks High	Birks Low	δ-ray	TRT Occ.	LAr x-talk	Calo Arrival	Weight Up	Weight Down	total Up	total Down
200GeV	0	±2	± 9	5	7	6	±5	5	6	-3	7	6	19	11
500GeV	2	±2	± 9	5	7	6	±5	0	1	-1	1	2	15	11
1000GeV	2	±2	± 9	5	7	6	±5	1	2	0	2	3	15	11
1500GeV	2	±2	± 9	5	7	6	±5	-1	-1	0	-1	-1	15	11
2000GeV	2	±2	± 9	5	7	6	±5	-2	-1	0	-1	-2	15	11
2500GeV	1	±2	± 9	5	7	6	±5	1	1	0	1	1	15	11
3000GeV	1	±3	± 9	5	7	6	±5	2	2	0	2	2	15	11
4000GeV	0	±9	± 9	5	7	6	±5	0	0	0	0	0	15	11
5000GeV	0	±0	± 9	5	7	6	±5	0	0	0	0	0	15	11
6000GeV	0	±0	± 9	5	7	6	±5	0	0	0	0	0	15	11

Table 15: Relative uncertainties on the signal efficiencies in percentages for Drell-Yan produced spin-$\frac{1}{2}$ HECOs of charge $|z| = 80$. The errors on the uncertainties are statistical. The total relative uncertainties are calculated as quadratic sums of the individual relative uncertainties including the 2.2% uncertainty on the luminosity measurement. Note that the δ-ray and material density uncertainties are taken as symmetric, as described in the text.

Spin-0 100e	eff.	MC Stat.	Det. material	G4 range cut	Birks High	Birks Low	δ-ray	TRT Occ.	LAr x-talk	Calo Arrival	Extrap.	Weight Up	Weight Down	total Up	total Down
200GeV	0	±4	± 15	1	1	-2	±1	-2	0	0	0.00	0	0	15	15
500GeV	1	±3	± 15	1	1	-2	±1	-1	0	0	0.00	0	0	15	15
1000GeV	3	±2	± 15	1	1	-2	±1	-1	0	0	-0.01	0	0	15	15
1500GeV	2	±2	± 15	1	1	-2	±1	-1	0	0	0.00	0	0	15	15
2000GeV	2	±3	± 15	1	1	-2	±1	-1	0	0	0.00	0	0	15	15
2500GeV	1	±3	± 15	1	1	-2	±1	-1	0	0	0.00	0	0	15	15
3000GeV	1	±4	± 15	1	1	-2	±1	-1	0	0	-0.01	0	1	15	15
4000GeV	0	±59	± 15	1	1	-2	±1	0	0	0	0.00	0	0	15	15
5000GeV	0	±0	± 15	1	1	-2	±1	0	0	0	0.00	0	0	15	15
6000GeV	0	±0	± 15	1	1	-2	±1	0	0	0	0.00	0	0	15	15

Table 16: Relative uncertainties on the signal efficiencies in percentages for Drell-Yan produced spin-0 HECOs of charge $|z| = 100$. The errors on the uncertainties are statistical. The total relative uncertainties are calculated as quadratic sums of the individual relative uncertainties including the 2.2% uncertainty on the luminosity measurement. Due to lack of Drell-Yan sample the extrapolation systematic uncertainty of charge 80e has been included as an approximation to account for using this method to calculate the efficiency. Note that the δ-ray and material density uncertainties are taken as symmetric, as described in the text.

Spin-$\frac{1}{2}$ 100e	eff.	MC Stat.	Det. material	G4 range cut	Birks High	Birks Low	δ-ray	TRT Occ.	LAr x-talk	Calo. Arrival	Extrap.	Weight Up	Weight Down	total Up	total Down
200GeV	0	±18	± 20	0	0	-4	±0	-2	-1	0	0.00	0	0	20	20
500GeV	0	±8	± 20	0	0	-4	±0	-1	0	0	0.00	0	0	20	20
1000GeV	1	±6	± 20	0	0	-4	±0	-1	0	0	-0.01	0	0	20	20
1500GeV	1	±6	± 20	0	0	-4	±0	-1	0	0	0.00	0	0	20	20
2000GeV	0	±8	± 20	0	0	-4	±0	-1	0	0	0.00	0	0	20	20
2500GeV	0	±9	± 20	0	0	-4	±0	-1	0	0	0.00	0	0	20	20
3000GeV	0	±13	± 20	0	0	-4	±0	0	0	0	-0.01	0	0	20	20
4000GeV	0	±157	± 20	0	0	-4	±0	0	0	0	0.00	0	0	20	20
5000GeV	0	±0	± 20	0	0	-4	±0	0	0	0	0.00	0	0	20	20
6000GeV	0	±0	± 20	0	0	-4	±0	0	0	0	0.00	0	0	20	20

Table 17: Relative uncertainties on the signal efficiencies in percentages for Drell-Yan produced spin-$\frac{1}{2}$ HECOs of charge $|z| = 100$. The errors on the uncertainties are statistical. The total relative uncertainties are calculated as quadratic sums of the individual relative uncertainties including the 2.2% uncertainty on the luminosity measurement. Due to lack of Drell-Yan sample the efficiency, TRT occ, LAr Cross Talk and Calorimeter Arrival systematics have been extrapolated from single particle efficiency maps. The extrapolation systematic uncertainty of charge 80e has been included as an approximation to account for using this method. Note that the δ-ray and material density uncertainties are taken as symmetric, as described in the text.

G Cross Section Limits with Only Statistical Uncertainty

To evaluate the effect of the systematic uncertainties in the cross section limits, a calculation of the cross section upper limit is done using only the statistical uncertainties for the efficiencies for each mass-charge point. The cross section limits differ by at most 12% (on average 3.2%) as compared to when the systematic uncertainties are included in the calculation. Figures 23-26 show the limits including statistical uncertainties only.

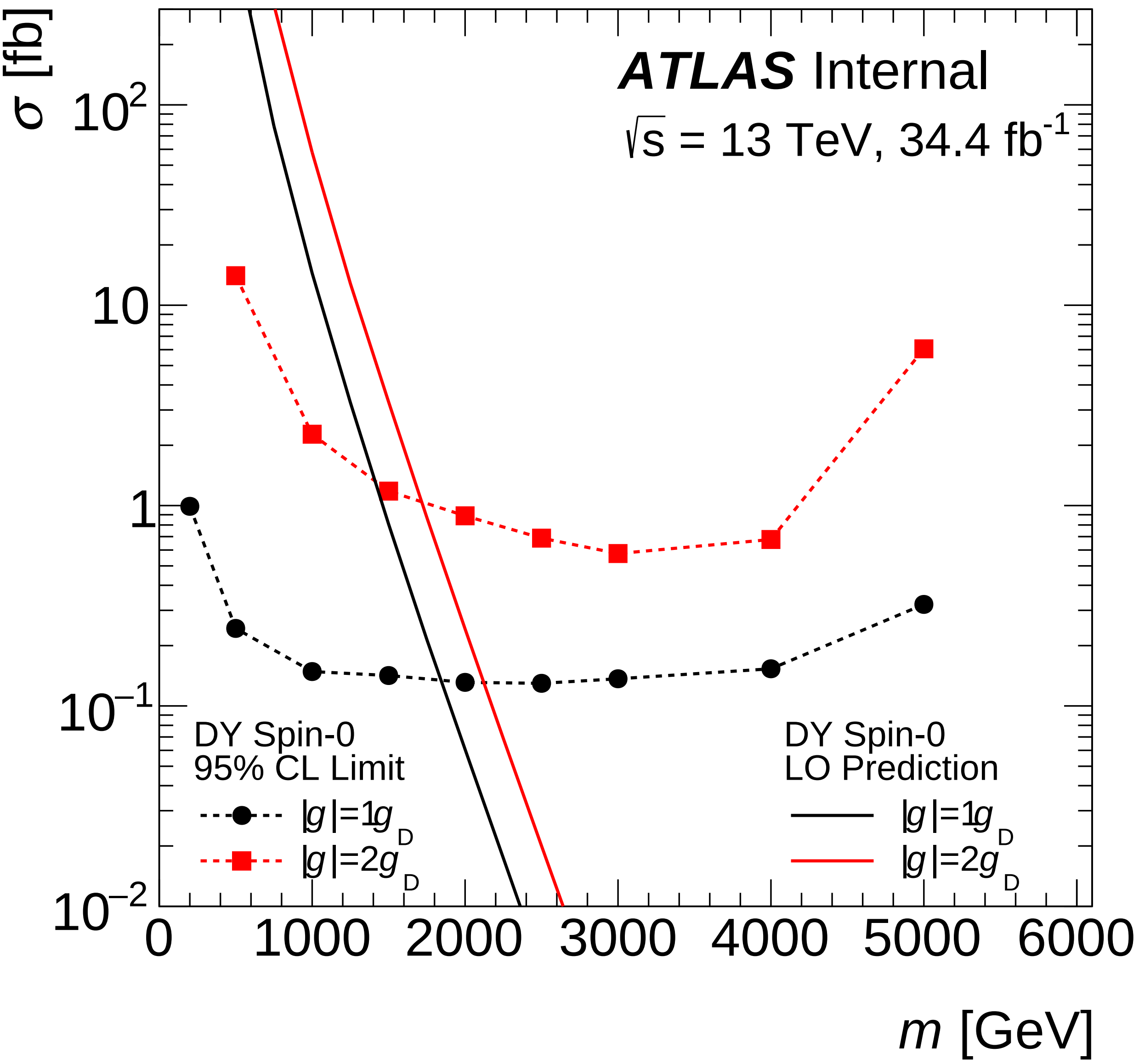

Figure 23: Observed 95% CL upper limits for Drell-Yan spin-0 monopoles as a function of HIP mass in various scenarios (dashed lines with markers). Only the statistical uncertainties were included in the upper limit calculations. Overlaid on the plots are the theoretical cross-sections (solid lines).

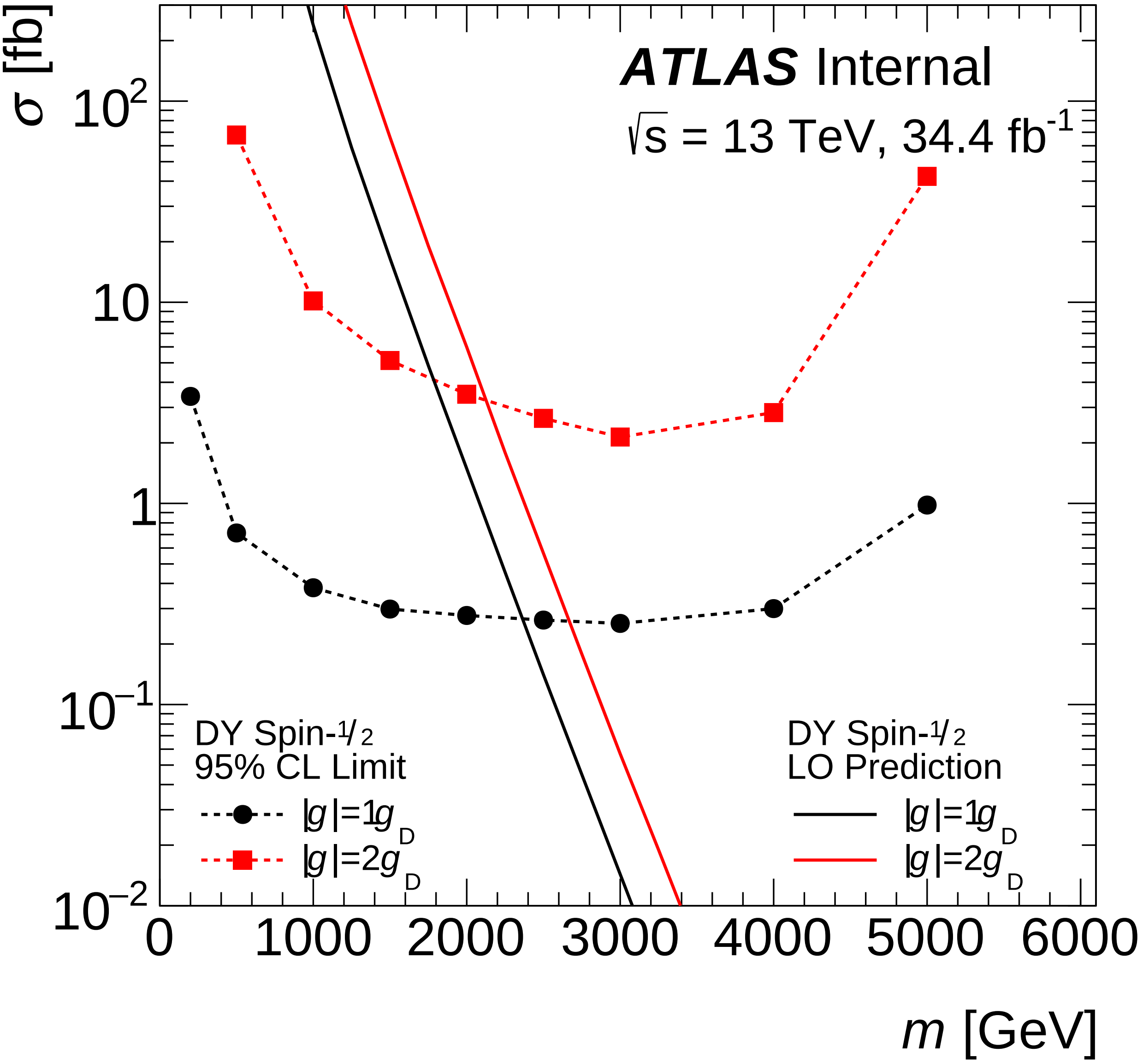

Figure 24: Observed 95% CL upper limits for Drell-Yan spin-$\frac{1}{2}$ monopoles as a function of HIP mass in various scenarios (dashed lines with markers). Only the statistical uncertainties were included in the upper limit calculations. Overlaid on the plots are the theoretical cross-sections (solid lines).

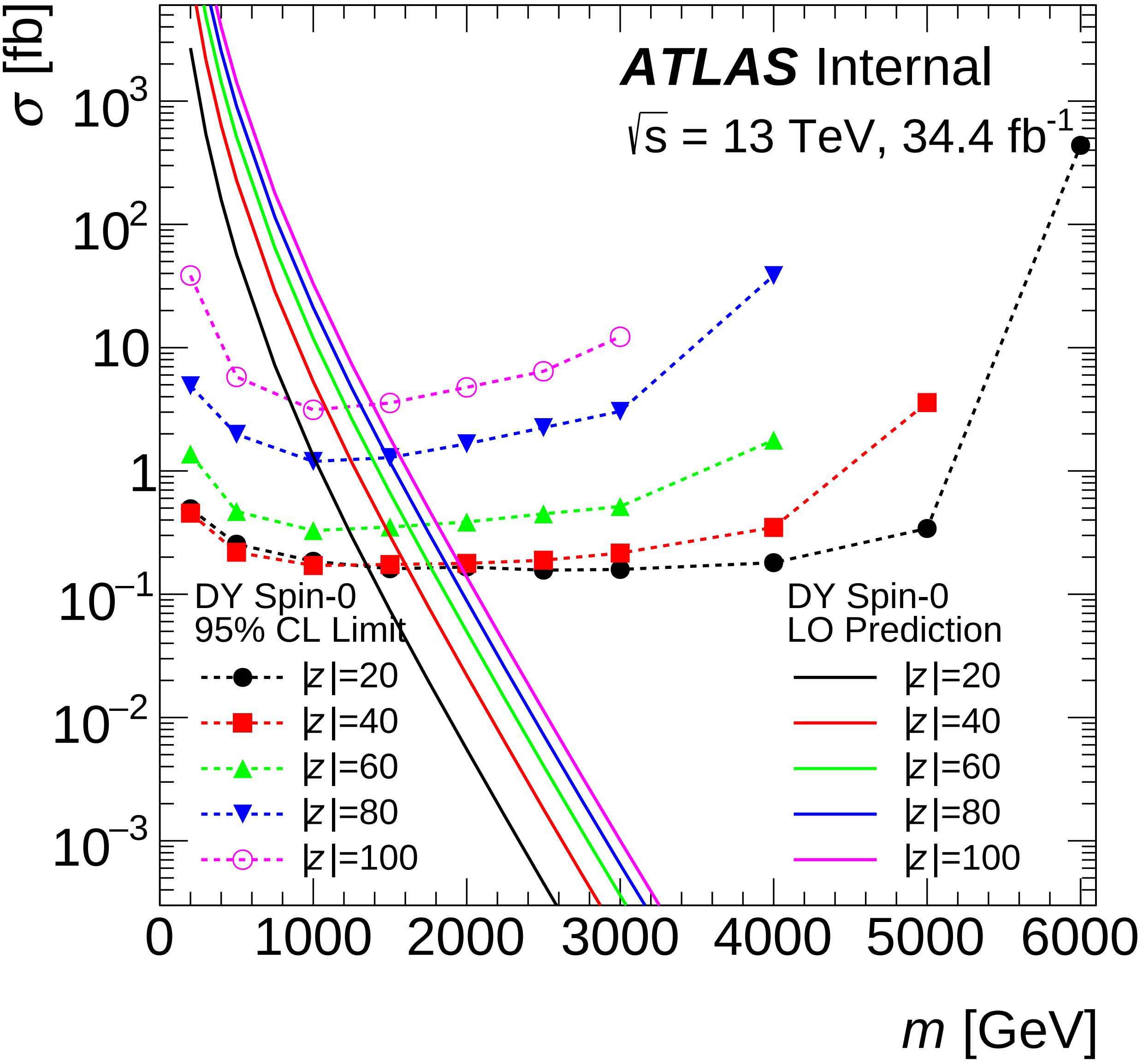

Figure 25: Observed 95% CL upper limits for Drell-Yan spin-0 HECOs as a function of HIP mass in various scenarios (dashed lines with markers). Only the statistical uncertainties were included in the upper limit calculations. Overlaid on the plots are the theoretical cross-sections (solid lines).

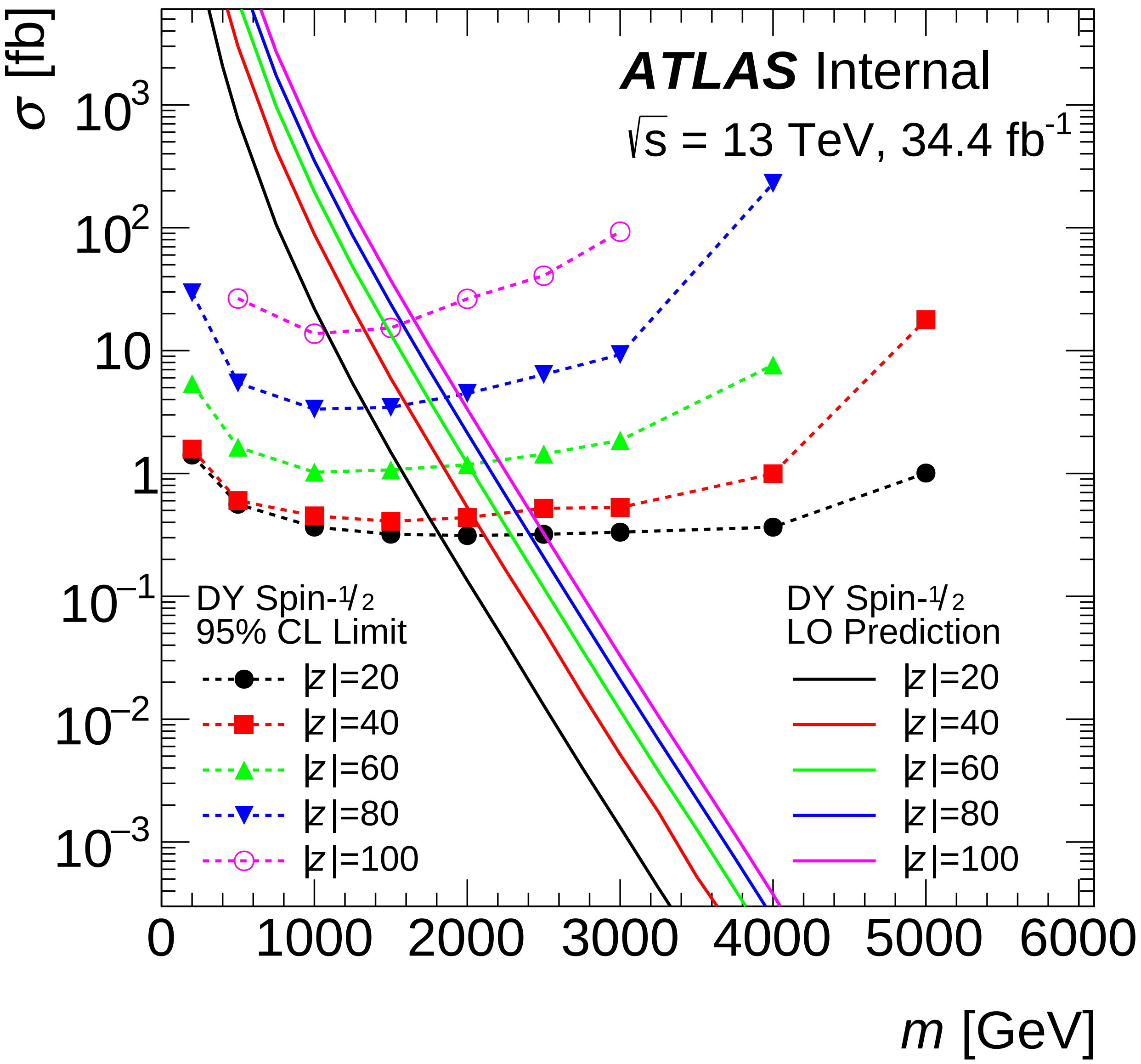

Figure 26: Observed 95% CL upper limits for Drell-Yan spin-$\frac{1}{2}$ HECOs as a function of HIP mass in various scenarios (dashed lines with markers). Only the statistical uncertainties were included in the upper limit calculations. Overlaid on the plots are the theoretical cross-sections (solid lines).